Spin-Exchange Optical Pumping and Nuclear Magnetic Resonance of ^{129}Xe

A thesis submitted to the University of Sheffield
for the degree of
Doctor of Philosophy in Physics

Graham Norquay

December 2014

The Medical School
Department of Cardiovascular Science
Unit of Academic Radiology
Royal Hallamshire Hospital
S10 2JF, Sheffield
United Kingdom

Abstract

The nuclear spin polarisation of ^{129}Xe can be increased by four to five orders of magnitude using the technique spin-exchange optical pumping (SEOP). The resulting enhancement in polarisation can be utilised to dramatically enhance the sensitivity of ^{129}Xe in nuclear magnetic resonance (NMR) applications. This thesis is concerned with the physics of SEOP and NMR spectroscopy of hyperpolarised ^{129}Xe. Its general aims are to optimise the production of hyperpolarised ^{129}Xe and to evaluate mechanisms that underpin NMR phenomena of ^{129}Xe in blood. These goals are pursued in the following four distinct projects:

Spin-exchange optical pumping physics

1. Optimisation and characterisation of a continuous-flow ^{129}Xe-Rb SEOP polariser operating at a mid-range cell pressure of 2 bars with xenon (Xe) concentrations of 3 %. It was found that the achievable polarisation during gas flow using an external cavity diode laser (ECDL) with 25 W incident on the SEOP cell (500 cm^3 volume) is ~15 % (flow rate of 100 sccm). The minimum number of photons required to induce a single ^{129}Xe nuclear spin flip was experimentally measured to be 30, which approaches the theoretical limit of 20 photons per spin flip.

2. Further optimisation of the SEOP polariser using a laser diode array (LDA), frequency-narrowed with an internal volume holographic grating (VHG), and collimated using a custom-built optical train (OT) telescope system. In this project, improved optical collimation over the 25 cm length of the SEOP cell was achieved with the optical train and the incident laser power was increased to 50 W. The ^{129}Xe polarisation

during gas flow was measured to be 45 % (100 sccm), a factor of three higher than that achieved with the ECDL. In addition, good agreement between experimental and the theoretical ^{129}Xe polarisations was observed using the LDA-VHG OT as an optical input.

Nuclear magnetic resonance of hyperpolarised ^{129}Xe

3. Evaluation of the relaxation and exchange dynamics of hyperpolarised ^{129}Xe in human blood at 1.5 T. It was found that the ^{129}Xe relaxation rate decreases non-linearly with increasing blood oxygenation. A two-site exchange model was used to evaluate the ^{129}Xe magnetisation dynamics in whole blood samples, enabling the determination of constants underpinning ^{129}Xe NMR relaxation and exchange in whole blood samples.

4. Using hyperpolarised ^{129}Xe NMR to probe pulmonary blood oxygenation. A non-linear relationship between the chemical shift of ^{129}Xe in red blood cells and blood oxygenation was determined *in vitro* on human blood samples at 1.5 T and 3 T. This relationship was used for dynamic monitoring of pulmonary blood oxygenation in healthy volunteers during breath-hold apnoea on a 3 T clinical scanner.

Acknowledgements

Firstly, I would like to express my appreciation and thanks to my supervisor Jim Wild. His supervision throughout my PhD has been excellent, giving me the flexibility and freedom to pursue my own ideas while stimulating my interest in NMR through the discussion of problems and experimental results.

I would like to thank Steven Parnell for helping me with the concepts and practical aspects of spin-exchange optical pumping physics. For helping with dissolved-phase ^{129}Xe spectroscopy experiments, I would like to thank General Leung for his enthusiasm and helpful experimental input. I am grateful to Neil Stewart for his help with experiments on the ^{129}Xe polariser, and for his careful and conscientious approach to proof-reading manuscripts. Thank you Jan Wolber for stimulating and helpful discussions on the theoretical and experimental aspects of ^{129}Xe NMR in blood.

I would also like to thank all of my colleagues – past and present – at the University of Sheffield for making helpful contributions to this project and for being great fun to work with. In chronological order, they are as follows: Salma Ajraoui, Martin Deppe, Peggy Xu, Juan Parra-Robles, Helen Marshall, Andrew Swift, Leanne Armstrong, Yvonne Steel, Gillian Tozer, Aneurin Kennerly, Stephen Reynolds, Felix Horn, Guilhem Collier, Madhwesha Rao.

Lastly, I would like to thank my parents Helen and Alan, my two brothers Mark and Paul and my partner Katie for all their support during these years.

This thesis was supported by grants from CRUK and ESPRC.

Contents

Chapter 1

Introduction

The exploration of the physical phenomenon of nuclear magnetic resonance (NMR) arose from measurements of nuclear spin in the early 1930s [1, 2] and the first observation of NMR in 1937 [3] (work for which Rabi was awarded the Nobel prize in Physics in 1944). The first observations of NMR in bulk materials were made independently in 1946 by Bloch, Hansen and Packard (proton resonance from water samples) [4] and Purcell, Torrey and Pound (proton resonance from a block of paraffin) [5]. Since those early experiments, NMR has developed into a broad field, and has widespread applications in many disciplines; from structural studies of chemical compounds, following the discovery of the NMR chemical shift [6], to medical diagnosis following the invention of magnetic resonance imaging (MRI) [7]. Conventional MRI relies on the high density of protons present in soft biological tissues, and is therefore not suitable for probing areas of the body with low tissue density, such as the lung airspaces, where the proton density is very low.

The use of hyperpolarised noble gas MRI for biomedical applications was first demonstrated in 1994 with hyperpolarised ^{129}Xe images of the airspaces of excised mouse lungs [8]. Following this, the first *in vivo* images of hyperpolarised ^{3}He and ^{129}Xe in human lungs were reported [9, 10]. Since

then, new techniques using hyperpolarised ^{3}He and ^{129}Xe MR have been developed, enabling numerous novel studies of lung structure and function [11-15]. Xe has the added benefit of being soluble in biological tissues, and will thus readily dissolve into blood and tissues within the lungs. To date, this solubility has been utilised in MR experiments to quantify Xe gas exchange [16-19] in the lungs and to monitor uptake in distal tissues such as the brain [20, 21]. Crucial to the success of these "dissolved-phase" ^{129}Xe NMR experiments is sufficiently high levels of ^{129}Xe polarisation (to enable signal detection of the ^{129}Xe dissolved in biological tissues and blood) and good knowledge of the ^{129}Xe NMR parameters underpinning the ^{129}Xe signal dynamics in human blood.

This thesis is concerned with the physics of spin-exchange optical pumping (SEOP) – a technique used to enhance nuclear polarisation – and NMR spectroscopy of hyperpolarised ^{129}Xe. Its main aims are to optimise the production of hyperpolarised ^{129}Xe and to evaluate the mechanisms that underpin NMR phenomena of ^{129}Xe in blood. After introducing the theory of NMR and in Chapter 2, Chapters 3 and 4 detail experiments and theoretical modelling used to optimise the production of hyperpolarised ^{129}Xe on a continuous-flow ^{129}Xe SEOP polariser. Chapters 5 and 6 are concerned with understanding the fundamental NMR properties of ^{129}Xe in human blood. Chapter 5 describes a series of systematic *in vitro* experiments – combined with a two-site (red blood cells and plasma) Xe exchange model – to determine the oxygenation dependence of the spin-lattice relaxation rate of ^{129}Xe dissolved in human blood. Chapter 6 investigates the feasibility of using ^{129}Xe NMR as a probe for pulmonary blood oxygenation *in vivo* by utilising the observation (from *in vitro* experiments) of a non-linear relationship between the ^{129}Xe red blood cell chemical shift and blood oxygenation.

Chapter 2

NMR and SEOP fundamentals

2.1 Introduction

This chapter covers the theory of NMR and SEOP relevant to the experimental work and results in this thesis. First, the phenomenon of NMR is explained from the point of view of a single spin magnetic moment, where the fundamental interactions with external and internal magnetic fields are described. The next section covers aspects of macroscopic magnetisation necessary to understand and interpret basic NMR experiments, where the equations of motion of the net magnetisation vector in the laboratory and rotating reference frames are introduced, and the Bloch equations describing the time evolution of interacting spins are derived. The solutions to the Bloch equations are then used to explain the concept of pulsed Fourier transform NMR spectroscopy. Next, the theory of spin-lattice relaxation applied to homonuclear and heteronuclear spin systems is covered, where the spectral density function is introduced to enable a quantitative description of the spin relaxation process. The chapter concludes with an introduction to the theoretical aspects of SEOP, the process used to enhance (hyperpolarise) the polarisation of the ^{129}Xe nuclei samples experimented upon in this thesis.

2.2 NMR principles

NMR stems from a quantum mechanical property of the nucleus: spin, a form of angular momentum. Unlike conventional forms of angular momentum, spin does not arise from particle rotations, but rather, like charge and mass, it is an intrinsic property of the particle itself. Atomic nuclei that exhibit a non-zero spin angular momentum, $\mathbf{I}$, in their ground state have an associated dipolar magnetic moment [22]

$$\boldsymbol{\mu} = \gamma\hbar\mathbf{I} \tag{2.1}$$

collinear with it, where γ is the gyromagnetic ratio, which takes a unique value for each nuclear species, and $\hbar$ is the reduced Planck's constant ($h/2\pi$). A spin system, $\big|\psi(t)\big\rangle$, can be described quantum mechanically by the time-dependent Schrödinger equation

$$i\hbar\frac{\partial}{\partial t}\big|\psi(t)\big\rangle = \mathcal{H}(t)\big|\psi(t)\big\rangle. \tag{2.2}$$

The time evolution of $\big|\psi(t)\big\rangle$ is determined by the Hamiltonian operator, $\mathcal{H}(t)$, which describes the total energy of the spin system. For a nucleus located within a static magnetic field, the spin interactions can be described phenomenologically by the NMR spin Hamiltonian [23]

$$\mathcal{H}_{\mathrm{N}} = \underbrace{\mathcal{H}_{\mathrm{Z}} + \mathcal{H}_{\mathrm{RF}}}_{\text{external}} + \underbrace{\mathcal{H}_{\mathrm{D}} + \mathcal{H}_{\mathrm{CS}} + \mathcal{H}_{J} + \mathcal{H}_{\mathrm{Q}}}_{\text{internal}}, \tag{2.3}$$

where $\mathcal{H}_{\mathrm{Z}}$ and $\mathcal{H}_{\mathrm{RF}}$ describe the static field (Zeeman effect) and the radio frequency (RF) interaction, which both act externally on the spin system. $\mathcal{H}_{\mathrm{D}}$ represents the direct (or through-space) dipole-dipole coupling between spins (technically, spin-bearing nuclei); $\mathcal{H}_{\mathrm{CS}}$ represents the chemical shift interaction due to nuclear shielding effects; $\mathcal{H}_{J}$ represents J-couplings, indirect spin-spin interactions mediated by electron spins; and $\mathcal{H}_{\mathrm{Q}}$, which represents quadrupole electric interactions of $I > 1/2$ nuclei with the

surrounding electric fields. $\mathcal{H}_{\mathrm{D}}$ to $\mathcal{H}_{\mathrm{Q}}$ are Hamiltonians that represent internal spin interactions (interactions originating from within the NMR-sensitive sample itself). Although the latter two interactions are important in the study of a variety of systems, they are not relevant to the experiments performed in this thesis, and are therefore not discussed in any further in this chapter.

2.2.1 External spin interactions

Static field interaction: Zeeman effect

In the presence of a static magnetic field, $\mathbf{B}_0$, an interaction energy of the amount $-\boldsymbol{\mu}\cdot\mathbf{B}_0$ exists, so that the dipole moment can be described by a simple Hamiltonian of the form

$$\mathcal{H}_{\mathrm{Z}} = -\boldsymbol{\mu}\cdot\mathbf{B}_0 = -\gamma\hbar\mathbf{I}\cdot\mathbf{B}_0 . \tag{2.4}$$

If the magnetic field is directed along the z-axis ($\mathbf{B}_0 = B_0\hat{z}$), then

$$\mathcal{H}_{\mathrm{Z}} = -\mu_z B_0 = -\gamma\hbar I_z B_0 , \tag{2.5}$$

where I_z denotes the z-component of angular momentum. The energies of the dipole moments will take discrete values according to the eigenvalues of this Hamiltonian, which are given by multiples ($\gamma\hbar B_0$) of the eigenvalues of I_z. The allowed energies are therefore

$$E_m = -m\gamma\hbar B_0 . \tag{2.6}$$

m is the referred to as the nuclear spin projection quantum number and may be any one of the $2I+1$ values $I, I-1, \ldots, -I$, where I represents the nuclear spin quantum number, which can take half-integer or integer values. This discretisation of nuclear dipole energy in the presence of an external static magnetic field is referred to as the nuclear Zeeman interaction, and for any value of I, the energy separation between adjacent levels is given by $\gamma\hbar B_0$. Fig. 2.1 below depicts degenerate Zeeman energy levels for $I = 1/2$ in the

absence of a static external magnetic field ($B_0 = 0$) and also the resulting energy level splitting in the presence of a finite external magnetic field ($B_0 \neq 0$) for a nucleus with a positive gyromagnetic ratio.

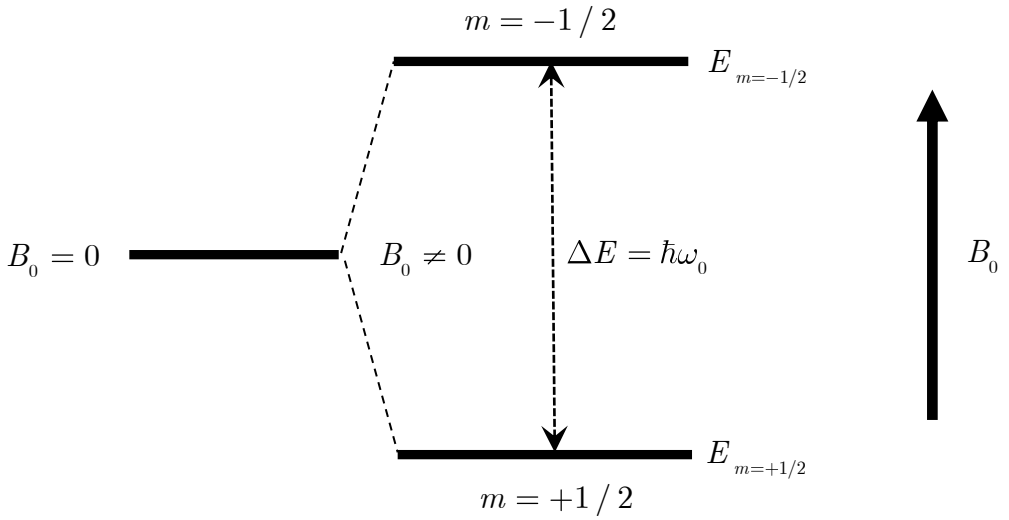

Figure 2.1: Zeeman energy levels for a spin-1/2 system with a positive gyromagnetic ratio.

The two allowed energies for $m = \pm 1/2$, according to Eq. 2.6, differ in value by

$$\Delta E = E_{m=-1/2} - E_{m=1/2} = \frac{1}{2}\gamma\hbar B_0 - \left(-\frac{1}{2}\gamma\hbar B_0\right) = \hbar\omega_0 , \tag{2.7}$$

where ω_0 is known as the Larmor frequency, the frequency associated with spin transitions between the nuclear energy levels. The sense of ω_0 depends on the sign of the gyromagnetic ratio of the nuclear species:

$$\omega_0 = -\gamma B_0 , \text{ for } \gamma > 0 \tag{2.8a}$$

and

$$\omega_0 = +\gamma B_0 , \text{ for } \gamma < 0 . \tag{2.8b}$$

It is worth noting that Planck's constant does not appear in the resonance equation, suggesting that this result is closely related to a classical picture.

Indeed, a classical treatment (as we shall see later in Section 2.2.3) also gives Eqs. 2.8a and 2.8b, where ω_0 is understood as the precession frequency of a macroscopic ensemble of nuclear magnetic moments around a static magnetic field, $\mathbf{B}_0$.

Radiofrequency field interaction

In an NMR experiment, nuclei are exposed to a transient oscillating magnetic field applied perpendicular to the static field. The effect of a linearly polarised oscillatory field, $\mathbf{B}_x = B_x \cos(\omega t)$, is most readily analysed by splitting it into two counter-rotating circularly polarised components, each with amplitude $B_1 = B_x / 2$ (see Fig. 2.2), denoted

$$\mathbf{B}_+ = B_1 \ \hat{x}\cos(\omega t) + \hat{y}\sin(\omega t) \tag{2.9}$$

$$\mathbf{B}_- = B_1 \ \hat{x}\cos(\omega t) - \hat{y}\sin(\omega t) \ , \tag{2.10}$$

where $\mathbf{B}_-$ and $\mathbf{B}_+$ differ simply by a substitution of ω with $-\omega$. One component will rotate in the same sense as the precession spin moments and is called the resonant component, while the other component rotates in the opposite sense and is called the non-resonant component. It can be shown that for $B_1 \ll B_0$, under normal conditions, the non-resonant component has no influence on the spins and may therefore be neglected. For generality, it is convenient to introduce the symbol ω_z, which represents the component of ω along the z-axis, and may therefore be positive or negative. It is then possible to consider a single circular field component

$$\mathbf{B}_1 = B_1 \ \hat{x}\cos(\omega_z t) + \hat{y}\sin(\omega_z t) \ , \tag{2.11}$$

which will give either sense of rotation, depending on the sign of ω_z. The spin Hamiltonian due to spin interactions with the transient RF field may therefore be written as [24]

$$\mathcal{H}_{\mathrm{RF}} = -\boldsymbol{\mu}\cdot\mathbf{B}_1 = -\gamma\hbar\mathbf{I}\cdot\mathbf{B}_1 = -\gamma\hbar B_1 \ I_x\cos(\omega_z t) + I_y\sin(\omega_z t) \ , \tag{2.12}$$

where $\mathbf{I} = I_x\hat{x} + I_y\hat{y} + I_z\hat{z}$ ($I_z = 0$ for spin interactions with an RF field applied orthogonal to the z-direction).

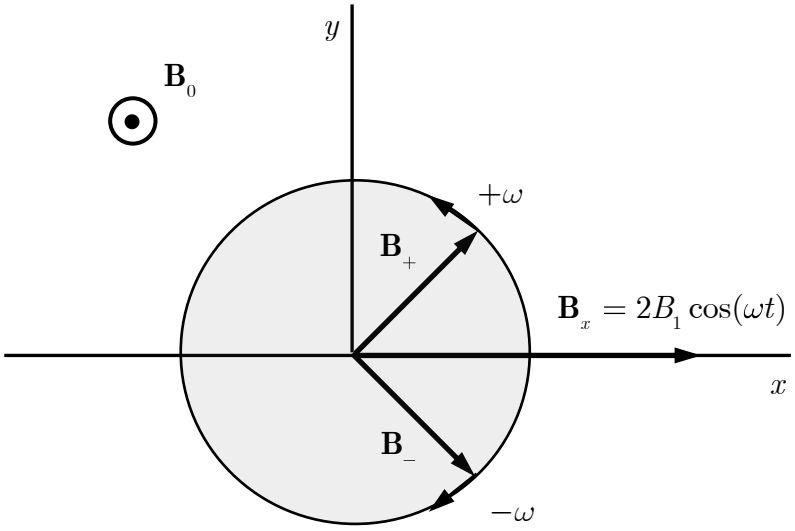

Figure 2.2: Decomposition of a linear oscillating field into two counter-rotating circularly polarised fields.

2.2.2 Internal spin interactions

Dipolar interaction

Within an assembly of nuclear spins, if each spin has an associated magnetic moment, magnetic fields are generated that loop around in the surrounding space corresponding to the direction of the spin magnetic moment. If neighbouring nuclei are a distance r apart and have magnetic moment μ, the fields they produce are of the order

$$B_{\text{loc}} = \frac{\mu_0}{4\pi}\frac{\mu}{r^3}. \tag{2.13}$$

The classical interaction energy between two magnetic dipole moments is [25]

$$E = \frac{\mu_0}{4\pi}\left[\frac{\boldsymbol{\mu}_1 \cdot \boldsymbol{\mu}_2}{r^3} - \frac{3(\boldsymbol{\mu}_1 \cdot \mathbf{r}_{12})(\boldsymbol{\mu}_2 \cdot \mathbf{r}_{12})}{r^5}\right], \tag{2.14}$$

where $\mathbf{r}_{12}$ is the radius vector from $\boldsymbol{\mu}_1$ to $\boldsymbol{\mu}_2$ ($\mathbf{r}$ could equally be taken from $\boldsymbol{\mu}_2$ to $\boldsymbol{\mu}_1$). Replacing the classical dipoles, $\boldsymbol{\mu}$, with their quantum equivalents, $\gamma\hbar\mathbf{I}$ (Eq. 2.1), and summing over all spin pairs within a nuclear spin system, yields the dipolar Hamiltonian:

$$\mathcal{H}_{\mathrm{D}} = \frac{\mu_0}{4\pi}\sum_{k}\sum_{j}^{k-1}\frac{\gamma_j\gamma_k\hbar}{r_{jk}^3}\left[\mathbf{I}_j\cdot\mathbf{I}_k - \frac{3(\mathbf{I}_j\cdot\mathbf{r}_{jk})(\mathbf{I}_k\cdot\mathbf{r}_{jk})}{r_{jk}^2}\right]. \tag{2.15}$$

Alternatively, the summation over pairs can be written

$$\begin{aligned}\mathcal{H}_{\mathrm{D}} &= \frac{\mu_0}{4\pi}\sum_{j<k}\frac{\gamma_j\gamma_k\hbar}{r_{jk}^3}\left[\mathbf{I}_j\cdot\mathbf{I}_k - 3(\mathbf{I}_j\cdot\hat{\mathbf{e}}_{jk})(\mathbf{I}_k\cdot\hat{\mathbf{e}}_{jk})\right]\\ &= \sum_{j<k} b_{jk}\left[\mathbf{I}_j\cdot\mathbf{I}_k - 3(\mathbf{I}_j\cdot\hat{\mathbf{e}}_{jk})(\mathbf{I}_k\cdot\hat{\mathbf{e}}_{jk})\right],\end{aligned} \tag{2.16}$$

where $\hat{\mathbf{e}}_{jk} = \mathbf{r}_{jk} / r_{jk}$ denotes a unit vector pointing in the direction of $\mathbf{r}_{jk}$ and

$$b_{jk} = \frac{\mu_0}{4\pi}\frac{\gamma_j\gamma_k\hbar}{r_{jk}^3} \tag{2.17}$$

is the dipolar coupling constant. Considering a single homonuclear (same γ) spin pair (j,k) separated by a distance r_{jk}, the dipolar interaction represented by Eqs. 2.15 and 2.16 can also be written

$$\mathcal{H}_{\mathrm{D}_{jk}} = \mathbf{I}_j\cdot\mathbf{D}\cdot\mathbf{I}_k = \begin{bmatrix} I_{jx} & I_{jy} & I_{jz}\end{bmatrix}\begin{bmatrix} D_{xx} & D_{xy} & D_{xz}\\ D_{yx} & D_{yy} & D_{yz}\\ D_{zx} & D_{zy} & D_{zz}\end{bmatrix}\begin{bmatrix} I_{kx}\\ I_{ky}\\ I_{kz}\end{bmatrix}, \tag{2.18}$$

where the matrix $\mathbf{D}$ is a rank-two tensor whose elements can be determined by inspection of Eq. 2.16. It is more useful, especially where it is necessary to consider rotational effects of spin dipoles, to represent the dipole vectors in spherical polar coordinates (r_{jk},θ_{jk},ϕ_{jk}). The dipolar interaction represented for a single pair of spins can be re-written in the spherical tensor formalism [26]:

$$\mathcal{H}_{\mathrm{D}_{jk}} = \sum_{m}(-1)^m F_2^m(\theta_{jk},\phi_{jk})T_2^{-m}\,, \tag{2.19}$$

where

$$F_2^m = -b_{jk}\ 24\ /\ 5\ ^{1/2}\ Y_2^m \tag{2.20}$$

and Y_2^m are the spherical harmonics of order 2 and component m, while the T_2^{-m} terms are products of spin operators [27]. In the limit of high magnetic field, where the dipolar interaction between spins is weak when compared to the Zeeman interaction, only the so-called 'secular' (diagonal matrix components), for which $m = 0$, are considered, and the 'non-secular' (off-diagonal terms) can be discarded. The Y_2^0 and T_2^0 terms are given by

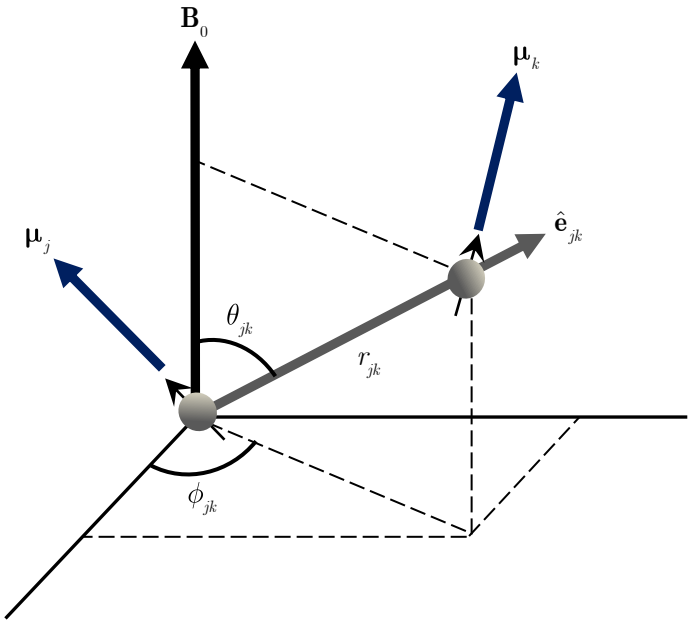

Figure: 2.3: Relationship between rectangular coordinates x, y, z (describing the position of spin j relative to spin k) and the polar coordinates $r_{jk}, \theta_{jk}, \phi_{jk}$. θ_{jk} is used in the calculation of secular dipole-dipole coupling.

$$Y_2^0 = (5\ /\ 4\pi)^{1/2}\frac{1}{2}(3\cos^2(\theta_{jk}) - 1) \tag{2.21}$$

and

$$T_2^0 = \frac{1}{\sqrt{6}}(3I_{jz}I_{kz} - \mathbf{I}_j \cdot \mathbf{I}_k)\,. \tag{2.22}$$

Inserting Eqs. 2.20, 2.21 and 2.22 into Eq. 2.19, the secular Hamiltonian term for a collection of homonuclear spin pairs is therefore

$$\mathcal{H}_{\mathrm{D}_0}(\theta_{jk}) = \sum_{j<k} b_{jk} \frac{1}{2}[(1-3\cos^2(\theta_{jk}))(3I_{jz}I_{kz} - \mathbf{I}_j \cdot \mathbf{I}_k)], \tag{2.23}$$

and it can be shown that for heteronuclear spin pairs, the secular Hamiltonian is given by [23]

$$\mathcal{H}_{\mathrm{D}_0}(\theta_{jk}) = \sum_{j<k} b_{jk} \frac{1}{2}\Big[(1-3\cos^2(\theta_{jk}))(2I_{jz}I_{kz})\Big]. \tag{2.24}$$

The dipole-dipole Hamiltonian is of great significance in describing nuclear spin systems. It is responsible for the anisotropic dipolar line-broadening observed in rigid solids, where linewidths of the order of kHz can render solid-state NMR signals unobservable under normal conditions. In liquids and gases, the situation is very different, as molecular motion causes θ_{jk} and ϕ_{jk} (and hence $\mathcal{H}_{\mathrm{D}_0}$) to rapidly fluctuate, which results in the dipolar Hamiltonian being averaged to approximately zero. Static dipolar broadening therefore makes no contribution to the NMR linewidth in liquids and gases. The rapidly fluctuating non-secular (off-diagonal) terms in $\mathcal{H}_{\mathrm{D}}$, however, can induce transitions between nuclear energy levels and thus contribute significantly to the transverse and longitudinal relaxation mechanisms, as we shall see later, in liquids and gases, as well as in solids.

Chemical shift

Atomic or molecular electrons can cause the local magnetic field surrounding a nucleus to vary. The change in field experienced by the nucleus alters the Larmor frequency in a way which is characteristic of the chemical environment. This effect is called the chemical shift. The physical process giving rise to chemical shifts can be described in two steps: 1) the externally applied field ($\mathbf{B}_0$) induces electric currents in atomic/molecular electron clouds and 2) the currents in turn generate a magnetic field, $\mathbf{B}_{\mathrm{induced}}$. The

magnetic field experienced at the nucleus is then a summation of the applied field and induced field

$$\mathbf{B}_{\text{loc}} = \mathbf{B}_0 + \mathbf{B}_{\text{induced}}. \tag{2.25}$$

The induced field is approximately linearly dependent on the applied field and may be written

$$\mathbf{B}_{\text{induced}} = -\sigma \mathbf{B}_0 , \tag{2.26}$$

so that the local field is given by

$$\mathbf{B}_{\text{loc}} = (1-\sigma)\mathbf{B}_0 , \tag{2.27}$$

where σ is the chemical shift tensor, which describes the extent to how "shielded" the nucleus is from the applied field; if the currents are set-up such that direction of $\mathbf{B}_{\text{induced}}$ opposes the applied field (positive σ), the field experienced at the nucleus is reduced in comparison to that which would be experienced by the 'bare' nucleus. The Hamiltonian for the chemical shift interaction is given by

$$\mathcal{H}_{\text{CS}} = -\boldsymbol{\mu} \cdot \mathbf{B}_{\text{induced}} = \gamma \hbar \mathbf{I} \cdot \sigma \mathbf{B}_0 . \tag{2.28}$$

In solids, the chemical shift may be anisotropic, and thus the tensor formalism is required to describe the effect. In liquids and gases, however, the nuclei tumble rapidly through every possible molecular orientation (NB: Xe, being a monatomic gas, has no preferred orientation) and thus any anisotropy effects are averaged out, rendering σ as a scalar.

2.2.3 Semi-classical treatment of nuclear magnetisation

So far the phenomenon of nuclear magnetism has been described by considering individual magnetic dipole interactions. This approach proves cumbersome when attempting to evaluate the net magnetisation of large numbers of spins within a given volume. In the semi-classical picture

described in this section, the dynamics of the sum of all magnetic dipole moments – the magnetisation vector, **M** – in a sample are described. Using this picture of magnetisation make basic experiments in NMR easier to understand, visualise and interpret.

Macroscopic magnetisation and Boltzmann equilibrium

According to the Boltzmann law of statistical mechanics, the populations, P_m, of the energy levels, E_m, are governed by $\exp(-E_m / kT) = \exp(m\gamma\hbar B_0 / kT)$, and the net equilibrium magnetisation of a sample containing N spins is [28]

$$M_0 = N\gamma\hbar \frac{\sum_{m=-I}^{I} m \exp(m\gamma\hbar B_0 / kT)}{\sum_{m=-I}^{I} \exp(m\gamma\hbar B_0 / kT)}, \tag{2.29}$$

where k is Boltzmann's constant and T is the sample temperature. In the case of nuclear magnetism, the ratio $\gamma\hbar B_0 / kT$ is almost always a very small number and it is possible to perform a linear expansion of Eq. 2.29 to approximate M_0 as

$$M_0 = \frac{N\gamma^2\hbar^2 I(I+1)}{3kT} B_0 . \tag{2.30}$$

For nuclei with spin $I = 1/2$ (e.g. for ^{1}H, ^{129}Xe and ^{3}He) the net (or equilibrium) magnetisation is equal to

$$M_0 = \frac{N\gamma^2\hbar^2 B_0}{4kT} = \frac{1}{2} N \mid \gamma \mid \hbar P_b , \tag{2.31}$$

where P_b is the Boltzmann polarisation, which defines the fractional population excess in one energy level relative to the other. Let the populations of the two m states, $+1/2$ and $-1/2$, be specified by $N_+ = \exp(-E_+ / kT)$ and $N_- = \exp(-E_- / kT)$, respectively, then P_b can be expressed as

$$P_{\mathrm{b}} = \frac{\Delta N}{N} = \frac{N_{+} - N_{-}}{N_{+} + N_{-}} = \tanh\frac{\Delta E}{2kT} \simeq \frac{|\,\gamma\,|\,\hbar B_0}{2kT} \quad , \tag{2.32}$$

for $\Delta E \,/\, kT \ll 1$. Typical field strengths used in NMR applications are of the order of one to several teslas, leading to small excesses of nuclear spins aligned with $\mathbf{B}_0$ at room temperature. For example, at a field of 1.5 T, the Boltzmann polarisations of ^{129}Xe, ^{31}P and ^{1}H nuclei are 1.4×10^{-6}, 2×10^{-6}, 5.1×10^{-6}. The polarisation of a given spin system is related to the sensitivity in NMR, which will be further discussed in Section 2.2.5.

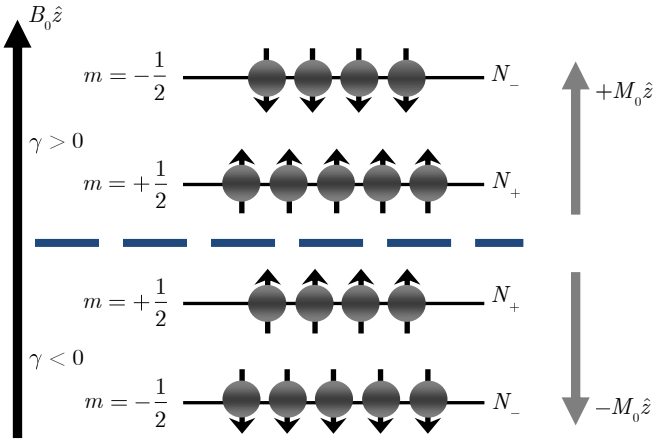

Figure 2.4: Spin populations, N_{+} and N_{-}, for spin-1/2 nuclear species in the presence of an applied field. The orientation of the spin angular momentum and the net equilibrium magnetisation, M_0, with respect to the z-component of the applied magnetic field is dependent upon the sign of the gyromagnetic ratio of the nucleus.

Equations of motion and the rotating reference frame

In the classical description of magnetism, while a spin is subject to an external field, $\mathbf{B}$, (which may vary with time) a torque of the amount $\boldsymbol{\tau} = \boldsymbol{\mu} \times \mathbf{B}$ acts on the spin magnetic moment. The equation of motion of the spin is given by equating $\boldsymbol{\tau}$ with the rate of change of angular momentum $\mathbf{J}$

$$\frac{\mathrm{d}\mathbf{J}}{\mathrm{d}t} = \boldsymbol{\tau} = \boldsymbol{\mu} \times \mathbf{B}\,, \tag{2.33}$$

and, since $\boldsymbol{\mu} = \gamma \mathbf{J}$, it is possible to write

$$\frac{\mathrm{d}\boldsymbol{\mu}}{\mathrm{d}t} = \gamma \boldsymbol{\mu} \times \mathbf{B}\,. \tag{2.34}$$

By writing the net magnetisation of N spins in a volume V

$$\mathbf{M} = \frac{1}{V} \sum_{j}^{N} \boldsymbol{\mu}_{j}\,, \tag{2.35}$$

combination of Eqs. 2.34 and 2.35 then gives

$$\frac{\mathrm{d}\mathbf{M}}{\mathrm{d}t} = \gamma \mathbf{M} \times \mathbf{B}\,, \tag{2.36}$$

which is the equation of motion of $\mathbf{M}$ for 'free' (i.e. non-interacting) spin ensembles in the laboratory frame. In order to solve Eq. 2.36, it is useful to introduce a rotating coordinate system, a technique that greatly assists in the description of the dynamics of $\mathbf{M}$ in NMR experiments.

Given a time-dependent vector, $\mathbf{A}(t)$, the time derivative, $\mathrm{d}\mathbf{A}/\mathrm{d}t$, computed in the laboratory frame, and $\partial \mathbf{A} \,/\, \partial t$, the time derivative computed in a coordinate system that is rotating with a constant arbitrary angular frequency, $\boldsymbol{\Omega}$, are related through

$$\frac{\mathrm{d}\mathbf{A}}{\mathrm{d}t} = \frac{\partial \mathbf{A}}{\partial t} + \mathbf{A} \times \boldsymbol{\Omega}\,. \tag{2.37}$$

Combination of Eqs. 2.36 and 2.37 gives the equation of motion of $\mathbf{M}$ in the rotating coordinate system,

$$\frac{\partial \mathbf{M}}{\partial t} = \gamma \mathbf{M} \times \left(\mathbf{B} + \frac{\boldsymbol{\Omega}}{\gamma} \right). \tag{2.38}$$

According to Eq. 2.38, the motion of $\mathbf{M}$ in the rotating coordinate system obeys the same equation as in the laboratory system, so long as the applied field, $\mathbf{B}$, is replaced by an effective field

$$\mathbf{B}_{\mathrm{e}} = \mathbf{B} + \frac{\mathbf{\Omega}}{\gamma}, \tag{2.39}$$

the sum of the laboratory field and a fictitious field $\mathbf{B}_{\mathrm{f}} = \mathbf{\Omega} / \gamma$. It is possible to solve the equation of motion of $\mathbf{M}$ for a static field $\mathbf{B} = \mathbf{B}_0$ by choosing a rotating frame with $\mathbf{\Omega} = -\gamma \mathbf{B}_0$ such that the effective field disappears. For $\mathbf{B}_{\mathrm{e}}$, $\partial \mathbf{M} / \partial t = 0$, and the magnetisation is a fixed vector in the rotating frame. This means that, with respect to the laboratory frame, $\mathbf{M}$ rotates with an angular velocity $\mathbf{\Omega} = -\gamma B_0 \hat{z}$, where γB_0 is the Larmor precession frequency, which is identical in magnitude to the resonance frequency derived for Zeeman energy transitions in Section 2.2.1 (Eqs. 2.8a and b).

Bloch equations

The Bloch equations describe, phenomenologically, the time evolution of $\mathbf{M}$ under the influence of transient magnetic fields for interacting spins. The heuristic argument leading to these equations is as follows.

1) The equation of motion of the nuclear magnetisation for an ensemble of spins was shown in Section 2.2.3 to be $\mathrm{d}\mathbf{M} / \mathrm{d}t = \gamma \mathbf{M} \times \mathbf{B}$ (Eq. 2.36).

2) In a static field, $B_z = B_0$, the magnetisation, M_z, approaches equilibrium, M_0, according to the equation $\mathrm{d}M_z / \mathrm{d}t = -(M_z - M_0) / T_1$. T_1 is called the spin-lattice or longitudinal relaxation time constant, which characterises the time taken for M_z to establish Boltzmann equilibrium.

3) Through interactions with a transient RF field, $\mathbf{B}_1$ (Eq. 2.11), applied orthogonal to the static field, the nuclear magnetisation may gain transverse components M_x and M_y. This 'transverse magnetisation', owing mainly to mutual spin-spin interactions, decays at a rate represented by the equations $\mathrm{d}M_x / \mathrm{d}t = -M_x / T_2$, $\mathrm{d}M_y / \mathrm{d}t = -M_y / T_2$, where T_2 is called the transverse or spin-spin relaxation time.

4) In the presence of an applied field, **B**, the sum of a static field and a much smaller RF field ($\mathbf{B}_0 + \mathbf{B}_1$), the motion of **M** due to relaxation can be superposed on the motion of free spins (Eq. 2.36), which leads to the equation of motion in the laboratory frame

$$\frac{\mathrm{d}\mathbf{M}}{\mathrm{d}t} = \gamma\mathbf{M}\times\mathbf{B} - \frac{M_x\hat{x} + M_y\hat{y}}{T_2} - \frac{M_z - M_0}{T_1}\hat{z} \qquad \text{(Lab. frame).} \qquad (2.40)$$

Consider a static field with amplitude $B_z = B_0 = -\omega_0 / \gamma$ and a RF field of amplitude $B_1 = -\omega_1 / \gamma$ that is rotating about z-direction at a frequency ω_z (whose sign may be positive or negative depending on the gyromagnetic ratio of the nucleus) in the vicinity of the value of ω_0 (i.e. a slightly off-resonance version of the circularly rotating field represented by Eq. 2.11). In the frame rotating around B_0 at a frequency $\omega_z \neq \omega_0$, the effective field is no longer zero and is given by

$$\mathbf{B}_\mathrm{e} = \left(B_0 + \frac{\omega_z}{\gamma}\right)\hat{z} + B_1\hat{x}' = \frac{(\omega_z - \omega_0)\hat{z} - \omega_1\hat{x}'}{\gamma} = \frac{\Delta\omega\hat{z} - \omega_1\hat{x}'}{\gamma}, \qquad (2.41)$$

where $\hat{x}', \hat{y}', \hat{z}' = \hat{z}$ are unit vectors in the rotating frame. In the rotating frame, the equation of motion is

$$\frac{\mathrm{d}\mathbf{M}}{\mathrm{d}t} = \gamma\mathbf{M}\times\mathbf{B}_\mathrm{e} - \frac{M'_x\hat{x}' + M'_y\hat{y}'}{T_2} - \frac{M_z - M_0}{T_1}\hat{z} \qquad \text{(Rot. frame),} \quad (2.42)$$

where M'_x and M'_y are the transverse components of **M** in the rotating frame. (NB: from now on, the primes shall be removed and the following treatments in this chapter, unless otherwise stated, will correspond to **M** in the rotating frame.) Making the substitution $\mathbf{M} = M_x\hat{x} + M_y\hat{y} + M_z\hat{z}$, Eq. 2.42 can be re-written as

$$\begin{aligned}
\frac{\mathrm{d}M_x}{\mathrm{d}t} &= +\Delta\omega M_y - M_x / T_2 \\
\frac{\mathrm{d}M_y}{\mathrm{d}t} &= -\Delta\omega M_x - \omega_1 M_z - M_y / T_2 \\
\frac{\mathrm{d}M_z}{\mathrm{d}t} &= \omega_1 M_y - (M_z - M_0) / T_1
\end{aligned} \tag{2.43}$$

which represents the Bloch equations in the rotating reference frame.

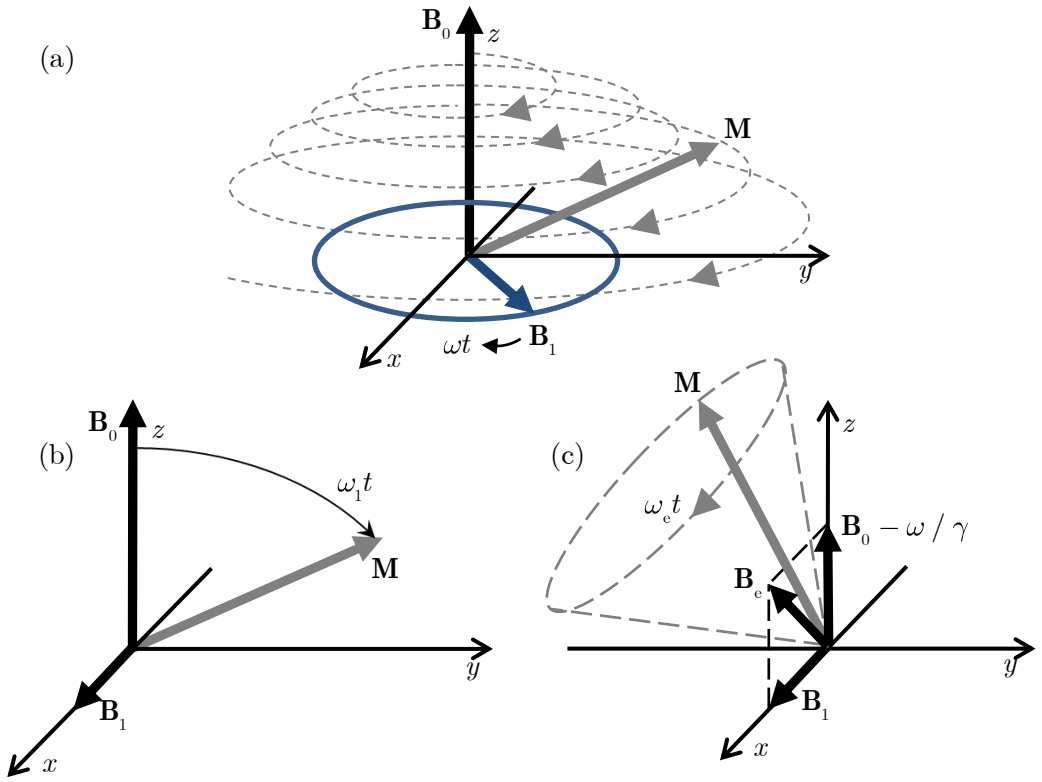

Figure 2.5: (a) Time evolution of the nuclear spin magnetisation, $\mathbf{M}$, in the laboratory frame, in the presence of a static field, $\mathbf{B}_0$, and a transverse rotating field, $\mathbf{B}_1$. When $\omega = \omega_0$, $\mathbf{M}$ simultaneously precesses about $\mathbf{B}_0$ at ω_0 and about $\mathbf{B}_1$ at ω_1. (b) Same as (a) but in the rotating frame where $\mathbf{B}_1$ is fixed in position. (c) Precession (at frequency ω_e) of $\mathbf{M}$ in the rotating frame when the RF field is off-resonant ($\omega \neq \omega_0$) around an effective field $\mathbf{B}_e$. Shown is the case in for a nucleus with positive gyromagnetic ratio where $\omega_z = -\omega$ in Eq. 2.41.

Pulsed Fourier transform NMR

In the following, we consider the evolution of **M** after the application of a $\mathbf{B}_1$ field applied for a given duration, t_{RF}. In the rotating frame, **M** is 'tipped' away from its equilibrium position, subtending an angle (with respect to the z-axis)

$$\theta = \gamma B_1 t_{\mathrm{RF}}. \tag{2.44}$$

During NMR experiments, RF 'pulses' (of given power and duration) are transmitted into a coil that is set up to generate a $\mathbf{B}_1$ orthogonal to $\mathbf{B}_0$ so that **M** is brought into the transverse plane according to Eq. 2.44. After $\mathbf{B}_1$ is turned off, the transverse components of **M** induce small currents in the coil that was used to transmit the pulse. **M** will then relax back to its equilibrium value, M_0, in a time characterised by the constant T_1.

In basic pulsed NMR experiments, where $T_1 \gg t_{\mathrm{RF}}$ (t_{RF} represents the duration over which the RF field is applied), the Bloch equations (Eq. 2.43) describe the time evolution of the nuclear magnetisation in the intervals separating RF pulses, where only $\mathbf{B}_0$ acts on **M**, so that Eq. 2.43 becomes

$$\begin{aligned}
\frac{\mathrm{d}M_x}{\mathrm{d}t} &= \Delta\omega M_y - (M_x / T_2) \\
\frac{\mathrm{d}M_y}{\mathrm{d}t} &= -\Delta\omega M_x - (M_y / T_2) \\
\frac{\mathrm{d}M_z}{\mathrm{d}t} &= (M_0 - M_z) / T_1 .
\end{aligned} \tag{2.45}$$

These three differential equations can be readily solved by introducing the complex transverse magnetisation, $M_t = M_x + iM_y$, which reduces Eq. 2.45 to [29]

$$\begin{aligned}
\frac{\mathrm{d}M_t}{\mathrm{d}t} &= -(1 / T_2 - 2i\pi\nu')M_t \\
\frac{\mathrm{d}M_z}{\mathrm{d}t} &= (M_0 - M_z) / T_1 ,
\end{aligned} \tag{2.46}$$

where $\nu' = \Delta\omega / 2\pi = (\omega_z - \omega) / 2\pi$ is the precession frequency in the rotating frame. Assuming initial conditions of $M_t(t=0) = M_0$ and $M_z(t=0) = 0$ – the condition after an RF pulse has tipped **M** fully into the transverse plane ($\theta = \pi / 2$ in Eq. 2.44) – the complex transverse magnetisation is obtained

$$M_t = M_0 \exp(-t / T_2) \exp(2i\pi\nu' t), \tag{2.47}$$

and, therefore, the solutions to the Bloch equations in the rotating frame can be written

$$\begin{aligned} M_x(t) &= M_0 \exp(-t / T_2) \cos(2\pi\nu' t) \\ M_y(t) &= M_0 \exp(-t / T_2) \sin(2\pi\nu' t) \\ M_z(t) &= M_0 \left[1 - \exp(-t / T_1)\right]. \end{aligned} \tag{2.48}$$

The meaning of T_1 and T_2 is apparent from inspection of Eq. 2.48: when $t \to \infty$, M_z recovers to equilibrium magnetisation, M_0, while any transverse magnetisation vanishes. The transverse relaxation time T_2 characterises the loss of coherence of spins, and thus reduction of the transverse magnetisation, within a sample. Spatial inhomogeneities of $\mathbf{B}_0$ result in a distribution of the precession frequency, ν', which contributes to the coherence loss in the transverse plane. T_2 is thus replaced by

$$1 / T_2^* = 1 / T_2 + 1 / T_2' \simeq 1 / T_2 + \gamma \Delta B_0 / 2\pi . \tag{2.49}$$

T_2 is mediated by spin-spin interactions, where each nuclear spin experiences a local magnetic field due to its neighbours, and T_2' characterises the coherence loss due to static $\mathbf{B}_0$ inhomogeneity. (It is clear from Eq. 2.49 that $T_2^* \leq T_2$.) The complex transverse magnetisation (Eq. 2.47) is then re-written $M_t = M_0 \exp(-t / T_2^*) \exp(2i\pi\nu' t)$. The transverse magnetisation components, M_x and M_y, contain cosine and sine factors, hence the NMR signal induced in the coil comprises damped cosine and sine functions. This signal, a superposition of damped cosine (sine) functions, is referred to as 'free

induction decay' (FID). In order to retrieve the frequency-domain NMR spectrum, a complex Fourier transform is performed on the complex signal, M_t

$$\mathcal{F}(M_t(t)) = \int_0^\infty M_t(t)\exp(-2i\pi\nu' t)\mathrm{d}t \tag{2.50}$$

Evaluation of the integral in Eq. 2.50 yields the Lorentzian function

$$\mathcal{F}(M_t(t)) = \frac{M_0 T_2^*}{1+4\pi^2 T_2^*(\nu-\nu')^2} - i\frac{M_0 T_2^* 2\pi(\nu-\nu')}{1+4\pi^2 T_2^*(\nu-\nu')^2}. \tag{2.51}$$

The first term (the real part of the Fourier transform) corresponds to an absorption Lorentzian lineshape with a maximum value of $M_0 T_2^*$ occurring at ν' and a full-width half maximum (FWHM) equal to $1/\pi T_2^*$. The second term (the imaginary part of the Fourier transform) corresponds to a dispersion Lorentzian lineshape with a maximum value of $M_0 T_2^*/2$ and a max-min peak distance of $1/\pi T_2^*$. (NB: In realistic cases, NMR lineshapes can be non-Lorentzian (Gaussian or Voigt) due to e.g. field inhomogeneities, diffusion and bulk sample motion.)

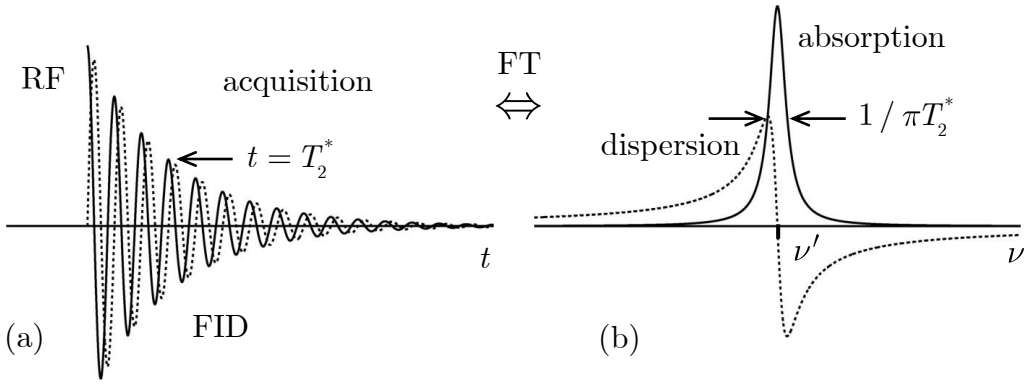

Figure 2.6: (a) Free induction decay following an RF pulse. The solid and dashed black lines represent the real and imaginary parts of the complex transverse magnetisation. (b) NMR spectrum after a Fourier transform. The real and imaginary parts of the Fourier transform are termed absorption and dispersion spectra, respectively. The full-width half maximum of the absorption Lorentzian has the value $1/\pi T_2^*$.

In practice, while post-processing of NMR spectra, it is generally necessary to 'phase' the spectrum by adding a factor $\exp(i\varphi)$ to M_t, where φ is chosen such that the absorption and dispersion lineshapes correspond to the real and imaginary parts of the spectrum, respectively.

2.2.4 Nuclear spin relaxation

In the presence of a static magnetic field, nuclear spins within a sample will reach a state of magnetic (thermal) equilibrium, where the spin moments exhibit net alignment with the static field, and the energy level population difference is given by the Boltzmann distribution. In order for a spin moment (in the case of $\gamma > 0$) that is antiparallel to the field to become parallel, it must lose energy. The medium in which this energy exchange occurs is referred to as the 'lattice' (the molecular environment of the nuclear spins).

The lattice – named so following the early studies of NMR relaxation in solids where the surroundings were genuinely a solid lattice – describes the thermodynamic ensemble in which all relaxation pathways available for the nuclear spins to transfer energy take place. The rate at which the nuclear magnetisation, **M**, establishes equilibrium depends on how efficient energy transfer is from the spin system to the lattice (hence the term spin-lattice relaxation). Within the context of an NMR experiment, **M** will relax back to equilibrium at a rate determined by spin-lattice interactions following application of an RF pulse.

For spin-1/2 nuclei, relaxation is caused by fluctuating magnetic fields (arising due to thermal motion of the molecules) at the sites of the nuclear spins. To quantify the effect that fluctuating fields have on nuclear relaxation at a given frequency, it is necessary to introduce the autocorrelation function.

Autocorrelation function of a fluctuating field

Consider a magnetic field, $F(t)$, that fluctuates randomly over time. These fields will have zero average, i.e. $\langle F(t) \rangle = 0$, where the angular bracket notation here refers to either the average field experienced by one spin over a long time, or the average field experienced by many spins instantaneously. These averages are assumed to be equivalent (ergodic hypothesis). Since the average field is zero, the magnitude of the fluctuating field is determined by consideration of the mean square value of the fluctuating field, $\langle F^2(t) \rangle \neq 0$. The autocorrelation function is used to describe how rapidly the field fluctuates with respect to a time interval $t + \tau$, and is defined:

$$G(\tau) = \langle F(t)F(t+\tau) \rangle. \tag{2.52}$$

If the interval τ is much longer than the time-scale of the fluctuations, then the system is said to lose its 'memory' – i.e. the function decorrelates with itself. In general, the autocorrelation function is large for small values of τ and tends to zero for large values τ. The so-called correlation time, τ_c, is used to characterise the loss of correlation; rapid fluctuations have small τ_c and slow fluctuations have large τ_c. If one assumes a simple exponential form for the autocorrelation function, τ_c is related to $G(\tau)$ by

$$G(\tau) = G(0)\exp(-|\tau|/\tau_c). \tag{2.53}$$

$G(\tau)$ has a maximum value of $\langle F^2(t) \rangle$ at $\tau = 0$, and approaches zero for $|\tau| \gg \tau_c$, as shown in Fig. 2.7. In practice, the correlation time depends on physical parameters of the spin system/lattice, such as temperature and viscosity. For example, correlation times are generally decreased by warming the sample (increase in temperature implies more rapid molecular motion) and the opposite holds true for sample cooling.

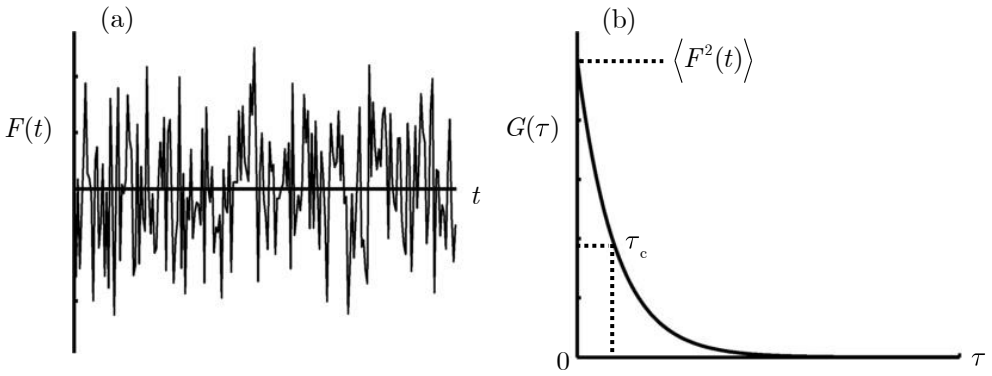

Figure 2.7: (a) Rapidly fluctuating magnetic field and (b) autocorrelation function of the fluctuating field with correlation time τ_c.

Spectral density

Fields that fluctuate at the Larmor frequency induce nuclear energy level transitions and thus contribute to relaxation. The amount of motion present at a given angular frequency, ω, within a system, can be measured using the spectral density function, which is twice the Fourier transform of the autocorrelation function

$$J(\omega) = 2\int_0^\infty G(\tau)\exp(-i\omega\tau)\mathrm{d}\tau\,. \tag{2.54}$$

The real part of the resulting integral leads to a Lorentzian

$$J(\omega) = G(0)\frac{2\tau_c}{1+\omega^2\tau_c^2} = 2G(0)\mathcal{J}(\omega)\,, \tag{2.55}$$

where $\mathcal{J}(\omega) = \tau_c / (1+\omega^2\tau_c^2)$ is the normalised spectral density. $J(\omega)$ for two different correlation times is shown in Fig. 2.8, where the area under the spectral density function remains fixed and is independent of τ_c. The maximum of the spectral density at the Larmor frequency, $J(\omega_0)$, is reached for $\omega_0\tau_c = 1$ (as shown in Fig. 2.9). The spin-lattice relaxation rate is thus expected to be the most rapid when this condition is satisfied.

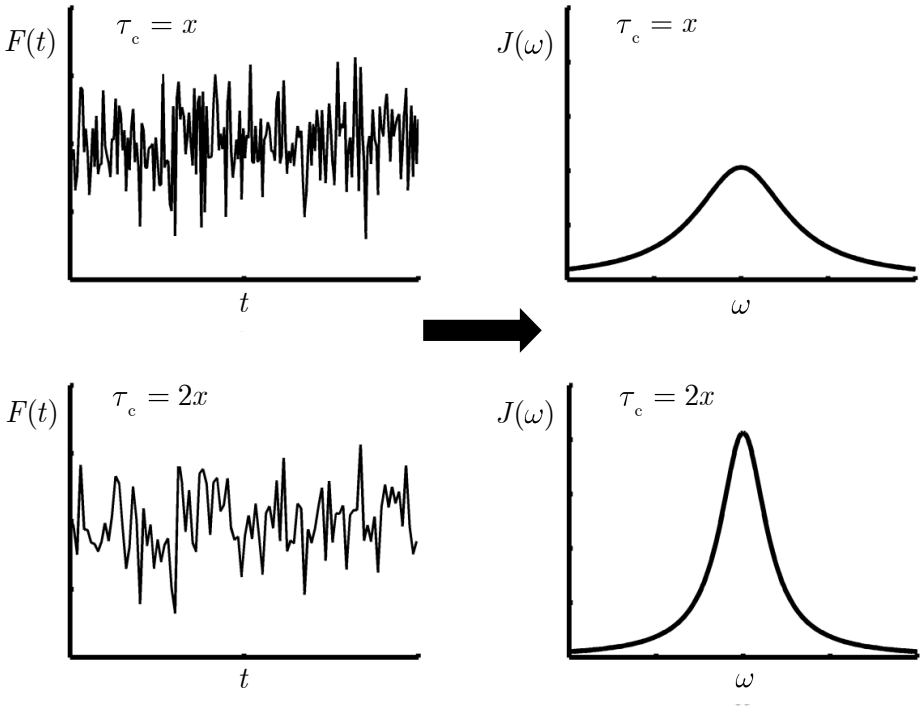

Figure 2.8: Spectral density functions for two fields fluctuating with different correlation times, τ_c. NB: the area under $J(\omega)$ is independent of τ_c.

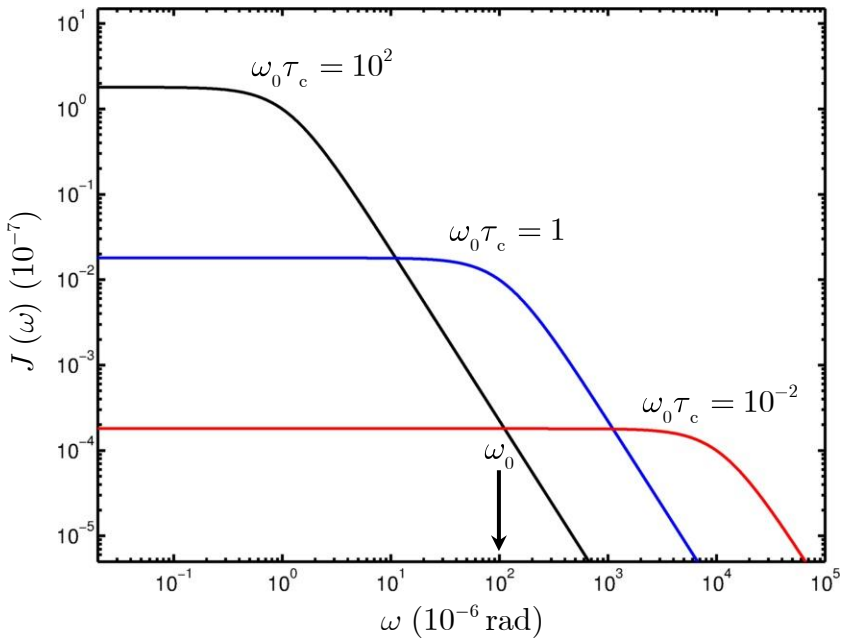

Figure 2.9: Spectral density for ^{129}Xe at 1.5 T for three different values of correlation time, τ_c. $J(\omega_0)$ has maximum value when $\omega_0\tau_c = 1$.

Transition probabilities

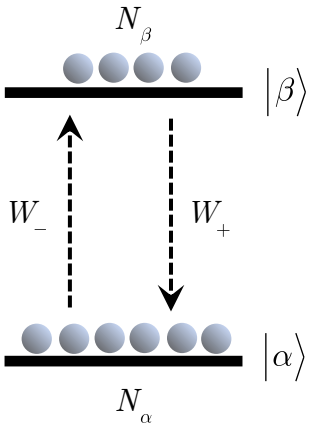

Figure 2.10: Dynamic balance between the two spin energy eigenstates, $|\alpha\rangle$ and $|\beta\rangle$, at thermal equilibrium.

Consider a spin-1/2 nuclear spin system with the two spin eigenstates denoted by $|\alpha\rangle$ and $|\beta\rangle$, where $|\alpha\rangle = |1/2, +1/2\rangle$ and $|\beta\rangle = |1/2, -1/2\rangle$ (notation $|I, m\rangle$), each populated with N_α and N_β spins. It can be shown that for spin-independent randomly fluctuating fields, the transition probabilities for spins going from $|\alpha\rangle$ to $|\beta\rangle$, W_-, and vice-versa, $|\beta\rangle$ to $|\alpha\rangle$, W_+, can be written [23]

$$\begin{aligned} W_- &= W(1 - P_\mathrm{b}) \\ W_+ &= W(1 + P_\mathrm{b}), \end{aligned} \tag{2.56}$$

where P_b is the Boltzmann polarisation, defined by Eq. 2.32 in Section 2.2.3, and W is the mean transition probability, which is given by

$$W = \frac{1}{2}\gamma^2 \left\langle F^2(t) \right\rangle \mathcal{J}(\omega_0). \tag{2.57}$$

The rate of change of spin state population between the two spin eigenstates can be written

$$\frac{\mathrm{d}N_\alpha}{\mathrm{d}t} = -W_- N_\alpha + W_+ N_\beta \tag{2.58}$$

and

$$\frac{\mathrm{d}N_{\beta}}{\mathrm{d}t} = +W_{-}N_{\alpha} - W_{+}N_{\beta}. \tag{2.59}$$

These are referred to as the master equations describing the spin system. The z-component of the macroscopic magnetisation vector, introduced in Section 2.2.3, is proportional to the fractional difference in the spin state populations. As a consequence, it follows that the time dependence of M_z can be written

$$\begin{aligned}\frac{\mathrm{d}M_z}{\mathrm{d}t} &= \frac{\mathrm{d}(N_{\alpha} - N_{\beta})}{\mathrm{d}t} \\ &= \frac{\mathrm{d}N_{\alpha}}{\mathrm{d}t} - \frac{\mathrm{d}N_{\beta}}{\mathrm{d}t}.\end{aligned} \tag{2.60}$$

By setting $N_{\alpha} + N_{\beta} = 1$ and substituting Eqs. 2.58 and 2.59 into Eq. 2.60, it follows that

$$\frac{\mathrm{d}M_z}{\mathrm{d}t} = -2W(M_0 - 1) \tag{2.61}$$

which is equivalent to $\mathrm{d}M_z / \mathrm{d}t$ in Eq. 2.45, provided M_0 is normalised to one and the spin-lattice relaxation rate $(1 / T_1)$ is set equal to

$$\frac{1}{T_1} = 2W. \tag{2.62}$$

Therefore, for a model of a fluctuating random field, the spin-lattice relaxation rate can be written

$$\frac{1}{T_1} = \gamma^2 \left\langle F^2(t) \right\rangle \mathcal{J}(\omega_0) = \gamma^2 \left\langle F^2(t) \right\rangle \frac{\tau_{\mathrm{c}}}{1 + \omega_0^2 \tau_c^2}. \tag{2.63}$$

The weakness of the above model is the assumption of spin-independent random fields. In a realistic spin system, the random fields have a molecular origin and must therefore be correlated with nuclear spin energy transfer through, for example, dipole-dipole interactions, whose influence on relaxation will be discussed in the next section.

Dipole-dipole relaxation

The most important mechanism for spin-1/2 nuclei is generally the through-space dipolar coupling between the spins. As described in Section 2.2.2, the secular part of the coupling averages to zero in isotropic liquids and gases, but the non-secular parts are capable of causing nuclear relaxation.

In liquids and gases, the fields imposed by spins on each other are manifest through random molecular/particulate motion. The correlation times of these random fields correspond to the correlation time of the particles. In general, small and large molecules/heavy particles have short and long correlation times, respectively. In addition, the correlation time is affected by the viscosity (increasing viscosity increases τ_c) and temperature (increasing temperature reduces τ_c) of the liquid/gas.

Consider a particle of spin **I** interacting with another particle of spin **S** (where the first particle is a nuclear spin and the second particle may be either a nuclear spin or unpaired electron). As with the random field model (non-interacting spins), relaxation for interacting spins can be described by considering the transition probabilities per unit time of the spins between energy levels, as was demonstrated first by Bloembergen, Pound and Purcell [30]. Fig. 2.11 shows the energy levels for a two spin system with the transition frequencies labelled. There are four possible energy eigenstates associated with the spins, $|\alpha\alpha\rangle$, $|\beta\alpha\rangle$, $|\beta\beta\rangle$ and $|\alpha\beta\rangle$ (where the first symbol refers to the spin eigenstate for spin **I** and the second symbol for spin **S**).

The transitions between the energy levels are denoted W_1^I, W_1^S, W_0 and W_2, distinguished according to which spins change spin state during the transition. Thus, W_1^I denotes a relaxation process involving an **I** spin flip; W_1^S denotes a relaxation process involving an **S** spin flip; W_0 is a relaxation

process in which both spins are flipped in opposite senses (flip-flop transition); and W_2 is a relaxation process in which both spins are flipped in the same sense (flip-flip transition). W_0, W_1 and W_2 indicate zero-, single- and double-quantum transitions, respectively.

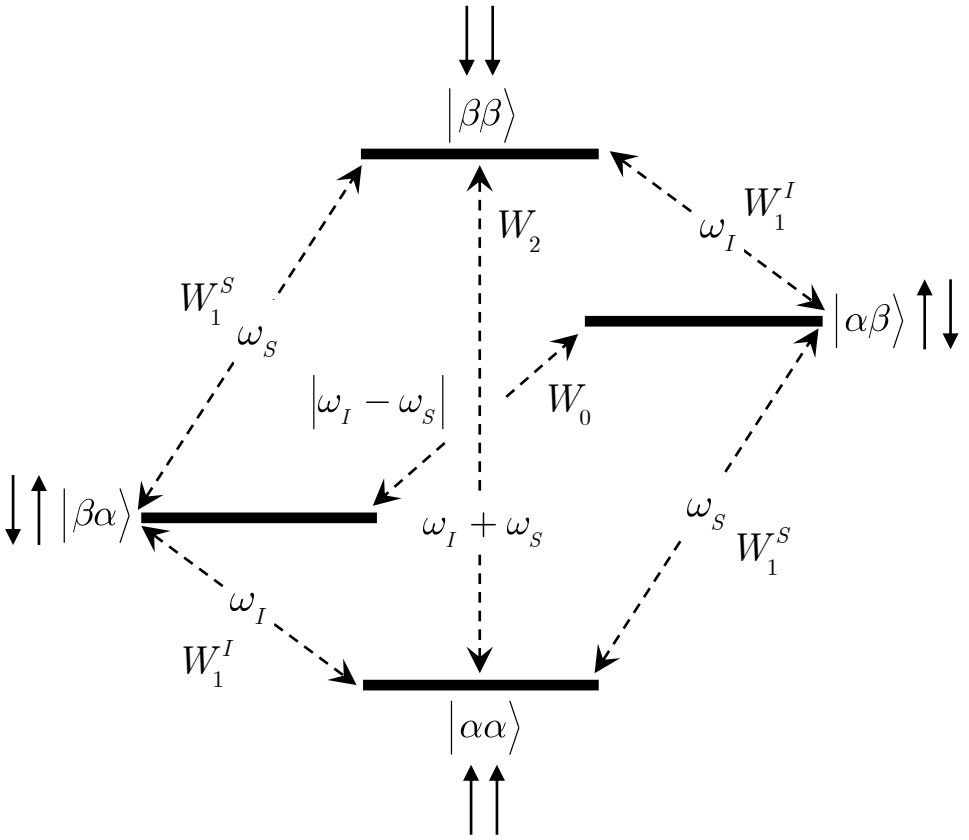

Figure 2.11: Transitions and associated rate constants for a system containing two spins, **I** and **S**.

Detailed calculations [31] provide the following results for the transition probabilities of a two-spin (**I** and **S**) system:

$$W_0 = \frac{1}{10} b^2 \mathcal{J}(\omega_I - \omega_S) \tag{2.64}$$

$$W_1^I = W_1^S = \frac{3}{20} b^2 \mathcal{J}(\omega_I) \tag{2.65}$$

$$W_2 = \frac{3}{5} b^2 \mathcal{J}(\omega_I + \omega_S)\,, \tag{2.66}$$

where b is the dipole-dipole coupling constant, as defined in Eq. 2.17. The return to equilibrium for the z-magnetisations of a two-spin system can be described completely by the Solomon equations [31]

$$\frac{\mathrm{d}\langle I_z\rangle}{\mathrm{d}t} = -\frac{1}{T_1^{II}}(\langle I_z\rangle - I_z^0) - \frac{1}{T_1^{IS}}(\langle S_z\rangle - S_z^0)$$

$$\frac{\mathrm{d}\langle S_z\rangle}{\mathrm{d}t} = -\frac{1}{T_1^{SI}}(\langle I_z\rangle - I_z^0) - \frac{1}{T_1^{SS}}(\langle S_z\rangle - S_z^0)\,, \tag{2.67}$$

with

$$\frac{1}{T_1^{II}} = W_0 + 2W_1 + W_2$$

$$\frac{1}{T_1^{IS}} = W_2 - W_0\,, \tag{2.68}$$

where $1/T_1^{II}$ and $1/T_1^{IS}$ are referred to as the auto-relaxation and cross-relaxation rate constants, respectively. In terms of spectral densities (see Eqs. 2.64–2.66), Eq. 2.68 can be written

$$\frac{1}{T_1^{II}} = \frac{1}{10}b^2\left[\mathcal{J}(\omega_I - \omega_S)) + 3\mathcal{J}(\omega_I) + 6\mathcal{J}(\omega_I + \omega_S)\right]$$

$$\frac{1}{T_1^{IS}} = \frac{1}{10}b^2\left[6\mathcal{J}(\omega_I + \omega_S) - \mathcal{J}(\omega_I - \omega_S)\right]. \tag{2.69}$$

Similar equations for T_1^{SS} and T_1^{SI} can be obtained by interchanging the indices I and S. For like spins ($\omega_I = \omega_S = \omega_0$), it can be shown the spin-lattice relaxation rate is given by

$$\frac{1}{T_1} = 2(W_1 + W_2) = \frac{3}{10}b^2\left[\mathcal{J}(\omega_0) + 4\mathcal{J}(2\omega_0)\right], \tag{2.70}$$

and the transverse relaxation rate

$$\frac{1}{T_2} = \frac{3}{20}b^2\left[3\mathcal{J}(0) + 5\mathcal{J}(\omega_0) + 2\mathcal{J}(2\omega_0)\right] \tag{2.71}$$

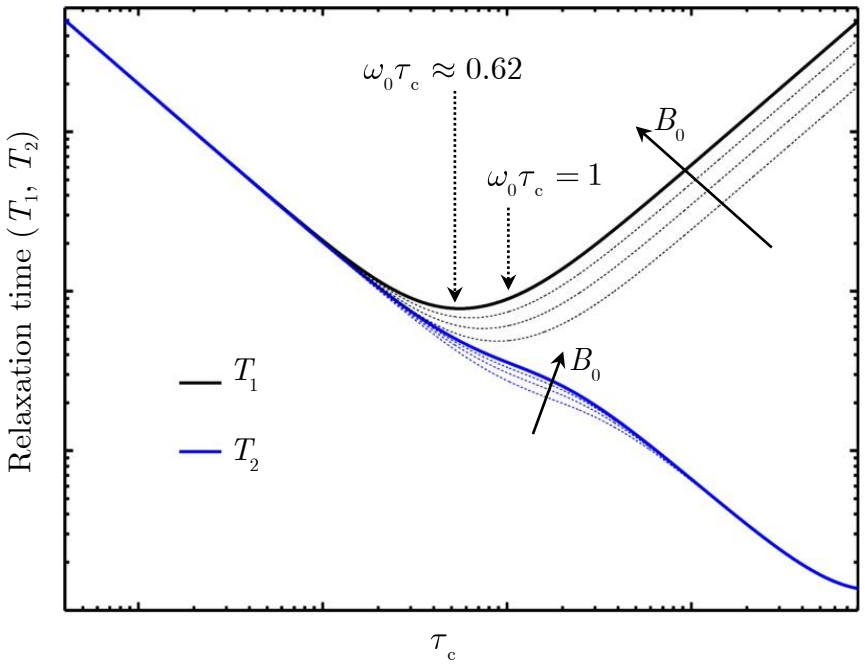

Figure 2.12: Variation of the relaxation times T_1 and T_2 as a function of correlation time, τ_c, due to dipole-dipole relaxation. Note the logarithmic scale on the x and y axes.

Whereas the longitudinal relaxation depends on the spectral densities at the Larmor frequency of **I** (or **S**), and at the frequencies $\omega_I + \omega_S$ and $\omega_I - \omega_S$, the transverse relaxation time is influenced by the spectral density at zero frequency ($\mathcal{J}(0)$) as well (Eq. 2.71). Therefore, the variations of T_1 and T_2 with correlation time are fundamentally different. Eqs. 2.70 and 2.71 are shown graphically in Fig. 2.12. At very short rotational correlation times, i.e. for $\omega_0\tau_c \ll 1$, the values of T_1 and T_2 are equal, a regime referred to as the extreme narrowing limit. As τ_c increases, both T_1 and T_2 decrease until T_1 passes through a minimum (for $\omega_0\tau_c \simeq 0.62$), whereafter T_1 increases while T_2 continues to decrease in the limit $\omega_0\tau_c \gg 1$. As a consequence, T_2 may become very small as the molecular mass increases (or the temperature/viscosity of the sample is reduced/increased), so the NMR peaks become progressively broader, while the T_1 may become very large. Therefore

in practice, for liquid samples, where $\omega_0\tau_c \ll 1$, both relaxation times tend to be very similar, and conversely, for solid samples, where $\omega_0\tau_c \gg 1$, the relaxation times may be substantially different, i.e. very long T_1 values and very short and T_2 values.

Other relaxation mechanisms

Magnetic interactions other than dipole-dipole interactions of nuclei contribute to NMR relaxation. For example, the anisotropy of the chemical shift tensor (CSA), which does not affect NMR spectra in liquids due to averaging as a result of fast molecular reorientation, but provides a relaxation mechanism in solids. Additional interactions, such as scalar coupling and quadrupolar interaction (which is relevant for nuclei with spin number $I > 1/2$), may play a role in certain spin systems. Quadrupolar interaction is a very efficient relaxation mechanism, and nuclei with spin $I > 1/2$ thus have short relaxation times. However, these interactions are not relevant for the results presented in this thesis and are therefore not discussed further.

2.2.5 NMR sensitivity

In section 2.2.3, the Boltzmann polarisation for a spin-1/2 system within a magnetic field, $\mathbf{B}_0$, in thermal equilibrium with a lattice temperature, T, was defined as

$$P_b \simeq \frac{|\gamma|\hbar B_0}{2kT}, \tag{2.72}$$

and the net magnetisation is related to P_b by

$$M_0 = \frac{1}{2} N\gamma\hbar P_b . \tag{2.73}$$

The NMR signal intensity following an RF pulse is proportional to M_0. At a typical NMR field strengths of 1.5 T and room temperature, Eq. 2.72 yields

relatively low polarisations: ^{129}Xe and ^{1}H polarisations of 1.4×10^{-6} and 5.1×10^{-6}, respectively. The high average ^{1}H spin concentration in the human body (80 M [32]), however, yielding a high ^{1}H M_0 (large N value in Eq. 2.73), and making it feasible to obtain clinical MR images with good signal-to-noise ratio (SNR). The low spin density of Xe in the gas phase results in a reduced M_0 compared to ^{1}H NMR in liquids; a typical ^{129}Xe NMR spectrum from thermally polarised ^{129}Xe on a 1.5 T GE scanner is shown in Fig. 2.13 (a).

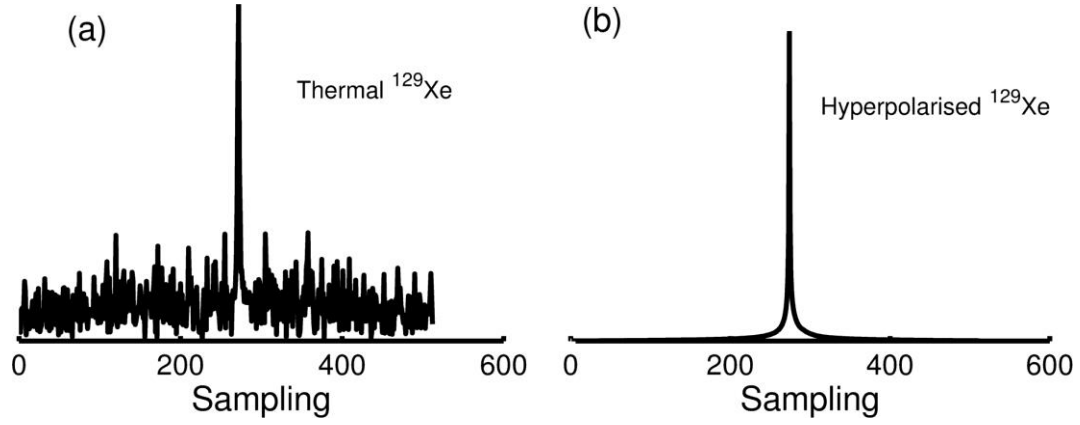

Figure 2.13: (a) Single-shot NMR spectrum (90° flip angle) from a 7.5 mL thermally polarised ^{129}Xe sample (Boltzmann polarisation). (b) Single-shot NMR spectrum (10° flip angle) from a 0.3 mL hyperpolarised ^{129}Xe sample.

Enhancement in the equilibrium magnetisation, and therefore detectable NMR signal, can be achieved – according to Eq. 2.72 and 2.73 – by increasing $\mathbf{B}_0$ (which becomes progressively costly and difficult) or by decreasing the temperature, T (which is unsuitable for certain samples – particularly living organisms). This is referred to the "brute force" approach. An alternative approach is to use a technique known as spin-exchange optical pumping (covered in the next section), which can be used to obtain nuclear polarisation increases of four to five orders of magnitude. A single-shot spectrum of ^{129}Xe that has been "hyperpolarised" is shown in Fig. 2.13 (b).

See below for a cartoon illustration of the nuclear polarisation enhancement using spin-exchange optical pumping to hyperpolarise ^{129}Xe.

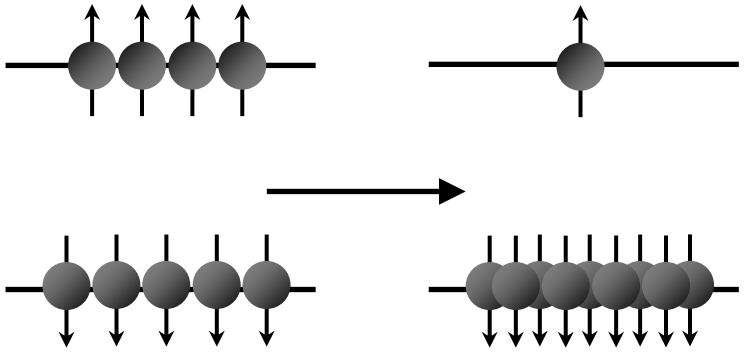

Figure 2.14: Schematic of the ^{129}Xe nuclear spin energy levels in thermal equilibrium (left) and after spin-exchange optical pumping (right).

2.3 Spin-exchange optical pumping with ^{129}Xe and Rb

Spin-exchange optical pumping is a two-step physical process involving (i) the optical pumping of electrons within an alkali vapour and (ii) subsequent spin-exchange collisions between noble gas atoms and the optically-pumped alkali vapour. In this section, the physics of these two processes is introduced to provide a theoretical underpinning to the experiments and modelling covered in Chapters 3 and 4 of this thesis.

2.3.1 Optical pumping with Rb

The principle idea upon which optical pumping relies, and for which Kastler received the 1966 Nobel prize in physics [33], is that the transfer of angular momentum from anisotropic resonant light to atoms or molecules, through scattering, induces ordering of electronic energy levels in which valence electrons become polarised. The alkali-metals are convenient choices for optical pumping because they each have a single unpaired valence electron (with well-defined selection rules), whose resonance wavelengths lie in the

visible and near-infrared part of the spectrum, compatible with inexpensive and powerful laser sources. Additionally, their relatively high volatility enables dense vapours to be produced at moderate temperatures.

Rubidium (Rb), from the Latin *rubidus* (meaning deep red), so named after the red lines observed in its emission spectrum [34], is the most commonly used alkali metal in optical pumping experiments. It has a low melting point of 39 °C, and the Rb vapour density at temperatures $>$ 39 °C can be estimated using the empirical vapour pressure curves as measured by Killian [35]

$$[\mathrm{Rb}] = \frac{10^{[10.55-(4132/T)]}}{k_{\mathrm{B}}T} \times 10^{-7}(\mathrm{cm}^{-3})\,, \tag{2.74}$$

where k_{B} is the Boltzmann constant and T is the absolute temperature in Kelvin (see Fig. 2.15 for a plot of [Rb] against T). An additional advantage of using Rb for optical pumping is the large separation between the D_1 (794.8 nm) and D_2 (780 nm) lines, which is wider than the typical linewidths of laser emissions (0.1 nm to 3 nm) resonant on the D_1 line.

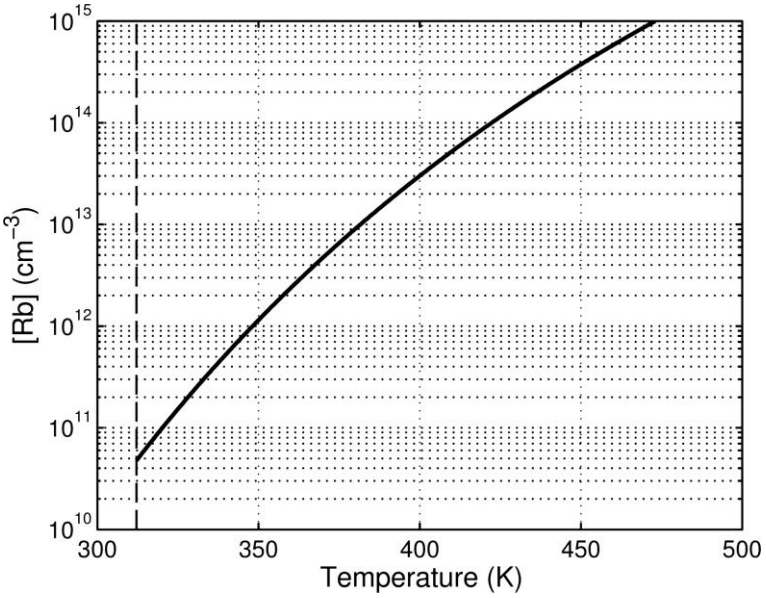

Figure 2.15: Rb density as a function of absolute temperature from Eq. 2.74. The vertical dashed line indicates the melting point of Rb (312 K).

Electronic energy levels of Rb atoms

Naturally occurring Rb comprises two isotopes: the stable ^{85}Rb (72.2 %) and the radioactive, primordial nuclide ^{87}Rb (27.8 %) (recently reported half-life of 4.96×10^{10} years [36]). The atomic number of Rb is Z=37, and the electron configuration is given by the Bohr model as [Kr]$5s^1$, so that Rb atoms are characterised by an inert noble gas krypton core plus a single, optically active valence electron in the *s* subshell. The spin-orbit interaction splits the 5p energy level into two components (fine structure): the first excited state, 5^2P_J, with $J = L + S = 1/2$ (where $S = 1/2$ is the electron spin angular momentum quantum number, $L = 1$ is the electron orbital angular momentum quantum number and J is the electron total angular momentum quantum number), characterised by the D_1 line (λ = 794.8 nm) and the second excited state, 5^2P_J, with $J = L + S = 3/2$, characterised by the D_2 line (λ = 780 nm). No fine structure is present in the ground state as $L = 0$ in the *s* subshell.

Both isotopes of Rb have nuclear spins: $I = 5/2$ for ^{85}Rb and $I = 3/2$ for ^{87}Rb; and the total angular momentum of the system is given by $\mathbf{F = I + J}$. The interaction between the electron total spin momentum and the nuclear spin angular momentum gives rise to further energy level splittings (hyperfine structure) for the ground state and two excited states. There are two hyperfine states for the each of the $5^2P_{1/2}$ and $5^2S_{1/2}$ energy levels, given by $F = I + 1/2$ and $F = I - 1/2$.

In the presence of an external magnetic field, $\mathbf{B}_0$, the ground-state Hamiltonian for an alkali metal is given by [37]

$$\mathcal{H}_g = \underbrace{A_g \mathbf{I}\cdot\mathbf{S}}_{Hyperfine} + \underbrace{\gamma_s S_z B_0 - \gamma_I I_z B_0}_{Zeeman}, \tag{2.75}$$

where A_g is the coupling coefficient for the magnetic dipole hyperfine interaction of the Rb nuclear spin, **I**, with the Rb electron spin, **S**. $\gamma_s S_z B_0$ and $\gamma_I I_z B_0$ are the Zeeman terms describing the magnetic dipole coupling of the nuclear and electron spins to the external field, respectively. The magnetic field values used in optical pumping experiments are typically small, such that the hyperfine interaction energy is dominant over the Zeeman splitting energy levels. See Fig. 2.16 for a schematic depicting the energy level splittings for both ^{85}Rb and ^{87}Rb isotopes. A detailed calculation of the energy levels can be found in ref. [38].

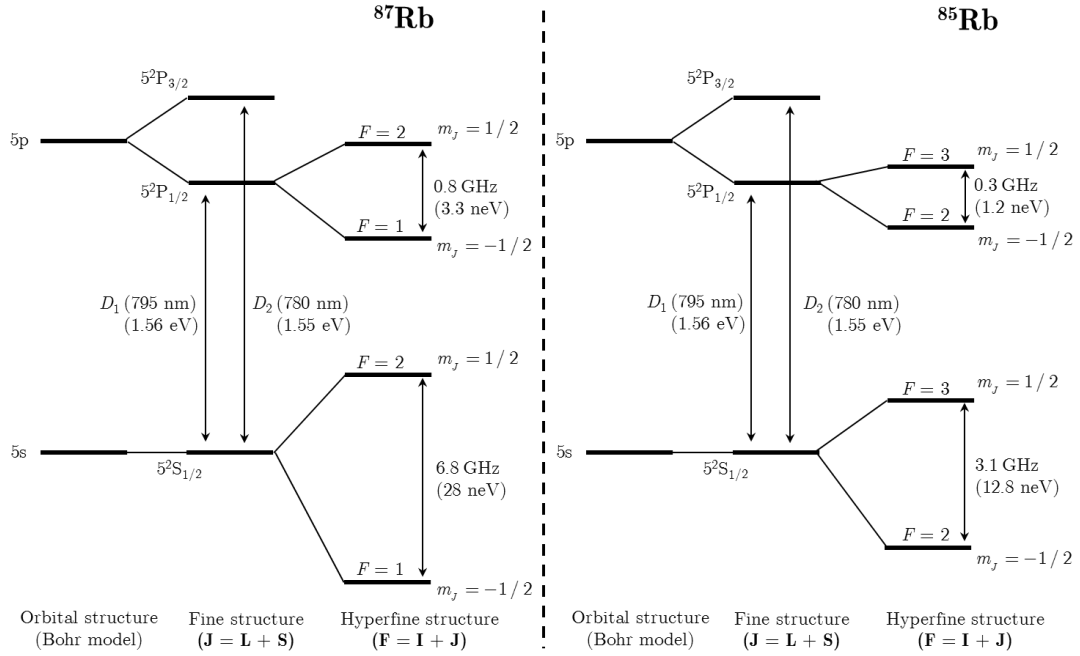

Figure 2.16: Energy level schemes of ^{87}Rb and ^{85}Rb for the Bohr model, the fine structure and the hyperfine structure (not drawn to scale). The D_1 excited state and ground state frequency splitting measurements can be found in refs. [39, 40] and ref. [41], respectively. NB: the Zeeman energy splittings have not been included here, nor has the hyperfine structure of the second excited state $5^2P_{3/2}$.

Depopulation optical pumping

Depopulation optical pumping refers to the selective excitation, and hence reduction in population, of a particular sublevel. A simplified Grotrian energy level diagram Rb, which neglects the nuclear spin and the hyperfine Zeeman splittings, is shown in Fig 2.17. Neglecting the nuclear spin of Rb is generally acceptable so long as pressure broadening of the D_1 line is sufficient to make the hyperfine Zeeman splittings unresolved. This is almost always the case as the pressure broadening for Rb in the presence of noble gases is 10 GHz per amagat or more [42], while all hyperfine splittings are <10 GHz. In the simplified Grotrian diagram shown in Fig. 2.17, left circularly polarised light parallel to an applied field (σ^+ helicity, photon spin $s_z = 1$) tuned to the D_1 transition line depopulates atoms from the $5^2S_{1/2}$ ground state into the Rb first excited state $5^2P_{1/2}$. Following the selection quantum rule $\Delta m = 1$, the laser light pumps atoms from only the $m_J = -1/2$ ground state into the $m_J = 1/2$ first excited state. (Note that for σ^- helicity, photon spin $s_z = -1$, laser light would pump atoms from the $m_J = 1/2$ ground state into the $m_J = -1/2$ first excited state following the selection rule $\Delta m = -1$.) From the $m_J = 1/2$ state, the atom will spontaneously decay into the two ground states with probabilities given by the Clebsch-Gordon coefficients (branching ratios): the probability decay from $5^2P_{1/2}$ ($m_J = 1/2$) to $5^2S_{1/2}$ ($m_J = -1/2$) is 2/3; from $5^2P_{1/2}$ ($m_J = 1/2$) to $5^2S_{1/2}$ ($m_J = 1/2$) it is 1/3. In practical ^{129}Xe SEOP experiments, buffer gases, N_2 and ^{4}He, are added to the optical cell containing the Rb atoms to equalise the sublevel populations in the excited state through a process known as collisional mixing. In collisional mixing, the atoms are transferred back and forth between the $5^2P_{1/2}$ $m_J = 1/2$ and $m_J = -1/2$ sublevels, which alters the branching ratio to 1/2 for both cases. Collisional mixing also occurs in the ground state, but to

a much lesser degree than in the excited state due to the spherically symmetric s subshell being less susceptible to wave function perturbation compared to the non-spherically symmetric p subshell.

Spontaneous radiative decay of the excited states can generate non-circularly polarised resonant photons. If the Rb vapour is dense and the average path length out of the cell is long, then the unpolarised photon will likely be reabsorbed by another Rb atom (depolarising the Rb atom in the process). After the photon is reabsorbed, the newly excited atom can again spontaneously decay by emitting another non-circularly polarised photon in the process. Many cycles of reabsorption and emission can occur, reducing the Rb vapour polarisation in a phenomenon known as radiation trapping.

Addition of N_2 molecules helps by reducing radiation trapping. Rb collisions with N_2 molecules quench the Rb atoms in the excited states nonradiatively; rather than photon transmission, the energy is transferred to the vibrational levels of the N_2 molecules [43].

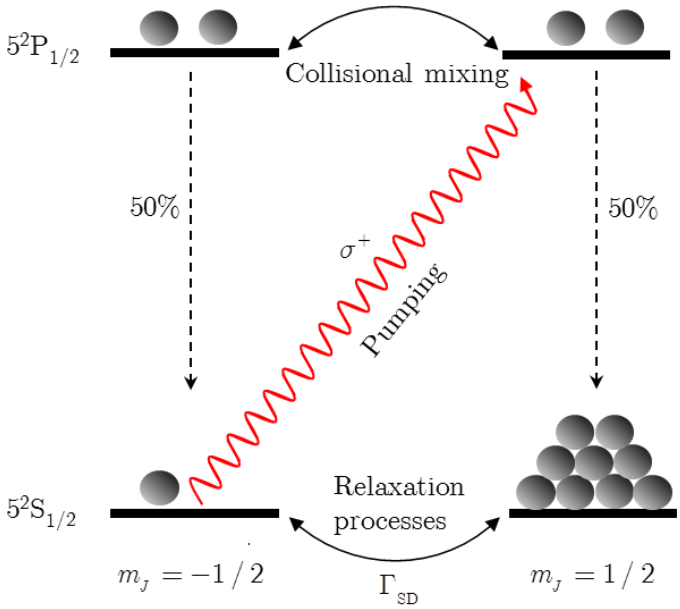

Figure 2.17: Optical pumping alkali metal atoms into the $m_J = 1/2$ state with left circularly polarised light. NB: in this schematic, the nuclear spin of Rb is neglected.

Optical pumping equations

Once a Rb atom is polarised to the ground state sublevel $m_J = 1/2$, it can be depolarised through ground state mixing via the following mechanisms: (i) absorption of non-circularly polarised after radiative Rb decay from the excited state – as mentioned above, addition of N_2 reduces this by absorbing the energy into its rotational and translational degrees of freedom, quenching the Rb electrons in the excited state to the ground state nonradiatively; (ii) Rb wall collisions; and (iii) interactions with gases present in the mixture. These ground state mixing contributions can be summed up and characterised by a spin-destruction rate, Γ_{SD}, which will be covered in more detail in Chapter 3, Section 3.2.1.

The number of Rb atoms being pumped from the $m_J = -1/2$ state to the final state $m_J = 1/2$ per second is given by the optical pumping rate

$$\gamma_{\mathrm{opt}}(\nu) = \int \Phi(\nu)\sigma_{\mathrm{s}}(\nu)\,, \tag{2.76}$$

where $\Phi(\nu)$ is the photon flux (number of photons per cm^2 per second) and $\sigma_{\mathrm{s}}(\nu)$ is the D_1 absorption cross section. For a given γ_{opt} and Γ_{SD}, the equation describing rate of change of the alkali electron spin is [44]

$$\frac{\mathrm{d}\left\langle S_z \right\rangle}{\mathrm{d}t} = \frac{1}{2}(1 - 2\left\langle S_z \right\rangle)\gamma_{\mathrm{opt}} - \left\langle S_z \right\rangle \Gamma_{\mathrm{SD}}\,, \tag{2.77}$$

where $(1 - 2\left\langle S_z \right\rangle)\gamma_{\mathrm{opt}}$ is the photon absorption rate, where each absorption deposits $\hbar/2$ unit of angular momentum. By defining the Rb polarisation, $P_{\mathrm{Rb}} = 2\left\langle S_z \right\rangle$ (with respect to an applied field in the z-direction), Eq. 2.77 can be solved to give a time-dependent Rb polarisation:

$$P_{\mathrm{Rb}}(t) = \frac{\gamma_{\mathrm{opt}}}{\gamma_{\mathrm{opt}} + \Gamma_{\mathrm{SD}}}\Big[1 - \exp(-(\gamma_{\mathrm{opt}} + \Gamma_{\mathrm{SD}})t)\Big]. \tag{2.78}$$

Rb polarisation saturation is typically achieved in times of the order 10–20 ms, which is sudden in comparison to the time scale for other processes in a

SEOP experiment (of the order of seconds and minutes), so that (during SEOP) a steady-state, cell-volume averaged Rb polarisation may be assumed

$$\left\langle P_{\mathrm{Rb}} \right\rangle = \frac{\gamma_{\mathrm{opt}}}{\gamma_{\mathrm{opt}} + \Gamma_{\mathrm{SD}}} \tag{2.79}$$

It is clear from this expression that in order to achieve high Rb polarisation, it is important to minimise Γ_{SD} while maximising γ_{opt}.

2.3.2 Rb-^{129}Xe spin-exchange

The key process in Rb-^{129}Xe SEOP is the collisional transfer of polarisation between the optically pumped Rb atoms and ^{129}Xe nuclei. The interaction Hamiltonian describing the collisions between Rb and Xe atoms is [45]

$$\mathcal{H}_{\text{Rb-Xe}} = A\mathbf{I}\cdot\mathbf{S} + \gamma\mathbf{N}\cdot\mathbf{S} + \alpha\mathbf{K}\cdot\mathbf{S}, \tag{2.80}$$

where $A\mathbf{I}\cdot\mathbf{S}$ is the hyperfine magnetic dipole interaction between the Rb electron spin $\mathbf{S}$ and its nuclear spin $\mathbf{I}$, $\gamma\mathbf{N}\cdot\mathbf{S}$ is the spin-rotation interaction between $\mathbf{S}$ and the rotational angular momentum, $\mathbf{N}$, (which contributes only to Rb spin destruction) of the Rb-^{129}Xe colliding pair and $\alpha\mathbf{K}\cdot\mathbf{S}$ is the magnetic dipole interaction between $\mathbf{S}$ and the ^{129}Xe nuclear spin $\mathbf{K}$. It is the term $\alpha\mathbf{K}\cdot\mathbf{S}$ that is responsible for Rb-^{129}Xe spin-exchange, where the coupling constant α denotes the Fermi contact interaction, given by [46, 47]

$$\alpha(R) = \frac{16\pi}{3}\frac{\mu_{\mathrm{B}}\mu_K}{K} \mid \psi(R) \mid^2, \tag{2.81}$$

where μ_{B} is the Bohr magneton, μ_K is the magnetic moment of the ^{129}Xe nucleus and $\psi(R)$ is the wave function of the Rb valence electron at the position of the ^{129}Xe nucleus (a distance R away from the Rb valence electron). The various angular momentum vectors denoted in Eq. 2.80 are illustrated in Fig. 2.18 below.

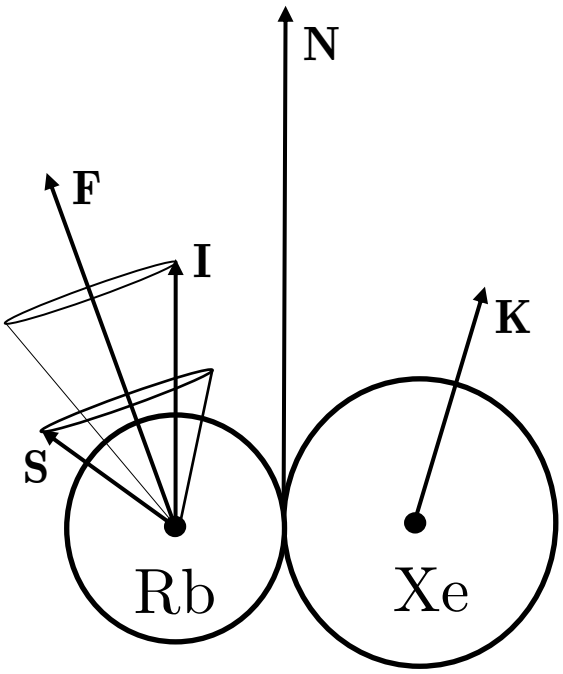

Figure 2.18: Angular momentum scheme of a RbXe molecule.

Rb-^{129}Xe spin-exchange occurs either while the Xe and Rb atoms are bound in van der Waals molecules or during simple binary collisions between Rb and Xe atoms (Fig. 2.19). The relative contribution of binary collisions and the formation and break-up of van der Waals molecules to the overall Rb-^{129}Xe spin-exchange rate, γ_{SE}, is covered for practical SEOP experiments in Chapter 3, Section 3.2.2.

For a given spin exchange rate, γ_{SE}, and ^{129}Xe relaxation rate, Γ, the rate equation governing the ^{129}Xe nuclear spin is given by

$$\frac{\mathrm{d}\left\langle K_z \right\rangle}{\mathrm{d}t} = \gamma_{\mathrm{SE}}\left[\left\langle S_z \right\rangle - \left\langle K_z \right\rangle\right] - \Gamma\left\langle K_z \right\rangle. \tag{2.82}$$

Defining the ^{129}Xe polarisation as $P_{\mathrm{Xe}} = 2\left\langle K_z \right\rangle$ (valid for a two-state spin system), Eq. 2.82 can be solved to obtain the ^{129}Xe polarisation build up with time:

$$P_{\mathrm{Xe}}(t) = \frac{\gamma_{\mathrm{SE}}}{\gamma_{\mathrm{SE}} + \Gamma}\left\langle P_{\mathrm{Rb}} \right\rangle\left[1 - \exp(-(\gamma_{\mathrm{SE}} + \Gamma)t)\right]. \tag{2.83}$$

Analogous to Eq. 2.79, the steady-state polarisation for ^{129}Xe is given by

$$P_{\mathrm{Xe}} = \frac{\gamma_{\mathrm{SE}}}{\gamma_{\mathrm{SE}} + \Gamma} \left\langle P_{\mathrm{Rb}} \right\rangle \ . \tag{2.84}$$

For high ^{129}Xe polarisations, it is therefore necessary to maximise γ_{SE} and P_{Rb} while minimising the ^{129}Xe spin relaxation rate.

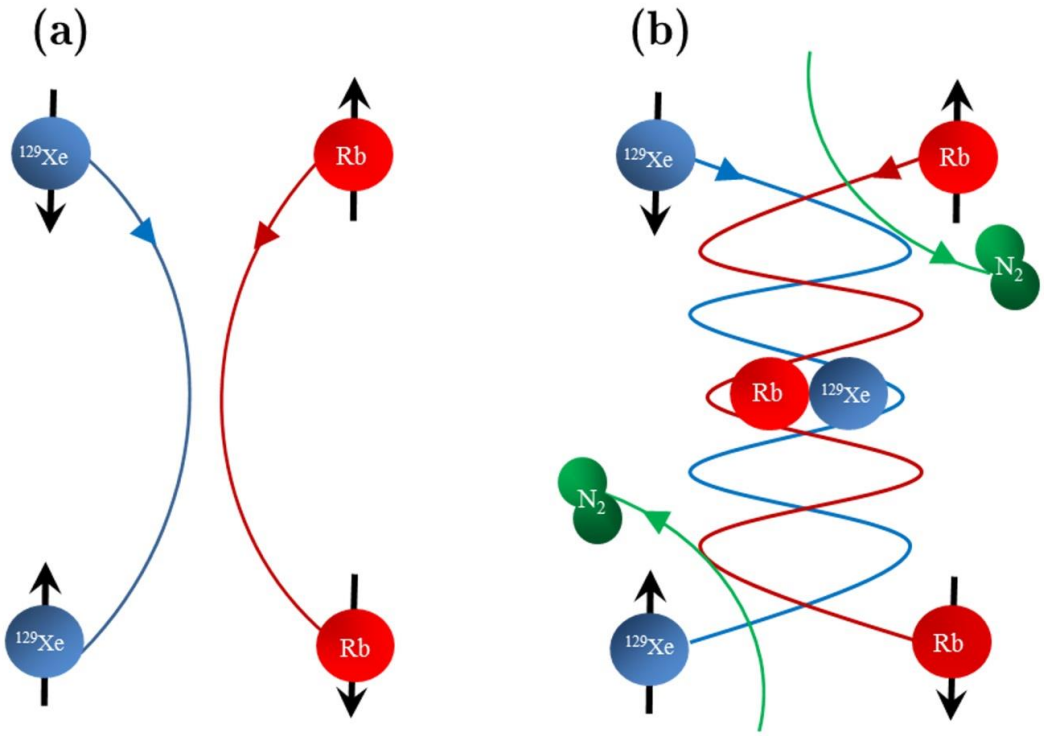

Figure 2.19: Rb-^{129}Xe spin-exchange process through (a) binary collisions and (b) the formation and breakup of RbXe van der Waals molecules. The third body in (b) is required to simultaneously satisfy conservation of energy and momentum.

In this section, the physics of spin-exchange optical pumping that forms the theoretical basis for the experiments and modelling in Chapter 3 of this thesis has been covered. A more complete overview can be found in refs. [44, 45] and a rigorous theoretical treatment on the theory of SEOP can be found in ref. [37].

Chapter 3

Optimisation of a continuous-flow ^{129}Xe SEOP polariser

3.1 Introduction

In this chapter, a home-built ^{129}Xe SEOP polariser is described and the process of production of polarised ^{129}Xe is optimised for routine *in vivo* lung imaging. The two most commonly used methods used to polarise ^{129}Xe with SEOP are referred to as "continuous flow" [48-54] and "stopped flow" (batch mode) [55-58]. Made feasible for large volume ^{129}Xe polarisation by Driehuys *et al.* [48], continuous flow SEOP utilises the fast spin-exchange rate between Rb and ^{129}Xe. The method developed by Driehuys *et al.* operates with a high gas density ($>$ 5 amg) cell combined with broad linewidth lasers (~2 nm FWHM available at the time) for optical pumping. The combination of broad linewidth lasers and a pressure-broadened Rb D_1 absorption line provides a good emission/absorption linewidth match, enabling efficient absorption of the polarised beam of photons from the laser. To mitigate Rb-Xe spin destruction at these high pressures (see Eqs. 3.2 and 3.4), low Xe partial pressure is needed in the cell, which means that for Xe

This chapter is based on the paper Norquay *et al.*, *J. Appl. Phys*, DOI: 10.1063/1.4776763

production, the ^{129}Xe needs to be polarised at low partial pressures and cryogenically collected using a liquid N_2 freeze-out process. During freeze-out, Xe is separated from the buffer gases He and N_2, accumulating over time as frozen Xe ice in a constant gas flow regime. This requires gas to be frozen out over a period of 30–60 minutes, typically providing 1 L of polarised gas at polarisations of 5–10 %. The gas polarised with these original flow systems has been demonstrated to provide diagnostic quality ^{129}Xe lung MRI images in clinical lung imaging studies [59].

An alternative approach developed at the University of New Hampshire [60] operates at low cell densities ($<$ 1 amg) using a very high power array ($>$ 1000 W) of narrow linewidth lasers. This system produces ^{129}Xe gas at high polarisation and very promising clinical lung MRI results have been reported [14]. Nevertheless, the low-pressure regime still necessitates cryogenic collection of the Xe, or alternatively some method of compression would have to be used. Moreover, the complicated glassware, low-pressure regime and complex high power laser system means that this system is expensive to build and is maintenance intensive. At low pressures (0.01–1 amg), the formation and break-up times of vdW molecules are sufficiently long that the Rb electron spin polarisation can be completely lost during a molecular lifetime and is referred to as the long molecular lifetime limit [61]. This long molecular lifetime regime is characterised by a rapid increase in the Rb electron spin relaxation rate with increasing gas density due to increasing rates of molecular formation. At higher densities (1–10 amg) the Rb electron spin relaxation becomes density independent as the increasing formation rate is compensated by a small relaxation probability in a single, short molecular lifetime. This is referred to as the short molecular lifetime limit and is the SEOP regime that is explored in this chapter where the cell density is 1.44 amg.

3.2 Equations for ^{129}Xe polarisation

As covered in Chapter 2, Section 2.3.1, to increase the efficiency of the optical pumping process, N_2 and He are added to the cell to act as buffer gases. N_2 prevents radiative emissions of uncontrolled circularly polarised or linearly polarised photons by quenching the Rb excited energy state into its vibrational levels [62] while He, with its lower Rb spin-destruction rate, is used at higher concentrations than N_2 and, through collisional broadening, causes an increase in the linewidth of the D_1 absorption line [42].

As derived in Chapter 2, (Eq. 2.79), the average, steady-state Rb polarisation, $\langle P_{\mathrm{Rb}} \rangle$, is given by $\langle P_{\mathrm{Rb}} \rangle = \gamma_{\mathrm{opt}} / (\gamma_{\mathrm{opt}} + \Gamma_{\mathrm{SD}})$, where γ_{opt} is the average optical pumping rate over whole cell volume, calculated by integrating over frequency, ν, the photon flux, Φ, and the Rb D_1 absorption cross section, σ_s, thus

$$\gamma_{\mathrm{opt}}(\nu, z) = \int \Phi(\nu, z)\sigma_s(\nu) \ . \tag{3.1}$$

The Rb spin polarisation destruction rate, Γ_{SD}, can be attributed to binary collisions with atoms in the SEOP mixture or the formation and break-up of short-lived Rb-Xe van der Waals molecules.

3.2.1 Practical expressions for Rb spin destruction

The spin destruction contribution from binary collisions can be written as

$$\Gamma_{\mathrm{SD}}^{\mathrm{BC}} = \sum_i [\mathrm{G}_i] \kappa_{\mathrm{SD}}^{\text{Rb-}i} \ , \tag{3.2}$$

where $\kappa_{\mathrm{SD}}^{\text{Rb-}i}$ is the Rb spin-destruction cross section for Rb binary collisions with each gas atom present in the SEOP cell, each with a number density

$[\mathrm{G}_i]$. The Rb number density is calculated using Eq. 2.74 from Chapter 2 and the individual gas densities are calculated using

$$[\mathrm{G}_i] = f_i \left(\frac{T_0}{T} \frac{P}{P_0} n_0 \right) \times 10^{-6} (\mathrm{cm}^{-3}), \tag{3.3}$$

where f_i is the fraction of each gas in the gas mixture, T_0 and P_0 are the standard temperature and pressure values of 273.15 K and 1 atm, T and P are the measured temperature and pressure inside the SEOP cell and $n_0 = 2.69 \times 10^{25} \mathrm{m}^{-3}$ is the Loschmidt constant, which defines the number of ideal gas atoms per cubic metre at 273.15 K and 1 atm. Values for $\kappa_{\mathrm{SD}}^{\mathrm{Rb\text{-}i}}$ have been reported as $\kappa_{\mathrm{SD}}^{\mathrm{Rb\text{-}Rb}} = 4.2 \times 10^{-13}$ $\mathrm{cm}^3\mathrm{s}^{-1}$ [63], $\kappa_{\mathrm{SD}}^{\mathrm{Rb\text{-}He}} = 1 \times 10^{-29}\ T^{4.26}$ $\mathrm{cm}^3\mathrm{s}^{-1}$ [63], $\kappa_{\mathrm{SD}}^{\mathrm{Rb\text{-}N_2}} = 1.3 \times 10^{-25}\ T^8$ $\mathrm{cm}^3\mathrm{s}^{-1}$ [64] and $\kappa_{\mathrm{SD}}^{\mathrm{Rb\text{-}Xe}} = 6.3 \times 10^{-17} (T - 273.15)^{1.17}$ $\mathrm{cm}^3\mathrm{s}^{-1}$ [61]. See Table 3.1 for comparative magnitudes of each cross section at a temperature of 373 K. The Rb-Xe spin destruction cross section was obtained from a measured cross section of 8.48×10^{-15} $\mathrm{cm}^3\mathrm{s}^{-1}$ at 253 K [61], where the $(T - 273)^{1.17}$ temperature dependence was observed. The Rb spin-destruction rate due to the formation and break-up of Rb-Xe van der Waals collisions has been estimated [65] as

$$\Gamma_{\mathrm{SD}}^{\mathrm{vdW}} = \left(\frac{66183}{1 + 0.92 \dfrac{[\mathrm{N}_2]}{[\mathrm{Xe}]} + 0.31 \dfrac{[\mathrm{He}]}{[\mathrm{Xe}]}} \right) \left(\frac{T}{423} \right)^{-2.5} \tag{3.4}$$

The total Rb spin-destruction rate is then $\Gamma_{\mathrm{SD}} = \Gamma_{\mathrm{SD}}^{\mathrm{BC}} + \Gamma_{\mathrm{SD}}^{\mathrm{vdW}}$, and a value for a gas-composition-specific vdW spin-destruction cross section, $\kappa_{\mathrm{SD}}^{\mathrm{vdW}}$, can be calculated as 1.79×10^{-16} $\mathrm{cm}^3\mathrm{s}^{-1}$ from $\Gamma_{\mathrm{SD}}^{\mathrm{vdW}} / [\mathrm{G}_{\mathrm{tot}}]$, where $[\mathrm{G}_{\mathrm{tot}}] = \sum [\mathrm{G}]_i = [\mathrm{Xe}] + [\mathrm{He}] + [\mathrm{N}_2]$ is the total gas density within the SEOP cell used in this study (see Table 3.1). From Eqs. 3.2 and 3.4, it is clear that in order to reduce the Rb spin destruction, the Xe concentration should be kept low within the cell, whereas He and N_2 can be held at higher pressures,

due to their spin-destruction cross sections being orders of magnitude smaller than that of Xe (Table 3.1).

3.2.2 Practical expressions for Rb-Xe spin exchange

Rb-Xe spin exchange, γ_{SE}, is dominated by Rb-Xe binary collisions at high pressure [66, 67] and short-lived Rb-Xe van der Waals interactions at low pressure [68]. Both the binary- and vdW-mediated spin exchange rates, $\gamma_{\mathrm{SE}}^{\mathrm{BC}}$ and $\gamma_{\mathrm{SE}}^{\mathrm{vdW}}$, are linearly proportional to the Rb density, [Rb], and are given by the following

$$\gamma_{\mathrm{SE}}^{\mathrm{BC}} = \kappa_{\mathrm{SE}}^{\mathrm{BC}}[\mathrm{Rb}] \tag{3.5}$$

$$\gamma_{\mathrm{SE}}^{\mathrm{vdW}} = \sum_i \frac{[\mathrm{Rb}]}{([\mathrm{G}_i]\,/\,\xi_i)}\,. \tag{3.6}$$

Combining the formula for the Rb-Xe spin-exchange rate due to the contribution from binary collisions and the contribution from Rb-Xe van der Waals molecules, the total spin exchange rate, γ_{SE}, can be calculated from

$$\gamma_{\mathrm{SE}} = \gamma_{\mathrm{SE}}^{\mathrm{vdW}} + \gamma_{\mathrm{SE}}^{\mathrm{BC}} = \left(\sum_i \frac{1}{([\mathrm{G}_i]\,/\,\xi_i)} + \kappa_{\mathrm{SE}}^{\mathrm{Rb\text{-}Xe}}\right)[\mathrm{Rb}] = (\kappa_{\mathrm{SE}}^{\mathrm{vdW}} + \kappa_{\mathrm{SE}}^{\mathrm{BC}})[\mathrm{Rb}]\,. \tag{3.7}$$

The parameter ξ_i denotes van der Waals specific rates for each gas atom with density $[\mathrm{G}_i]$. $\xi_{\mathrm{Xe}} = 5230$ Hz [68]; $\xi_{\mathrm{N_2}} = 5700$ Hz calculated by Rice and Raftery [69] from Zeng *et al.* [70]; and $\xi_{\mathrm{He}} = 17000$ Hz calculated by Driehuys *et al.* [48] from Cates *et al.* [68]. $\kappa_{\mathrm{SE}}^{\mathrm{vdW}}$ and $\kappa_{\mathrm{SE}}^{\mathrm{BC}}$ are the spin exchange cross sections from vdW interactions and binary Rb-Xe collision, respectively. $\kappa_{\mathrm{SE}}^{\mathrm{vdW}}$ is calculated from the summation term in Eq. 3.7 as 3.46×10^{-16} $\mathrm{cm^3 s^{-1}}$ (specific to the gas composition used in this study: 3 % Xe, 10 % N_2 and 87 % He at 2 bars) and $\kappa_{\mathrm{SE}}^{\mathrm{BC}}$ has been reported as 2.17×10^{-16} $\mathrm{cm^3 s^{-1}}$ [66]. It is worth noting that in this regime the vdW spin exchange cross section is a factor of 1.6 larger than the binary spin exchange cross section. See Fig. 3.1

for a summary of the mechanisms that determine the spin-exchange optical pumping efficiency.

3.2.3 ^{129}Xe polarisation during gas flow

Following Eq. 2.83 derived in Chapter 2, the nuclear spin polarisation of ^{129}Xe generated through spin exchange with polarised Rb atoms during gas flow after a given residency time t_{res} in the cell is given by

$$P_{Xe}(t_{res}) = \frac{\gamma_{SE}}{\gamma_{SE} + \Gamma}\langle P_{Rb}\rangle\left[1 - \exp(-(\gamma_{SE} + \Gamma)t_{res})\right] \tag{3.8}$$

where Γ is the rate of loss of nuclear ^{129}Xe polarisation. Γ is thought to be dominated by wall relaxation, which depends on the cell geometry (surface area/volume) and its surface relaxation properties (paramagnetic centres) [71]. The atomic residency time in the cell can be calculated using $t_{res} = V[G_a]/Q$, where V is the cell volume, $[G_a]$ is the gas density is amagat (amg), where 1 amg = $n_0 = 2.69 \times 10^{25}$ m^{-3}) and Q is the gas flow rate measured in sccm (standard cubic centimetres per minute).

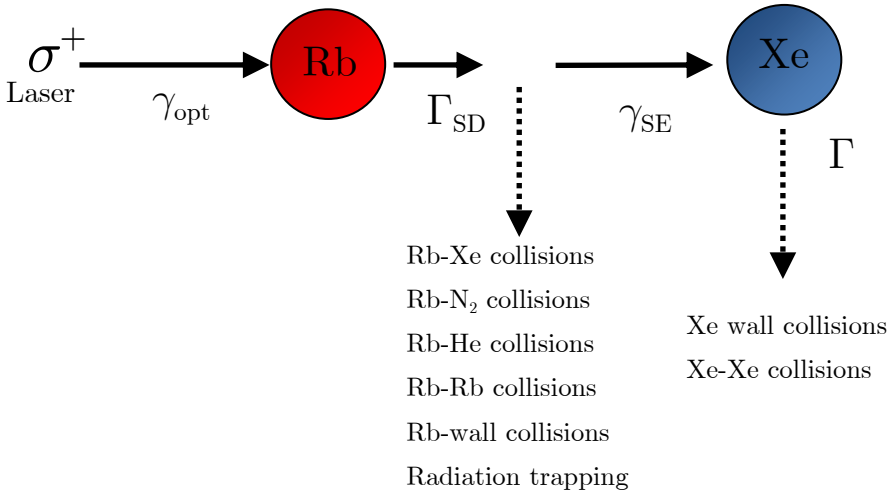

Figure 3.1: Illustration of the mechanisms that determine the efficiency of Rb-^{129}Xe spin-exchange optical pumping.

Cell constituent	Rb	He	N_2	Xe
Atomic density (cm^{-3})	5.82×10^{12} [35]	3.38×10^{19}	3.88×10^{18}	1.16×10^{18}
$\kappa_{SD}^{Rb\text{-}i}$ (cm^3s^{-1})	4.2×10^{-13} [63]	9.04×10^{-19} [63]	6.75×10^{-18} [64]	1.09×10^{-14} [61]

Interaction	Symbol	Spin destruction rate (Hz)	Symbol	Spin exchange rate (Hz)
Binary	Γ_{SD}^{BC}	1.27×10^{4}	γ_{SE}^{BC}	1.26×10^{-3}
vdW	Γ_{SD}^{vdW}	6.94×10^{3} [65]	γ_{SE}^{vdW}	2.01×10^{-3} [68]
Total	Γ_{SD}	1.96×10^{4}	γ_{SE}	3.27×10^{-3}

Table 3.1: Upper half: calculated number densities of atoms in the cell and binary spin-destruction cross sections, $\kappa_{SD}^{Rb\text{-}i}$. Lower half: vdW and binary spin-destruction and spin-exchange rates. All cross sections and rates correspond to a SEOP cell at a temperature 373 K, pressure of 2 bar (temperature and pressure of the cell when filling it with the gas mixture, total gas number density of 1.44 amg) and a gas composition of 3 % Xe, 10 % N_2 and 87 % He.

3.3 Experimental procedure

3.3.1 Polariser components

The polariser was developed in Sheffield over the last seven years and consists of the following:

Field coil

(i) Helmholtz B_0 coil (Acutran, PA, USA) with diameter 80 cm and $B_0 \approx$ 3 mT driven by a DC power supply delivering a current of 7.4 A.

Optical cell and ^{129}Xe NMR

(ii) A cylindrical Pyrex optical SEOP cell (25 cm length, 5 cm diameter) (Fig. 3.3) filled with $<$ 1 gram of molten Rb that was pipetted into the cell inside an argon gas glove box. NB: The cell was not surface treated prior to

Rb distillation. The cell is located at the isocentre of the B_0 field within a non-magnetic calcium silicate oven with glass windows. The oven is heated with an inline air process heater (Omega, CT, USA) fed from a compressed air line, and the oven temperature was measured using a three-terminal resistance temperature detector (RTD-3–1PT100K2515, Omega, CT, USA) placed 2 cm from the cell.

In order to examine cell-wall relaxation effects, the T_1 of the ^{129}Xe in the cell was measured cold (~293 K) in order to limit effects of Rb spin exchange from distorting the measurement. A ^{129}Xe gas $T_1 = 1/\Gamma$ of 48 ± 1 min (Fig. 3.4) using enriched (86 % ^{129}Xe) Xe was measured (TR = 5 min) in the SEOP cell using a home built NMR spectrometer with a surface RF coil placed on the top of the cell. (From this, it can be concluded that cell wall relaxation [$\Gamma = 3.5\times10^{-4}$ in Eq. 3.8] is not significant in the SEOP cell.)

NMR spectrometer

The hardware required for NMR spectroscopy on the SEOP cell comprises a PC with a data acquisition card (National Instruments, NI-6251, 1.25 MS/s sample rate, Berkshire, UK), a BNC connection box, a home-made transmit-receive cross diode pair duplexer (Fig. 3.2) and a combined transmit/receive (Tx/Rx) surface coil, which is grounded to the aluminium frame of the B_0 coils. Additionally, a variable capacitance box (100 pF to 11 μF) is employed to alter tuning of the coil such that the resonance frequency can be adjusted for different field strengths. The combined Tx/Rx surface coil is 3 cm in diameter (hand-wound from 0.25 mm copper wire with 100 turns) and has a quality factor, Q, of ~10. Typical ring down times for the coil are of the order 6 ms. The relatively simplicity of the hardware arises from the passive T-R switch duplexer, which consists of four (high speed) diodes and two resistors, enabling the use of a single Tx/Rx coil to measure SEOP ^{129}Xe signals.

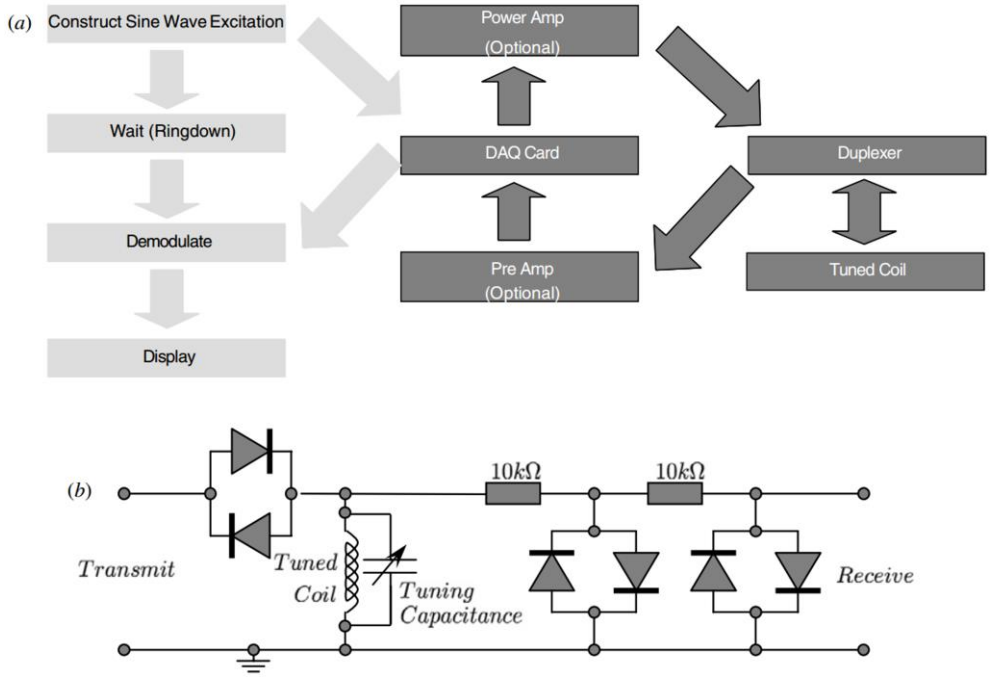

Figure 3.2: (a) Simplified flow diagram of the spectrometer design. The software functions are shown in light grey, whilst hardware is in dark grey. (b) Circuit diagram for low-frequency passive duplexer switch. Taken with permission from ref. [72].

The signal generation, acquisition and processing is performed by custom-software written in LabVIEW in combination with the National Instruments data acquisition card, which is connected to a PC via USB. Typical excitation pulses are 0.15 ms long with an amplitude of 0.8 V. The pulse duration can be varied to lengths of up to 2 ms and amplitudes of 10 V are available under the current card. Timing of the start of data collection is via the internal trigger of the card, which is essential to avoid timing discrepancies. If timing is not performed accurately, signal averaging cannot be performed due to the relative phase differences between successive pulses. The accuracy of the timing was checked by averaging successive pulses, which confirmed the synchronisation of the Tx output to the Rx triggering. Full details of the hardware and software can be found in ref. [72].

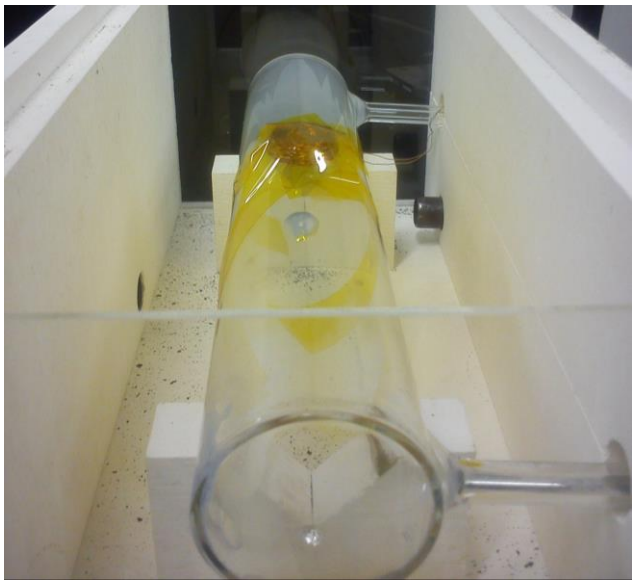

Figure 3.3: Photo of optical cell containing droplet of Rb. The NMR coil can be seen on top of the cell, held in place with heat-resistant Kapton tape. Note that in this photo the lid has been removed from the ceramic oven housing.

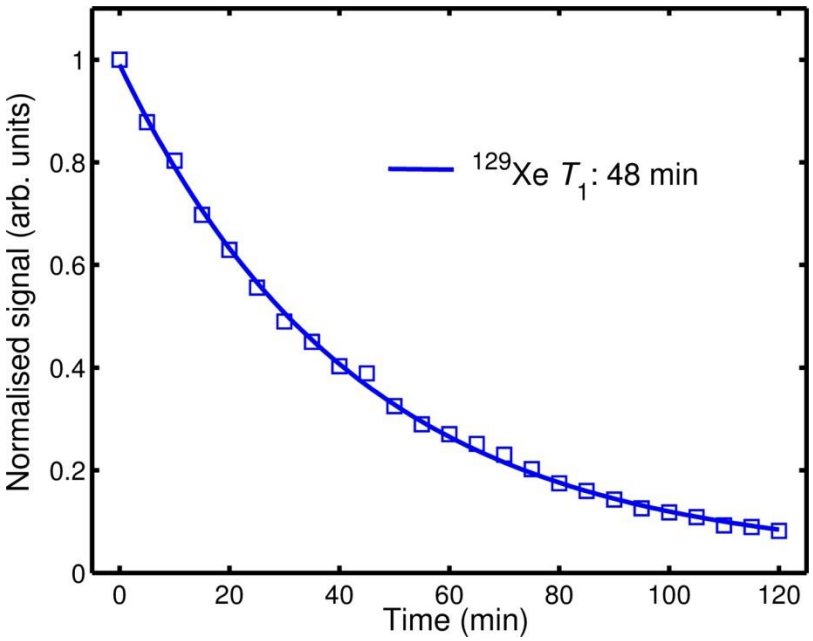

Figure 3.4: ^{129}Xe T_1 in the SEOP cell. Measurement was performed in a cold cell to eliminate Rb vapour.

External cavity diode laser

(iii) An external cavity diode laser (ECDL) (based on the design of Chann *et al.* [73] and constructed in house) was used for optical pumping. A 100 W laser diode array (LDA) bar (n-light, Vancouver, USA) with a pre-attached fast-axis collimation cylindrical microlens was used in conjunction with a Littrow-mounted grating for frequency narrowing. The DC supply current to the diode was 90 A, which produces an output power at the diode of ~38 W. The diode is cooled with a continuous flow of water passing through the diode mount. In our ECDL configuration (see Fig. 3.5 for ray diagram and schematic), an afocal telescope is used to image each emitter onto a Littrow-mounted holographic grating (40 mm×40 mm 2400 lines/mm). The first and second lenses, l_1 and l_2 in the telescope have focal lengths of f_1 = 62 mm and f_2 = 250 mm, respectively, providing a magnification of ~4. The λ/2 plate is set such that 2/3 of the laser power (25 W) is transmitted through the polarising beam splitting cube (PBS) towards the optical cell while the remaining 1/3 (13 W) passes through the PBS onto the grating. The frequency-selected first order diffraction fringe from each emitter is then re-imaged back through the external cavity as feedback to the diode, while the zeroth order forms the output.

The equation for the feedback condition in a Littrow cavity for light incident on the holographic grating with a propagation direction $\hat{x}\sin\alpha\sin\phi + \hat{y}\sin\alpha + \hat{z}\cos\alpha\cos\phi$ with respect to the optical axis is

$$\lambda = 2d\sin\ \theta - \phi\ \cos\alpha \tag{3.9}$$

or

$$\Delta\lambda / \lambda_0 \approx -\alpha^2 / 2 - \phi\cot\theta\,, \tag{3.10}$$

where θ is the angle between the optical axis (x-direction in Fig 3.5) and the grating normal that satisfies the Bragg condition $\lambda_0 = 2d\sin\theta$, ϕ is the

angular spread due to the LDA bar "smile" (small curvature of the emitter alignment) – which was observed to be negligible in our set-up (see Appendix A for alignment procedure) – and α is the divergence of the light along the slow axis. The laser emission was centred on 794.77 nm and the FWHM as a result of the narrowing was measured to be 0.09 $\pm$ 0.01 nm [74] (see Fig. 3.17 for laser spectrum).

The light emerging from the PBS along the z-axis towards the cell is shaped into a square using a cylindrical lens, l_3 (focal length 80 mm). It is then focussed onto a biconvex lens, l_4 (focal length 25 mm), after which it travels through a $\lambda/4$ plate to produce left circularly polarised light. Finally, the diverging beam is focussed onto a plano-convex lens, l_5 (focal length 250 mm) such that that parallel collimated light emerges incident on the optical cell.

Cryostat and holding field for frozen Xe

(iv) A cryostat consisting of spiral-shaped (8 rings) glassware, submerged in a thermally-insulted cup containing liquid N_2, was used to separate Xe from the buffer gases ^{4}He and N_2. The glassware containing frozen Xe is located at the centre of a 0.3 T static field generated by a NdBFe permanent magnet (Cermag, Sheffield, UK). See Fig 3.12 for Xe frozen within the cryostat.

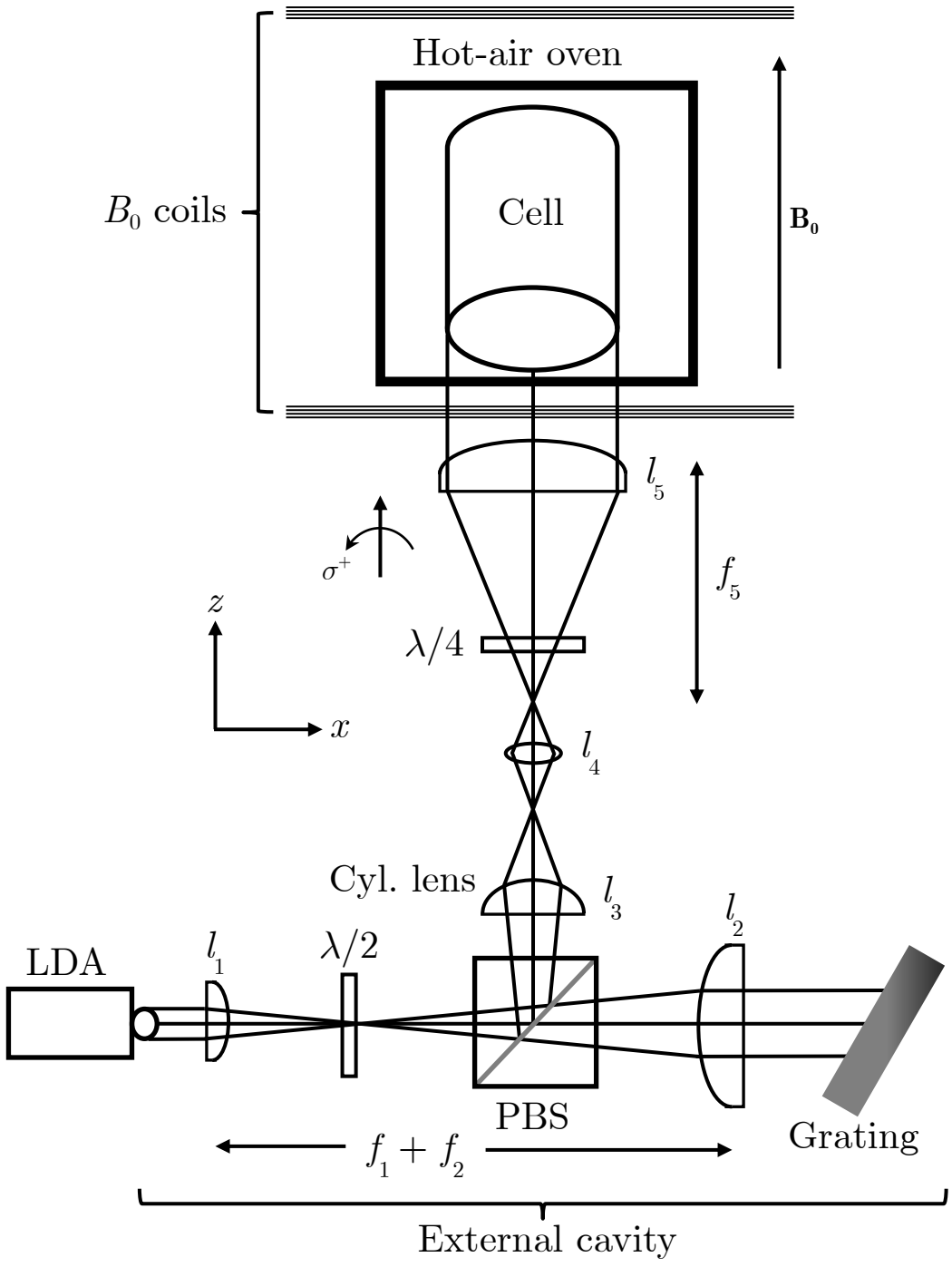

Figure 3.5: Schematic of frequency-narrowed laser diode array bar (DAB) in spin-exchange optical pumping apparatus.

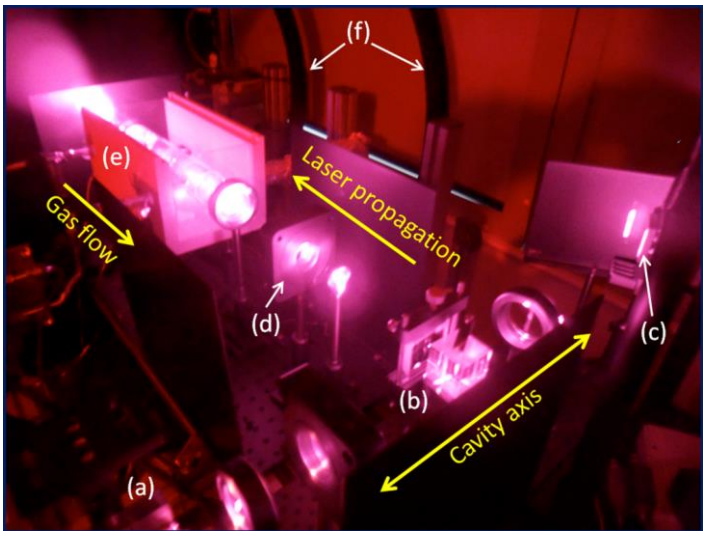

Figure 3.6: Photo of SEOP apparatus. (a) Laser diode array bar. (b) Polarising beam-splitter cube (1/3 feedback along cavity axis, 2/3 transmission along cell axis). (c) Holographic grating (2400 lines/mm). (d) λ/4-wave plate. (e) Ceramic oven for housing cell (lid removed). (f) B_0 coils.

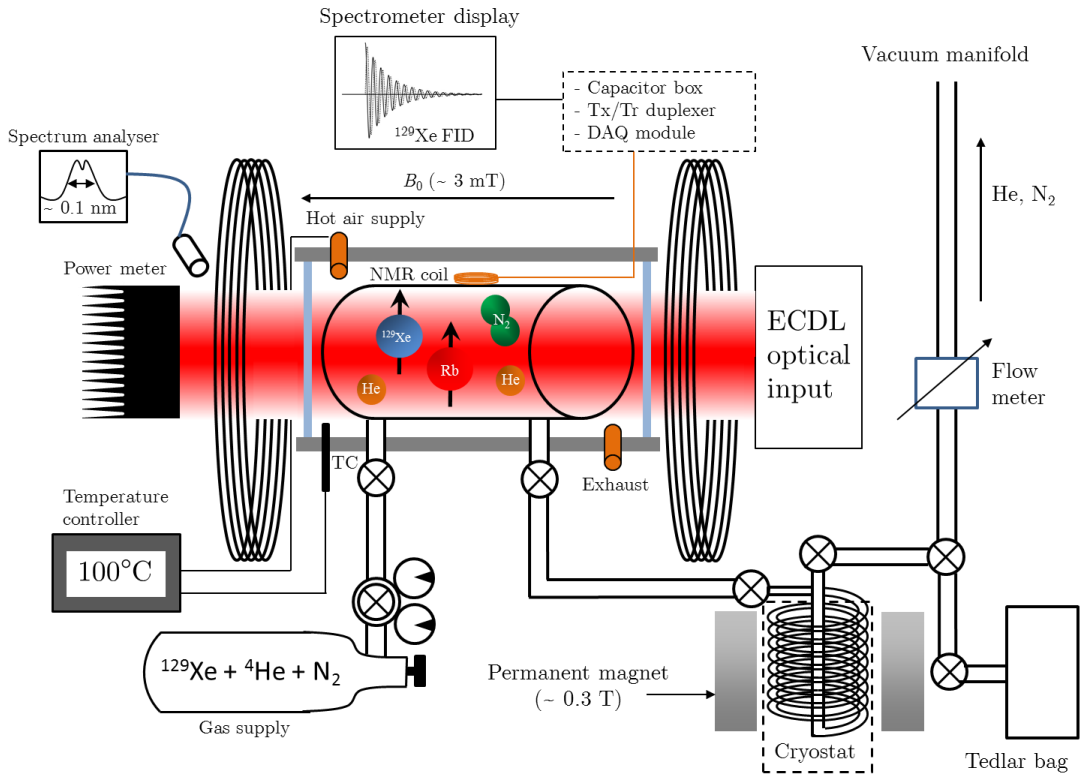

Figure 3.7: Schematic of continuous-flow apparatus for large-volume production of hyperpolarised ^{129}Xe.

3.3.2 Absolute polarisation measurements

For the generation of all hyperpolarised ^{129}Xe samples, a gas mixture of 3 % isotopically enriched Xe (86 % ^{129}Xe), 10 % N_2 and 87 % He (Spectra Gases, UK) was flowed through the cell using a mass flow controller (Aalborg, Caché, Denmark), with a total gas pressure of 2 bar. The cell temperature was first optimised under flow-mode. 3 % Xe samples were collected directly from the cell at two different flow rates (300 and 500 sccm) by dispensing the SEOP gas mixture into a 1 L Tedlar plastic bag (Jensen, Coral Springs, Fl). The bag was then transported to a 1.5T GE HDx system (GE Healthcare, Milwaukee, WI), whereupon 10 mL samples were decanted into an evacuated plastic syringe. Transport to the MR system took approximately two minutes and polarisation losses were measured to be negligible ($<$ 1 %). An FID signal from the syringe sample was recorded following a 10° RF excitation pulse using a homebuilt saddle coil of 7.5 cm length and 3 cm diameter (Fig. 3.9), tuned to resonate at a frequency of 17.66 MHz. Each FID was deliberately acquired with a low flip angle to ensure radiation-damping effects were avoided [75, 76]. The Q of the coil (peak energy stored in the circuit divided by the energy dissipated through Ohmic resistance) was measured in S_{21} mode on a network analyser (Agilent ENA series, 5061A, Keysight Technologies, CA, USA) to be 106. In S_{21} mode, an RF signal is generated and transmitted through the coil and received in a search coil. The search coil is brought into proximity of the RF coil being tested, exciting an oscillation in the RF coil, which is in turn then received by the search coil. This results in a positive gain, and the RF resonance is displayed on the analyser as a positive peak (see Fig. 3.8).

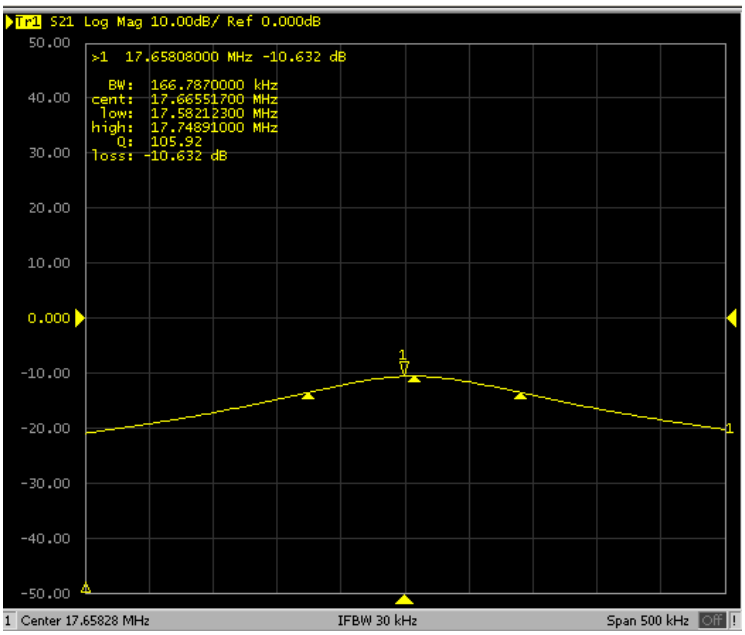

Figure 3.8: Measurement of the quality factor, Q, on the using the S_{21} on the Network Analyser. Central pointer marks the centre frequency peak and the outer two are located at approximately 3 dB to measure bandwidth.

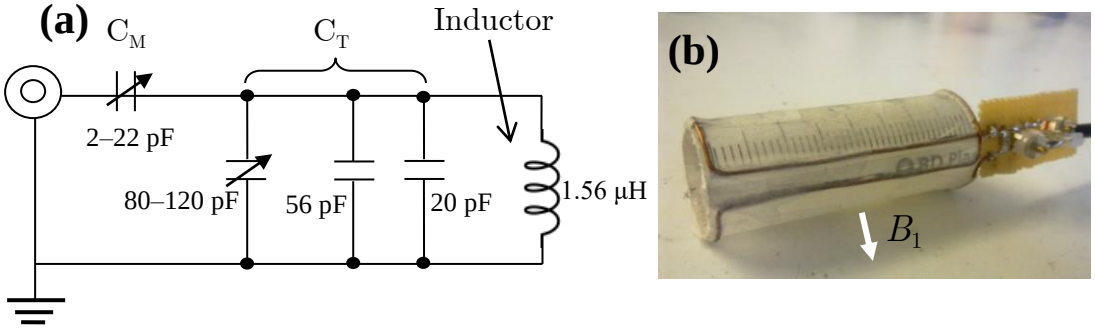

Figure 3.9: Saddle coil constructed and tuned to 17.66 MHz for ^{129}Xe polarisation measurements on a 1.5 T clinical scanner. **(a)** Schematic of coil tuning circuit. **(b)** Photo of the built coil (3 cm diameter and 7.5 cm length).

This process of recording the ^{129}Xe FID on the 1.5 T scanner with the saddle coil was repeated with different cell temperatures and the optimum temperature for the two gas flow rates of 300 and 500 sccm was found to be approximately 373 K (Fig. 3.14 (a)). The signal from the hyperpolarised ^{129}Xe samples was calibrated using the signal from a thermal ^{129}Xe sample (syringe

containing 5 mL enriched Xe (86 % ^{129}Xe), 5 mL oxygen, $T_1 \simeq 6$ s) – see Fig. 3.10. The thermally polarised signal was obtained by averaging 100 pulse-acquisitions (TR = 35 s, FA = 90°). The polarisation, $P_{\mathrm{Xe}}^{\mathrm{cell}}$, of the hyperpolarised ^{129}Xe sample collected from the cell at a given flow rate was then calculated using

$$P_{\mathrm{Xe}}^{\mathrm{cell}} = \frac{S_{\mathrm{HP}}}{S_{\mathrm{therm}}} \frac{\sin(\alpha_{\mathrm{therm}})}{\sin(\alpha_{\mathrm{HP}})} \frac{\varepsilon_{\mathrm{therm}}}{\varepsilon_{\mathrm{HP}}} \frac{V_{\mathrm{therm}}}{V_{\mathrm{HP}}} P_{\mathrm{Boltz}} \tag{3.11}$$

where S_{HP} and S_{HP} are the signal amplitudes from hyperpolarised ^{129}Xe and thermally-polarised ^{129}Xe gas samples, respectively; α_{HP} and α_{therm} represent the respective flip angles used in acquiring signals; $\varepsilon_{\mathrm{HP}}$ and $\varepsilon_{\mathrm{therm}}$ denote the isotopic abundances of ^{129}Xe within the Xe samples; V_{HP} and V_{therm} are the volumes of Xe gas in the samples; and P_{Boltz} is the ^{129}Xe Boltzmann polarisation ($P_{\mathrm{Boltz}} = 1.45\times10^{-6}$ for ^{129}Xe nuclei in a B_0 field of 1.5 T at a temperature of 293 K). The advantage of using this method is that, because the sample is located in the bore of the MR system, the polarisation calculated reflects what the *in situ* ^{129}Xe polarisation would be when performing *in vivo* MRI experiments with larger volumes of hyperpolarised ^{129}Xe.

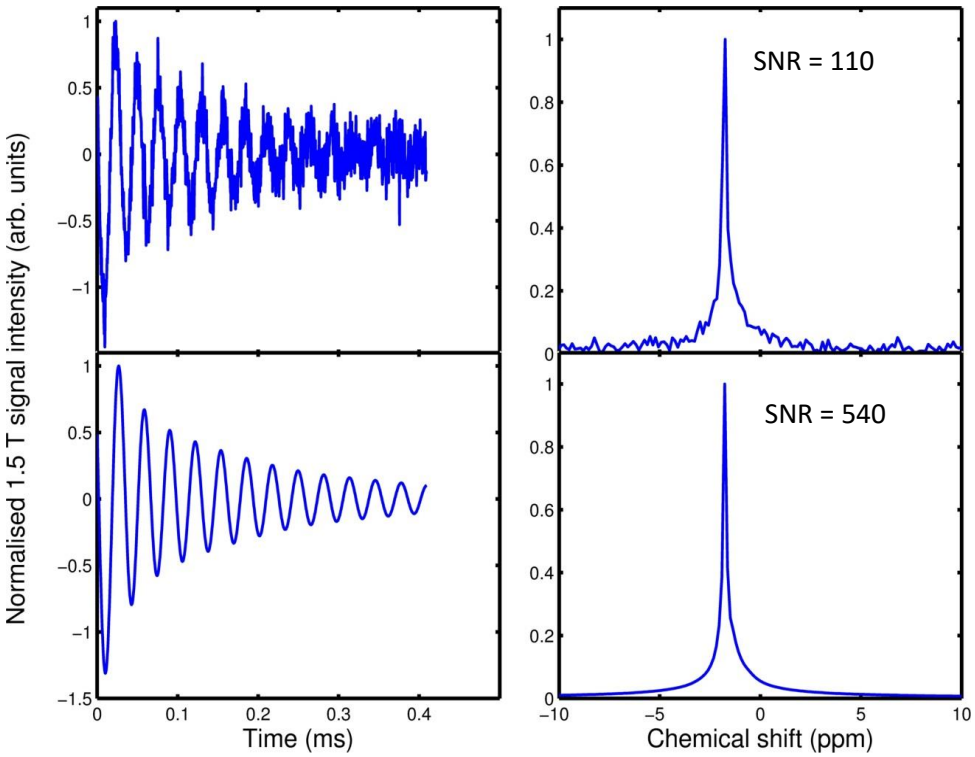

Figure 3.10: Comparison of single-shot (volume 0.33 mL) hyperpolarised (bottom) and 100-transient average (volume 5 mL) thermal (top) ^{129}Xe gas signals. On the left are the real parts of the time-domain FID signals and on the right are the Fourier transformed, frequency-domain signals (magnitude spectra) of the FIDs.

3.3.3 Optical pumping rate modelling

A simple computational model was produced in order to compare established optical pumping efficiency theory with our experimental findings. The model uses MATLAB code (R2011b, MathWorks, Natick, MA) to solve the numerical integral for the optical pumping rate, γ_{opt} (Eq. 3.1), which is solved for discrete values along the z-axis (laser propagation direction) [52, 53, 77]. The value of γ_{opt} is then used to calculate the alkali polarisation. The Rb D_1 linewidth was estimated from Romalis *et al.* [42], where a value of 26 GHz (0.05 nm) was calculated based on an 18 GHz/amg broadening for a gas mixture of density 1.44 amg. The spin-destruction and spin-exchange cross sections are those which are

used in Eqs. 3.2 and 3.7. The alkali density [Rb], was determined from the Killian formula (Eq. 2.74) assuming oven temperature as measured with a thermocouple at the cell wall. The laser wavelength was set to the peak of the D_1 absorption (794.77 nm) and a laser FWHM of 0.09 nm was assumed based on measurement. Detailed experimental determination of [Rb] was not possible, and in a realistic case this should be affected by laser heating [78], as should the gas temperature in the cell. Nevertheless, assumption of optical pumping with a cell at nominal temperature equilibrated with that of the oven provides a starting point for the modelling.

Model

The optical pumping rate is dependent on the photon absorption cross section, σ_s, and on the photon flux from the laser, Φ, traversing the cell length z and is defined (Eq. 3.1) $\gamma_{opt}(z,\nu) = \int \Phi(z,\nu)\sigma_s(\nu)d\nu$. The photon absorption cross section has a Lorentzian lineshape that varies with frequency, ν, according to [77]

$$\sigma_s(\nu) = \sigma_0 \frac{\Gamma_{Rb}^2}{4(\nu - \nu_{D_1})^2 + \Gamma_{Rb}^2}, \tag{3.12}$$

where Γ_{Rb} is the FWHM of the pressure-broadened Rb electron D_1 Lorentzian line (26 GHz for 1.44 amg gas density) with a peak amplitude

$$\sigma_0 = \frac{2r_e cf}{\Gamma_{Rb}} \tag{3.13}$$

and centre frequency, ν_{D_1}. Here r_e is the classical electron radius, c is the speed of light and f is the oscillator strength of the D_1 transition, which has been found to be 0.337 [79]. We have estimated the photon flux to vary with z and ν according to

$$\Phi(z,\nu) = I(\nu)\exp(-\lambda^{-1}(z,\nu)), \tag{3.14}$$

where $I(\nu)$ defines a Gaussian beam with an intensity that varies with frequency:

$$I(\nu) = I_0 \exp\{-[(\nu - \nu_{las}) / \Gamma_{las}]^2\} \tag{3.15}$$

where

$$I_0 = P / Ah\sqrt{\pi}\Gamma_{las}\nu_{las} \tag{3.16}$$

denotes the beam intensity on the cell front, with P denoting the incident power on a flat cell face of cross sectional area, A, h is Planck's constant and Γ_{las} is the standard deviation of the Gaussian laser spectrum with centre frequency ν_{las}. λ^{-1} is the position-dependent absorption length, which for a circularly polarised beam with positive helicity, σ^+, illuminating the cell is given by [77]

$$\lambda^{-1}(z,\nu) = \sigma_s(\nu)[\mathrm{Rb}](1 - P_{\mathrm{Rb}}(z)). \tag{3.17}$$

Eq. 3.1 and Eqs. 3.12–3.17 can be combined to give an expression for the optical pumping rate that can be solved numerically with a Simpson's integral over a frequency range $\left[\nu_{min}, \nu_{max}\right]$ for discrete z values

$$\begin{aligned}\gamma_{opt}(z,\nu) = \int_{\nu_{min}}^{\nu_{max}} \Phi(z,\nu)\sigma_s(\nu) = I_0 \exp[-(\nu - \nu_{las}) / \Gamma_{las}]^2 \exp(-\lambda^{-1}) \\ \times\ \sigma_0 \frac{\Gamma_{Rb}^2}{4(\nu - \nu_{D_1})^2 + \Gamma_{Rb}^2} d\nu,\end{aligned} \tag{3.18}$$

where $\nu_{min} = \nu_{las} - 5\Gamma_{las}$ and $\nu_{max} = \nu_{las} + 5\Gamma_{las}$. This integration was performed for 25 values of z in increments of 1 cm for a 25 cm cell. The Rb polarisation could then be calculated using Eq. 2.77 for each z value, whereupon an average Rb polarisation was estimated by summing the calculated values and dividing by cell length. The average Rb polarisation, $\left\langle P_{\mathrm{Rb}} \right\rangle$, was then used to estimate the ^{129}Xe polarisation for a range of cell temperatures and flow rates (e.g., see Figs. 3.14 and 3.15 for modelled ^{129}Xe polarisations). NB: Chann *et al.* [80] demonstrated skew-light effects on the

light absorption efficiency at very small angles. With minimal skew-light observed with our ECDL, these effects have not been included in the modelling.

3.3.4 Polarisation vs. flow rate

^{129}Xe was polarised in continuous-flow mode at different gas flow rates through the cell. At each gas flow rate, the gas was collected directly from the cell and a signal was acquired from a hyperpolarised ^{129}Xe sample on the 1.5 T MRI system, as described above. Following each change in flow rate, the gas mixture was flowed through the cell for five minutes to allow for any laser heating effects to stabilise and to achieve a steady flow-rate-specific polarisation level within the cell [78, 81, 82] prior to gas collection.

3.3.5 Accumulation of frozen Xe

The T_1 of frozen Xe in the freeze-out glassware was next investigated. At a fixed flow rate of 300 sccm, the Xe mixture exiting the cell was collected in cryogenic glassware made from Pyrex glass with a spiral shape (Fig. 3.11 (a)), whereupon the gas mixture would enter the glassware flowing around and down the rings, deposit frozen Xe, and exit up through the vertical return tube in the centre of the spiral. The permanent magnet produced a static field of 0.3 T (Section 3.3.1, **(iv)**) across the glassware and the path of the Xe from the cell to the glassware was routed through 6.35 mm (outer diameter) Tygon tubing (Saint-Gobain, France). The path was checked for magnetic field inhomogeneity using a Hall probe (GM08 Gaussmeter, Hirst Magnetics, Falmouth, UK). The permanent magnet's field did not vary more than 0.01 T per cm^3 over the volume within which the cryogenic glassware is kept during freeze-out, so it can be assumed to be sufficiently homogeneous so as not to cause significant T_1 shortening [83].

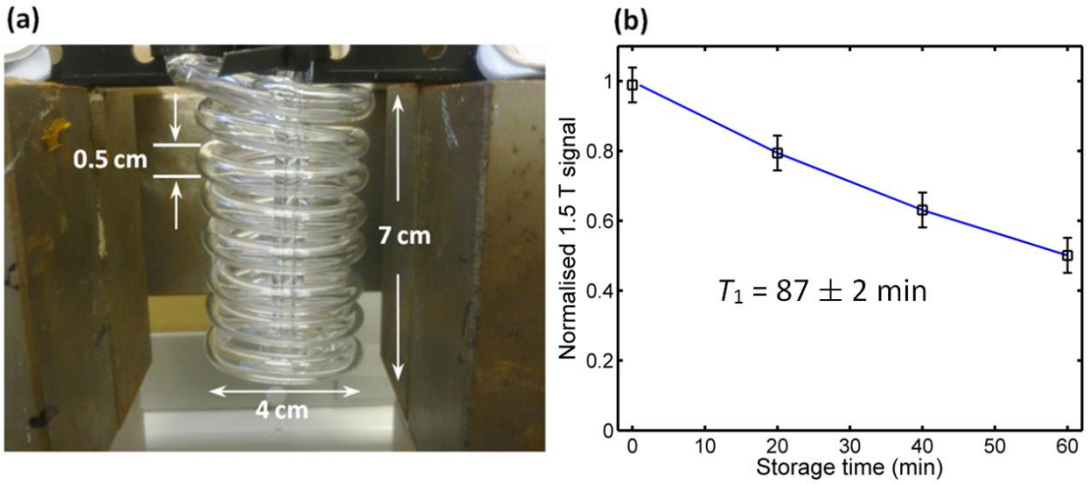

Figure 3.11: (a) Freeze-out cryogenic glassware within holding magnetic field of 0.3 T. (b) T_1 of frozen Xe held within the freeze-out glassware. A T_1 of 87 ± 2 minutes was estimated by performing an exponential fit (blue line) to the FID signal decrease as a function of storage time.

After ten minutes of frozen Xe accumulation, gas flow through the cell was stopped and the Xe was kept frozen within the cryogenic glassware for a range of storage times, t_s. During this time, liquid N_2 in the cryostat was maintained at a constant level (Fig. 3.12). Each storage-time batch of frozen Xe was sublimated into a Tedlar bag by immersion of the glassware in warm water and transported to the 1.5 T system for signal acquisition. In the above procedure, it was assumed that any potential polarisation losses due to the frozen Xe solid-gas phase transition would be the same for each t_s-accumulation as the volume of Xe collected is the same. A T_1 for the frozen Xe was calculated by fitting the decrease in FID signal amplitude to an exponential decay over increasing storage times, t_s (Fig 3.11 (b)).

Figure 3.12: Photo of cryostat (thermally insulated cup filled with liquid N_2) and Xe frozen within the Pyrex spiral glassware.

3.3.6 Polarisation vs. accumulation time

During freeze-out, a given volume of Xe was collected for a length of time defined as the accumulation time, t_a. It would be expected during a freeze-out procedure that, for a given t_a, a ^{129}Xe spin-ensemble contained within a layer of the Xe sample that was frozen at an earlier time would have undergone a greater amount of spin-lattice relaxation compared to spins in a layer of ^{129}Xe frozen at a later time, resulting in lower and higher polarisation values, in the respective layers. After time t_a, the frozen sample is sublimated into the gas phase and collected in a Tedlar plastic bag, resulting in mixing and an averaged polarisation of the ^{129}Xe spin-ensemble within the bulk Xe gas mixture given by [48]

$$P_{Xe}^{acc}(t_{res}, t_a) = P_{Xe}^{cell}(t_{res}) \frac{T_1}{t_a} \left[1 - \exp(-t_a / T_1)\right] \tag{3.19}$$

where $P_{\mathrm{Xe}}^{\mathrm{cell}}$ is the ^{129}Xe polarisation exiting the cell after a given residency time, t_{res}, and entering the glassware at $t_{\mathrm{a}} = 0$ (Eq. 3.8). To experimentally obtain $P_{\mathrm{Xe}}^{\mathrm{acc}}$, Xe was collected in the glassware during a continuous-flow freeze-out for different accumulation times in the range 10–60 minutes. Upon reaching the end of each t_{a}, the frozen Xe was sublimated into a Tedlar bag and transported to the 1.5 T MR system for signal acquisition.

3.3.7 Photon efficiency

A theoretical photon efficiency was calculated by adapting the spin transfer efficiency formula derived by Bhaskar *et al.* [84] so that it includes vdW cross sections for spin exchange and destruction

$$\eta_{\mathrm{theory}} = \frac{\kappa_{\mathrm{SE}}^{\mathrm{BC,vdW}}}{\kappa_{\mathrm{SD}}^{\mathrm{BC,vdW}} + f\kappa_{\mathrm{SE}}^{\mathrm{BC,vdW}}} = \frac{\kappa_{\mathrm{SE}}^{\mathrm{BC}} + \kappa_{\mathrm{SE}}^{\mathrm{vdW}}}{(\kappa_{\mathrm{SD}}^{\mathrm{Rb\text{-}Xe}} + \kappa_{\mathrm{SD}}^{\mathrm{vdW}}) + f(\kappa_{\mathrm{SE}}^{\mathrm{BC}} + \kappa_{\mathrm{SE}}^{\mathrm{vdW}})} \qquad (3.20)$$

where f is the enrichment fraction (0.86) of ^{129}Xe. It is worth noting that Bhaskar *et al.* calculated the spin transfer efficiency by considering only binary Rb-Xe spin cross sections and concluded the efficiency to be independent of both laser power and temperature.

An experimental photon efficiency, η_{exp}, defined as the ratio of ^{129}Xe polarisation rate to the photon absorption rate in the cell volume, V, was determined under flow conditions (for a gas residency time, t_{res}, equal to an empirically determined spin up time, τ_{emp} – see Figs. 3.15 and 3.16) and was calculated using [85]

$$\eta_{\mathrm{exp}} = \frac{[\mathrm{Xe}]VP_{\mathrm{Xe}}^{\tau_{\mathrm{emp}}}}{\tau_{\mathrm{emp}}} \frac{1}{\Delta\phi} \qquad (3.21)$$

where $\Delta\phi$ is the number of photons being absorbed within the cell volume per second and $P_{\mathrm{Xe}}^{\tau_{\mathrm{emp}}}$ is the ^{129}Xe polarisation measured at a flow rate of 625 sccm. The laser power transmitted through to the back of the cell was measured while the SEOP gas mixture was flowing through the cell at 625 sccm. Measurements

were made while the cell was cold (293 K), P_{cold}, and hot (373 K), P_{hot}, and $\Delta\phi$ was calculated from $\Delta\phi(\lambda,T) = (P_{\text{cold}} - P_{\text{hot}}) / E_p$, where E_p is the energy of a single photon carried within the laser beam with an centre wavelength of 794.77 nm.

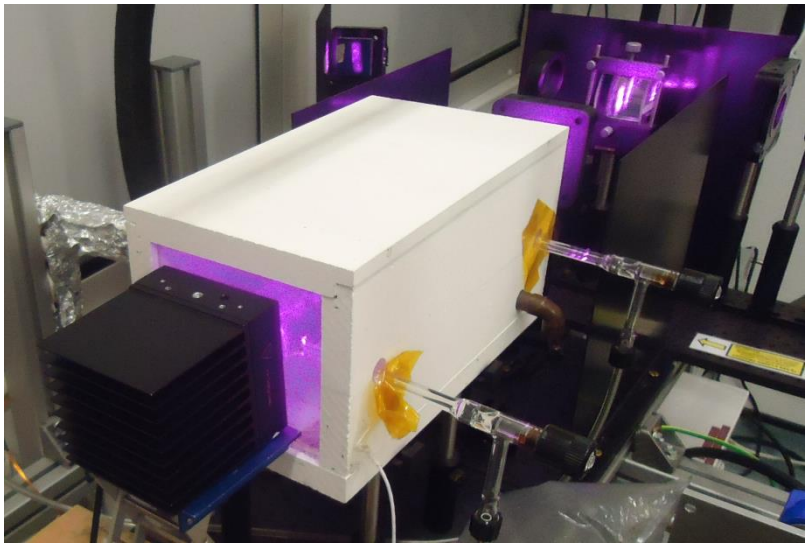

Figure 3.13: Experimental set-up for photon absorption measurement. The power meter is placed at the back of the cell, recording the transmitted light under hot (Rb vapour) and cold (no Rb vapour) cell conditions.

3.3.8 *In vivo* ^{129}Xe lung MRI

^{129}Xe lung ventilation images were acquired with varying polarisations and inhaled volumes of ^{129}Xe. The gaseous volumes of enriched Xe (86 % ^{129}Xe) collected were 300, 400, 600 and 800 mL (see Fig. 3.19 for the respective production rates and freeze-out accumulation times for each of the sample volumes). The Tedlar bag containing the thawed-out Xe was topped up to 1 L with medical grade N_2. All of the ^{129}Xe was polarised for human inhalation under a site-specific UK regulatory manufacturing licence from the MHRA. Lung MRI imaging was performed using a 3 T Philips Achieva scanner system (Philips, Best, Netherlands) with quadrature flex T-R coils (CMRS,

Brookfield, WI) on a healthy female volunteer (26 years old) with written consent and approval from the national research ethics committee. A 2D spoiled gradient echo sequence was used. 2D sequence details: 96×96 matrix size; field of view 384×384 mm; slice thickness 15mm; receive bandwidth 15.6 kHz; echo time 4.1 ms; repetition time 18.2 ms; flip angle 9°. Centric phase encode ordering was used to maximise the obtainable SNR [86].

3.4 Experimental results

3.4.1 ^{129}Xe polarisation vs. cell temperature

The results of temperature optimisation under gas flow show that the cell gave optimum polarisation while it was held at a temperature of 373 K (Fig. 3.14, (a)). This is slightly offset from the modelling, which gave a similar temperature dependence, but instead resulted in an optimum temperature under gas flow to be 385 K (Fig. 3.14 (b)). This offset is most likely due to the temperature of gas in the cell not being the same as the experimentally measured oven temperature of 373 K due to laser heating effects, discussed below in Section 3.4.2. With the temperature set at 373 K, the ^{129}Xe polarisation was found to decrease non-linearly as the gas flow rate through the cell was increased, consistent with earlier findings [53, 60, 87].

3.4.2 ^{129}Xe polarisation vs. gas flow rate

The exponential build-up portion of Eq. 3.8 $(1-\exp(-(\gamma_{SE}+\Gamma)t_{res}))$, where $t_{res}=V[G_a]/Q$, was fitted to the data in Fig. 3.15 to extrapolate an empirical spin exchange rate, γ_{SE}^{emp}, of 0.0143 Hz, which is approximately a factor of four higher than the calculated theoretical value (Eq. 3.7, Table 3.1) of 0.0033 Hz. In order to estimate the expected polarisation for a cell temperature of 373 K and pressure of 2 bar, a simple model that utilises the

spin exchange and destructions rates (Eqs. 3.2, 3.4 and 3.7) was used along with a simple numerical integration of the optical absorption of the laser light along the cell [88]. $P_{\mathrm{Xe}}^{\mathrm{cell}}$ was modelled for different cell residency times (flow rates) by using

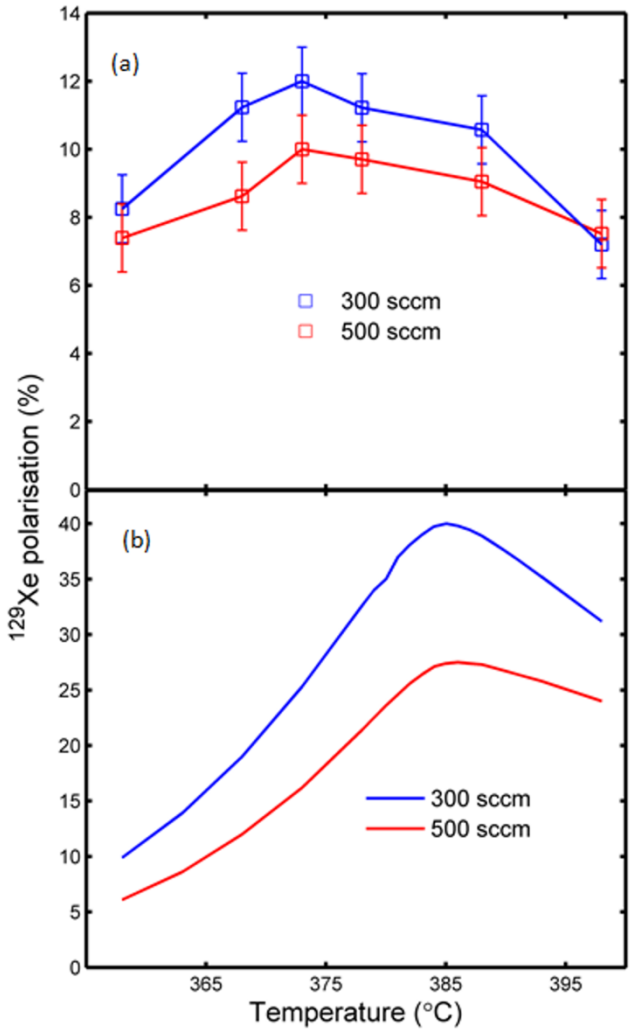

Figure 3.14: (a) Experimental ^{129}Xe polarisation vs. cell temperature at gas flow rates of 300 and 500 sccm. Hyperpolarised ^{129}Xe (samples obtained without cryogenic accumulation) signals were measured in the 1.5 T system. NB: blue and red lines are guides for the eye. (b) modelled polarisation vs. cell temperature.

the theoretical spin exchange rate, $\gamma_{\mathrm{SE}}^{\mathrm{theory}}$ (Table 3.1), a theoretical Rb polarisation, $\left\langle P_{\mathrm{Rb}} \right\rangle$, of 95 % and a ^{129}Xe spin-destruction rate, Γ, equal to $1 / T_1^{\mathrm{cell}} = 3.5\times10^{-4}$ Hz. For a typical operating flow rate of 300 sccm, the theoretical ^{129}Xe polarisation was calculated to be 24 %, which is a factor of 2 larger than the experimentally measured polarisation of 12 $\pm$ 1 % (Fig. 3.15). Also, the theoretical and experimentally measured ^{129}Xe polarisation curves diverge at low flow rates. At low flow rates, gas in the cell has a greater amount of time to undergo heat exchange and is therefore more prone to laser heating effects (Walter *et al.* [78] found in a cell without gas flow that the cell temperature increased by approximately 105 K when 15 W of laser light was incident on the cell). The photon flux is most intense at the front of the cell and thus laser heating may cause an increase in [Rb] at the cell front. With a relatively long cell length of 25 cm, this could lead to a "hot-spot" of [Rb] resulting in fewer Rb exchange sites for ^{129}Xe nuclei traversing the cell length, as a result decreasing the average ^{129}Xe polarisation. Indeed, EPR was recently used [53] to probe spatial inhomogeneity in the alkali polarisation, which showed an area of depleted Rb polarisation along the *z*-axis of a cylindrical cell.

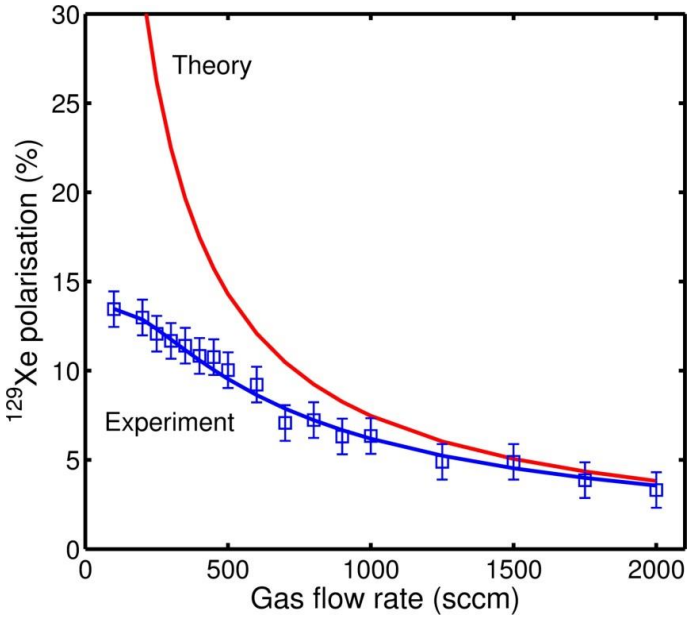

Figure 3.15: ^{129}Xe polarisation vs. gas flow rate through the cell. The red line represents the modelled polarisation for different gas flow rates (residency times), where a theoretical spin exchange rate, $\gamma_{\mathrm{SE}}^{\mathrm{theory}}$, of 0.0033 Hz was used along with a theoretical equilibrium polarisation (infinite residency time) of 86 %. The blue line shows a fit (using Eq. 3.8 with $t_{\mathrm{res}} = V[\mathrm{G_a}]/Q$) to the experimental polarisation data. From the fit, an empirical spin up of $\tau_{\mathrm{emp}} = 1/(\gamma_{\mathrm{SE}}^{\mathrm{emp}} + \Gamma) = 68$ s. was determined.

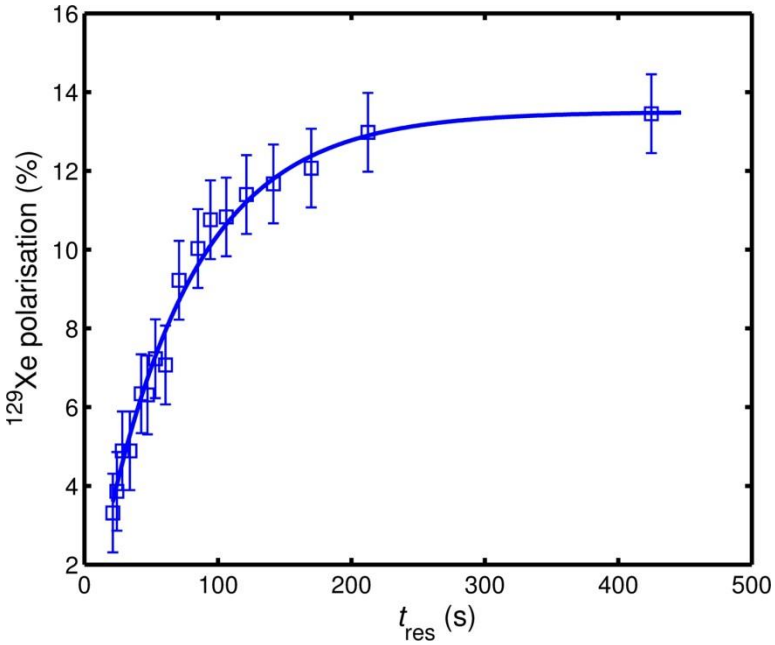

Figure 3.16: Experimental ^{129}Xe polarisation as a function of gas residency time in the SEOP cell, with $\tau_{\mathrm{emp}} = 68$ s.

3.4.3 Photon efficiency

The laser power was measured at 13.7 W and 7.8 W when the cell was cold (293 K) and hot (373 K), respectively, giving an absorbed laser power of 5.9 W (43 %) and therefore a photon absorption rate, $\Delta\phi$, of 2.36×10^{19} photons per second (at 625 sccm). Given that the FWHM of the laser (~0.1 nm) is not much greater than pressure broadened Rb D_1 linewidth in the cell (0.05 nm, see Section 3.3.3), it can be assumed that the laser and cell are reasonably well matched for efficient optical pumping.

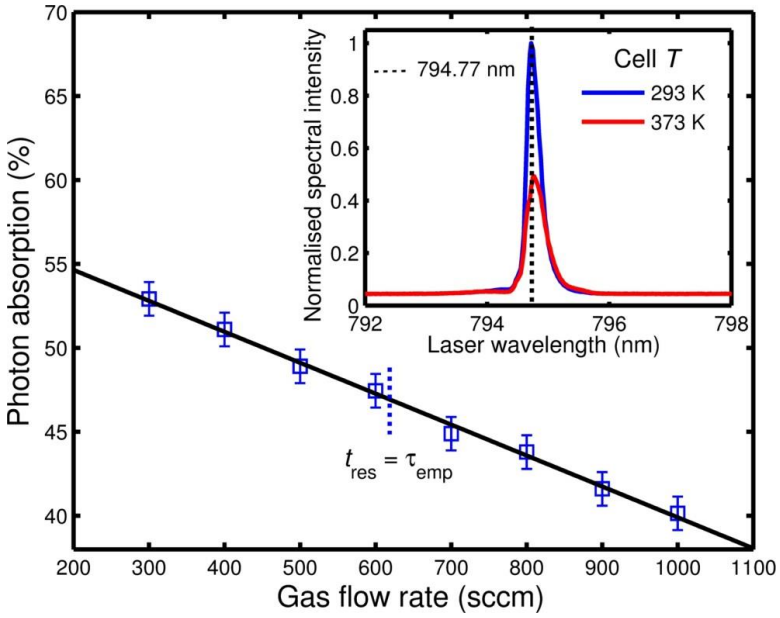

Figure 3.17: Linear dependence of photon absorption with gas flow rate through the cell. Blue dashed line indicates the flow rate at which the gas residency time is equal to the empirically determined spin up time, τ_{emp}.

Despite this, it is worth noting that the laser power incident upon the cell was measured to be 25 W, whereas the laser power measured at the back of the cold cell was measured to be only 13.7 W. The loss in power here is assumed to be a result of scattering and reflection of the laser light from the cell walls and also from the glass windows of the oven. A theoretical photon

efficiency η_{theory} was calculated (Eq. 3.20) to be 0.049, higher than the previously reported theoretical efficiency of 0.043 [84]. The difference in efficiency reported here may be attributed to the inclusion of vdW interactions in the efficiency calculation. Furthermore, whereas the photon efficiency was previously considered to be temperature independent [84], both the binary and vdW spin-destruction cross sections calculated in this study are dependent upon T, thus rendering a theoretical photon efficiency that may change with temperature. Using Eq. 3.21, an experimentally determined photon efficiency was calculated for a gas mixture flowing through the cell (T = 373 K) at a rate of 625 sccm (the flow rate at which $t_{res} = 1/(\gamma_{\text{SE}}^{\text{emp}} + \Gamma) = \tau_{\text{emp}} = 68$ s. The polarisation (Fig. 3.15) at this flow rate was measured as 8.6 %, giving a $P_{\text{Xe}}^{\tau_{\text{emp}}}$ value in Eq. 3.21 of 0.086. Using the measured photon absorption rate, $\Delta\phi$, a ^{129}Xe fraction, f, of 0.86 and a cell volume of 491 cm^3 gives an experimental photon efficiency, $\eta_{\text{exp}} = 0.031$, which is approaching the theoretical limit of $\eta_{\text{theory}} = 0.049$. Experimentally and theoretically, therefore, $1/\eta_{\text{exp}} = 32$ and $1/\eta_{\text{theory}} = 20$ photons are required per ^{129}Xe spin flip.

3.4.4 Frozen ^{129}Xe spin-lattice relaxation

The T_1 of the frozen ^{129}Xe (see Fig. 3.11 (b)) was calculated as 87 ± 2 minutes. This value is lower than what has previously been measured at a similar temperature and magnetic field in a recent solid-state ^{129}Xe NMR experiment [89], where a value of ~2.5 hours was reported. In an earlier study [90], a T_1 for solid-state ^{129}Xe was measured as ~2.5 hours and it was concluded that below a temperature of 120 K, and above 55 K (Debye temperature for Xe, the temperature above which phonons are free to move), the interaction thought to be dominant for ^{129}Xe relaxation in its frozen state

is an inelastic spin-phonon scattering process resulting from a nuclear spin-rotation interaction. For those solid-state ^{129}Xe T_1 measurements [89-91], Xe held within a glass cell was submerged as a bulk sample in liquid N_2, which is thought to result in the formation of rigid-lattice Xe face centred cubic polycrystalline solid. For Xe freezing under flow in spiral cryogenic glassware, such as in our system, the resulting Xe frost that is formed is less dense and may be prone to additional relaxation effects from the diffusion of gaseous oxygen into the frost [92]. Indeed, oxygen may well be present in the circuit given the vacuum of ~4 mbar. Without *in situ* T_1 measurements of the frozen ^{129}Xe, these explanations for a lower than previously reported T_1 are somewhat speculative. Nevertheless, the value reported here is still encouragingly long, allowing for high SNR (~100) images from hyperpolarised ^{129}Xe accumulated over a long freeze time of 80 minutes (see Fig. 3.19 (d)).

3.4.5 ^{129}Xe polarisation vs. accumulation time

Fig. 3.18 shows a predicted model of the ^{129}Xe polarisation, $P_{\mathrm{Xe}}^{\mathrm{acc}}$, (Eq. 3.19) decay during accumulation. Using the measured T_1 value of 87 $\pm$ 2 minutes in the model shows good agreement with the experimental data. The percentage loss in the polarisation is approximately 10 % within an accumulation time of 40 minutes, which is typical of the time needed on this SEOP system to produce 400 mL Xe volumes for *in vivo* studies.

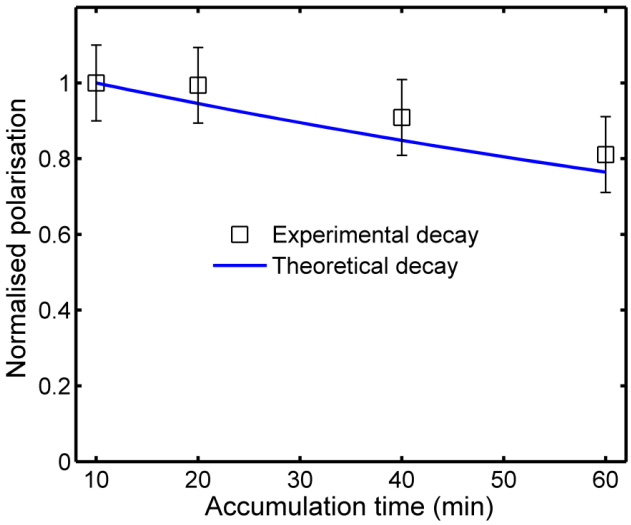

Figure 3.18: Predicted model of the ^{129}Xe polarisation, $P_{\mathrm{Xe}}^{\mathrm{acc}}$, (Eq. 3.19) decay during accumulation. Using the measured T_1 value of 87 $\pm$ 2 minutes in the model shows good agreement with the experimental data. The percentage loss in the polarisation is approximately 10 % within an accumulation time of 40 minutes, which is typical of the time needed to produce Xe volumes for *in vivo* studies ^{129}Xe on this SEOP system.

3.4.6 ^{129}Xe ventilation lung images

The ^{129}Xe gas ventilation images in Fig. 3.19, (a) and (b) demonstrate that an image from a smaller volume of ^{129}Xe produced at a lower gas flow rate results in comparable SNR (~50) to an image acquired with double the gas volume at a higher flow rate. In addition, Fig. 3.19, (c) and (d) show that for a given flow rate of 300 sccm, doubling the accumulation time, and therefore the volume of hyperpolarised ^{129}Xe, results in an image with approximately double the SNR (increase from 50 to 100), confirming that T_1 losses during extended freeze out periods are not a major concern.

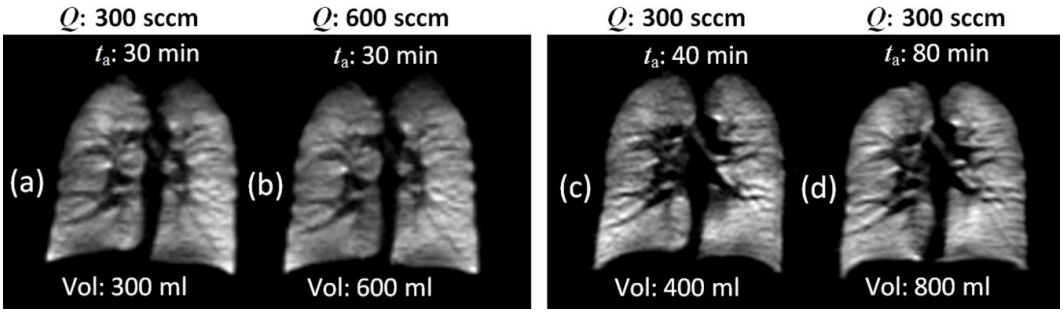

Figure 3.19: *In vivo* gas-phase human lung images from a healthy volunteer at 3 T. (a) and (b) are 2D images of hyperpolarised ^{129}Xe acquired from isotopically enriched gas mixtures (86 % ^{129}Xe) flowed through the cell at volumetric flow rates (Q) of 300 and 600 sccm; (c) and (d) are 3D images of hyperpolarised ^{129}Xe, both produced at a flow rate of 300 sccm for different accumulation times, t_a. Respective SNR values calculated for lungs in images (a), (b), (c) and (d): 56; 52; 49; and 102.

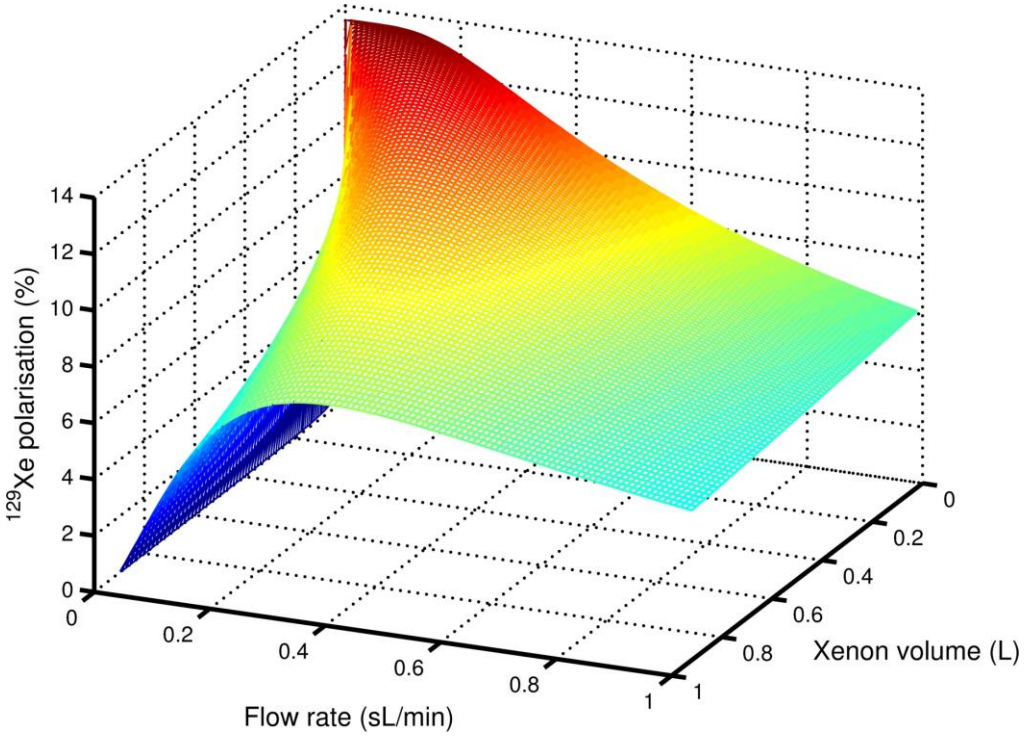

Figure 3.20: 3D ^{129}Xe production map showing the flow rate that result in the highest ^{129}Xe polarisations for a given volume of accumulated Xe (based on Eqs. 3.8 and 3.19)

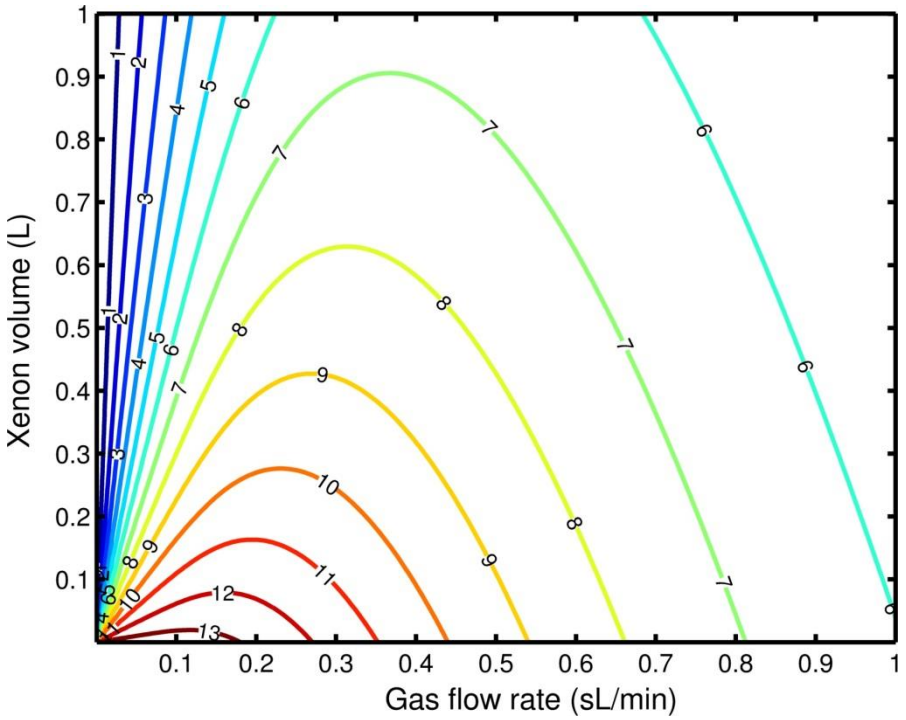

Figure 3.21: 2D ^{129}Xe production map showing the flow rate that result in the highest ^{129}Xe polarisations for a given volume of accumulated Xe (based on Eqs. 3.8 and 3.10).

3.5 Conclusions

In this chapter, it has been shown a large volume cell (~500 cm^3) operating at a mid-range pressure (2 bars with 3 % Xe mix) works well in combination with a spectrally narrowed laser in a SEOP system for production of hyperpolarised ^{129}Xe for *in vivo* lung MRI. The experimental photon efficiency (30 photons per ^{129}Xe spin flip) was measured to approach the theoretical efficiency, which predicts that at least 20 photons are required to induce each ^{129}Xe spin flip. Although the theoretical and experimental ^{129}Xe polarisations are in reasonable agreement at high gas flow rates through the SEOP cell, they diverge at low flow rates, suggesting a break down in the theoretical model for long gas residency times which could be due to Rb runaway caused by laser heating. Finally, image SNR comparisons show that low-volumes (<

400 mL) of hyperpolarised ^{129}Xe gas produced using this system provide high quality ^{129}Xe lung MR images.

Chapter 4

Further optimisation of ^{129}Xe SEOP polariser with an LDA-VHG optical train input

4.1 Introduction

In the previous chapter, a mid-pressure ^{129}Xe SEOP polariser equipped with an ECDL was optimised for routine *in vivo* lung imaging. It was observed that at high gas flow rates, experimentally measured ^{129}Xe polarisations agree well with theory, and that at low gas flow rates, this agreement breaks down, suggesting an experimental ^{129}Xe polarisation limit. The aim of this chapter was to investigate ^{129}Xe polarisation improvements through the incorporation of an optical input with higher power output and better transverse and longitudinal beam homogeneity compared to the ECDL.

4.2 Volume holographic gratings

The use of volume holographic gratings (VHGs) – also known as volume Bragg gratings (VBGs) – to stabilise lasers (and accurately setting the

This chapter is based on work presented by Norquay *et al.* at PiNG14, 2014.

wavelength for fibre-optic telecommunications) was first incorporated in the 1980s with 1.55 μm semiconductor lasers [93]. Through the utilisation of wavelength-selective feedback into a laser diode, VHGs are able to 'lock' the lasing wavelength to that of the grating. This feature of VHGs serves to narrow the laser linewidth, decrease the temperature dependence of the emission wavelength, reduce aging-related wavelength changes and, in the case of diode array bars, each emitter is locked to the same wavelength, generating a far narrower combined emission linewidth than that in the case of unlocked arrays [94].

Physically, VHGs comprise individual VHG elements recorded in the bulk of photosensitive glasses, e.g. lithium niobate (LiNbO3) [95, 96]. These elements contain Bragg planes of varying index of refraction that extend over the whole volume of the material. VHGs are able to retro-reflect a narrow band of emitted laser light by operating as single-wavelength mirrors (Fig. 4.1) with a spectral selectivity that is determined by the number of Bragg planes that light traverses inside the glass [97]:

$$\frac{\Delta\lambda}{\lambda} = \frac{\lambda}{2nd} = \frac{\Lambda}{d} = \frac{1}{N}, \tag{4.1}$$

where λ is the Bragg wavelength, $\Delta\lambda$ is the bandwidth of the filtered (reflected/diffracted) wavelengths, d is the thickness of the VHG, n is the bulk refractive index of the medium containing the grating, Λ is the grating spacing (period of the grating) and N is the number of grating planes that fit in the thickness of the material. (NB: Eq. 4.1 represents the case for wave-locking applications, where the diffracted beam is anti-parallel to the incident beam and the Bragg condition $\lambda = 2n\Lambda\cos(\theta)$ – where θ is the angle of incidence (in the medium) – is reduced to $\lambda = 2n\Lambda$.)

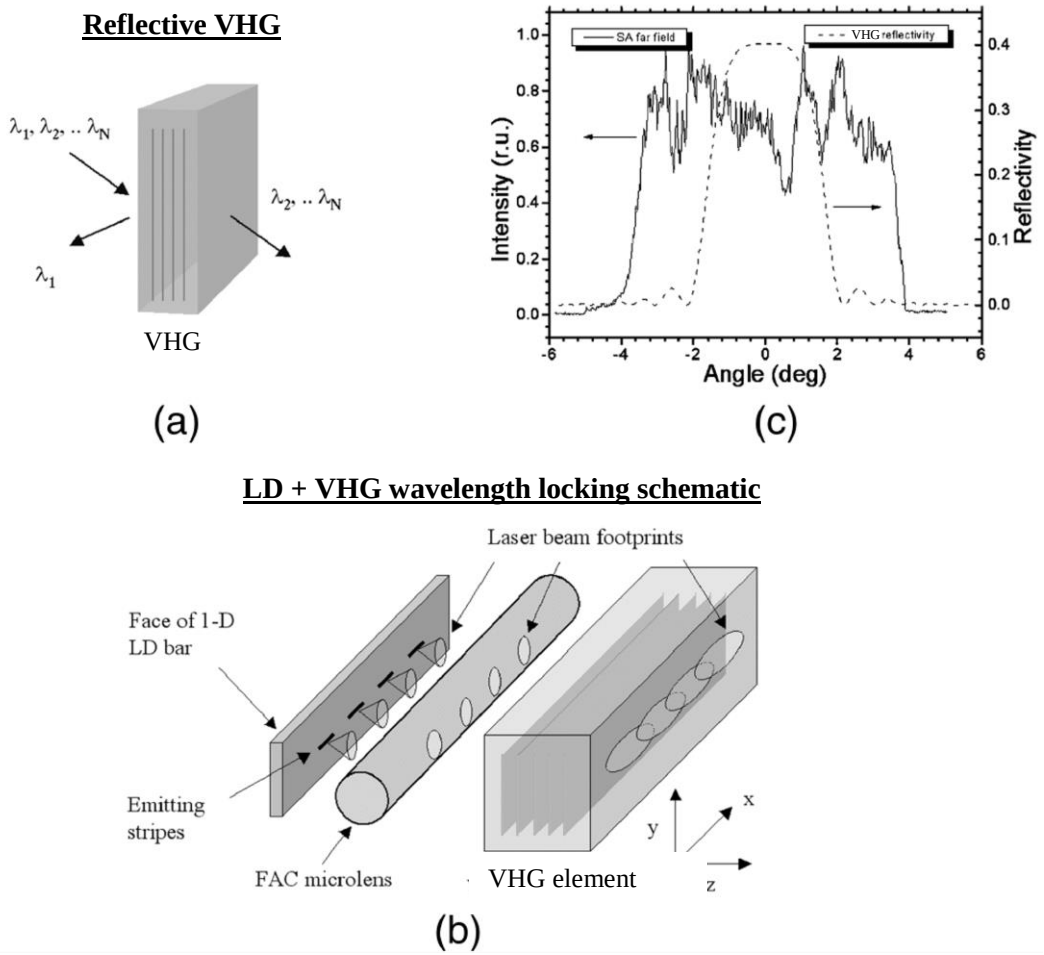

Figure 4.1: (a) Operation of a reflective VHG element. For broadband light, only incident illumination satisfying the Bragg condition is efficiently reflected (all wavelengths outside the VHG reflectivity band pass through unaffected). (b) Schematic of a laser diode (LD) bar wavelength narrowing by incorporation of an external VHG element. The VHG is placed after the lens, reflecting a narrowband of light directly back into the laser cavity. (c) Comparison of the slow axis (SA) divergence of a typical broad-area laser diode with the dependence of the reflectivity of a VHG (0.8 mm thick) on the incident angle for a given wavelength. Figure adapted with permission from ref. [97].

4.3 LDA with internal VHG for SEOP

A laser diode array (LDA) module that contains the VHG as an internal component of the laser diode itself was developed by QPC Lasers (CA, USA). The LDA-VHG devices (Fig. 4.2 (a)) are produced in a similar way [98]

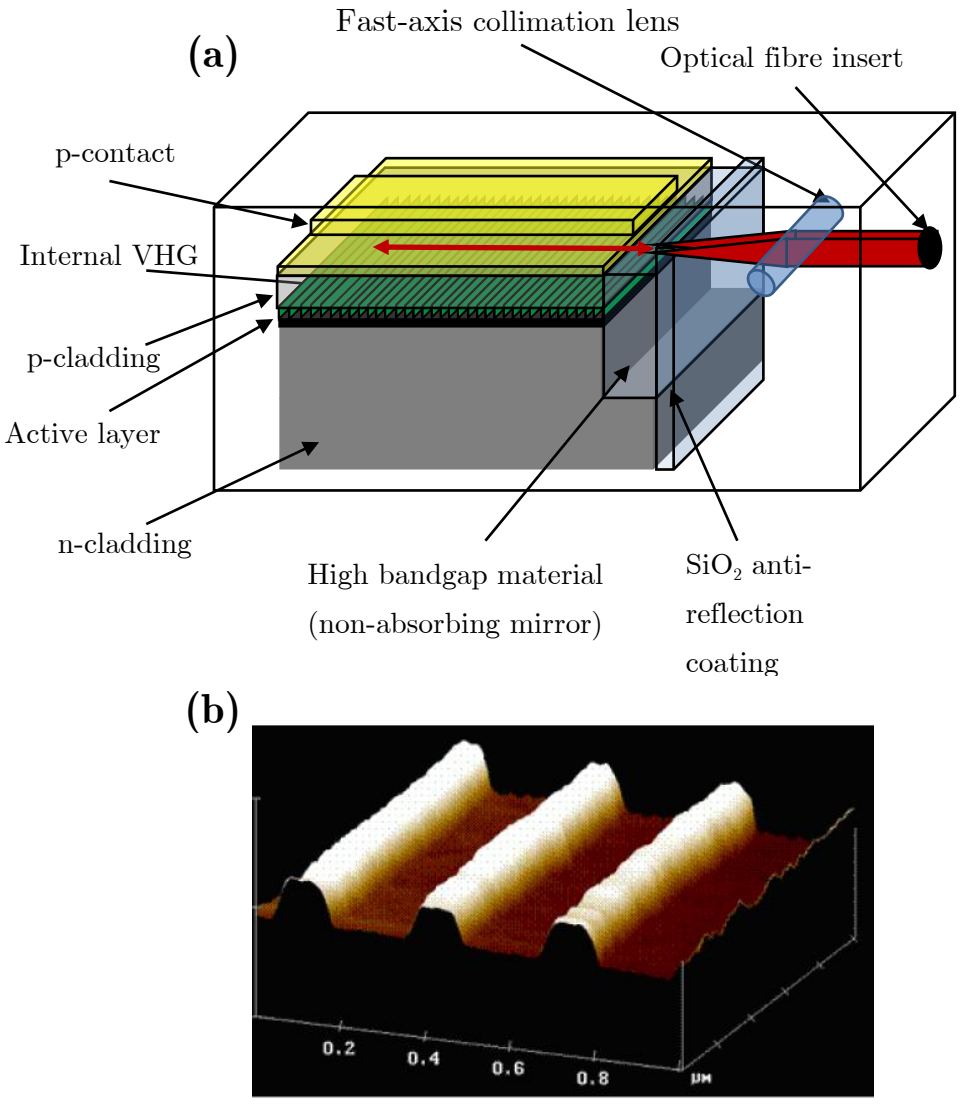

Figure 4.2: Schematic of an AlGaAs laser diode array (LDA) that is frequency-narrowed with internally embedded volume holographic gratings (VHGs). (b) Atomic force microscope (AFM) image of an internal grating. Figure adapted with permission from ref. [98].

to that of conventional laser diodes. During the substrate growth process, the holographic gratings are defined after the first epitaxial growth by optical lithography into a photoresist layer, where it is etched into the cladding (Fig. 4.2 (b)). Subsequently, the cladding is regrown on top of the gratings to yield the top electrical contact.

The LDA used in this project (Brightlock™ Ultra-100, QPC, CA, USA) has a maximum power output of 125 W and was designed to operate with a centre wavelength emission of 795 nm. For collimation over the length of the SEOP cell, an integrated optical train (OT) telescope was used (Fig. 4.3). The OT comprises a 51 mm optical fibre (with ~97 % linear polarisation preservation) attached to the LDA-VHG output; two plano-convex lenses, l_1 and l_2 with focal lengths of 4.5 mm and 350 mm, respectively; one polarising beamsplitter (PBS) cube; and a $\lambda/4$ plate. The integrated LDA-VHG OT design set-up is shown in Figs. 4.3 and 4.4 below.

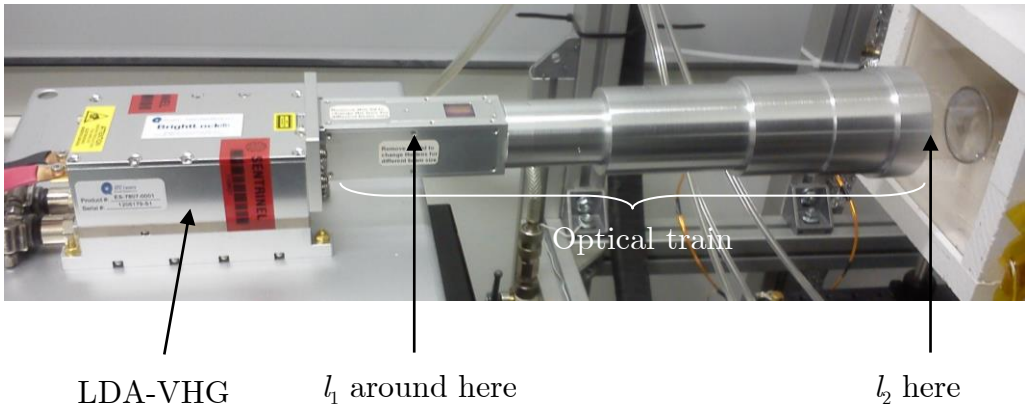

Figure 4.3: Photo of laser diode array volume holographic grating with integrated optical train for beam collimation.

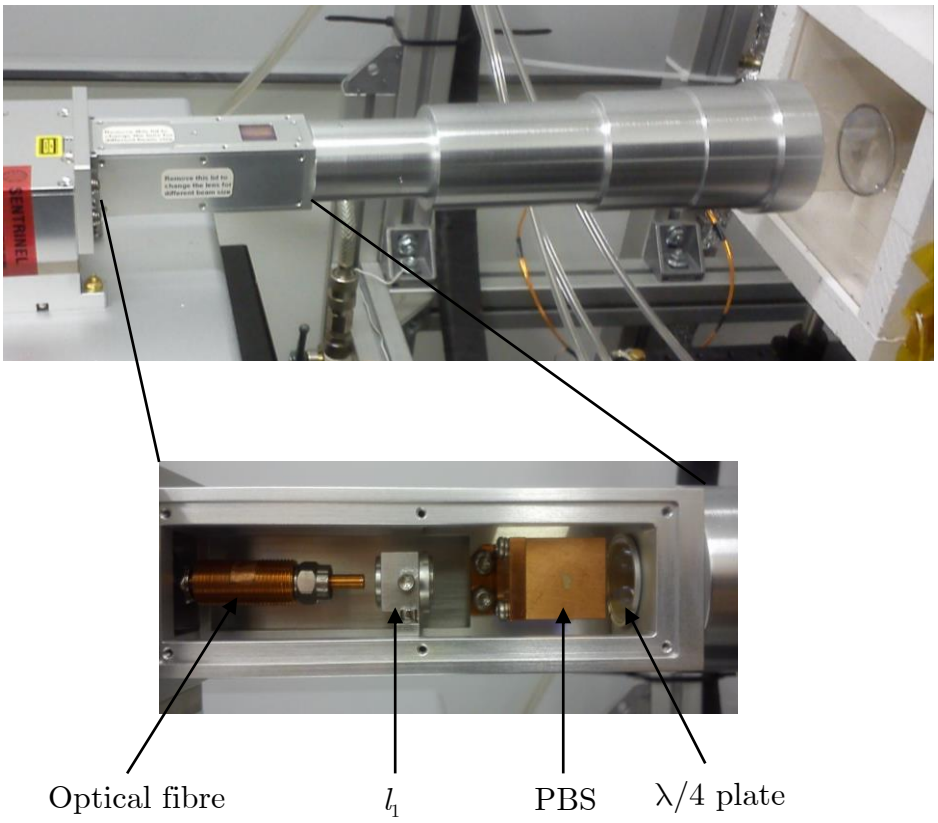

Figure 4.4: Photo of functional components within the optical train.

4.4 Laser power measurements

To determine the optimal running power, NMR signal measurements were performed for three laser powers: 10 W, 50 W and 100 W. In addition to measuring the NMR signal, the percentage of power absorption as a function of cell temperature was calculated for all incident laser powers.

4.4.1 Experimental procedure

The running temperatures and input currents that were needed to produce a spectral emission with a centre wavelength of 794.77 nm for each power were determined first (Fig 4.5). The spectral profile was recorded for a range of input currents (powers) and the FHWM were determined from Gaussian

fits to the spectra (see Fig. 4.6). The FWHMs over the full power range were extrapolated to be ~0.3 nm, with a variation of $< \pm 0.05$ nm.

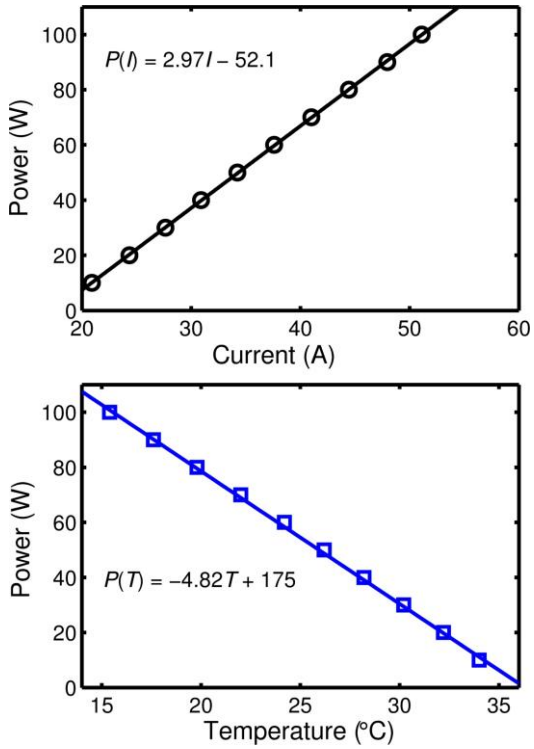

Figure 4.5: Running currents and temperatures to achieve a 794.77 nm centre wavelength over the full power output range for the LDA-VHG.

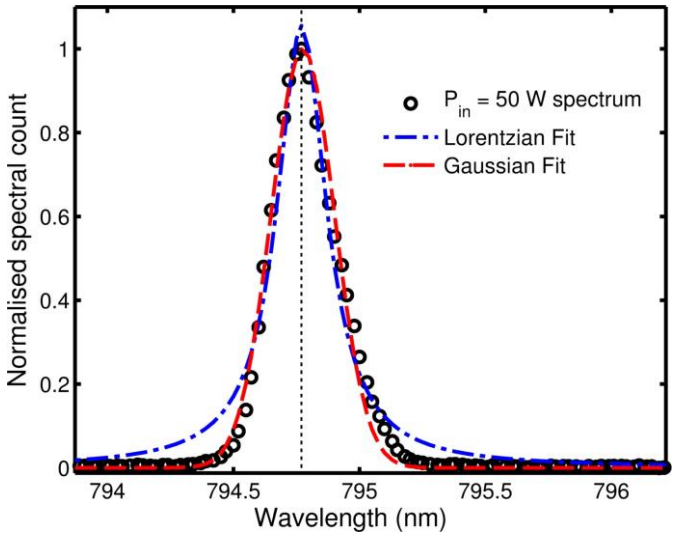

Figure 4.6: LDA-VHG spectrum for a power output of 50 W. FHWM of ~0.3 nm was extrapolated from a Gaussian fit on the recorded spectrum.

By comparing the power measured at the front of the cell, P_{in}, with the power measured at the back of the cell, P_{back}, while the SEOP cell was cold (room temperature), the power drop over the length of the SEOP cell in the absence of Rb vapour was determined to be 62 % (see Fig. 4.7).

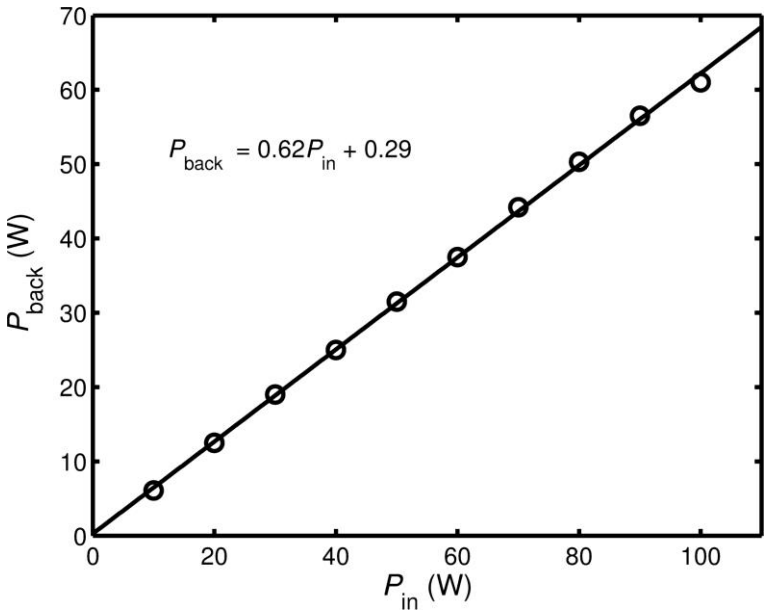

Figure 4.7: Plot of power measured at the back vs. power incident on the cell for a cold SEOP cell. A power drop of 62 % occurs over the cell length for all incident laser powers.

To determine the power absorption for a range of cell temperatures, a similar technique described in Section 3.3.7 was used. The percentage absorption was calculated from $(P_{\text{cold}} - P_{\text{hot}}) / P_{\text{cold}}$, where the power readings correspond to readings from the back of the cell (to factor out laser power losses through reflection, scattering and absorption from the cell itself), so that any observed power drop should be due only to laser absorption from Rb vapour.

Absorption experiments from three power inputs (10 W, 50 W and 100 W) were completed. For each power input, the oven temperature was increased from 60 °C to a maximum of 150 °C. After each temperature change, to

allow for thermal stabilisation, we waited 30 min before measuring the power absorption. In addition to measuring the power absorption at each cell temperature and laser power, ^{129}Xe NMR signals (average from 20 FID transients) were recorded.

4.4.2 Results

For the incident laser powers of 10 W and 50 W, the absorbed power was observed to increase sigmoidally as a function of oven temperature (Fig. 4.8); by converting oven temperature to cell [Rb] using the Killian formula (Eq. 2.74), the absorbed power percentage exhibited an exponential build-up curve with increasing [Rb] (Fig 4.9). At an incident power of 100 W, the laser absorption saturated at an oven temperature of 90 °C, suggestive of a higher [Rb] in the cell than calculated by the Killian formula. It is likely that apparent increase in [Rb] is a result of Rb runaway effects (laser heating) taking place at an incident laser power of 100 W.

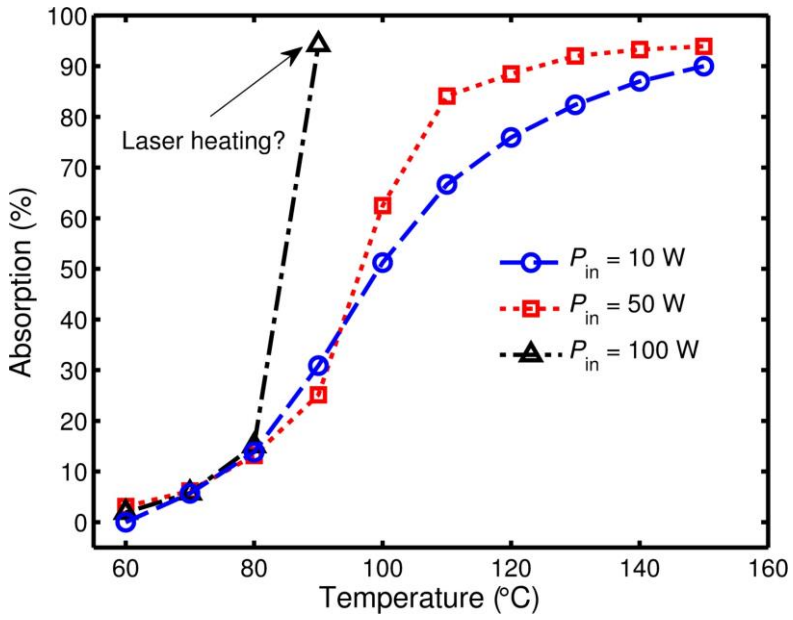

Figure 4.8: Laser absorption in the SEOP cell as a function of oven temperature for three incident powers.

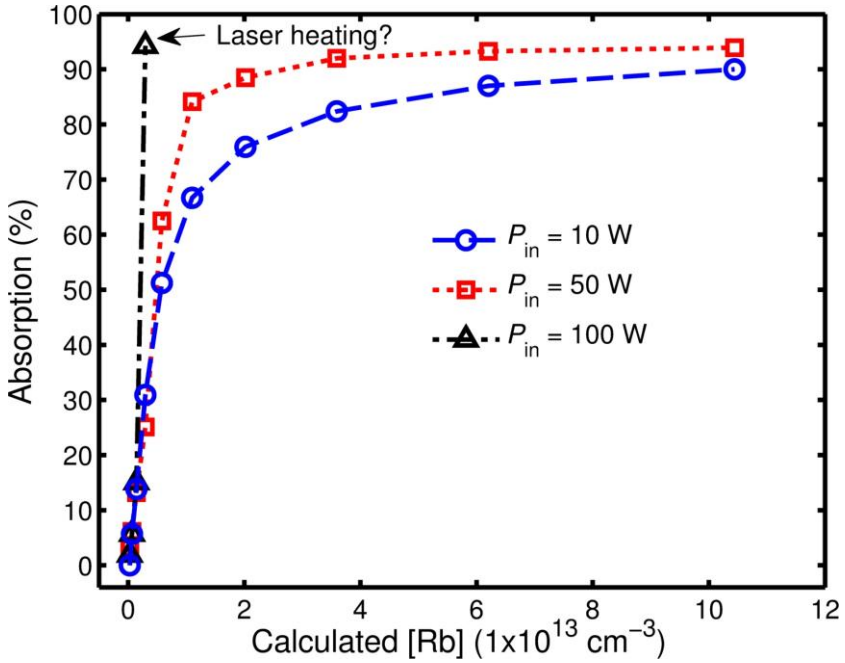

Figure 4.9: Laser absorption in the SEOP cell as a function of calculated Rb density (Eq. 2.74) for three incident laser powers.

The NMR signal, as measured from the static cell, peaked while the oven temperature was at 90 °C (calculated [Rb] = 0.3×10^{13} cm^{-1}) for 10 W and 50 W incident laser powers (Fig. 4.10). The peak signal measured while illuminating the cell with 50 W incident power was a factor of ~1.5 higher than the signal measured while 10 W power was used, thereby demonstrating a clear advantage to using higher laser power. However, while the power incident on the cell was 100 W, the NMR signal was observed to decrease dramatically upon increasing the oven temperature from 80 °C to 90 °C. This observation of signal decrease further suggests that, at 100 W, the Rb density inside the cell is higher (increased Rb spin destruction from Rb-Rb interactions) than that predicted by the Killian formula (Eq. 2.74).

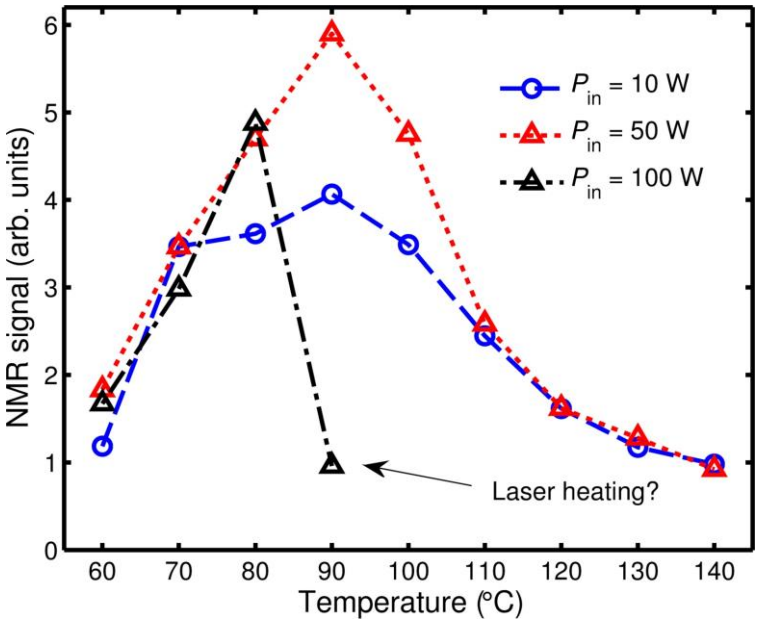

Figure 4.10: ^{129}Xe NMR signal in the SEOP cell as a function of oven temperature for three incident laser powers.

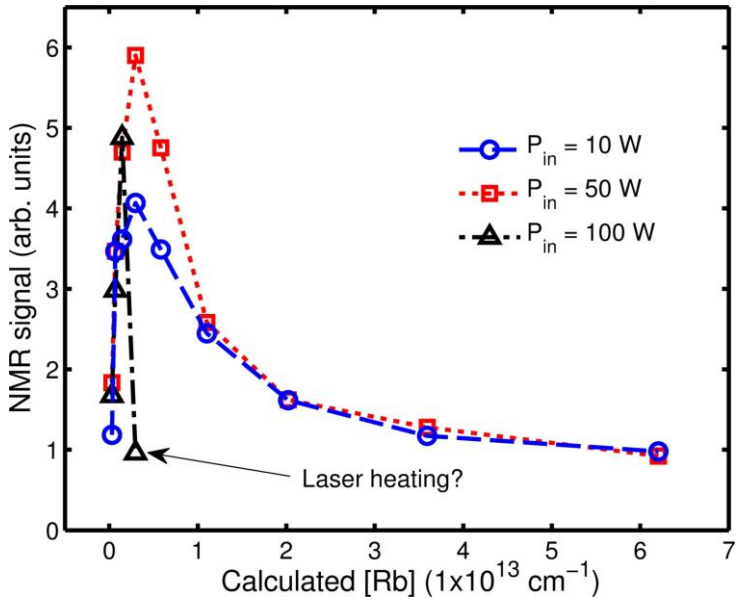

Figure 4.11: ^{129}Xe NMR signal in the SEOP cell as a function of calculated Rb density (Eq. 2.74) for three incident laser powers.

4.5 ^{129}Xe polarisation vs. gas flow rate

To enable comparison with the ECDL data presented in Section 3.4.2, the ^{129}Xe polarisation was evaluated as a function of gas flow rate through the cell while illuminating the SEOP cell with 50 W incident power from the LDA-VHG. The same ^{129}Xe polarisation measurement technique as described in Section 3.3.2 was used, where the ^{129}Xe polarisation was measured in the bore of a 1.5 T scanner.

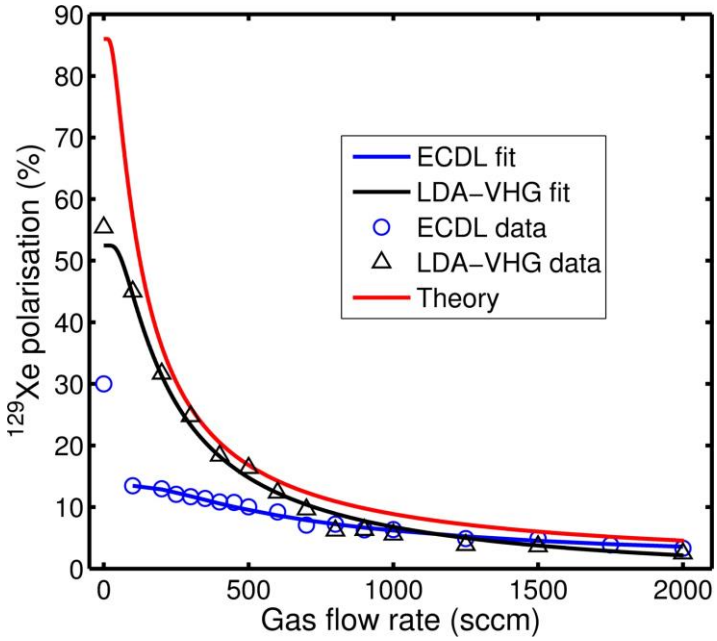

Figure 4.12: Comparison between ^{129}Xe polarisation vs. gas flow rate curves from ECDL and LDA-VHG optical inputs.

It can be seen from Fig. 4.12 that the experimental data obtained using the LDA-VHG OT is in much better agreement with theory than the data obtained using the ECDL. Most notably, whereas the ECDL ^{129}Xe polarisation values diverge from theory at gas flow rates $<$ 1000 sccm, the LDA-VHG OT ^{129}Xe polarisation holds well with theory, even at gas flow

rates as low as 100 sccm. This improved agreement with theory is most likely a result of better beam collimation from the LDA-VHG OT over the cell length compared to the ECDL. Better optical illumination over the whole cell length would act to increase the average Rb polarisation per unit cell length, thus increasing the effective time that ^{129}Xe is undergoing spin-exchange during cell transit (more exchange sites per unit length) for a given gas flow rate. The spin exchange time of ~300 s extrapolated by fitting Eq. 3.8 to the LDA-VHG ^{129}Xe polarisation vs. gas flow rate data agrees well with the theoretically predicted value of 305 s (see Section 3.4.2 and Table 3.1). The discrepancy between the spin exchange times measured using the ECDL and LDA-VHG OT is unexpected and requires further investigation. The static ^{129}Xe polarisation limit with the LDA-VHG OT was measured to be 60 %. Higher laser powers (increased γ_{opt} and thus P_{Rb}) may be necessary to achieve higher ^{129}Xe polarisations; moving towards higher laser powers, however, would require some form of thermal management (to reduce the detrimental effects of Rb runaway), e.g. designing a SEOP cell to have a Rb pre-saturator, as has been successfully demonstrated in ref. [52]. An alternative approach to mitigate laser heating, and enable high incident laser powers, is to operate at lower Rb densities. This approach has been adopted recently on a batch-mode SEOP system where the authors report near-unity (96 %) ^{129}Xe polarisation [56]. The disadvantage to using low Rb densities, however, is a decrease in the Rb-^{129}Xe spin-exchange rate (Eqs. 3.5, 3.6 and 3.7); in continuous-flow mode, to obtain high volumes of ^{129}Xe, fast flow rates are needed (^{129}Xe residency times may be less than one minute). Therefore, in order to maximise the ^{129}Xe polarisation in continuous-flow, fast spin-exchange rates (high Rb densities) are desirable so that the ^{129}Xe nuclear ensemble is given sufficient time to reach close to saturation polarisation levels (i.e. Xe residency time should be greater than the spin up time).

Alternatively, to increase the residency time (and hence ^{129}Xe polarisation exiting the cell), the SEOP cell volume can increased – see Fig. 4.13 (a) and (b) for comparison between a ^{129}Xe production map from the LDA-VHG OT incident on 500 mL (current cell volume) and 2000 mL cell volumes. Fig. 4.14 shows an example of the image quality attainable from 1000 mL of hyperpolarised naturally-abundant (26 % ^{129}Xe) Xe on a 3 T scanner using the LDA-VHG OT as an optical input for ^{129}Xe-Rb SEOP.

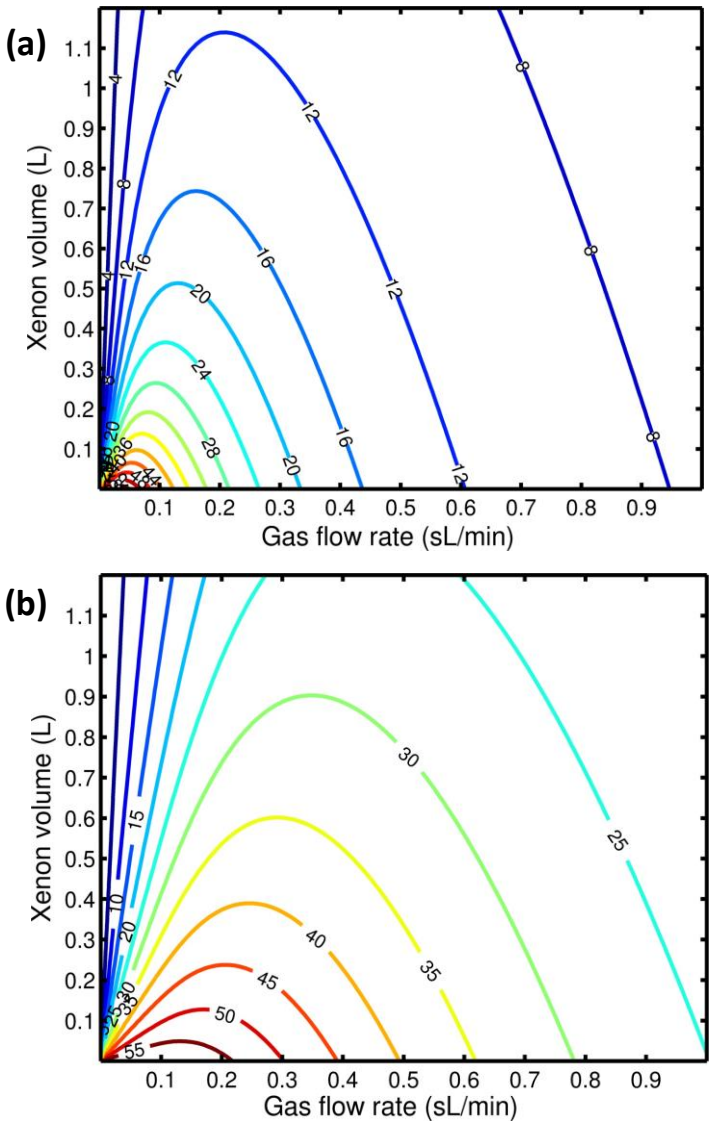

Figure 4.13: Hyperpolarised ^{129}Xe production maps corresponding to 500 mL (a) and 2000 mL (b) cells. Input parameters: saturation ^{129}Xe polarisation = 60 %; spin exchange time = 300 s; and T_1 of frozen ^{129}Xe = 87 min.

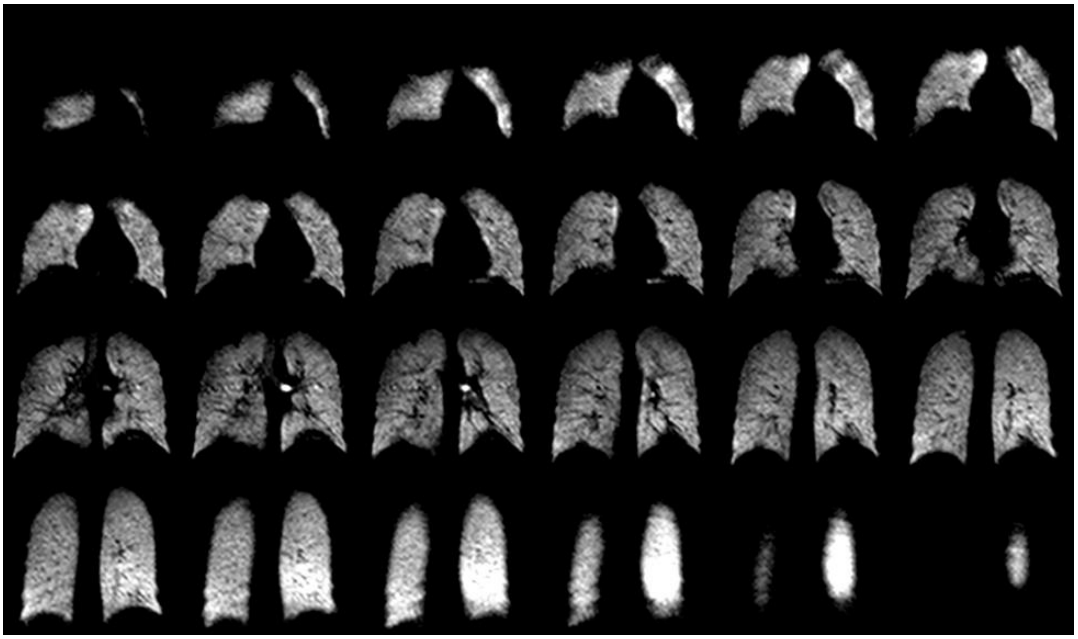

Figure 4.14: *In vivo* 3 T ventilation images of 1 L of hyperpolarised naturally-abundant (26 % ^{129}Xe) Xe using a bSSFP sequence with the following parameters: TE/TR = 1.47 ms/4.7 ms; flip angle = 12°; bandwidth = ± 8.5 kHz; and voxel size = 4.2×4.2×8 mm.

4.6 Conclusions

In this chapter, a laser diode array with an internal frequency-narrowing volume holographic grating was tested on a continuous-flow ^{129}Xe SEOP polariser. It was observed that at the maximum power output of 100 W, laser heating (Rb runaway) has a detrimental effect on the ^{129}Xe NMR signal. At a moderate incident power of 50 W, no significant Rb runaway problems were encountered and good agreement between experimental and theoretical ^{129}Xe polarisations was observed under flow conditions. To mitigate laser heating problems at high laser powers, it may be beneficial to incorporate a Rb presaturator into the optical cell. In addition, it is clear from Xe production maps that to combine high production rates with high ^{129}Xe polarisations, it is necessary to use cells of the order of litre volumes.

Chapter 5

^{129}Xe relaxation and exchange in human blood

5.1 Introduction

The solubility of Xe in various biological tissues and fluids, coupled with its large associated range of chemical shifts (100s of ppm), make hyperpolarised ^{129}Xe an attractive probe for *in vivo* MR studies of gas exchange in the lungs [17, 18] and perfusion of distal tissues and tumours [20, 21]. Integral to the design and feasibility of hyperpolarised ^{129}Xe MR perfusion experiments is an accurate knowledge of the spin-lattice relaxation rate of ^{129}Xe in blood, as it is necessary for accurate modelling of the ^{129}Xe signal evolution while Xe is carried in the blood to the target tissues and organs of interest. The ^{129}Xe relaxation rate in blood has been studied in previous NMR experiments performed by several groups. In work conducted at a field strength of 4.7 T with hyperpolarised ^{129}Xe, Albert *et al.* [99] found that the ^{129}Xe spin-lattice relaxation time, T_1, in red blood cells (RBC) increased with blood oxygenation, measuring values of 4 s and 13 s in deoxygenated and oxygenated blood, respectively. The same group also performed

This work is based on Norquay *et al., Magn. Reson. Med.* DOI:10.1002/mrm.25417, 2014

measurements with thermally polarised ^{129}Xe samples and found the ^{129}Xe-RBC T_1 in deoxygenated and oxygenated blood samples to be lower with values of 2.7 ± 0.22 s and 7.88 ± 0.16, respectively [100]. Wolber *et al.*, [101] at a field strength of 1.5 T, also reported an increase in ^{129}Xe T_1 with blood oxygenation (2.88 ± 0.27 s deoxygenated and 5.71 ± 0.35 s oxygenated blood), and found the T_1 $(1/T_1)$ in a further study to increase (decrease) non-linearly with blood oxygenation [102]. In addition, both groups found the ^{129}Xe T_1 to be highest in blood that had been equilibrated with carbon monoxide; Albert *et al.* reported a value of 11 ± 2 and Wolber *et al.*, a value of 7.84 ± 0.47 s.

In a study conducted by Tseng *et al.*, [103] with blood-foam at a field strength of 4.7 T, the opposite dependence of T_1 on blood oxygenation was observed when compared with [99] and [101]. The T_1 was reported to decrease from 40 s in deoxygenated blood to 20 s in oxygenated blood, and it was deduced that interactions between Xe and paramagnetic bubbles of O_2 gas in the blood was the principal cause of spin-lattice relaxation. The interior of the bubbles, within the blood-foam, provide a residency space for gaseous Xe and O_2 and the skin on the bubbles provides a surface compartment for the oxygen-exposed Xe to dissolve into. Xe gas and paramagnetic oxygen gas in the bubbles (undergoing nuclear-electron dipole-dipole T_1 relaxation) can readily exchange with the dissolved Xe in this regime and the effect of oxygen on the ^{129}Xe T_1 may have been overestimated as such.

In the experimental work reported in this chapter, ^{129}Xe-RBC relaxation was examined over the widest yet range of blood oxygenations (sO_2 values from 0.06–1.00). The experimental design used in this work eliminates gas bubble formation whilst also removing the need to add Xe-saturated saline

into the blood samples (hence eliminating associated dilution effects) [99, 101]. The physical mechanism governing the variation in ^{129}Xe-RBC relaxation rate with blood oxygenation is discussed, and a quantitative analysis is provided to determine parameters that underpin ^{129}Xe relaxation and exchange in whole blood samples. In addition, ^{129}Xe and ^{1}H relaxation rates were measured in saline solution that had different concentrations of dissolved paramagnetic $GdCl_3$ to evaluate the relative strengths of the dipole-dipole interaction between $GdCl_3$ unpaired electrons and ^{1}H and ^{129}Xe nuclei.

5.2 Blood: structure and function

5.2.1 Structure of haemoglobin

Oxygen has a low solubility in aqueous solutions and cannot be carried in sufficient quantities to tissues if it is dissolved in only blood serum. Haemoglobin molecules within red blood cells provide an efficient means of transporting oxygen from the lungs to tissues around the body using a reversible binding process [104]. Human haemoglobin is approximately spherical in shape with dimensions 65×55×50 Å [105]) and contains two α and two β polypeptide chains, making it a tetrameric protein (see Fig. 5.1). Each of the four chains comprise one haem, a prosthetic group consisting of a single iron atom bound (in its ferrous Fe^{2+} state) to an organic ring structure (protoporhyrin).

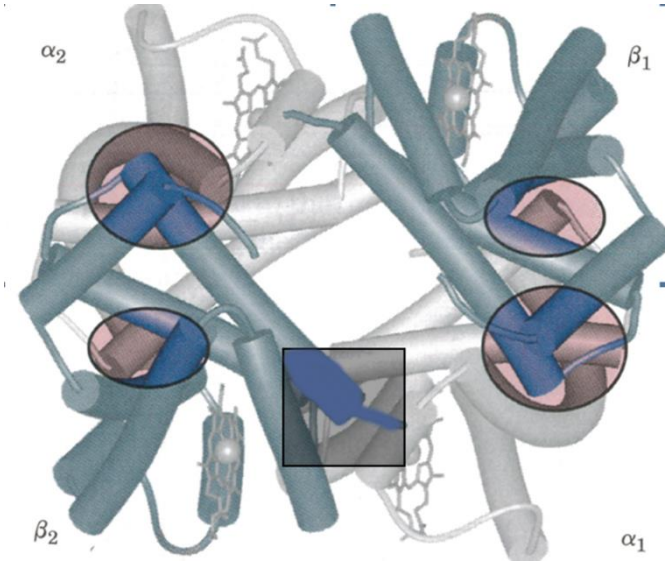

Figure 5.1: Interactions between haemoglobin subunits – α subunits are light and β subunits are dark. The cylinders represent helical segments within α (141 protein residues each) and β (146 protein residues each) polypeptide chains. The strongest interactions occur between unlike subunits (highlighted). When oxygen binds, the largest structural change occurs at the $\alpha_1\beta_2$ contact (square highlight) and a noticeable change is also observed in the $\alpha_2\beta_1$ contact. Figure adapted from Lehninger Principles of Biochemistry 6e, by David l. Nelson and Michael M. Cox, Copyright 2013 by W. H. Freeman and Company. Used by permission of the publisher [106].

5.2.2 Structural change of haemoglobin on binding oxygen

Oxygen binds (reversibly) to the Fe^{2+} molecules within each haem, so that there are four available oxygen binding sites per haemoglobin molecule. Oxygenation of haemoglobin causes such extensive structural change to haemoglobin that two distinct crystalline forms have been revealed using X-ray analysis: deoxyhaemoglobin [107] and oxyhaemoglobin [108]. The quaternary conformations of deoxyhaemoglobin and oxyhaemoglobin are named the T state (T for “tense”) and R state (R for “relaxed”). The quaternary structural change preserves haemoglobins two-fold symmetry by

taking place almost entirely across the $\alpha_1\beta_2$ and $\alpha_2\beta_1$ interfaces, with relatively little change observed at the $\alpha_1\beta_1$ and $\alpha_2\beta_2$ contacts (see Fig 5.2). Indeed, T and R were originally called "tense" and "relaxed", respectively, because the ("tense") T state is stabilised ("relaxed") by adjustments in ion pair numbers, mainly at the $\alpha_1\beta_2$ and $\alpha_2\beta_1$ interfaces, during oxygen binding and transition into the R state).

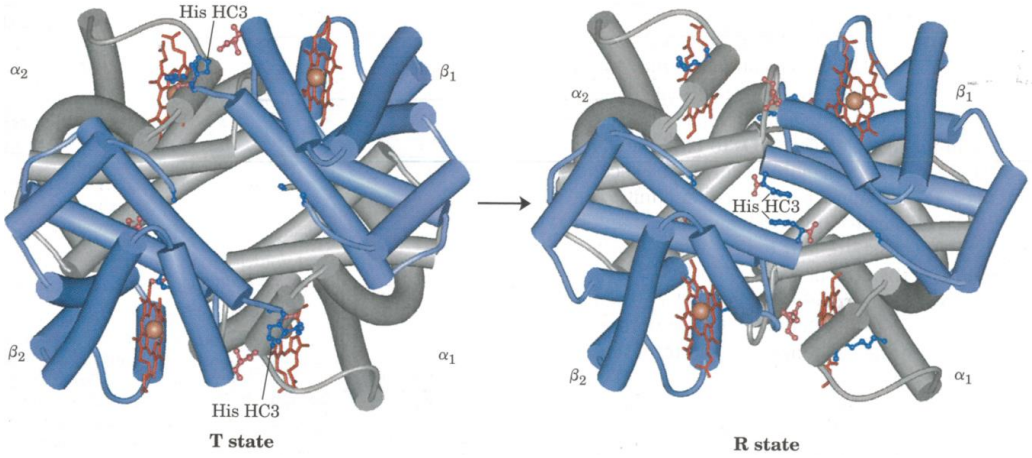

Figure 5.2: T to R state transition. Haemoglobin undergoes a transition from a low affinity oxygen state (the T state, deoxyhaemoglobin) to a high affinity state (the R state, oxyhaemoglobin) as more O_2 molecules are bound to the haem iron. Here, the α subunits are depicted as grey and the β subunits blue. The most dramatic structural changes are observed at the $\alpha_1\beta_2$ and $\alpha_2\beta_1$ interfaces. Note the narrowing of the pocket between the two β subunits as a result of the T to R transition. Figure taken from Lehninger Principles of Biochemistry 6e, by David l. Nelson and Michael M. Cox, Copyright 2013 by W. H. Freeman and Company. Used by permission of the publisher [106].

5.2.3 Haemoglobin binds oxygen cooperatively

For blood to successfully transport oxygen from the lungs to other tissues around the body, Haemoglobin must bind oxygen efficiently in the lungs (where the oxygen partial pressure, pO_2, is ~100 mm Hg) and release oxygen

in the tissues (where pO_2 ~30 mm Hg). The relative stabilities of the T and R states vary with fractional oxygen saturation; in the absence of O_2 molecules (or another ligand), the T state is more stable than the R state and vice versa, where all ligand binding sites are occupied (i.e. the T state has a low affinity for O_2 and the R state a high affinity for O_2).

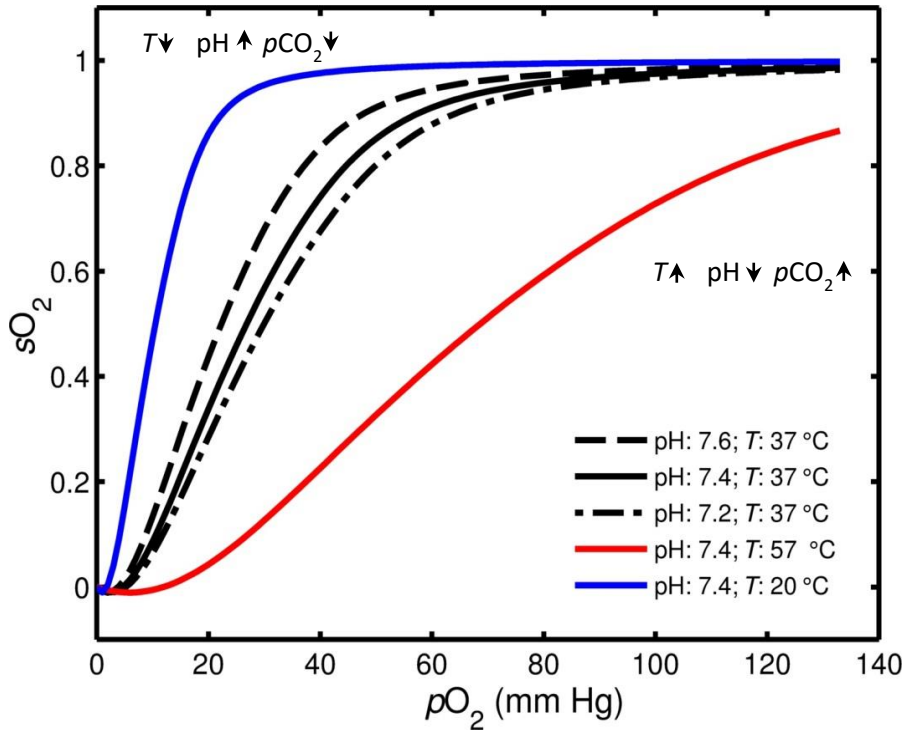

Figure 5.3: Oxygen-haemoglobin dissociation curves for different blood temperatures and pH values of whole blood. The pH of blood is 7.6 in the lungs and 7.2 in tissues. sO_2 is the fraction of haemoglobin molecules that are fully oxygenated.

The R to T transformation is an equilibrium process, so that haemoglobin molecules, at intermediate levels of fractional saturation (one, two or three bound O_2 molecules), continually interconvert between the R and the T states. The relationship between the pO_2 in the blood and the fraction of haemoglobin present that is fully oxygenated, sO_2, is known as the oxygen-haemoglobin dissociation curve, shown in Fig. 5.3. The process can be understood qualitatively by consideration of successive binding of O_2

molecules within a single haemoglobin molecule. The first molecule of O_2 that interacts with deoxyhaemoglobin binds weakly, because it binds to a subunit that is in the T state. By merit of its binding, however, conformational changes take place that make it easier for additional O_2 molecules to bind to adjacent subunits – i.e. the T to R transition occurs more freely in the second subunit once O_2 is bound in the first subunit. The final (fourth) O_2 molecule will bind to haem that is close to being in the R state, and hence will bind with much higher affinity than the first molecule. The O_2-haemoglobin binding curve, sigmoidal in shape, can be understood as a composite of those of its R and T states. The shape of the curve is altered by physiological parameters such as pH (Bohr effect), temperature, and amount of carbon dioxide present (related to pH) in the blood – see Fig 5.3.

5.2.4 Xe-haemoglobin binding

Xe has a large, polarisable electron cloud and, mainly through van der Waals interactions (London dispersion forces), is able to form transient bonds to a number of macromolecules that contain hydrophobic cavities [109-111]. Although Xe has no relevant biological function, owing to its lipophilic nature, it is frequently used in X-ray crystallography as a probe to identify the locations of non-polar haemoglobin/myoglobin cavities which may be involved in gas ligand (e.g. CO, O_2 and NO) migration [112-115]. The first X-ray crystallography experiments reporting Xe binding in blood and performed in the sixties by Schoenborn *et al.*, identified only one Xe binding site in both sperm whale Mb [116] (proximal to the iron haem) and horse haemoglobin [117] (distal to the iron haem). Following from this, Tilton *et al.* [118] examined crystal structures of myoglobin pressurised under several atmospheres of Xe gas, revealing not only one, but four unique Xe-Mb binding sites.

Xe has most recently been used to examine CO and O_2 within human haemoglobins [115, 119], and Savino *et al.* [120], who examined hydrophobic cavity patterns in human deoxyhaemoglobin, identified a total of 12 Xe docking sites per deoxyhaemoglobin tetramer: four Xe binding sites are located in the α_1 subunit, three in α_2 and two in each β subunit. An extra Xe atom is located at the surface of the β_2 subunit (labelled as Xe ext in Fig. 5.4, (b)). It was shown, from the topological differences in the Xe cavity sites (Fig. 5.4 (a)) that there is no correspondence between Xe occupation in myoglobin and in haemoglobin α chains.

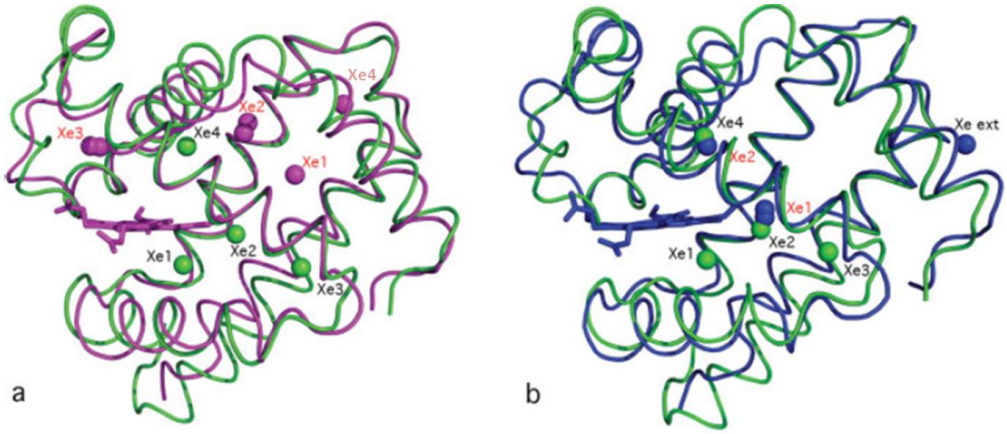

Figure 5.4: Xe binding sites in haemoglobin and myoglobin molecules. (a) haemoglobin α chains (purple) and (b) haemoglobin β chains superimposed to Mb (green). The haem groups are represented as sticks. The pink Xe4 in the α chain is located approximately at the Xe binding site identified by Schoenborn in horse haemoglobin [117] distal (38 Å) to the haem iron. The Xe site closest to the haem iron in the α chain is Xe3, which is proximal (~9 Å) to the haem iron. Figure adapted with permission from [120].

5.3 Two-site exchange model

5.3.1 Fractional populations and Xe exchange rates

For ^{129}Xe nuclei freely diffusing between RBCs and plasma within whole blood samples, a two-site exchange process is considered:

$$\mathrm{RBC} \underset{k_b}{\overset{k_a}{\rightleftharpoons}} \mathrm{PLASMA}\,, \tag{5.1}$$

where k_a and k_b denote the exchange rates of ^{129}Xe diffusing from RBCs to plasma and vice versa. For dynamic equilibrium, the fractional populations of ^{129}Xe in RBCs and plasma, p_a and p_b, are related to the residency times $\tau_a(\equiv k_a^{-1})$ and $\tau_b(\equiv k_b^{-1})$ by

$$p_a = \frac{\tau_a}{\tau_a + \tau_b} \text{ and } p_b = \frac{\tau_b}{\tau_a + \tau_b}, \tag{5.2}$$

where $p_a + p_b = 1$, and the time taken, τ_{ex}, for the system to establish dynamic equilibrium is [121, 122]

$$\frac{1}{\tau_{ex}} = \frac{1}{\tau_a} + \frac{1}{\tau_b} = k_{ex} = k_a + k_b\,, \tag{5.3}$$

where k_{ex} is defined as the exchange rate constant. Combination of Eqs. 5.2 and 5.3 yields

$$\tau_{ex} = p_a\tau_b = p_b\tau_a\,. \tag{5.4}$$

The ratio of residency times of ^{129}Xe in the plasma and RBCs can be estimated by recasting Eq. 5.4 with fractional magnetisations in place of fractional populations,

$$M_a\tau_b = M_b\tau_a \Rightarrow \frac{M_b}{M_a} = \frac{\tau_b}{\tau_a}\,. \tag{5.5}$$

M_a and M_b are the fractional ^{129}Xe magnetisations in RBCs and plasma. With knowledge of the residency time ratio and the equilibrium time constant, τ_{ex}, which has been calculated previously by Bifone *et al.* [123] to be 12 ms, Eq. 5.3 can be rearranged so that the individual ^{129}Xe residency times in RBCs and plasma are

$$\tau_a = \left(\frac{\tau_a}{\tau_b} + 1\right)\tau_{ex} \quad \text{and} \quad \tau_b = \left(\frac{\tau_b}{\tau_a} + 1\right)\tau_{ex}. \tag{5.6}$$

The magnetisation ratio, M_b / M_a, will depend on the haematocrit (HCT) – defined as the red blood cell concentration of the blood samples – and the relative Xe solubilities in plasma and RBCs. Defining HCT as [A] and the concentration of plasma (1−HCT) as (1−[A]), the Xe residency times vary with HCT and plasma concentrations in whole blood according to

$$\frac{M_b}{M_a} = \frac{\delta_b(1-[A])}{\delta_a[A]} = \frac{\tau_b}{\tau_a} \Rightarrow \lambda_{ba} = \frac{\tau_b[A]}{\tau_a(1-[A])}, \tag{5.7}$$

where $\delta_b / \delta_a = \lambda_{ba}$ is the plasma-RBC partition coefficient for Xe (~0.3 for whole blood at 20 °C [124]) and δ_b, δ_a refer to the Xe solubility in plasma and RBCs, respectively. Combination of Eqs. 5.6 and 5.7 leads to Xe-RBC and Xe-plasma residency times as functions of RBC concentration, [A]

$$\tau_a([A]) = \left(\frac{\lambda_{ab}[A]}{(1-[A])} + 1\right)\tau_{ex} \quad \text{and} \quad \tau_b([A]) = \left(\frac{\lambda_{ba}(1-[A])}{[A]} + 1\right)\tau_{ex}. \tag{5.8}$$

$\lambda_{ab} = 1 / \lambda_{ba}$ is the RBC-plasma partition coefficient for Xe. Expressions for Xe-RBC and Xe-plasma exchange rates, k_a and k_b, are readily obtained by taking the inverses of τ_a, τ_b and substituting τ_{ex} with k_{ex}^{-1} in Eq. 5.8, giving

$$k_a([A]) = \left(\frac{(1-[A])}{\lambda_{ab}[A] + (1-[A])}\right)k_{ex} \quad \text{and} \quad k_b([A]) = \left(\frac{[A]}{\lambda_{ba}(1-[A]) + [A]}\right)k_{ex}. \tag{5.9}$$

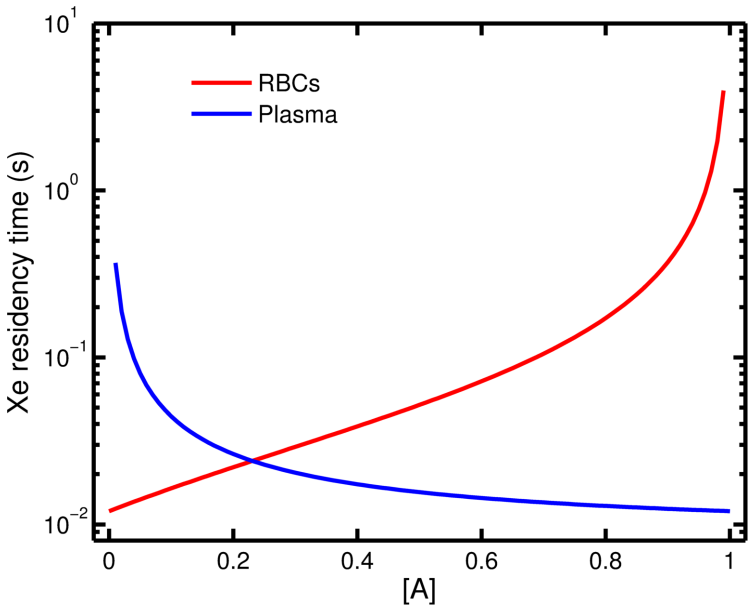

Figure 5.5: Simulated Xe residency times in RBCs and plasma, τ_a and τ_b, as a function of RBC concentration, [A], in whole blood at 20 °C using published Xe RBC-plasma and Xe plasma-RBC partition coefficients [124]. Note the log scale on the y axis.

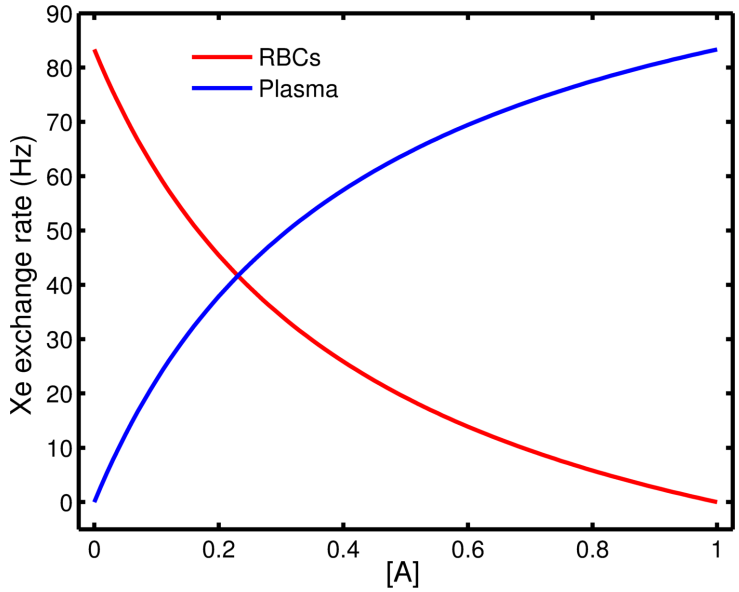

Figure 5.6: Simulated exchange rates of Xe diffusing from RBCs to plasma and vice versa, k_a and k_b, as a function of RBC concentration, [A], in whole blood at 20 °C using published Xe RBC-plasma and Xe plasma-RBC partition coefficients [124].

5.3.2 ^{129}Xe magnetisation dynamics in whole blood

It is assumed that the ^{129}Xe resonance frequency at each site, ω_a and ω_b, is distinct, with a frequency difference given by $\Delta\omega = |\omega_a - \omega_b|$; the magnetisation dynamics of ^{129}Xe nuclei undergoing exchange between plasma and RBCs may then be described by coupled rate equations by extending previous NMR analysis of water protons diffusing between plasma and RBCs [125]

$$\begin{aligned}\frac{dM_a(t)}{dt} &= -(R_{1,a} + k_a)M_a(t) + k_b M_b(t) \\ \frac{dM_b(t)}{dt} &= -(R_{1,b} + k_b)M_b(t) + k_a M_a(t),\end{aligned} \tag{5.10}$$

where $R_{1,a}(\equiv 1/T_{1,a})$ and $R_{1,b}(\equiv 1/T_{1,b})$ are the intrinsic NMR relaxation rates of dissolved ^{129}Xe nuclei in RBCs and plasma. Such systems have been considered in detail by Woessner [126] and the general solutions to Eq. 5.10 are

$$\begin{aligned}M_a(t) &= A_+ \exp(-\phi_+ t) + A_- \exp(-\phi_- t) \\ M_b(t) &= B_+ \exp(-\phi_+ t) + B_- \exp(-\phi_- t),\end{aligned} \tag{5.11}$$

where

$$2\phi_\pm = (R_{1,a} + R_{1,b} + k_a + k_b) \pm \left[(R_{1,a} - R_{1,b} + k_a - k_b)^2 + 4k_a k_b\right]^{1/2}, \tag{5.12}$$

and the coefficients A and B depend on the fractional volume of the RBCs and plasma (and the solubility of Xe in each compartment), as well as on $\phi_\pm$. The fast rate constant, ϕ_+, reflects the ^{129}Xe magnetisation dynamics of Xe diffusing between RBCs and plasma, whereas the slow rate constant, ϕ_-, describes ^{129}Xe magnetisation decay due to spin-lattice relaxation. Eq. 5.12 can be split into its fast and slow rate components, giving

$$2\phi_+ = (R_{1,a} + R_{1,b} + k_a + k_b) + \left[(R_{1,a} - R_{1,b} + k_a - k_b)^2 + 4k_a k_b\right]^{1/2} \tag{5.13}$$

and

$$2\phi_{-} = (R_{1,a} + R_{1,b} + k_a + k_b) - \left[(R_{1,a} - R_{1,b} + k_a - k_b)^2 + 4k_a k_b\right]^{1/2} \quad (5.14)$$

The ^{129}Xe exchange rates, k_a and k_b, have been previously measured by Bifone *et al.* [123] in (slightly diluted) whole blood to be of the order of tens of Hz, whereas the ^{129}Xe relaxation rates, $1/T_{1,a}$ and $1/T_{1,b}$, are in the sub Hz range, based on previous measurements by Wolber *et al.* [101] and Albert *et al.* [99]. Considering the typical inter-pulse delay times used in ^{129}Xe-blood relaxation rate measurements (0.15–0.5 s) [102], inserting the fast decay rate constant, ϕ_{+}, into Eq. 5.11 with $k_a, k_b \gg R_{1,a}, R_{1,b}$ causes $A_{+}\exp(-\phi_{+}t)$ and $B_{+}\exp(-\phi_{+}t) \rightarrow 0$, so that the solutions to Eq. 5.10 become

$$M_a(t) = A_{-}\exp(-\phi_{-}t)$$
$$M_b(t) = B_{-}\exp(-\phi_{-}t), \quad (5.15)$$

suggesting that in the case of $k_a, k_b \gg R_{1,a}, R_{1,b}$, the ^{129}Xe magnetisations in both the plasma and RBC compartments decay with a common rate constant, ϕ_{-} (Eq. 5.15), which we shall refer to as the observable ^{129}Xe relaxation rate, $R_1 (\equiv 1/T_1)$, in whole blood samples. The ^{129}Xe relaxation rate in the plasma pool, $1/T_{1,b}$, is assumed to be dominated by dipole-dipole interactions with dissolved paramagnetic molecular oxygen, and therefore should change linearly with oxygen concentration, $[O_2]$, according to

$$\frac{1}{T_{1,b}} = r_{O_2}[O_2] + \frac{1}{T_{1,b}^0}, \quad (5.16)$$

where r_{O_2} is the ^{129}Xe-O_2 relaxivity in plasma and $1/T_{1,b}^0$ is the ^{129}Xe relaxation rate in the absence of dissolved oxygen. The intrinsic relaxation rate of ^{129}Xe in RBCs, $1/T_{1,a}$, can be obtained by rearranging Eq. 5.14 (with $\phi_{-} = 1/T_1$, $R_{1,a} = 1/T_{1,a}$ and $R_{1,b} = 1/T_{1,b}$), thus

$$\frac{1}{T_{1,a}} = \frac{T_{1,b}\left[T_1(k_a + k_b - 1)\right] - T_1(k_a T_1 - 1)}{T_1\left[T_{1,b}(k_b T_1 - 1) + T_1\right]}. \quad (5.17)$$

5.4 Experimental techniques

5.4.1 Hyperpolarised ^{129}Xe gas preparation

For the generation of all hyperpolarised ^{129}Xe samples, a gas mixture of 3 % isotopically-enriched Xe (86 % ^{129}Xe), 10 % N_2 and 87 % He (Spectra Gases, UK) was flowed through the cell using a mass flow controller (Aalborg, Caché, Denmark), and collected cryogenically using a freeze-out process [127]. A gas flow rate through the cell of 300 sccm was maintained during the freeze-out, resulting in the production of ~200 mL of gaseous Xe (^{129}Xe polarisation of 10 to 15 %) over a time period of 20 min. The cell temperature and pressure was maintained at 373 $\pm$ 1K and 2 bars, respectively, throughout the spin-exchange optical pumping process.

5.4.2 Blood sample preparation and analysis

To prepare all blood samples, whole blood was withdrawn by a clinician from three self-consenting volunteers by venipuncture and transferred into lithium heparin vacuum containers approximately 2 to 3 hours prior to the start of the NMR experiments. All blood samples were allowed to equilibrate to a temperature of 20 $\pm$ 2 °C (the temperature at which the scanner room is maintained). Prior to conducting the NMR experiments, the Xe was first dissolved into the blood. To ensure effective mixing, the Xe and blood were passed through an exchange module [128, 129] (Superphobic MicroModule 0.5 X 1 G680 Contactor, Membrana, USA), which provided an exchange surface area of 100 cm^2. To perform the mixing, 10 mL of Xe gas was passed unidirectionally through the inside of thin-walled hollow-fibre tubes within the exchange module (Fig. 5.7) at a rate of ~1 mL/s, while the blood was

passed back and forth over the outside of the tubes for ~10 s to ensure a sufficient concentration of Xe was dissolved into the blood. Using this mixing technique enables microscopic mixing, whilst also eliminating the formation of gas bubbles in the blood. Immediately after the mixing process, 2 mL of the Xe-blood mixture was drawn up into a 3 mL syringe contained within a custom-built solenoid coil, and the sample was then ready for NMR signal acquisition.

A clinical blood gas analyser (Radiometer, ABL80, UK) was used to analyse the blood sample and determine the necessary physiological parameters such as sO_2, pO_2, pCO_2, HCT and pH. Immediately after acquiring NMR spectra (see Section 5.4.4), approximately 0.1 mL of blood was withdrawn directly from the NMR sample syringe and taken to the blood gas analyser for analysis.

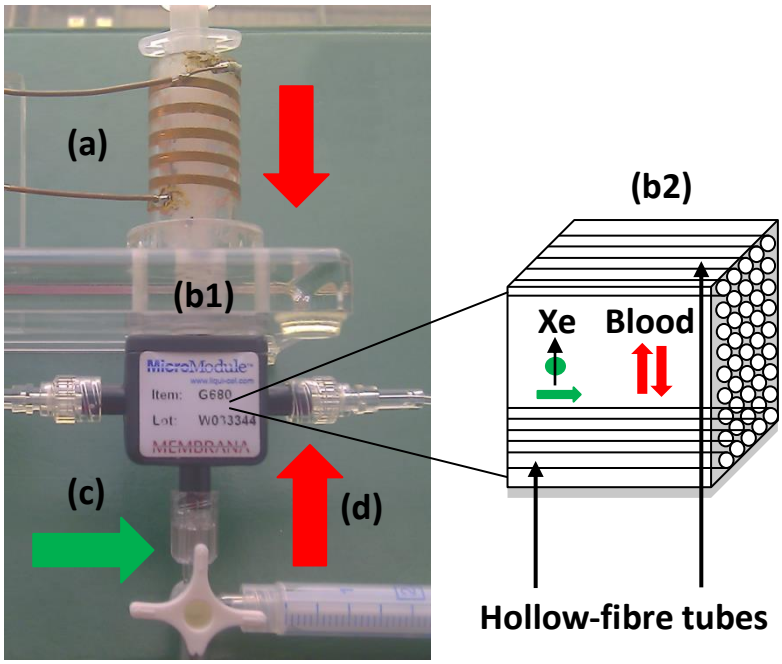

Figure 5.7: (left) Photograph of Xe-blood exchange apparatus and (right) cross section of exchange module. Xe, (c), is pushed through the hollow-fibre tubes of the exchange module, (b1) and (b2), unidirectionally at a rate of ~1 mL/s, while the blood, (d), is passed into and out of the membrane and the sample volume (3 mL syringe enclosed within a custom-built solenoid RF coil, (a)).

Therefore, the sO_2 values of the samples measured at 20 °C were corrected using the numerical technique of Kelman [130] that accounts for shifts in the standard oxygen dissociation curve in blood due to changes in temperature, pH, and pCO_2 (see Fig. 5.8). In order to increase the blood sO_2 from its venous value (0.60–0.80), upon finishing each NMR acquisition, 1–3 mL of O_2 was passed through the exchange module at a rate of ~0.2 mL/s and exchanged with the blood in the same way as it was for Xe. After mixing the blood and O_2, the exchange module was flushed with ~20 mL of N_2 gas (without passing blood through the system) to remove the O_2 from the Xe gas spaces. To decrease the blood oxygen saturation to values lower than 0.60, a saline suspension of sodium dithionite ($Na_2O_4S_2$) was mixed with blood external to the exchange module. Stock solutions were prepared at concentrations of 100 mg of $Na_2O_4S_2$ per 1 mL of saline (0.9 % w/v sodium chloride) and the suspension was added to the blood at a concentration of 0.05 mL saline per 1 mL blood using a 1 mL syringe for mixing. The sodium dithionite reduces the partial pressure of extracellular molecular oxygen within the blood sample, thereby causing depletion of oxygen in the RBCs [131]; with this technique, it was possible to reduce the blood sO_2 as low as 0.06 at 20 °C.

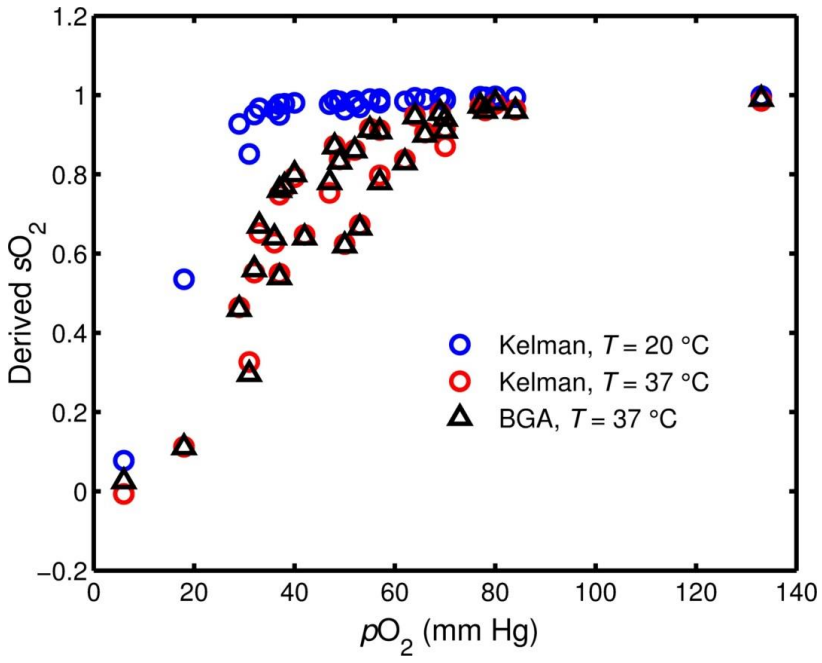

Figure 5.8: Derived blood oxygenation, sO_2, vs. measured blood oxygen partial pressure, pO_2. The blood oxygenation was derived numerically (see Section 5.4.2) from blood pO_2, pH and pCO_2 values measured using a blood gas analyser. The blue and red circles correspond to oxygenation values derived using numerical methods based on Kelman [130] assuming blood sample temperatures of 20 °C (sample temperature at which the NMR was performed) and 37 °C, respectively, and the black triangles correspond to oxygenation values derived by the blood gas analyser (which assumes a sample temperature of 37 °C).

It is worth noting that as a result of the slight dilution incurred, the sodium dithionite samples had lower levels of HCT, with the lowest recorded being 38 %. This HCT is still within the range of HCT values observed in the different volunteers' blood samples (37–57 %); therefore, we assume the small dilution to be negligible with respect to changes in ^{129}Xe relaxation. Finally, a single blood sample was equilibrated with carbon monoxide, using the same mixing procedure as described above for oxygen.

5.4.3 Plasma sample preparation

To obtain isolated plasma, 20 mL of whole blood, withdrawn as described above, was stored vertically in four 5 mL lithium heparin vacuum containers for ~5 hours to ensure the plasma had separately sufficiently, allowing 6 mL of plasma to be extracted from the four tubes using a 10 mL syringe. The concentration of molecular O_2 in plasma $[O_2]$ was calculated using

$$[O_2] = \delta_{pl} pO_2 \tag{5.18}$$

where $\delta_{pl} = 1.63\times10^{-3}$ mmHg^{-1} mM is the solubility coefficient of O_2 in isolated plasma at 20 °C [132] and pO_2 is the O_2 partial pressure in the plasma, measured with the blood gas analyser. To lower the plasma pO_2 value, a stock solution of sodium dithionite (same concentration to that used in the whole blood samples) was added to the plasma; to increase the plasma pO_2 value, room air was added into the exchange module and mixed with plasma, as described above.

5.4.4 NMR spectroscopy

For all ^{129}Xe-blood NMR spectroscopy experiments, a 1.5 T MR scanner (GE Signa HDx, Milwaukee, WI) was used in conjunction with a home-built, 6-turn solenoid RF coil (2 cm diameter, 4 cm length) tuned to resonate at 17.66 MHz. Prior to performing T_1 measurements, excitation flip angles were determined for blood samples by applying a series of rectangular hard pulses (pulse width 500 μs) centred on the ^{129}Xe-RBC resonance frequency (~220 ppm away from the ^{129}Xe gas resonance) with inter-pulse delay times (TR) of 40 ms. For all T_1 acquisitions, the receiver bandwidth was set to 2.5 kHz and the number of sample points was set to 512 for 500 ms TR values and to 256 for 150 ms TR values; for flip angle calibrations, in order to achieve very short TRs, the bandwidth and sample points were set to 10 kHz and 64,

respectively. A zeroth order phase correction was performed to enable signal analysis of the absorption spectra (see Fig. 5.9 for phase correction of the ^{129}Xe-RBC resonance).

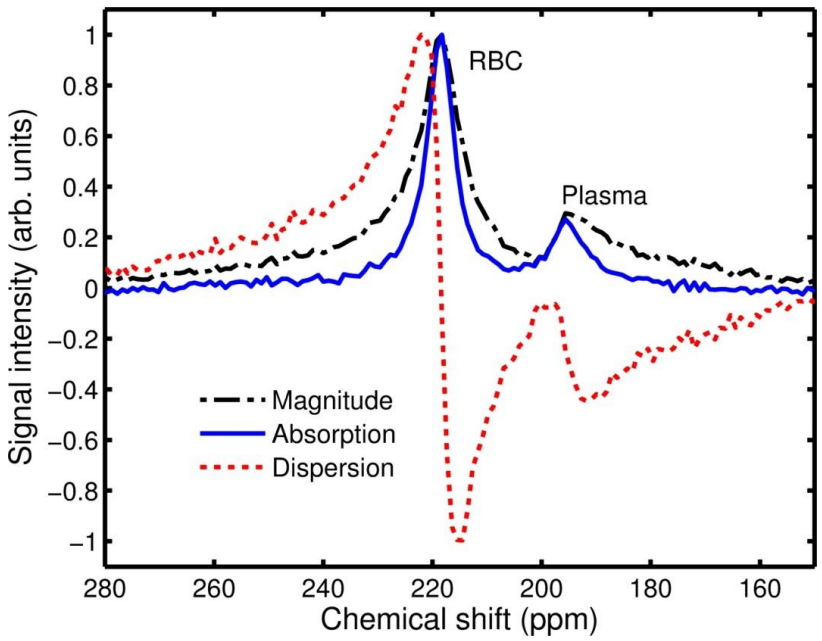

Figure 5.9: ^{129}Xe spectrum in whole blood. The peaks at 196 and 220 ppm correspond to ^{129}Xe dissolved within blood plasma and red blood cells, respectively. All data analyses were done using the absorption part of the ^{129}Xe-blood signal, obtained by performing zeroth order phase corrections on the real and imaginary parts of the Fourier transformed spectra.

The measured ^{129}Xe-RBC signal decrease was fitted to $(\cos\alpha)^{n-1}$, where α is the flip angle to be calibrated and n is the RF pulse number. Separate flip angle calculations were performed for each experiment and all values fell within the range 13.5 to 15°. After calibrating the flip angle, the blood samples were remixed with hyperpolarised ^{129}Xe and a T_1 measurement sequence was applied consisting of 15–20 pulses with TR values of 150 ms and 500 ms for blood sO_2 ranges of 0.06–0.80 and 0.80–1.00, respectively. ^{129}Xe T_1s were calculated by fitting the decay in the ^{129}Xe-RBC and ^{129}Xe-plasma NMR signals to the relationship,

$$S_n = S_0 \sin\alpha(\cos\alpha)^{n-1} \exp\left[-(n-1)\mathrm{TR}/T_1\right], \tag{5.19}$$

where S_0 is the signal intensity at time $n = 1$. The signals that were fitted to Eq. 5.19 were determined by integrating over the ^{129}Xe-RBC and ^{129}Xe-plasma resonance peaks in the phased absorption spectrum. (See Fig. 5.10 for typical ^{129}Xe-blood decay spectra, with an inset showing fits to the ^{129}Xe-RBC and ^{129}Xe-plasma signal decays.)

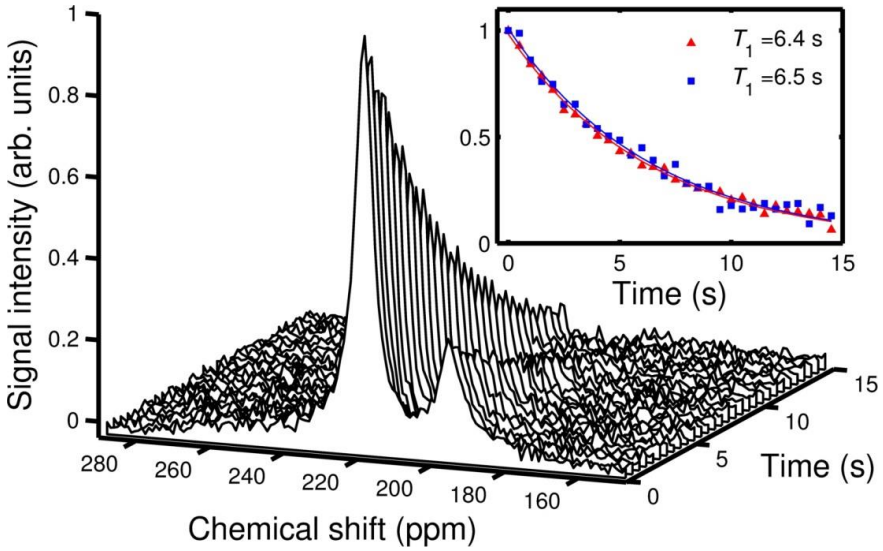

Figure 5.10: Decaying spectra from ^{129}Xe dissolved in blood acquired with 20 hard pulses of 500 μs width (and inter-pulse delay = 0.5 s). The inset shows a fit performed on the decreasing ^{129}Xe NMR signal (integrals of ^{129}Xe-RBC and ^{129}Xe-plasma absorption peaks) in order to establish ^{129}Xe-RBC (red triangles) and ^{129}Xe-plasma T_1 values (blue squares). The decaying spectra represent a blood sample with $s\mathrm{O}_2 = 0.98$.

A non-linear least squares fitting routine using the Levenberg-Marquardt method was implemented in MATLAB and used for all T_1 calculations. The same NMR parameters above were used for T_1 acquisitions on the isolated plasma samples, apart from the TR, which was set to 4 s.

The ratio of ^{129}Xe-plasma and ^{129}Xe-RBC magnetisations, M_b/M_a, was estimated by integrating the area under the RBC and plasma resonances and

averaging over 20 pulses under dynamic equilibrium where TR $\gg \tau_{ex}$ (see Fig. 5.11).

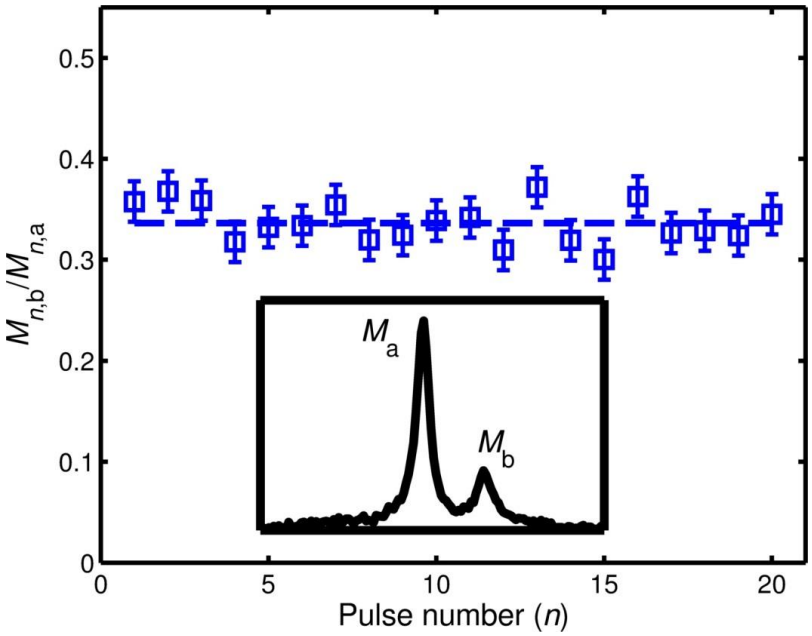

Figure 5.11: Ratio of ^{129}Xe-plasma magnetisation to ^{129}Xe-RBC magnetisation over a 20-pulse acquisition. The blue line is the mean value magnetisation ratio over all pulse acquisitions for a blood sample with a haematocrit of 0.48 at 20 °C.

5.4.5 Preparation of $GdCl_3$-saline samples

A $GdCl_3$-saline stock solution was prepared to a concentration of 2.9×10^{-3} mM and added incrementally at volumes of 0.1 mL into a fixed-volume (10 mL) closed saline system. To ensure good mixing, the saline mixture was passed between two syringes and, once sufficiently mixed, it was pushed into a third syringe contained within either a ^{1}H or ^{129}Xe coil for NMR spectroscopy (see Fig. 5.12).

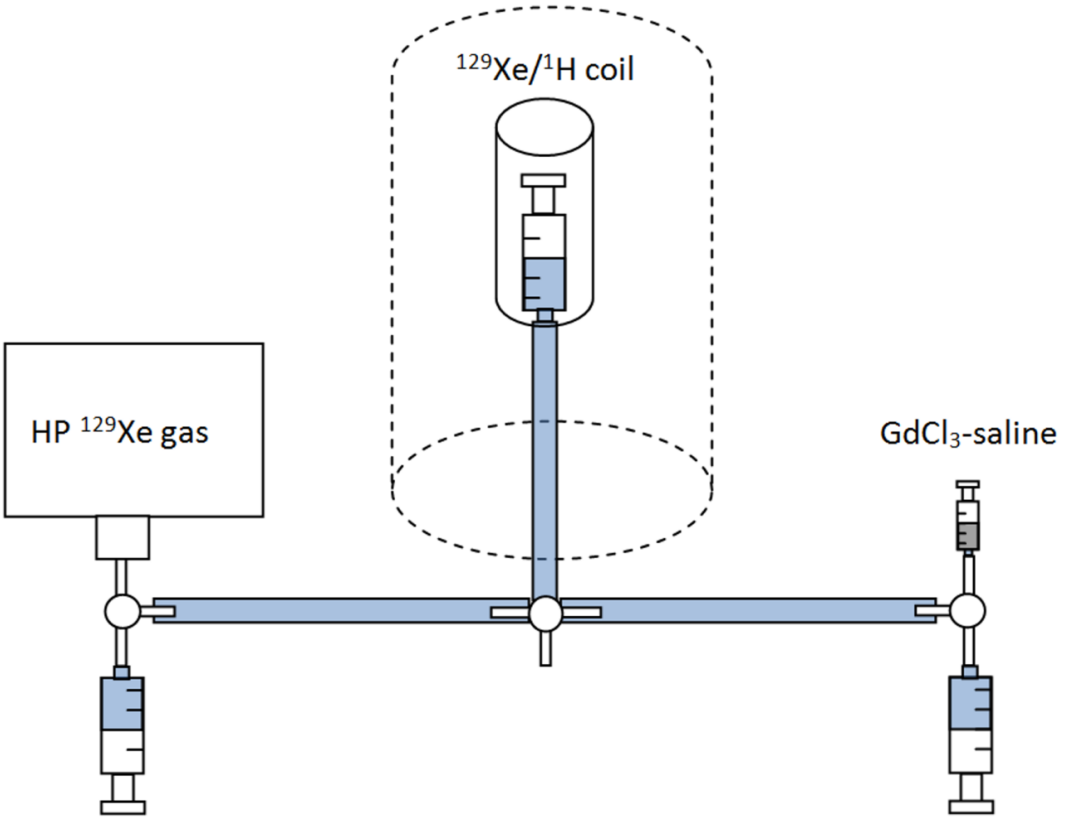

Figure 5.12: Experimental set-up for ^{129}Xe-$GdCl_3$ and ^{1}H-$GdCl_3$ relaxivity measurements. 10 mL of saline was kept in a closed system and stock $GdCl_3$-saline solution was added in increments of 0.1 mL to vary the $GdCl_3$ concentration. The $GdCl_3$ was mixed evenly by pushing the saline solution back and forth with two 10 mL syringes. Once mixed, the solution was pushed into a third syringe located within ^{1}H or ^{129}Xe volume coil for T_1 NMR measurements.

5.4.6 ^{129}Xe- and ^{1}H-saline NMR spectroscopy

For T_1 measurements of ^{1}H in saline, a Look-Locker pulse sequence [133] was performed using a GE 1.5 T Birdcage RF coil, where an initial saturation pulse of 90° was followed by a train of small flip angle pulses of $\alpha = 1.5°$ separated by TRs of < 1 s. The ^{1}H-saline T_1 values were calculated for saline samples containing different concentrations of paramagnetic $GdCl_3$ using the following relationship [134]

$$T_1 = \frac{\mathrm{TR}}{\frac{\mathrm{TR}}{T_1^*} + \ln[\cos\alpha]}, \tag{5.20}$$

where T_1^* is calculated by fitting the ^{1}H-saline proton signal, S_n, following a 90° pulse, to

$$S_n = S_0\left[(1 - \exp(-n\mathrm{TR} / T_1^*)\right], \tag{5.21}$$

where S_0 is the signal at $t = \infty$. For T_1 measurements of ^{129}Xe in saline, the same sequence described in Section 5.4.4 was used with a longer TR of 20 s and the ^{129}Xe signal was fitted to Eq. 5.19.

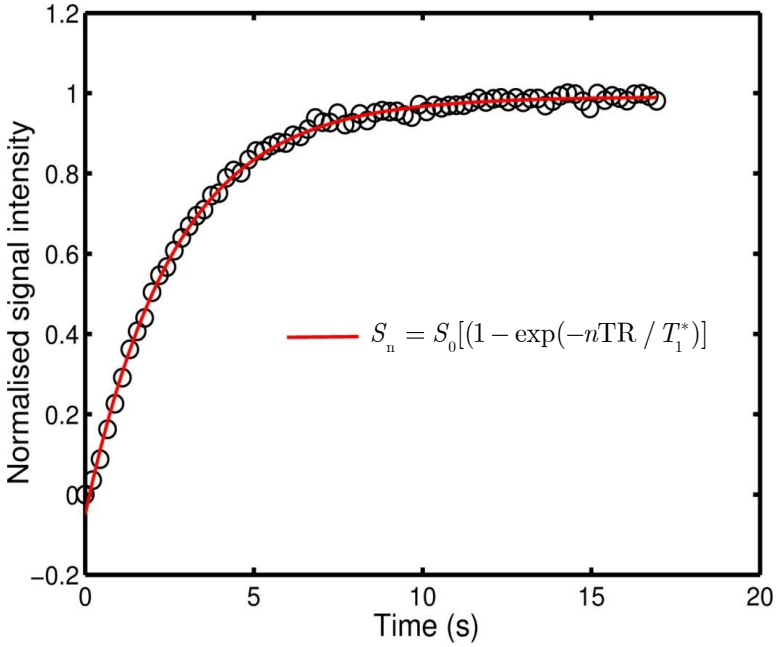

Figure 5.13: Look-locker ^{1}H-saline T_1 measurement. Following an excitation pulse of ~90°, the ^{1}H signal is sampled with small excitation pulses of 1.5° with an inter-pulse delay time of 0.22 s. The above fit corresponds to the ^{1}H in a saline sample without any $GdCl_3$ and the T_1* was measured to be 2.7 s.

5.5 Results

5.5.1 ^{129}Xe relaxation in whole blood

Measurements of the ^{129}Xe relaxation times and rates in human whole blood samples were made over a blood oxygenation range of $s\mathrm{O}_2 = 0.06$–1.00. Blood gas analysis parameters are shown in Table 5.1, alongside ^{129}Xe T_1 values corresponding to venous blood ($s\mathrm{O}_2$ range 0.60–0.80), arterial blood ($s\mathrm{O}_2$ range 0.95–1.00) and blood outside the physiological range ($s\mathrm{O}_2 < 0.60$). (NB: all blood samples were obtained through venipuncture [see Section 5.4.2] and hereafter blood is referred to as venous or arterial for $s\mathrm{O}_2$ ranges of 0.60–0.80 and 0.95–1.00, respectively.) In addition, a T_1 relaxation value for blood equilibrated with CO is included.

^{129}Xe-blood NMR spectra obtained from all samples exhibited two distinct resonance peaks from Xe dissolved in blood plasma and RBCs. While the ^{129}Xe peak in plasma, located 196 ppm downfield from the ^{129}Xe gas reference at 0 ppm, was found to be fixed in centre frequency over the full range of blood oxygenation values, the ^{129}Xe-RBC chemical shift increased from 220 ppm in approximately fully deoxygenated blood ($s\mathrm{O}_2 = 0.06$) to 224 ppm in completely oxygenated blood ($s\mathrm{O}_2 = 1.00$). This shift has been previously observed, and can be explained by a decrease in ^{129}Xe chemical shift shielding constant with increasing blood oxygenation [101, 102].

A typical dataset showing the decay in signal from ^{129}Xe-blood spectra over a number of NMR acquisitions is shown in Fig. 5.10. The T_1 values calculated from the ^{129}Xe signal decay in RBCs were found to be the same, within experimental error, as the T_1 values calculated from the ^{129}Xe signal decay in plasma, thus confirming the prediction of Eq. 5.15 (for $k_\mathrm{a}, k_\mathrm{b} \gg R_{1,\mathrm{a}}, R_{1,\mathrm{b}}$) that the ^{129}Xe magnetisations in plasma and RBCs in whole

blood samples decay with a common observable T_1. The overall ^{129}Xe-blood relaxation rate, $1/T_1$, was found to be non-linearly dependent on blood oxygenation, over an $s\mathrm{O}_2$ range of 0.06–1.00, as shown in Fig. 5.14, (c) and (d). The non-linear relationship between $1/T_1$ and $s\mathrm{O}_2$ can be fitted to the empirical equation

$$\frac{1}{T_1} = \kappa\left[1 - \exp(r_{s\mathrm{O}_2} s\mathrm{O}_2)\right] + \frac{1}{T_1^{\mathrm{dHb}}}, \tag{5.22}$$

where κ is a scaling constant, $r_{s\mathrm{O}_2}$ is defined here to be a relaxivity index characterising the rate of change of ^{129}Xe relaxation as a function of blood oxygenation and $1/T_1^{\mathrm{dHb}}$ is the relaxation rate for fully deoxygenated blood ($s\mathrm{O}_2 = 0.00$). The values of these constants, obtained by fitting Eq. 5.22 to the ^{129}Xe relaxation rate values measured in plasma and RBCs – shown in Fig. 5.14, (c) and (d) – were derived to be $\kappa = 4.6\times10^{-6}\ \mathrm{s}^{-1}$, $r_{s\mathrm{O}_2} = 11.1$ and $1/T_1^{\mathrm{dHb}} = 0.42\ \mathrm{s}^{-1}$ ($T_1^{\mathrm{dHb}} = 2.38$ s). In addition, by setting $s\mathrm{O}_2$ equal to 1.00 in Eq. 5.22, one can obtain the relaxation rate of ^{129}Xe in fully oxygenated blood, $1/T_1^{\mathrm{oHb}} = 0.13\ \mathrm{s}^{-1}$ ($T_1^{\mathrm{oHb}} = 7.7$ s).

The measured values of ^{129}Xe T_1 range from 2.2 s in approximately fully deoxygenated blood ($s\mathrm{O}_2 = 0.06$) to 7.8 s in fully oxygenated blood ($s\mathrm{O}_2 = 1.00$). The rate of change of ^{129}Xe relaxation with respect to oxygenation is relatively slow in the $s\mathrm{O}_2$ range 0.06–0.90, with the T_1 increasing from a value of 2.2 s to only 2.8 s; above $s\mathrm{O}_2 = 0.90$, the rate of change of relaxation with blood oxygenation is much more rapid. The average range of ^{129}Xe T_1 in arterial blood samples from three separate volunteers ('A1–A3' in Table 5.1) was calculated to be 3.6 ± 0.2 s ($s\mathrm{O}_2 \simeq 0.95$) to 7.0 ± 0.9 s ($s\mathrm{O}_2 \simeq 1.00$). Blood equilibrated with CO was found to have a ^{129}Xe T_1 of 7.9 ± 0.1 s, in good agreement with the highest T_1 value of 7.8 s measured in fully oxygenated blood. (NB: The T_1 values quoted above correspond to signal

data from ^{129}Xe in RBCs (equally we could have quoted the ^{129}Xe-plasma T_1 s.).

Samp	T_1 (s)	$1/T_1$ (s^{-1})	n	sO_2	pO_2 (mmHg)	pCO_2 (mmHg)	pH	ctHb (mM)
A1	3.4–7.8	0.29–0.13	11	0.96–1.00	33–133	27–74	7.13–7.5	9–12
A2	3.7–7.2	0.27–0.14	11	0.95–1.00	36–80	10–50	6.96–7.6	7.6–10.6
A3	3.6–6.1	0.28–0.16	4	0.97–0.99	47–84	23–48	7.14–7.4	8.1–8.7
V2	2.8	0.36	1	0.80	31	65	6.93	7.8
D2	2.2, 2.3	0.45, 0.43	2	0.06, 0.47	6, 18	89,77	6.94, 6.92	7.4, 7.8
CO	7.9	0.13	2	–	–	–	–	–
P	11.4–20.4	0.09–0.05	7	–	2–303	7–96	6.8–7.5	–

Table 5.1: ^{129}Xe relaxation times, T_1, and rates, $1/T_1$, calculated from n samples for a variety of blood oxygenation, sO_2, values. The samples are as follows: arterial (defined here to be the range $sO_2 = 0.95$–1.00) blood from three volunteers (numbered A1–A3); a single venous blood sample, V2 (defined for $sO_2 = 0.60$–0.80); a blood sample equilibrated with carbon monoxide, CO; blood samples outside the physiological blood oxygenation ($sO_2 < 0.60$), D2; and samples of isolated plasma solution, P. The concentration of haemoglobin in the blood is denoted ctHb. sO_2 values were derived numerically from pO_2, pCO_2, and pH values that were measured on a blood gas analyser (see Section 5.4.2, Fig. 5.8).

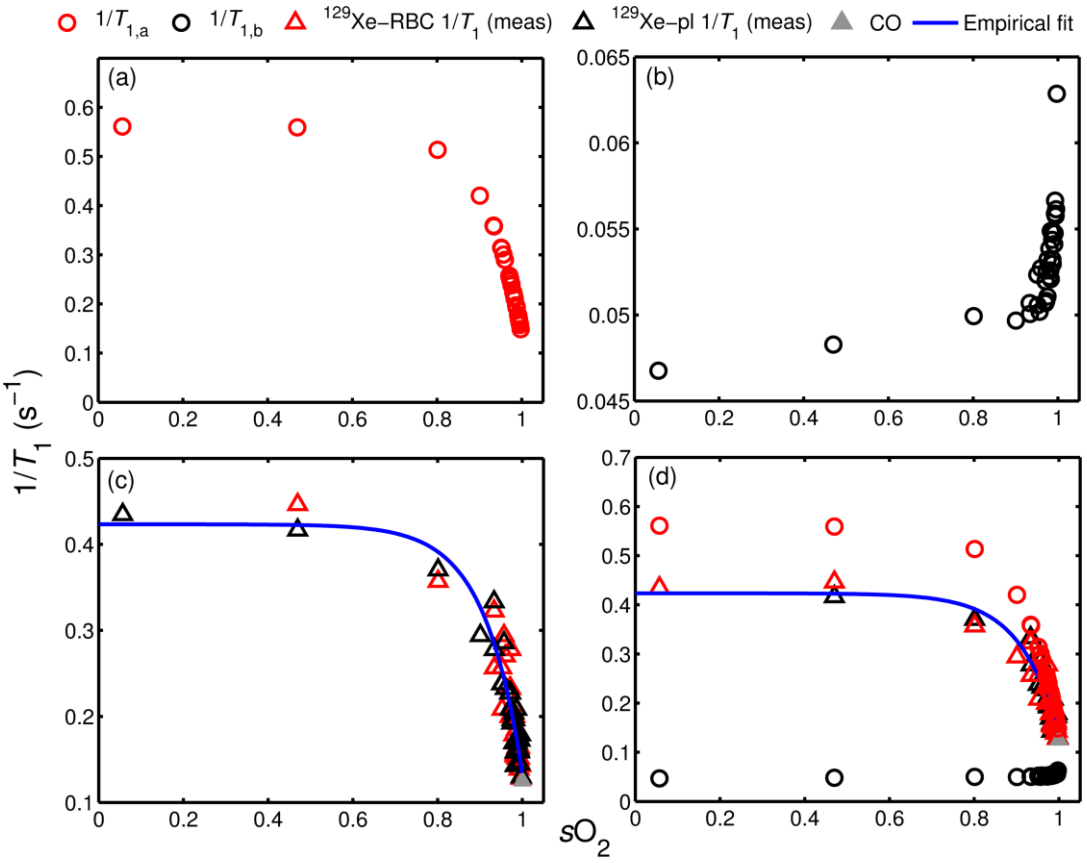

Figure 5.14: The ^{129}Xe relaxation rates from NMR experiments performed on six different blood samples taken from three separate volunteers covering the full blood oxygenation range. (a) and (b) show predicted intrinsic ^{129}Xe relaxation rates in RBCs, $1/T_{1,a}$, and plasma, $1/T_{1,b}$, respectively: $1/T_{1,a}$ was calculated using Eq. 5.17, and $1/T_{1,b}$ was calculated from Eq. 5.16. The data in (c) are the measured ^{129}Xe relaxation rates in RBCs (red triangles) and plasma (black triangles). An empirical function (Eq. 5.22) was fitted to the data, where the following constants were determined: $\kappa = 4.6\times10^{-6}\ \mathrm{s}^{-1}$, $r_{sO_2} = 11.1$ and $1/T_1^{dHb} = 0.42\ \mathrm{s}^{-1}$ ($T_1^{dHb} = 2.38$ s). The solid gray triangle represents the ^{129}Xe relaxation rate for a blood sample that was equilibrated with carbon monoxide and (d) presents all data plotted together. The temperature of all blood samples was 20 °C.

5.5.2 ^{129}Xe relaxation in isolated plasma

The ^{129}Xe relaxation rate in isolated plasma, $1/T_{1,b}$, was found to increase linearly with increasing dissolved O_2 concentration, as predicted by Eq. 5.16,

which was fitted to the data to obtain the ^{129}Xe-O_2 relaxivity in plasma, $r_{O_2} = 0.075\ s^{-1}\,mM^{-1}$, and the ^{129}Xe spin-lattice relaxation rate in isolated plasma in the absence of molecular oxygen, $1/T_{1,b}^0 = 0.046\ s^{-1}$ ($T_{1,b}^0 = 21.7$ s) – see Fig. 5.15. The concentration of O_2 in plasma within whole blood can be calculated by using Eq. 5.18 with a previously measured O_2-plasma solubility coefficient (for whole blood), $\delta_{wb} = 1.69\times10^{-3}\ mmHg^{-1}\ mM$, assuming a haemoglobin concentration value of 9.3 mM (15 g/dL) and sample temperature of 20 °C [135]. The highest pO_2 value in whole blood samples used throughout this study was measured to be 133 mmHg, which corresponds to an O_2 concentration of 0.22 mM.

One can ascertain, therefore, the contribution of dissolved unbound molecular O_2 to ^{129}Xe relaxation in whole blood to be negligible as for the highest oxygen concentration of 0.22 mM, the relaxation contribution from oxygen, $r_{O_2}[O_2] = 0.017\ s^{-1}$, is significantly smaller than the lowest experimentally measured ^{129}Xe relaxation rate of $1/T_1 = 0.13\ s^{-1}$ in whole blood equilibrated with CO.

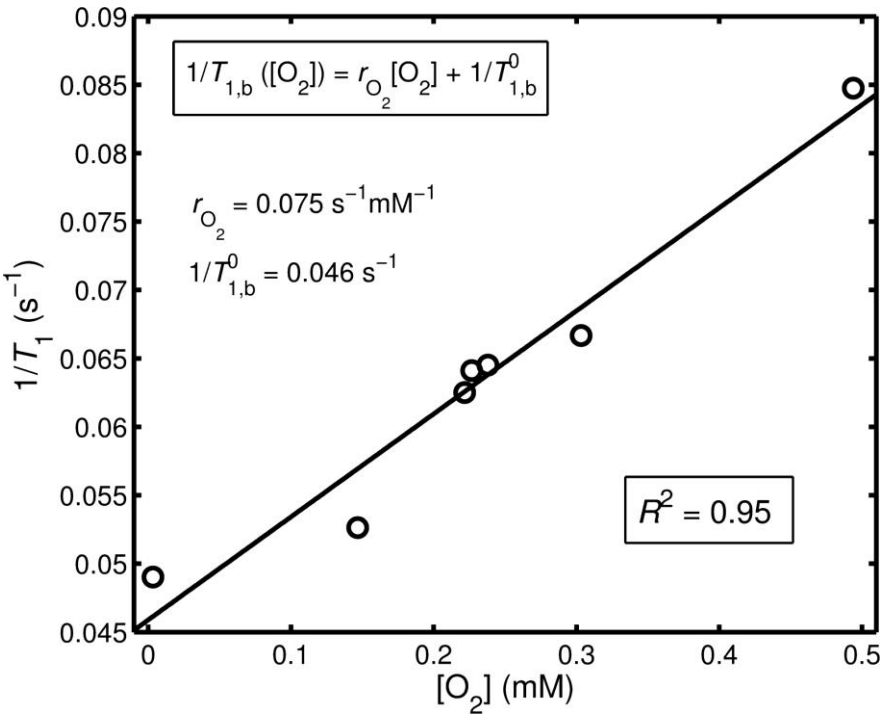

Figure 5.15: ^{129}Xe relaxation rates from NMR experiments performed on isolated plasma samples for a range of oxygen concentrations, $[O_2]$. A linear fit (with a coefficient of determination $R^2 = 0.95$) was performed on the data using the boxed equation, allowing determination of the ^{129}Xe-O_2 relaxivity in plasma, $r_{O_2} = 0.075\ s^{-1}\,mM^{-1}$ and the ^{129}Xe relaxation rate in the absence of dissolved molecular oxygen, $1/T^0_{1,b} = 0.046\ s^{-1}$.

5.5.3 Intrinsic ^{129}Xe relaxation in RBCs

Using the result that the observed ^{129}Xe relaxation rate, $1/T_1$, in whole blood samples is the same in RBCs and plasma over the full blood oxygenation range, it is possible to calculate the intrinsic ^{129}Xe relaxation rate for Xe dissolved in RBCs (at 0.5 HCT), $1/T_{1,a}$, as a function of sO_2 by using results from Eqs. 5.9, 5.16 and 5.22. The relationship between $1/T_{1,a}$ and sO_2 is shown graphically in Fig. 5.14 (a). Intrinsic relaxation rates for ^{129}Xe in RBCs in fully oxygenated blood, $1/T^{oHb}_{1,a} = 0.15\ s^{-1}$, and fully deoxygenated blood, $1/T^{dHb}_{1,a} = 0.56\ s^{-1}$, were calculated by setting sO_2 to 1.00 and 0.00 in Eq. 5.22,

and inserting the respective T_1 values into Eq. 5.17 along with k_a, k_b values corresponding to blood with HCT = 0.5.

5.5.4 ^{129}Xe RBC-plasma exchange rates

The measured ratios of ^{129}Xe-plasma to ^{129}Xe-RBC magnetisations were used to calculate Xe-RBC and Xe-plasma of residency times/exchange rates (Eqs. 5.5 and 5.6) and Xe plasma-RBC partition coefficients (Eq. 5.7) for a range of HCT values. The mean Xe plasma-RBC partition coefficient calculated for blood at 20 °C over a HCT range of 0.39 to 0.54 was calculated to be 0.36 ± 0.04, which is in reasonable agreement with the Xe plasma-RBC partition coefficient of ≈ 0.3 calculated previously from red cell suspensions at 20 °C by Chen *et al.* [124]. See Table 5.2 for calculated values of residency times/exchange rates and Xe plasma-RBC partition coefficients.

HCT	M_b / M_a	τ_b (ms)	k_b (ms^{-1})	τ_a (ms)	k_a (ms^{-1})	λ_{ba}
0.39	0.56	18.7	0.053	33.5	0.03	0.36
0.48	0.36	16.3	0.061	45.3	0.022	0.33
0.54	0.34	16.1	0.062	47.3	0.021	0.4

Table 5.2: Ratio of ^{129}Xe-plasma magnetisation to ^{129}Xe-RBC magnetisation, M_b / M_a; residency times, τ_b and τ_a, and exchange rate constants, k_b and k_a, for Xe in plasma and RBCs; and calculated Xe plasma-RBC partition coefficients, λ_{ba}, for three haematocrit (HCT) values. All values presented in the table correspond to whole blood samples at a temperature of 20 °C.

5.5.5 ^{129}Xe relaxation vs. HCT

For a fixed blood oxygenation, Eq. 5.14 can be used to simulate how the observed relaxation rate, $1/T_1$ (ϕ_-), changes with red blood cell concentration, HCT ([A]). For example, for fully oxygenated blood ($s\mathrm{O}_2 = 1$,

$p\mathrm{O}_2$ ~80 mmHg) at 20 °C, the constants $R_{1,\mathrm{a}}$ ($1/T_{1,\mathrm{a}}^{\mathrm{oHb}} = 0.15$ s^{-1}) and $R_{1,\mathrm{b}}$ ($1/T_{1,\mathrm{b}}^{sO_2=1} = 0.056$ s^{-1}) are used with the variables k_{a} and k_{b} (Eq. 5.9) to compute $1/T_1$ as a function of [A]. Fig. 5.16 shows a non-linear increase in $1/T_1$ with increasing [A] for four blood oxygenations. For fully oxygenated blood, at [A] = 0, $1/T_1 = 1/T_{1,\mathrm{b}}^{sO_2=1}$; and at [A] = 1, $1/T_1 = 1/T_{1,\mathrm{a}}^{\mathrm{oHb}}$ – i.e., as expected, the simulated observable ^{129}Xe relaxation rate equals the intrinsic ^{129}Xe relaxation rates in plasma and RBCs at zero RBC and zero plasma concentrations, respectively, for a given blood oxygenation.

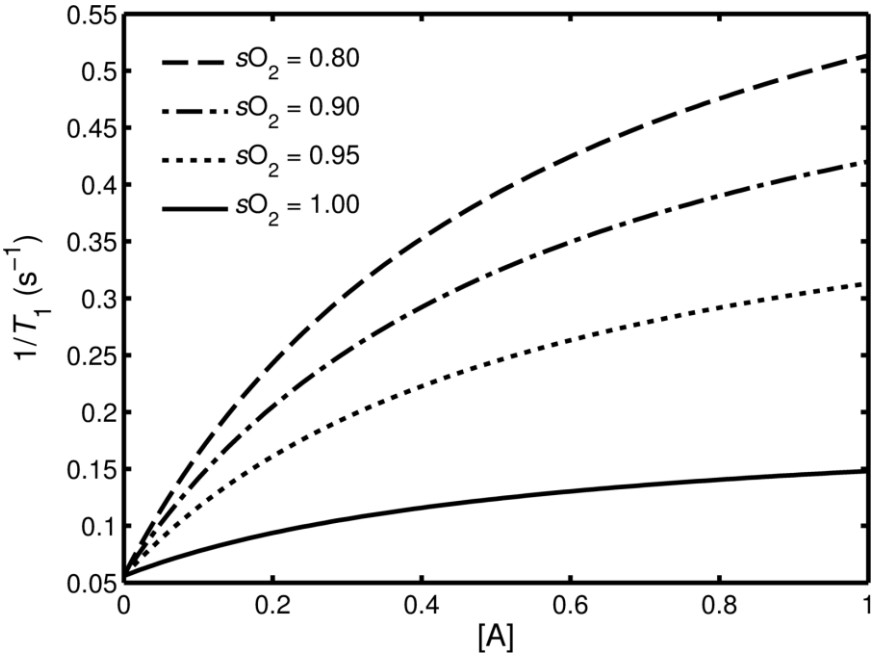

Figure 5.16: Simulated observable ^{129}Xe relaxation rate in whole blood vs. red blood cell concentration, [A], for a blood oxygenation range of 0.80–1.00.

5.5.6 ^{129}Xe- and ^{1}H-$GdCl_3$ relaxation in saline

Both ^{129}Xe and ^{1}H relaxation rates in saline were found to increase linearly with increasing concentration of $GdCl_3$ suspended in the saline solution. ^{129}Xe-Gd and ^{1}H-Gd relaxivities were extrapolated to be 0.53 s^{-1} mM^{-1} and 5.9 s^{-1}

mM^{-1}, respectively by performing a linear fit on the data (Fig. 5.17). Interestingly, the ratio of these relaxivities (~11) is close to what one might predict assuming a heteronuclear dipole-dipole interaction in the extreme narrowing limit ($T_1 = T_2$), where the relaxation rate can be approximated using [31]

$$\frac{1}{T_1} = \frac{\hbar^2 \gamma_I{}^2 \gamma_S{}^2}{r^6} \tau_c , \tag{5.23}$$

where γ_I is the gyromagnetic ratio of the nuclear spin, **I**, and γ_S is the gyromagnetic ratio of the electronic spin, **S**, of a paramagnetic ion, r is the spin-spin separation distance and τ_c is the correlation time (the time characterising significant field fluctuations at the nuclear spin, **I**, brought about by the electronic magnetic moments of the neighbouring paramagnetic ion). Assuming the same correlation time and spin-spin separation distances of ^{129}Xe and ^{1}H spins from the $GdCl_3$ electron spins, and inserting their respective gyromagnetic ratios of -11.777 MHz^{-1} T^{-1} and 42.576 MHz^{-1} T^{-1} into Eq. 5.23, one obtains a ratio, $(1/T_1^{^1H})/(1/T_1^{^{129}Xe})$, of approximately 13, which is in reasonable agreement with the ratio of 11 for the relaxivities.

5.6 ^{129}Xe-RBC relaxation mechanisms

As first demonstrated by Pauling and Coryell [136], the fully deoxygenated form of haemoglobin – deoxyhaemoglobin, Hb_4 (spin = 2) – is paramagnetic, whilst the fully oxygenated form – oxyhaemoglobin, Hb_4O_8 (spin = 0) – and carboxyhaemoglobin (haemoglobin with carbon monoxide bound to it) are both diamagnetic. In addition, it was shown by Coryell *et al.* [137] that blood sO_2 measurement is essentially an ensemble average measure of the superposition of the two extreme haemoglobin states, Hb_4 and Hb_4O_8, with

only a very small contribution from the three intermediate haemoglobin states (Hb_4O_2, Hb_4O_4 and Hb_4O_6).

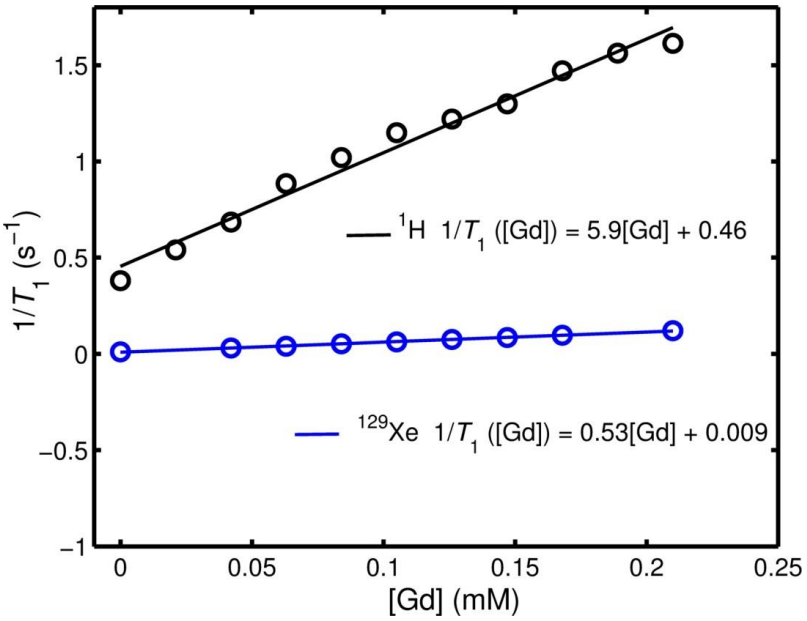

Figure 5.17: Relaxation rates of ^{129}Xe and ^{1}H in saline solution containing different concentrations of paramagnetic $GdCl_3$. The ^{129}Xe-$GdCl_3$ and ^{1}H-$GdCl_3$ relaxivities are given by the gradients of the linear slopes as 0.53 s^{-1} mM^{-1} and 5.9 s^{-1} mM^{-1}, respectively.

Furthermore, Coryell *et al.* determined that the relative fractions of haemoglobin in the fully deoxygenated and fully oxygenated state vary approximately linearly with blood oxygenation (see Fig. 5.18). The observed non-linear decrease in the ^{129}Xe relaxation rate with increasing blood oxygenation (decreased net paramagnetism of the haemoglobin molecules) agrees with the findings of Wolber *et al.*, [138] in which a non-linear relationship between the ^{129}Xe relaxation rate and blood oxygenation was also observed with the same direction of trend albeit over a smaller oxygenation range. Evaluation of the relaxation mechanisms contributing to the change in ^{129}Xe relaxation with RBC oxygenation is substantially more complicated

than evaluation of the change in ^{129}Xe relaxation due to varying O_2 concentration in plasma, and hence a rigorous, fully quantitative treatment is beyond the scope of this thesis chapter. Despite this, the potential relaxation mechanisms are explored in the following.

Two relaxation mechanisms are considered: (i) dipole-dipole spin-lattice relaxation from ^{129}Xe-Hb_4 (in the case of deoxyhaemoglobin) and ^{129}Xe-^{1}H interactions; (ii) dipole-dipole cross-relaxation of ^{129}Xe to protons at the Xe-haemoglobin binding sites via the spin-induced nuclear Overhauser effect (SPINOE) [139]. Both of these mechanisms depend very strongly on the proximity of ^{129}Xe to the neighbouring proton spins and paramagnetic Hb_4, as can be seen by noting the r^6 dependence in Eq. 2.69 and 2.70 in Chapter 2, Section 2.2.4, where r is the inter-nuclear and nuclear-ion separation distances. Therefore, accurate knowledge of the Xe-haemoglobin (Xe-Hb) binding sites is needed to evaluate the relative dipole-dipole and cross-relaxation contributions to the ^{129}Xe relaxation.

As mentioned in Section 5.2.4, Savino *et al.* [120], by examining hydrophobic cavity patterns deoxygenated human haemoglobin, identified a total of twelve Xe binding sites per Hb_4 tetramer. The Xe binding sites in oxygenated haemoglobin were not considered in this study. The haemoglobin molecule undergoes a significant structural change as it makes the transition from the deoxyhaemoglobin conformation to the conformation (Fig. 5.2 in Section 5.2.2). For example, when an O_2 molecule leaves a haem group, the radius of the iron atom increases and the atom moves out of the haem plane by ~70 pm [140], which would affect most strongly the Fe^{2+} dipole coupling to ^{129}Xe nuclei at the Xe3 and Xe1 binding sites in the α and β haemoglobin chains (Fig. 5.4). With these conformational changes, it is thus possible – and indeed likely – that the number/locations of Xe binding sites is/are different in deoxyhaemoglobin when compared to oxyhaemoglobin. Without knowledge

of the locations of Xe atoms in oxyhaemoglobin, it is not possible to accurately estimate the relative changes in dipole-dipole spin-lattice relaxation and dipole-dipole cross-relaxation interaction strengths.

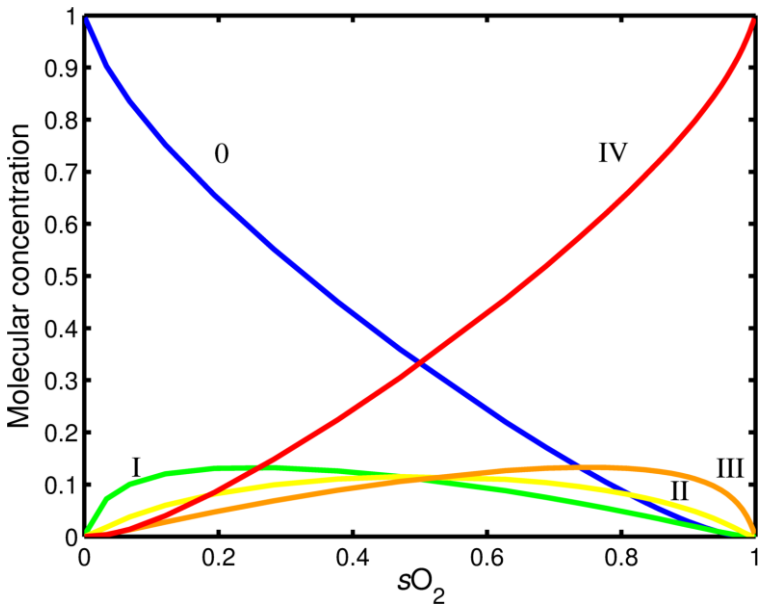

Figure 5.18: Concentrations of molecular haemoglobin species as functions of blood oxygenation. 0 = Hb_4; I = Hb_4O_2; II = Hb_4O_4; III = Hb_4O_6; IV = Hb_4O_8 in horse haemoglobin. Data extrapolated from [137] with permission. Copyright 1939 by American Chemical Society.

Despite this, it is possible to make some assumptions in order to gain insight into the mechanisms driving the non-linear change in the ^{129}Xe relaxation rate with blood oxygenation. Let us assume the following: (i) dipole-dipole ^{129}Xe-Hb_4 interactions is the dominant relaxation process (over ^{129}Xe-^{1}H dipole-dipole and ^{129}Xe-^{1}H SPINOE interactions); (ii) the Xe-Hb binding site locations do not change with blood oxygenation (i.e. the ^{129}Xe-haem distances do not change); and (iii) from the findings of Coryell *et al.* [137], the concentration of paramagnetic Hb_4 changes approximately linearly with blood oxygenation. If these assumptions are valid, one would expect to observe a linear change in the ^{129}Xe relaxation rate with blood oxygenation.

However, the observation of a non-linear change in ^{129}Xe relaxation rate with blood oxygenation suggests that if dipole-dipole ^{129}Xe interactions with paramagnetic Hb_4 were the dominant relaxation process, the number/location of Xe-Hb binding sites must change with blood oxygenation. Considering ^{129}Xe cross-relaxation to protons, polarisation transfer in SPINOE is most rapid when Xe is temporarily bound, thus if the Xe-Hb binding sites do indeed change with blood oxygenation, one would expect a concomitant change in the ^{129}Xe-^{1}H cross-relaxation rate. As highlighted above, knowledge of the Xe-Hb binding sites in oxyhaemoglobin is crucially required before attempting a quantitative description of the complicated underlying relaxation mechanisms responsible for the change in ^{129}Xe relaxation with blood oxygenation.

5.7 Conclusions

In this chapter, a non-linear dependence of the ^{129}Xe longitudinal relaxation rate on blood oxygenation has been reported over the largest yet range of blood oxygenation values. The most rapid rate of change in ^{129}Xe blood relaxation rate is seen in the blood oxygenation range sO_2 0.90 to 1.00, suggesting ^{129}Xe relaxation is highly sensitive to changes in arterial blood oxygenation and less sensitive to changes in venous blood oxygenation. The quantitative relaxation and exchange analysis shown in this chapter has implications for future studies of Xe transport from the lungs to distal tissues, organs and tumours and should provide a sound experimental basis upon which to design novel MR experiments for these purposes. Given knowledge of average blood oxygenation in the circulation and the transit time to the target tissue of interest, the signal evolution of ^{129}Xe can be modelled based upon these findings.

Chapter 6

^{129}Xe chemical shift in human blood: *in vitro* and *in vivo* studies

6.1 Introduction

It was shown in the previous chapter that the ^{129}Xe relaxation rate in human blood exhibits a non-linear dependence on blood oxygenation and could thus be used to probe blood oxygenation non-invasively. In this chapter, the ^{129}Xe chemical shift is investigated as a function of blood oxygenation *in vitro* and is subsequently tested as a probe for pulmonary oxygenation *in vivo* in healthy human lungs. Discussed below are the diagnostic and clinical benefits of tissue and blood oxygenation measurements, along with the challenges of non-invasive *in vivo* tissue/blood oxygenation measurement. Changes in tissue oxygenation may provide an insight into extent of disease; for example, in the discrimination of the penumbra following stroke [138] or identification of ischemia following myocardial infarction [141]. Furthermore, hypoxia limits the efficacy of radiotherapy in the treatment of tumours [142]. In asthma and COPD, hypoxia can influence the lifetime and the functionality of neutrophils

The work in this chapter was presented at the PING14, 2014, and is currently being prepared for submission to Magnetic Resonance in Medicine.

that are associated with inflammation in the lungs [143]. Surface blood oxygenation can be measured with an infrared finger probe, but is depth limited. The accepted gold standard method of determining deep tissue oxygenation is by polarographic electrodes, as pioneered in the late 1950s [144]. This invasive method, however, samples only a small amount of tissue and is able to provide assessment of oxygenation for only limited tissue volumes. Owing to this limitation, oxygenation is usually estimated using surrogate techniques, such as the monitoring of mixed venous oxygenation, heart rate, blood pressure and oxygen saturation at the jugular bulb. However, these estimates can prove inaccurate as distal tissue oxygenation is not necessarily well represented by the more proximal measurements, or vice versa [145].

MR perfusion imaging can be used to measure blood delivery to a tissue, however oxygen supply and demand can be independent of one another, e.g. revascularisation of fibrotic tissue provides blood flow out of proportion to metabolic demand. Likewise, tissues with low levels of perfusion have an adequate oxygen supply while at rest, but an inadequate oxygen supply during periods of increased metabolic demand. Tissue perfusion alone therefore does not completely describe underlying physiology [146] and thus direct, non-invasive measurement of blood oxygenation may be of interest in many clinical settings, as well as being interest from a physiological perspective.

As the treatment planning of many diseases depends on tissue oxygenation (e.g. radiotherapy response in hypoxic tumours [147]), several attempts have been made to quantify regional oxygenation using MRI. A promising method is the use of blood oxygen level dependent (BOLD) MRI [148], where oxygen and carbogen levels are cycled to generate images that indicate impaired oxygen uptake [149]. However, this technique provides only relative estimates

of tissue oxygen partial pressure [150] since there are endogenous variations in magnetisation relaxation parameters that can confound these measurements and thus make absolute oxygen concentration detection difficult. Moreover, BOLD signal response is a mixture of T_2^* dephasing and diffusion due to microscopic susceptibility gradients and is therefore very much dependent upon the means of measurement, for example choice of pulse sequence and field strength. Techniques that introduce exogenous tracers for MR oximetry, such as Overhauser enhanced MRI of unpaired radicals [151, 152] and ^{19}F MRI [153], are promising for measurement of blood oxygenation, however these have yet to be demonstrated in humans. In the lungs, the T_1 of inhaled hyperpolarised ^{3}He [154] has been used to quantify regional alveolar oxygen concentration, but regional ventilation-perfusion mismatch and impaired gas transfer across the alveolar capillary interstitial barrier means this does not necessarily reflect the capillary blood oxygenation.

Xe has been in routine clinical use for many years as a tracer of blood perfusion [155] and the physiological effects of Xe gas administration are well known and characterised [156, 157]. With hyperpolarised ^{129}Xe, as previously mentioned, the signal can be detected at low concentrations as an exogenous *in vivo* contrast agent, and owing to its large, loosely bound electron cloud, ^{129}Xe NMR is highly sensitive to the Xe chemical environment, exhibiting a marked change in the resonance frequency when dissolved in different biological fluids and tissues [158, 159].

Three distinct NMR peaks are observed *in vivo* when ^{129}Xe gas is inhaled into the lungs. The largest peak originates from ^{129}Xe gas in the air spaces and the two other peaks, centred approximately 200 ppm away from the gas peak, have been attributed to ^{129}Xe dissolved in alveolar tissue/blood plasma and in RBCs [160, 161]. Physiologically important information about gas

exchange and uptake can be derived from the signal amplitudes and exchange kinetics of these distinct ^{129}Xe resonances [12, 162]. Furthermore the ^{129}Xe resonance frequency in RBCs has been shown to be sensitive to blood oxygen saturation, $s\mathrm{O}_2$ [163]. Mechanisms for the ^{129}Xe chemical shift dependence on blood oxygenation are not yet fully understood; the dependence is currently thought to be due to the conformational changed of haemoglobin as it binds and releases oxygen molecules [163].

In the study reported in this chapter, spectra of hyperpolarised ^{129}Xe dissolved in samples of human blood were obtained in order to accurately determine the relationship between the ^{129}Xe RBC resonance frequency and $s\mathrm{O}_2$ over a wider blood oxygenation range than previously investigated. Using this relationship, measurements of RBC sO_2 *in vivo* in healthy human lungs were then derived using whole lung NMR spectroscopy measurements in a simple challenge of lung oxygen desaturation during breath-hold apnoea. A technique for the non-invasive detection of blood sO_2 *in vivo* using hyperpolarised ^{129}Xe is hereby demonstrated.

6.2 Experimental techniques

6.2.1 Hyperpolarised ^{129}Xe gas preparation

For the *in vitro* and *in vivo* studies, the gas was prepared in the same way as described in Section 5.4.1; a gas mixture of 3 % isotopically enriched Xe (86 % ^{129}Xe), 10 % N_2 and 87 % He was flowed through a glass cell (volume ~500 cm^3; temperature 373 K; total gas pressure 2 bar) at a flow rate of 300 sccm and upon exiting the cell, the Xe was cryogenically separated and collected in its frozen state over a time of 20 min (Xe volume 200 mL) for *in vitro* samples and 60 (Xe volume 600 mL) min for *in vivo* samples.

6.2.2 Blood sample preparation and analysis

See Chapter 5, Section 5.4.2, for blood sample preparation and sample oxygenation analysis.

6.2.3 *In vitro* NMR spectroscopy

A custom-built, 8-turn solenoid coil of 15 mm inner diameter was used for transmission/reception at the frequency of ^{129}Xe dissolved in RBCs and plasma. The gas exchange membrane, described in Section 5.4.2, was positioned near the sensitive volume of the NMR coil to reduce the Xe-blood transit time and thus minimise T_1 relaxation. To calibrate the excitation flip angle, a small sample of the hyperpolarised ^{129}Xe-blood mixture was placed within the active coil volume. Hard pulses of duration 500 μs were used to acquire spectra, and from these data, the flip angle was determined from a fit to the signal decay (see Section 5.4.4 for more details).

Spectra were acquired on both 1.5 T (GE, 14M5, USA) and 3 T (Philips, Achieva, Netherlands) MRI scanners. At 1.5 T and 3 T, pulse-acquire measurements were made with 1024 points, a receiver bandwidth of 2.5 kHz and a TR of 6 s. Blood was extracted from the sensitive coil volume after each NMR experiment and analysed in a blood gas analyser as described in Section 5.4.2.

FID data from 1.5 T and 3 T were imported into MATLAB for spectral analysis. Zero-order phase corrections were performed on the raw data and absorption spectra, Re[L], were fitted in the chemical shift (δ) domain to a linear combination of two Lorentzians

$$\mathrm{Re}[L](\delta) = \mathrm{A}_{\mathrm{r}} \frac{\frac{1}{2}\Gamma_{\mathrm{r}}}{(\delta - \delta_{\mathrm{r}}^{0})^{2} + (\frac{1}{2}\Gamma_{\mathrm{r}})^{2}} + \mathrm{B}_{\mathrm{p}} \frac{\frac{1}{2}\Gamma_{\mathrm{p}}}{(\delta - \delta_{\mathrm{p}}^{0})^{2} + (\frac{1}{2}\Gamma_{\mathrm{p}})^{2}}, \qquad (6.1)$$

where A_{r} and B_{p} are the amplitudes of the RBC and plasma ^{129}Xe resonances; δ_{r}^{0}, δ_{p}^{0} are the chemical shifts of the ^{129}Xe-RBC and ^{129}Xe-plasma maxima; and Γ_{r}, Γ_{p} are the FWHMs of the two peaks. Fig. 6.1 shows an example of a fit from a noisy *in vitro* 1.5 T ^{129}Xe-blood spectrum.

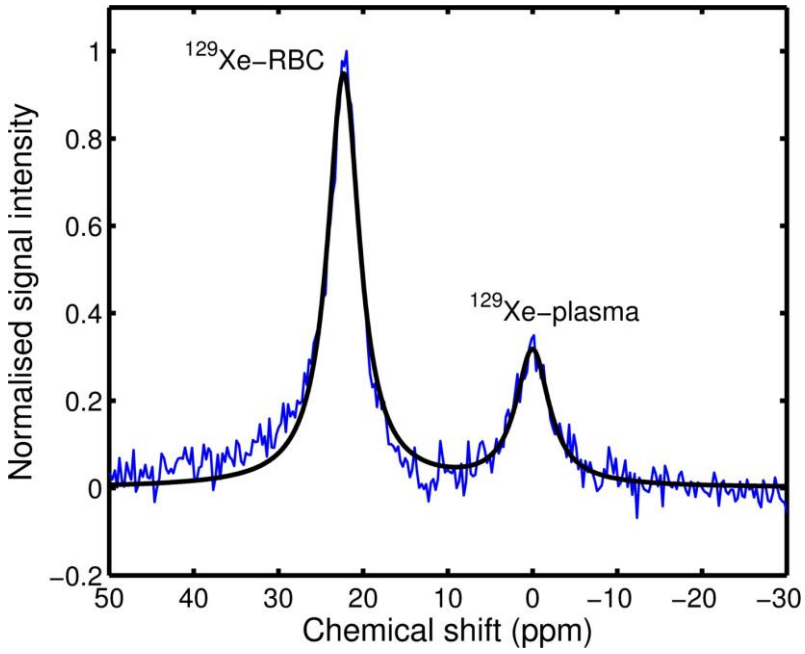

Figure 6.1: Single-shot ^{129}Xe-blood spectrum at 1.5 T. The absorption spectrum was fitted to a linear combination of two Lorentzians to determine peak positions.

The 3 T data were filtered (combination of Gaussian and exponential apodisation functions) and phased using spectroscopy analysis software built into the 3 T Philips console (Fig. 6.2). Once the data were filtered and phased, the absorption spectra were exported into MATLAB where the ^{129}Xe-RBC and ^{129}Xe-plasma peak positions were determined.

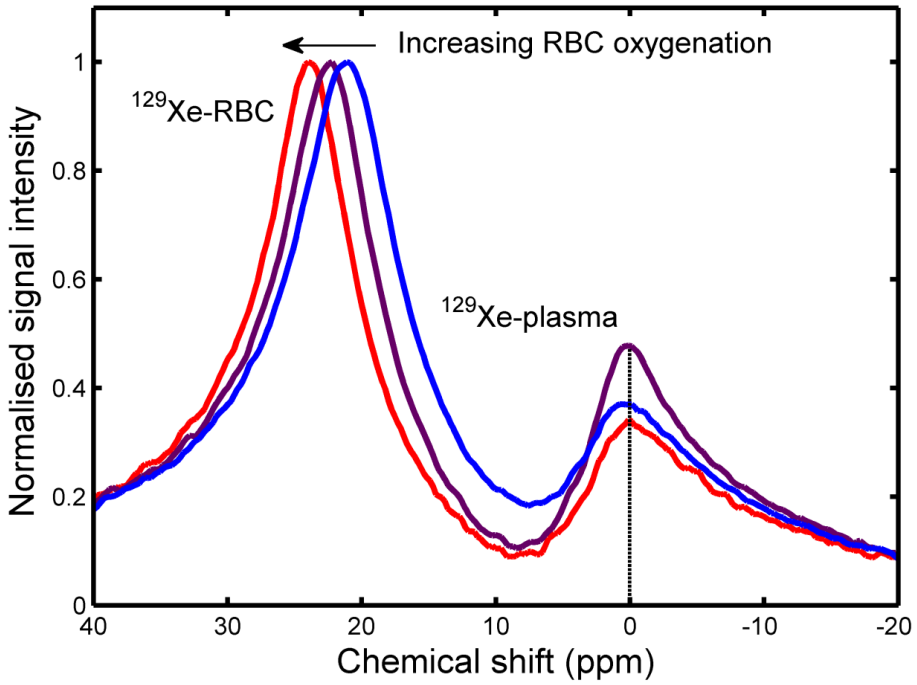

Figure 6.2: 3 T ^{129}Xe-blood spectral peaks. With increasing oxygenation, the peak associated with ^{129}Xe dissolved in RBCs is seen to shift measurably towards a higher resonance frequency.

6.2.4 *In vivo* NMR spectroscopy

Whole-lung spectroscopy experiments were performed at 3 T (Philips, Achieva, Netherlands). A 0.36 ms 90° hard pulse centred ~200 ppm downfield from the gaseous ^{129}Xe resonance was used for excitation of the ^{129}Xe dissolved in blood and tissues. See Fig. 6.3 below for relative signal intensities of peaks corresponding to gaseous ^{129}Xe (^{129}Xe-gas), ^{129}Xe dissolved in red blood cells (^{129}Xe-RBC) and ^{129}Xe dissolved in parenchymal tissue and blood plasma (^{129}Xe-TP) in the lungs.

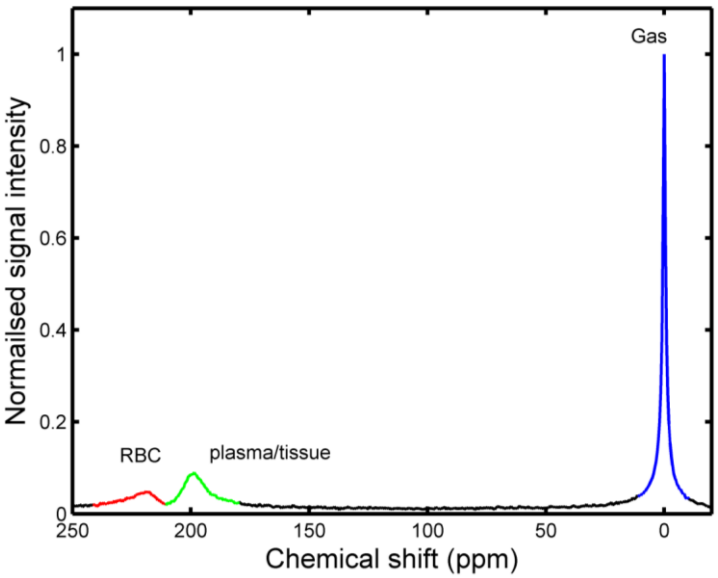

Figure 6.3: NMR spectrum of ^{129}Xe acquired from the human lungs after a hard pulse excitation centred 220 ppm away from the gas peak (depicted here as a large peak outlined in blue, with narrow spectral width). Spectral peaks associated with plasma/tissue and RBCs are an order of magnitude smaller and have broader linewidths (shorter T_2*s) than the ^{129}Xe-gas peak.

Two separate pulse-acquire sequences with inter-pulse delay times of 100 ms and 800 ms were used, and the effective flip angle excitation on the ^{129}Xe gas peak was determined to be 2.5° – see Fig. 6.4. For TR = 800 ms breath-hold experiments, 2048 samples were acquired at 3 kHz and 2048, corresponding to a spectral resolution of 1.46 Hz (0.04 ppm). To achieve TR = 100 ms, the number of samples had to be decreased to 128, reducing the spectral resolution to 0.7 ppm. A custom-built, flexible quadrature transmit/receive coil tuned to 35.32MHz was used (Clinical MR Solutions, USA). For detection of the dissolved-phase ^{129}Xe signal, 600 mL of hyperpolarised Xe gas topped up with N_2 to 1 L was administered via inhalation, from functional residual capacity, to two healthy male volunteers.

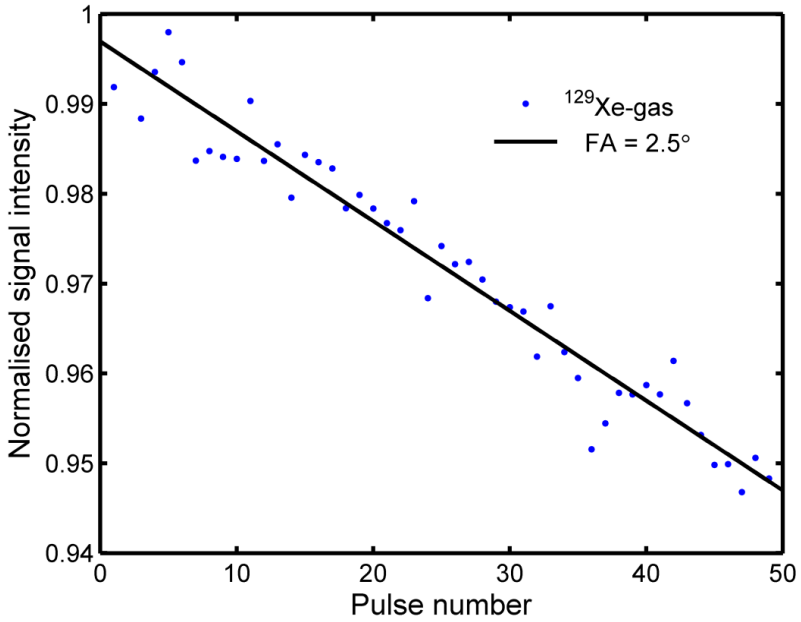

Figure 6.4: ^{129}Xe-gas resonance flip angle calibration for a hard pulse centred on the ^{129}Xe-dissolved resonance.

6.3 Results and discussion

6.3.1 *In vitro* calibration

The relationship between the chemical shift of ^{129}Xe and sO_2 of blood was calibrated in a controlled *in vitro* environment. NMR spectra were acquired immediately after mixing blood extracted from volunteers with hyperpolarised ^{129}Xe. The resonance frequency of ^{129}Xe dissolved in plasma was used as a reference as it was found not to vary as a function of blood oxygenation *in vitro*. Increasing RBC oxygenation causes an increase in the resonance frequency of ^{129}Xe dissolved in RBCs. The RBC-plasma peak separation increases from approximately 20.5 ppm, when the blood is in a completely deoxygenated state, to approximately 26 ppm when the blood is in a fully oxygenated state. This observed chemical shift vs. oxygenation behaviour is consistent when the same experiment is performed at magnetic field strengths of 1.5 T and 3 T. To quantify the change in RBC-plasma peak

separation, δ, as a function of blood oxygenation, the peak ^{129}Xe-RBC and ^{129}Xe-plasma locations, δ_r^0 and δ_p^0, were determined by fitting the spectra to Eq. 6.1. Blood gas analysis was performed immediately after acquiring the NMR spectra in order to quantify blood oxygen saturation, $s\mathrm{O}_2$. The extracted peak positions are plotted as a function of $s\mathrm{O}_2$ in Fig. 6.5, where it is observed that the chemical shift of ^{129}Xe in RBCs appears to be non-linearly dependent on the measured $s\mathrm{O}_2$, consistent with the previous observations of Wolber *et al.* [163] made over a smaller range of $s\mathrm{O}_2$ values. The data were fit to an empirical equation

$$\delta(\mathrm{sO}_2) = \alpha \exp(\beta s\mathrm{O}_2) + \delta_0 \,, \tag{6.2}$$

where α and β are empirical constants and δ_0 is the RBC-plasma peak separation in fully deoxygenated blood (see Fig. 6.5 below).

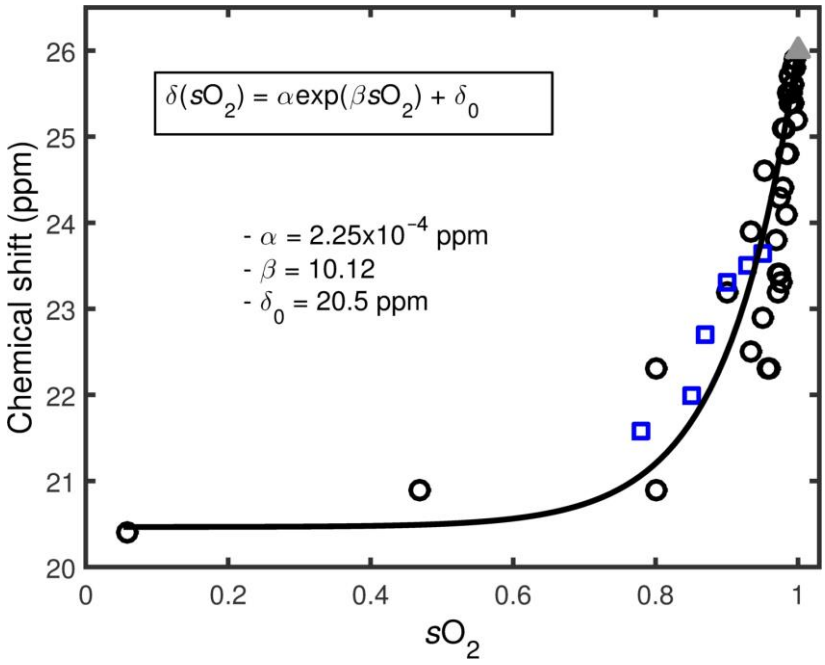

Figure 6.5: The separation between the RBC peak and the plasma peak plotted against the measured blood oxygen saturation, $s\mathrm{O}_2$. Data from two field strengths are denoted by black open circles (1.5 T) and blue open squares (3 T). The black line is a fit to the data using Eq. 6.2 and the grey triangle represents blood equilibrated with carbon monoxide (simulating fully oxygenated blood).

The similarity in the measured ^{129}Xe chemical shift values at 1.5 T and 3 T shown in Fig. 6.5 above suggests that the relationship between the ^{129}Xe chemical shift and blood oxygenation is not strongly affected by the static magnetic field strength.

The observation of a non-linear dependence of ^{129}Xe-RBC chemical shift on blood oxygenation in previous work [163] over a similar ^{129}Xe chemical shift range led to the hypothesis that this effect is a result of a co-operative binding mechanism of haemoglobin [164, 165]; conformational changes of the haemoglobin molecule after binding of each oxygen molecule may alter the Xe-haemoglobin binding affinity/binding locations (see ref. [120] and Section 5.2.4 for Xe-haemoglobin binding sites). As mentioned in Section 5.6, Coryell [137] found the bulk susceptibility of haemoglobin changed linearly as a function of sO_2, despite the conformational changes in the protein [120] caused by co-operative binding.

In addition, it was shown that a single haemoglobin molecule has the highest probability of being in one of the two states of extreme oxygen saturation. At half saturation ($sO_2 = 0.50$), haemoglobin with 1-3 bound oxygen molecules comprises only a third of the total population, with the bulk of the haemoglobin molecules being in one of two states – either completely saturated with 4 bound oxygen molecules, or desaturated with 0 bound oxygen molecules [137]. The net oxygen saturation, and thus the net magnetic susceptibility, is the ensemble average for the entire population. Furthermore, as noted previously [163], the size of the observed ^{129}Xe-RBC chemical shift (~6 ppm difference between oxy- and deoxyhaemoglobin) is larger than the 0.25 ppm chemical shift predicted by a model based on the difference in bulk magnetic susceptibility between the two extreme oxygenation sates [163]. Therefore, an alternative mechanism to bulk

susceptibility changes in haemoglobin must be driving the observed change in ^{129}Xe-RBC chemical shift with blood oxygenation.

6.3.2 ^{129}Xe-RBC chemical shift mechanisms

The resonance frequency of ^{129}Xe in solution is determined by the local magnetic field experienced at the nucleus, which is mediated by the screening or shielding constant, σ:

$$\omega_{\text{obs}} = \gamma B_{\text{eff}} \tag{6.3}$$

$$B_{\text{eff}} = (1-\sigma)B_0 \tag{6.4}$$

$$\omega_{\text{obs}} = \gamma(1-\sigma)B_0 \tag{6.5}$$

where ω_{obs} is the observed resonance frequency, γ the gyromagnetic ratio, B_0 the applied field and B_{eff} the effective field at the nucleus. Following the pioneering work by Buckingham *et al.* [166], it is known that the screening constant, σ, of a nucleus can be expressed as the sum of the screening constant of the individual nucleus, σ^0, and a term arising due to the presence of a solvent medium, σ_{m}, thus

$$\sigma = \sigma^0 + \sigma_{\text{m}} \tag{6.6}$$

$$\sigma_{\text{m}} = \sigma_{\text{a}} + \sigma_{\text{e}} + \sigma_{\text{w}} + \sigma_{\text{b}} \tag{6.7}$$

where σ_{a} is a contribution from molecular anisotropy effects, σ_{e} the polar effect caused by an electric field, σ_{w} due to the van der Waals forces between the solute and solvent and σ_{b} indicates the shielding arising from bulk magnetic susceptibility effects. $\sigma_{\text{b}} < 0$ for a paramagnetic susceptibility, leading to an increase of B_{eff} and hence ω_{obs}. For ^{129}Xe dissolved in solution at body temperature, the anisotropic and electric field terms are zero [167] leaving only the bulk susceptibility and van der Waals terms to contribute to the shielding constant.

As already mentioned in Section 5.6, oxyhaemoglobin is known to be diamagnetic ($\sigma_b > 0$), whereas deoxyhaemoglobin, with four unpaired electrons, has a significant paramagnetic moment ($\sigma_b < 0$). Thus, as RBC oxygenation increases, σ_b also increases and should result in a decrease in B_{eff} and a concomitant decrease in ω_{obs}. However, the chemical shift observed in the data presented here moves towards higher resonance frequencies with increasing oxygenation, opposite to that expected if bulk magnetic susceptibility were the principle mechanism.

This observation is in agreement with previous results, suggesting that the frequency shift in dissolved ^{129}Xe is dominated by the van der Waals shielding contribution, σ_w [168].

Stephen [169] has demonstrated that the van der Waals deshielding experienced by a nucleus within a solvent is proportional to the mean square electric field, $\bar{F}^2$, at that nucleus brought about by fluctuations among the electrons located on the neighbouring solvent molecules, i.e.:

$$-\sigma_w = B\bar{F}^2, \tag{6.8}$$

where B is the 'shielding hyperpolarisability' [170], which is large for ^{129}Xe, whose nucleus is surrounded by a large, easily deformed electron cloud. As a result of this high shielding hyperpolarisability, the chemical shift of dissolved ^{129}Xe in a solvent is very sensitive to small differences in the dispersion fields acting with liquid solvents.

The approach commonly used previously to correlate solvent-induced ^{129}Xe chemical shifts with $\bar{F}^2$ is to use a continuum model to describe the solvent [171, 172]. Specifically, the mean square field, $\bar{F}^2$, is equated to the square of the Bayliss-McRae function [172], $\bar{F}^2 \propto [g(n)]^2 = [(n^2-1)/(2n^2+1)]^2$, where n is the solvent index of refraction. More recently, Lim *et al.*, [173], studying the chemical shifts of ^{129}Xe in liquid haloalkanes, showed a linear

proportionality between the ^{129}Xe van der Waals shielding constant, σ_w, and the solvent refraction density ($\rho^R = (n^2 - 1)/(n^2 + 2)$). The refractive indices of oxyhaemoglobin and deoxyhaemoglobin have been recently measured in a study conducted by Zhernovaya *et al.* [174], wherein no significant difference between the refractive index of deoxygenated and oxygenated haemoglobin (within the visible range of the spectrum) was reported; the observed ^{129}Xe-RBC chemical shift change with blood oxygenation cannot, therefore, be predicted using the whole blood refractive index.

Experiments using Mössbauer spectroscopy [175] suggest that the electron cloud of haemoglobin is drawn towards the highly electronegative oxygen molecule in oxyhaemoglobin, but is more evenly distributed in deoxyhaemoglobin. As ^{129}Xe forms transient van der Waal bonds with haemoglobin, the net electron cloud is likely to become more distorted and pulled away from the ^{129}Xe nucleus while it is bound within the more electronegative oxyhaemoglobin state. This would act to reduce the van der Waals shielding, σ_w, and would generate a shift to higher dissolved ^{129}Xe resonance frequency, in agreement with the observed data. In addition to changes in the electronegativity of the haemoglobin molecules with blood oxygenation, the binding sites and locations of Xe, as discussed in Section 5.6, may be changing as the haemoglobin makes transitions between the oxy- and deoxyhaemoglobin states. As the extent of the shielding constant σ_w is strongly dependent on the separation between a nucleus and the molecules giving rise to fluctuating electric fields [170], changes in position would greatly alter the magnitude of the mean square field, $\overline{F}^2$, experienced by the ^{129}Xe nucleus within haemoglobin. Without accurate knowledge of the Xe binding sites in both forms of haemoglobin, a full description of the ^{129}Xe chemical shift changes with blood oxygenation is not possible here.

6.3.3 *In vivo* detection of ^{129}Xe-RBC chemical shift

To determine whether a similar shift in the resonance frequency of ^{129}Xe in RBCs could be detected *in vivo* as a potential probe for blood oxygenation, NMR spectra were acquired during breath-hold apnoea, which provides a simple model for blood oxygenation modulation.

Fig. 6.6 shows a waterfall plot of representative ^{129}Xe-dissolved spectra acquired as a function of time during one such experiment. The ^{129}Xe resonance located at 0 ppm corresponds to ^{129}Xe dissolved in parenchymal tissue and blood plasma and the resonance located downfield is from ^{129}Xe dissolved in RBCs.

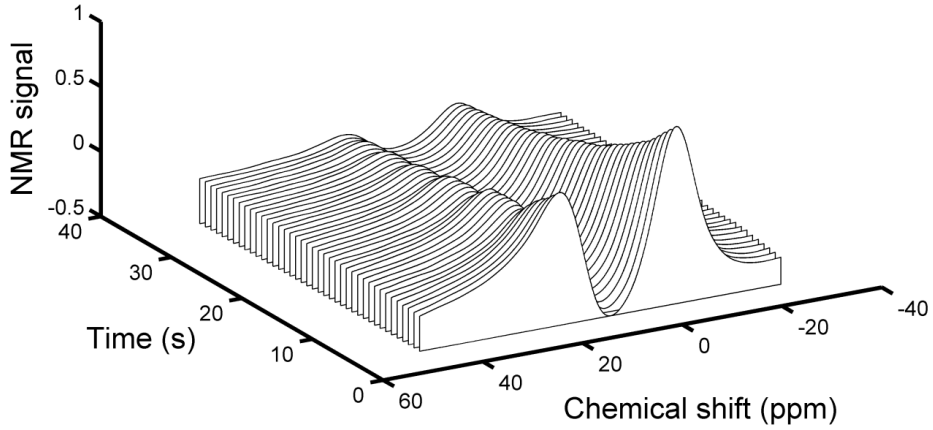

Figure 6.6: A waterfall plot of typical time series ^{129}Xe-dissolved spectra. The resonance at 0 ppm is ^{129}Xe dissolved in parenchymal tissue and blood plasma (TP) and the resonance downfield is from ^{129}Xe dissolved in RBCs. Each spectrum was acquired using a flip angle of 90° and a TR of 800 ms. The decay in both compartments follows approximately the T_1 relaxation (due to the presence of oxygen in the lungs and RF excitation) of the ^{129}Xe-gas, the magnetisation reservoir that acts to replenish the ^{129}Xe-dissolved signal between RF pulses.

For the experiments with a TR of 800 ms, the ^{129}Xe-TP signal decays monotonically over the breath-hold period (see Fig. 6.7). It is assumed that this signal decay follows the T_1 of the ^{129}Xe gas (dominated by the presence of paramagnetic oxygen in the lungs), which acts as a magnetisation reservoir, replenishing the ^{129}Xe-dissolved magnetisation in between RF pulses. With this assumption, a T_1 fit (corrected for ^{129}Xe-gas signal decay due to RF excitations of 2.5° on the ^{129}Xe-gas resonance) was performed on the decaying ^{129}Xe-TP signal, resulting in an approximate ^{129}Xe-gas T_1 value of 18.8 s, which is in good agreement with previously measured ^{129}Xe-gas T_1 values of ~20 s [15]. Although the ^{129}Xe-RBC signal decays with the same general rate, it does not decay monotonically; instead, it is modulated periodically over the breath-hold time (see Fig. 6.7).

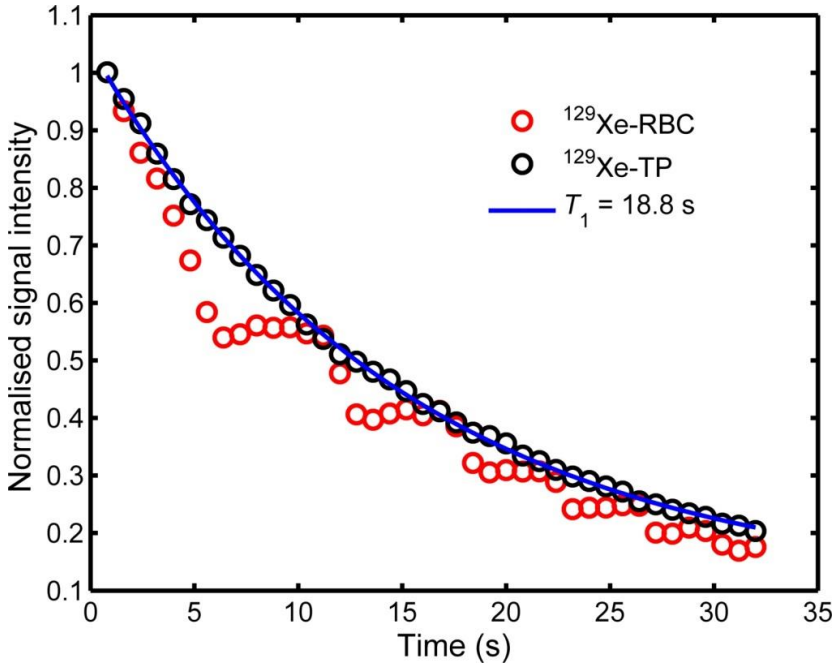

Figure 6.7: Decaying *in vivo* ^{129}Xe-dissolved signal in human lungs. The red and black circles represent ^{129}Xe in RBCs (^{129}Xe-RBC) and parenchymal tissue/blood plasma (^{129}Xe-TP), respectively. While the ^{129}Xe-TP signal decays monotonically, the ^{129}Xe-RBC signal does not. The blue line is an exponential fit to the decaying ^{129}Xe-TP signal, from which a ^{129}Xe-gas T_1 was estimated.

In order to view this oscillatory decay behaviour more clearly, the ^{129}Xe-RBC signal was normalised with the T_1 decay of the ^{129}Xe-gas polarisation reservoir (^{129}Xe-RBC data divided by the fitted exponential – see Fig. 6.8). The trough-to-peak time interval is ~4 s at the start of the breath-hold, reducing to ~2 s towards the end of the breath-hold.

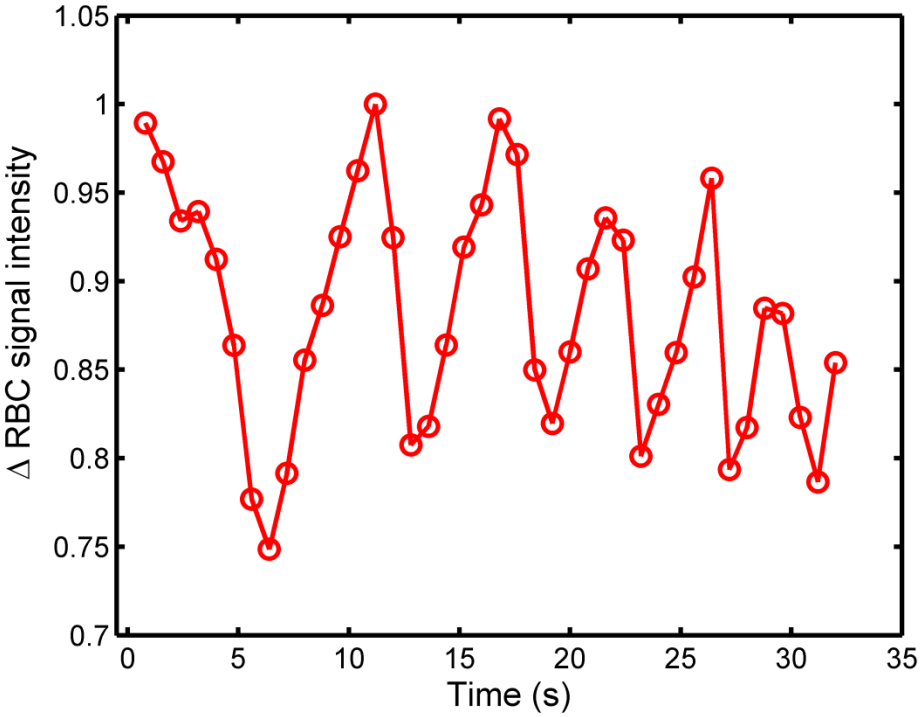

Figure 6.8: Modulation of the *in vivo* ^{129}Xe-RBC signal in healthy human lungs during breath-hold apnoea (^{129}Xe-RBC signal divided by fitted exponential in Fig. 6.7).

The ^{129}Xe-RBC resonance decreases by approximately 1 ppm over the breath-hold period (Fig. 6.9), whereas the ^{129}Xe-TP resonance remains fixed in position. As with the ^{129}Xe-RBC signal change, the ^{129}Xe-RBC chemical shift exhibited a periodic modulation, as shown in Fig. 6.10. Eq. 6.2 was then used to calculate blood oxygenation values from the measured *in vivo* chemical shift values, where it is estimated that the blood oxygenation decreases by ~5 % over the breath-hold period (Fig. 6.10).

Measurements of changes in oxygen partial pressure ($p\mathrm{O}_2$) as a function of breath-hold have been done in both animal and human lungs using hyperpolarised ^{3}He MR [176, 177]. It was shown in humans that over short breath-holds (< 40 s), the decrease in $p\mathrm{O}_2$ can be approximated by the linear relationship,

$$p\mathrm{O}_2 = p_0 - Rt \tag{6.9}$$

where R is the rate of oxygen decrease and p_0 is the initial $p\mathrm{O}_2$ [176]. In that study, R was calculated to be 1.9 mbar s^{-1} (1.43 mmHg s^{-1}). Assuming an initial lung $p\mathrm{O}_2$ of 105 mmHg for the volunteers in this study, Eq. 6.9 yields, after 30 s of apnoea, a $p\mathrm{O}_2$ value of 62 mmHg, which corresponds to an $s\mathrm{O}_2 > 0.90$ (from the oxygen haemoglobin dissociation curve shown in Fig. 5.3, Section 5.2.3), so that the low drop of ~5 % $s\mathrm{O}_2$ calculated in this study is not physiologically unrealistic.

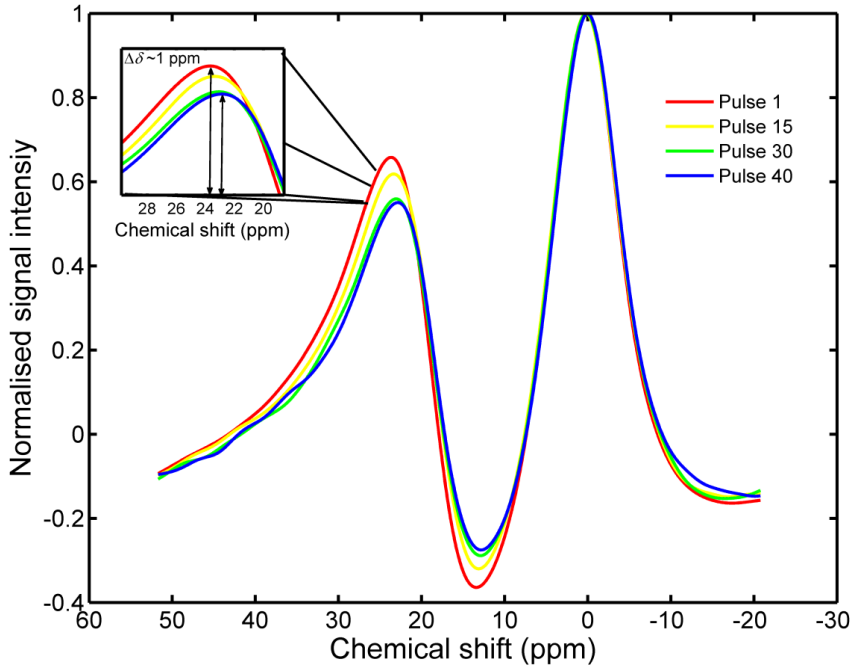

Figure 6.9: *In vivo* ^{129}Xe-dissolved spectra at different time points during the breath-hold. The ^{129}Xe-RBC chemical shift decreases by ~1 ppm throughout the breath-hold, whereas the ^{129}Xe-TP remains fixed in position.

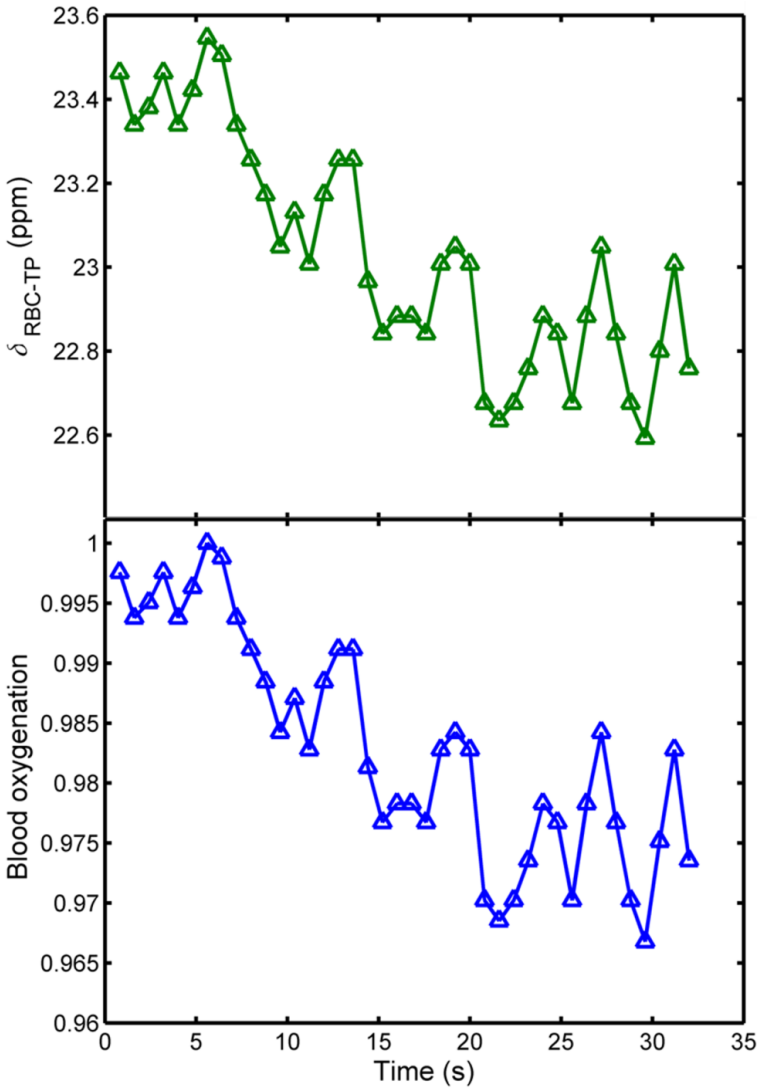

Figure 6.10: Top: ^{129}Xe-RBC chemical shift in human lungs over an *in vivo* breath-hold where a clear periodic motion is observed. Bottom: calculated blood oxygenation from the measured ^{129}Xe-RBC chemical shifts using Eq. 6.2.

As shown in Fig. 6.11, the blood oxygenation values calculated from the ^{129}Xe-RBC chemical shift oscillate over the breath-hold apnoea period at the same frequency as the ^{129}Xe-RBC signal amplitude modulation, with a 180° phase difference – i.e. the blood oxygenation maxima coincide with the ^{129}Xe-RBC signal minima – suggestive of a link between pulmonary oxygenation and ^{129}Xe-RBC signal changes.

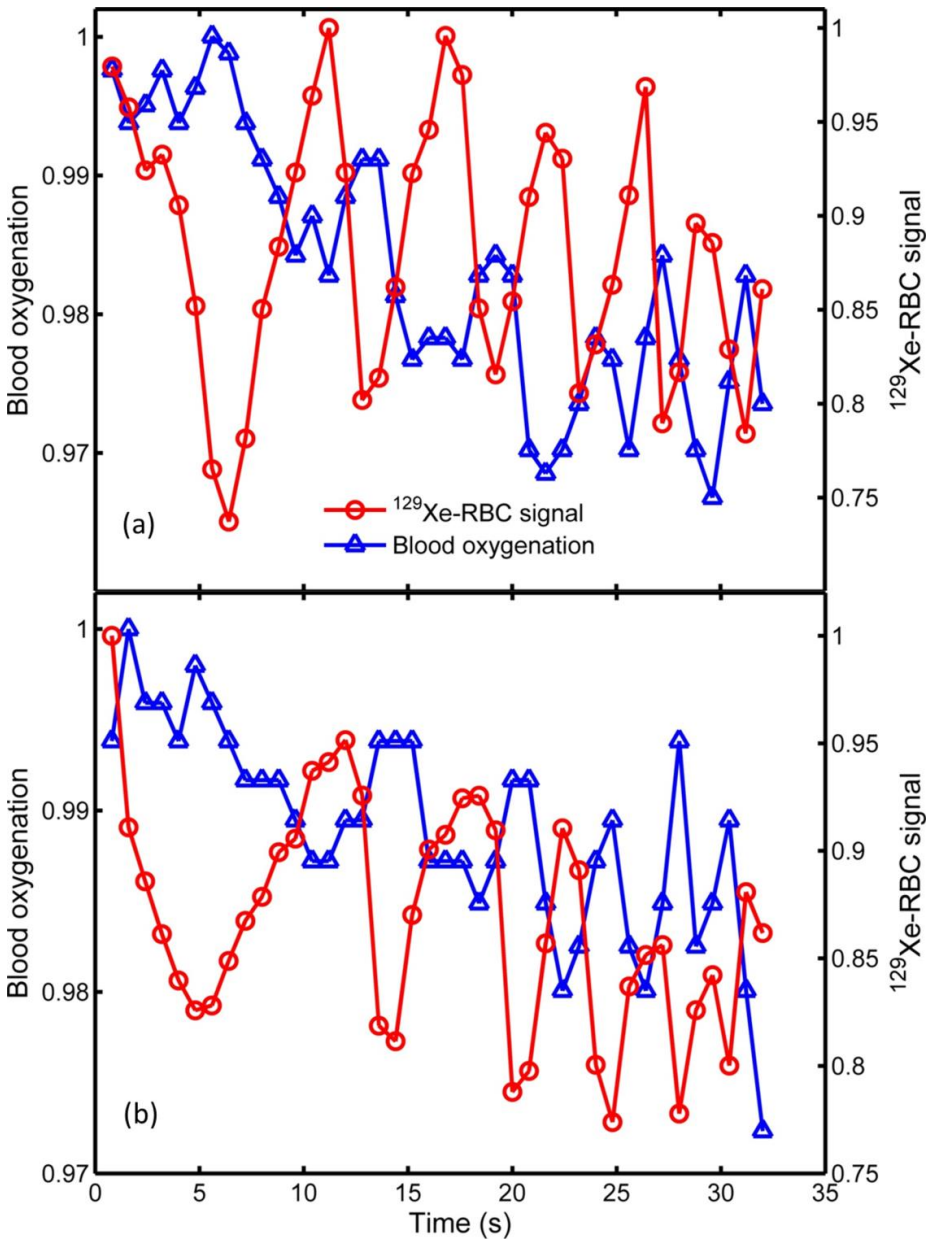

Figure 6.11: *In vivo* lung blood oxygenation and ^{129}Xe-RBC signal over breath-hold apnoea from two healthy volunteers, (a) and (b). The blood oxygenation and ^{129}Xe-RBC signal oscillate at the same frequency where the blood oxygenation maxima/minima coincide with ^{129}Xe-RBC signal minima/maxima.

Ruppert *et al.* [178] previously observed ^{129}Xe-RBC (and ^{129}Xe-TP) signal modulations (peak-to-peak signal times of ~1 s, TR of 100 ms), suggestive of a higher frequency component arising from cardiac pulsation. The experiment with increased temporal resolution performed here (TR = 100 ms), confirmed

the observations of Ruppert *et al.* [178] where the ^{129}Xe-RBC and ^{129}Xe-TP signals oscillate at rates of the same order as cardiac pulsation rates (Fig. 6.13). The signal oscillations shown in Fig. 6.11 thus most likely represent undersampling of the observed higher-frequency signal oscillation at TR = 100 ms (on the order of cardiac pulsation frequencies) shown in Figs. 6.12 and 6.13.

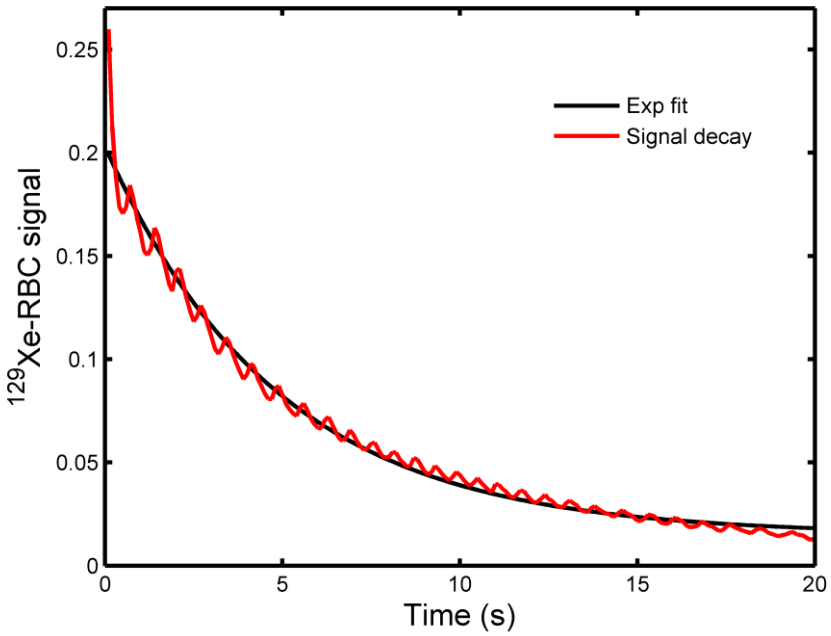

Figure 6.12: *In vivo* ^{129}Xe-RBC signal in the lungs as a function of breath-hold time for a TR of 100 ms.

For faster-sampled experiments at TR = 100 ms, the spectral resolution was limited to 0.7 ppm, which is not sufficient to spectrally discriminate changes in the ^{129}Xe-RBC chemical shift over the breath-hold. Cardiac-gated acquisitions may be a way in which to probe ^{129}Xe-RBC chemical shifts (blood oxygenations) at specific time points in the cardiac cycle to assess the feasibility of using ^{129}Xe NMR to track pulmonary blood oxygenation throughout the cardiac cycle.

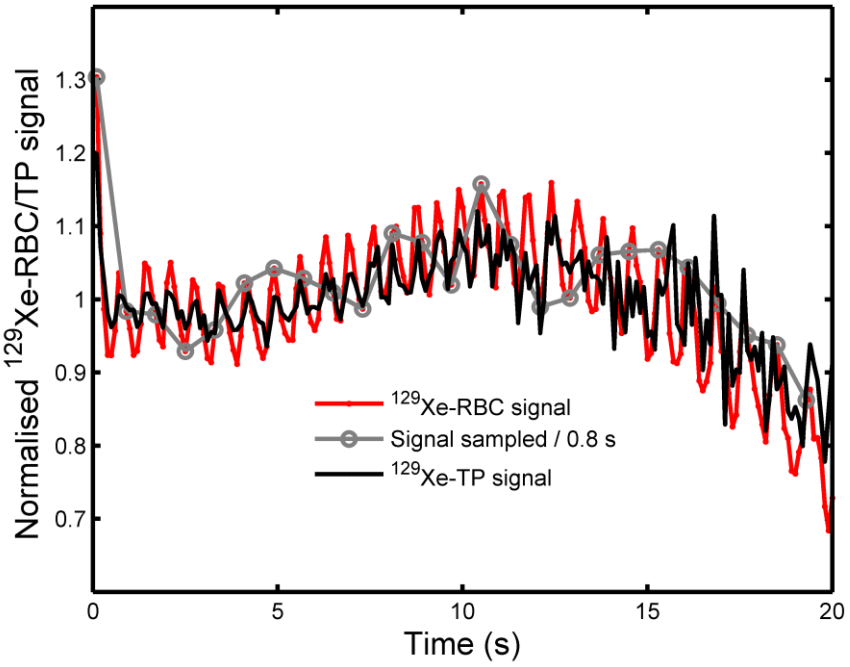

Fig 6.13: *In vivo* ^{129}Xe-RBC and ^{129}Xe-TP signal changes as a function of breath-hold time for TR = 100 ms normalised to the fitted exponential in Fig. 6.12. The grey line illustrates the effect of undersampling the higher-frequency oscillation observed for TR = 100 ms.

As well as providing a potential means of probing pulmonary blood, this dissolved ^{129}Xe spectroscopy technique may also have applications outside of the lungs. Mazzanti *et al.* [179] have recently shown that the signal of ^{129}Xe dissolved in the brain can be modulated in a manner responsive to stimulus, suggestive that a blood flow/perfusion component is at work. Moreover, dissolved ^{129}Xe spectra from the human brain have been successfully acquired [20], suggesting that ^{129}Xe can be detected in organs quite distal from the point of uptake in the lungs.

Finally, to help determine whether the underlying mechanisms driving the change in ^{129}Xe relaxation and ^{129}Xe-RBC chemical shift with blood oxygenation are related, a correlation plot of the variation of the two NMR parameters is shown in Fig. 6.14. The plot reveals that changes in ^{129}Xe $1/T_1$ and ^{129}Xe-RBC chemical shift are well correlated, with a coefficient of

determination of $R^2 = 0.82$. This suggests strongly that the underlying physical mechanism driving these observed changes in chemical shift and relaxation is the same. As the chemical shift and relaxation rate of ^{129}Xe in solvents is strongly dependent on inter-molecular separations, it is likely that oxygen-modulated Xe binding is largely responsible for the observed oxygenation dependencies.

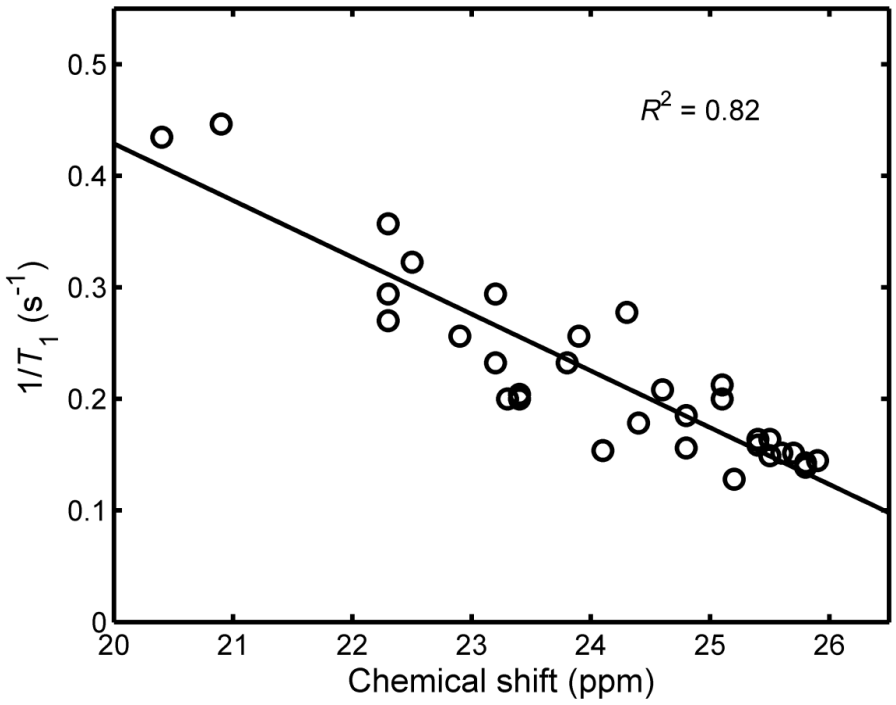

Figure 6.14: Correlation of ^{129}Xe relaxation rate, $1/T_1$, and ^{129}Xe-RBC chemical shift in whole blood samples for a range of blood oxygenations.

6.4 Conclusions

In this chapter, the feasibility of using hyperpolarised ^{129}Xe as an exogenous NMR probe of tissue oxygenation in humans has been explored. A non-linear relationship between the measured sO_2 values and the NMR resonance frequency of ^{129}Xe dissolved in RBCs has been observed *in vitro*. This

relationship was evaluated over the entire range of possible blood oxygenation values and appears to be independent of magnetic field strength.

Furthermore, this relation has been used to derive lung blood sO_2 values via *in vivo* dissolved ^{129}Xe whole-lung spectroscopy experiments conducted at breath-hold apnoea on a 3 T whole-body system. To date, we are not aware of any other means of non-invasively measuring this important physiological parameter. The common modulation frequency of blood oxygenation and ^{129}Xe-RBC signal change is interesting and further work with cardiac gating is underway to understand this newly observed phenomenon with hyperpolarised ^{129}Xe.

Chapter 7

Conclusions

This thesis involved the characterisation and optimisation of hyperpolarised ^{129}Xe production on a continuous-flow spin-exchange optical pumping ^{129}Xe polariser and NMR experiments with hyperpolarised ^{129}Xe dissolved in human blood (*in vitro* and *in vivo*). The original work completed in this thesis can be summarised by the following findings:

- A continuous-flow ^{129}Xe spin-exchange optical pumping polariser with a moderate incident power of 25 W from an external cavity diode laser (ECDL) was optimised to enable good-quality lung images with low doses (300 mL) of hyperpolarised ^{129}Xe. Measurements of ^{129}Xe polarisation as a function of gas flow rate through the SEOP cell, along with a polarisation model of accumulating frozen ^{129}Xe (using a measured T_1 of ~90 minutes for ^{129}Xe snow in the cryostat), enables extrapolation of the optimum gas flow rate to use for a given desired volume of ^{129}Xe.
- The optical input was changed from the external cavity diode array to a more powerful (50 W incident) and compact laser diode array with internal volume holographic gratings and an integrated optical train (LDA-VHG OT) for improved beam collimation. The

maximum attainable polarisation during gas flow (100 sccm) was increased from ~15 % using the ECDL to ~45 % using the LDA-VHG OT. Whereas a breakdown in agreement between theoretical and experimental ^{129}Xe polarisations was observed for the ECDL, good agreement between experiment and theory was observed with the LDA-VHG OT, even at low flow rates. At high input laser power (100 W), increased photon absorption and a decrease in NMR signal measurements suggested Rb runaway (laser heating) effects. To mitigate laser heating, work is underway to incorporate a Rb presaturator into the SEOP optical cell. In addition, based on Xe production maps, it was shown that large volume cells (~2000 mL) are needed (to increase the Xe gas residency time and thus ^{129}Xe polarisation as gas exits the SEOP cell into the cryostat) to achieve high ^{129}Xe polarisation for fast gas flow rates. Therefore, as well as incorporating an Rb presaturator, work is underway to scale up the cell volume from 500 mL to 2000 mL.

- A series of *in vitro* Xe-blood dissolution experiments were performed to characterise the NMR parameters underpinning ^{129}Xe relaxation and exchange dynamics in human blood. A non-linear increase in the ^{129}Xe relaxation rate with decreasing blood oxygenation was established. From a two-site exchange model, 10 constants describing ^{129}Xe NMR relaxation and exchange in isolated red blood cells (RBCs) and isolated plasma, as well in whole blood samples were determined. Knowledge of these constants should provide a sound experimental basis for experiments involving modelling of the signal dynamics of ^{129}Xe as it travels in the blood from lungs to distal tissues.
- A non-linear relationship between ^{129}Xe-RBC chemical shift and blood oxygenation was established *in vitro* on 1.5 T and 3 T clinical

scanners. This relationship was used to calculate pulmonary blood oxygenations from ^{129}Xe-RBC chemical shift NMR measurements *in vivo* during breath-hold apnoea on a 3 T clinical scanner. In addition, a correlation between ^{129}Xe-RBC signal changes and blood oxygenation changes (both found to modulate with a common frequency) was observed in two separate healthy volunteers. This warrants further investigation, and cardiac-gated ^{129}Xe spectroscopy is currently underway to ascertain the feasibility of using hyperpolarised ^{129}Xe spectroscopy to monitor blood oxygenation at specific time points within the cardiac cycle. To date, we are not aware of any other means of non-invasively measuring *in situ* pulmonary blood oxygenation.

Appendix A

ECDL alignment standard operating procedure

A.1 Optical apparatus

This document describes the procedure for re-alignment of the optical elements for the external cavity diode laser (ECDL) as shown below. Alignment should be carried-out at least every 6 months. In the current arrangement, 1/3 of the laser power should be reflected down the optic axis by the beam-splitter, and 2/3 transmitted to the cell.

A.2 Initial measurements

i) Prior to any measurements with the laser, the water chiller/cooler should be started (flick the on switch and press start). This ensures the laser diode is kept cool whilst in operation. Allow 20–30 minutes for the chiller to reach a temperature of 28.5 °C.

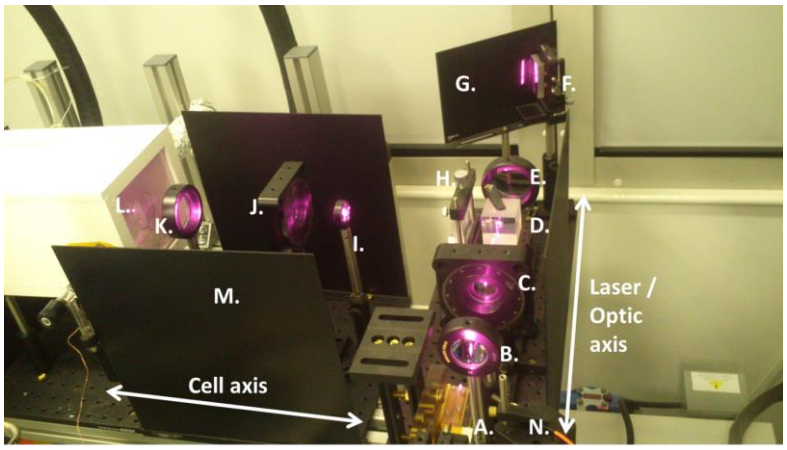

Figure A.1: arrangement of optical elements for the ECDL. A. Laser diode; B. Lens 1 (plano-convex); C. Half wave plate; D. Polarising beam-splitting cube; E. Lens 2 (plano-convex); F. Holographic grating; G. Back screen; H. Lens 3 (cylindrical lens); I. Lens 4 (bi-convex lens); J. Quarter wave plate; K. Lens 5 (plano-convex); L. Cell; M. Side screen (of which there are 3); N. Optical fibre.

ii) Before moving any optical elements, as a reference point, the transmitted laser power down the cell axis should be measured using the power meter. For this, the laser should be turned on with the operating current set to 90A. It will take approximately 5 minutes for the laser temperature to stabilise at around 44 degrees. The power meter should be held as close to the cell as possible (as shown in Figure 2), to provide an estimate of the power incident on the cell. Note: The wavelength of light should be set to 795nm in the settings on the power meter control.

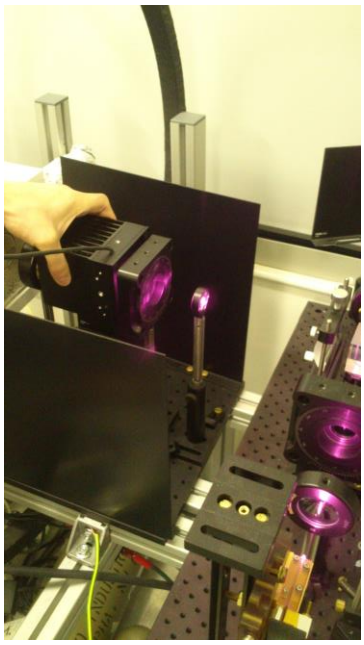

Figure A.2: Measurement of the laser power after the laser beam has passed through all the optical elements. This gives an approximate idea of the power delivered to the cell.

A.3 Alignment down the external cavity

The principle aim of this stage is to ensure that the laser beam position at the end of the optic axis (back screen) is coincident with the centre position of the cell. Before moving any optical elements, the laser should be switched off (leaving the cooler on).

i) "Drop" all the optical elements along the optic axis (elements B to E – see Fig A.1). Hold the top of each element, whilst slowly turning the screw on the side of the base of the element (anticlockwise to loosen). When loose, lower the element so that it sits on the base. Note: Lens 2 may not drop low enough, and therefore should be completely removed from its base.

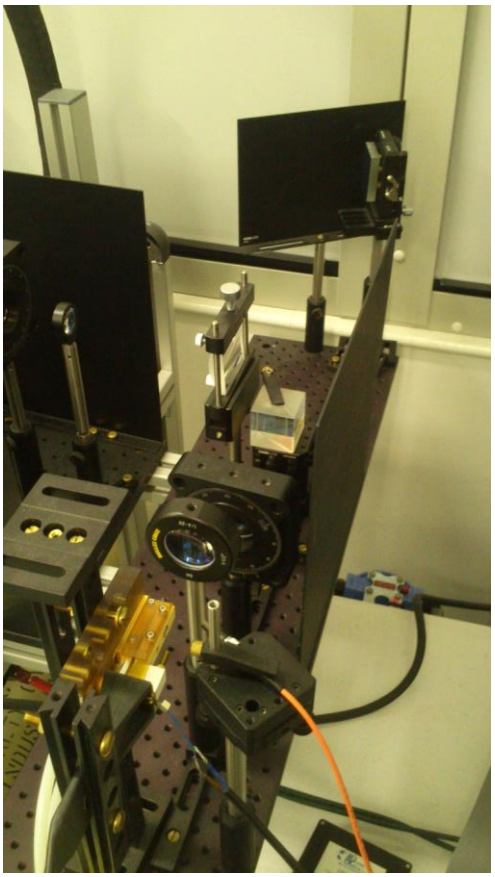

Figure A.3: "Dropping" the optical elements. The laser light now passes directly over the top of these elements, straight onto the grating / screen.

ii) Record the height of the centre of the cell (as measured from the optical bench – see Fig. 4) with a ruler; an accuracy of $\pm$ 5mm is sufficient. Note: the centre of the cell *does not* coincide exactly with the position of the inlet and outlet lines.

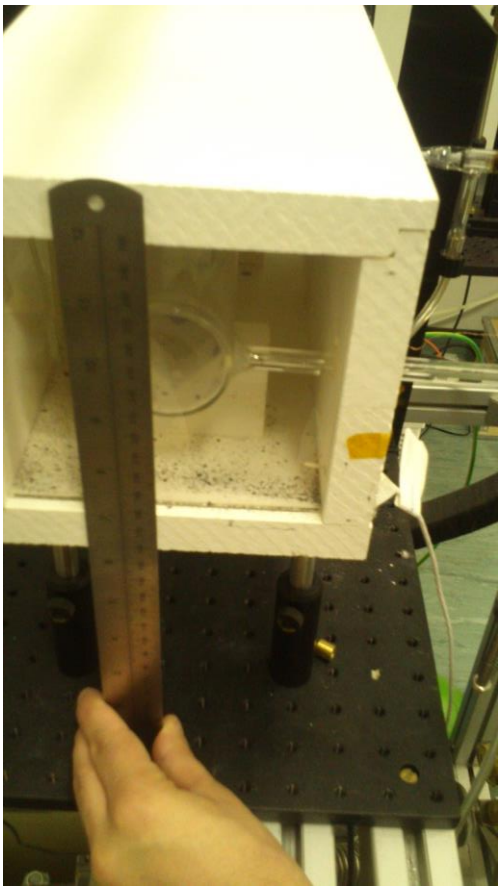

Figure A.4: Recording the height of the centre of the cell, with reference to the optical bench.

iii) Place a piece of masking tape roughly in the centre of the back screen (Fig. 5). Using the ruler, mark the height of the cell on the masking tape with a marker pen. At this point, the holographic grating should be removed, by unscrewing from its base. The back screen can then be rotated such that it lies exactly perpendicular to the optic axis.

iv) For convenience, remove the side screen on the right of the optic axis (see Fig 1), by unscrewing (anticlockwise) from the optical bench. This will allow better access to the optical elements. For laser alignment, the laser can now be operated at low power, (set the operating current to e.g. 25A or 30A, and turn the laser back on).

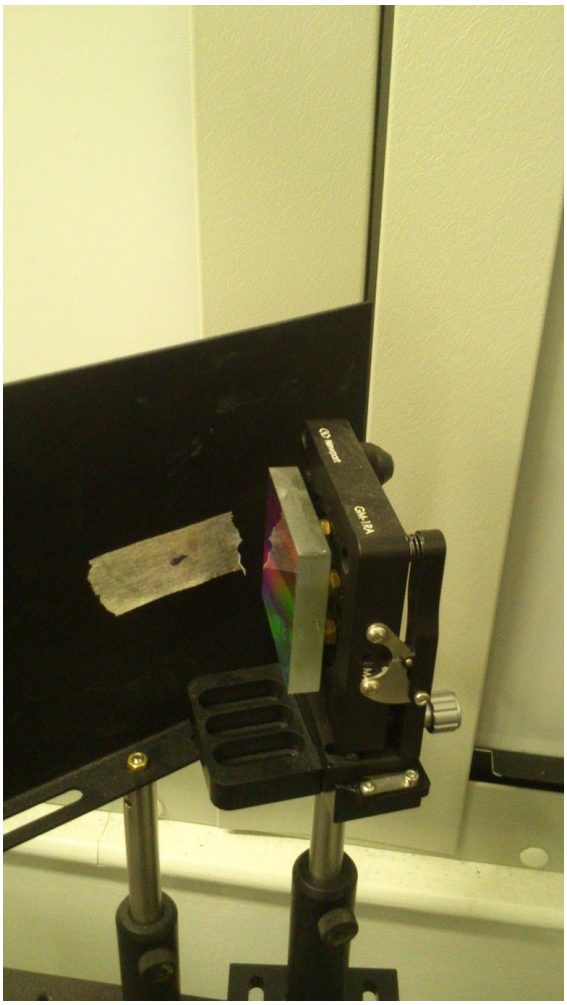

Figure A.5: Mark the cell height on the back screen, such that the position of the laser beam can be precisely aligned with the cell in the vertical direction.

v) During alignment, it is practical to focus on one piece of apparatus at a time (working with more than one at the same time will provide complications, as altering one piece of apparatus can affect another). Starting with lens 1, lift the lens into the path of the laser beam, and see how the height of the lens affects the position of the beam on the back screen (drop your goggles and carefully view the beam on the back screen). This lens principally controls the height of the beam, and so it should be adjusted until the centre of the beam on the back screen is aligned with the cell height

mark (its position along the optic axis can also be adjusted if required by unscrewing the base piece and sliding it along the optical bench).

vi) Lens 2 focusses the beam onto the grating. Mount this lens back into position and view how its height and position along the optical axis affects the position and appearance of the laser beam on the back screen.

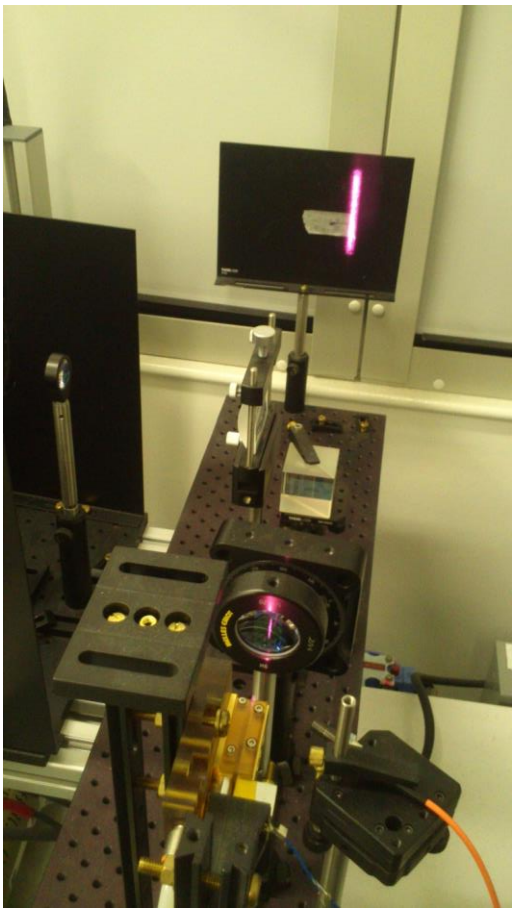

Figure A.6: The laser beam passing through the first lens at low power. The vertical position of this lens should be adjusted so that the beam passes through the glass part of the element (i.e. there are minimal losses from light hitting the periphery of the element). However, some losses cannot be avoided and it is more important to align the beam height correctly with that of the centre of the cell.

The position of lens 2 should be altered until the individual diode bars from the laser can be clearly seen on the back screen. Moving this lens will affect

the focus / resolution of these bars. By unscrewing the base of this element, its position along the optic axis can be altered. A compromise should be achieved between minimal loss at the optic (due to light not passing exactly through the centre of the lens) and optimum resolution of the diode bars on the screen.

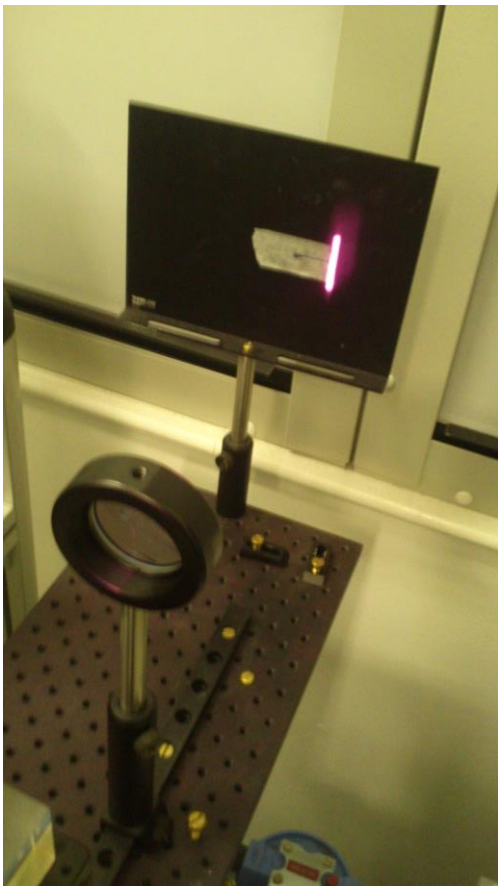

Figure A.7: After passage through the second lens, the vertical extent of the laser beam on the back screen is reduced. Also, the individual diode bars should become focused.

vii) For reference, take a power measurement at the end of the optic axis by holding the power meter in front of the back screen. This should still be done at low power (driving current of ~30 A)

This step can be repeated after alignment of each subsequent optical element, by placing the power meter immediately after that element.

viii) Turn off the laser and rotate the back screen to approximately its original position. Mount the holographic grating back into position. As shown in Fig 8, the angle of the face of the grating, to the optic axis, is fairly small. The height of the grating should be such that the mark on the masking tape lies roughly in the centre (vertically) of the element.

Figure A.8: After fixing the base of the holographic grating, it should be rotated within its base until the reflected and transmitted laser beams are concordant. (To do this, unscrew the element from its base my turning the screw on the side of the base anticlockwise. Two pieces of paper should be positioned so that the beam from the laser passes through central space, and then the reflected beam position can be viewed on the back of the paper by dropping your goggles. Twist the grating until the reflected beam cannot be seen on the paper (i.e. it is passing back through the central space), and then secure it to its base.

To ensure the position of the laser beam reflected from the grating (along the cell axis direction), is coincident with the beam from the laser, the laser should firstly be activated at low power (~25 A current). Doing this at high laser powers could cause damage to the laser, if a large power is reflected back toward the diode. Two pieces of paper should be positioned as in Fig 8, such that there is a narrow gap which the beam from the laser can pass through. The beam reflected off the grating should be aligned with the first laser beam, by rotating the grating about its base until the beam passes back through the space between the papers. It is best to do this with two people. Note: at this stage only an approximate alignment of the grating is required (i.e. ensure that the beam is well-collimated with respect to the external cavity).

ix) Finally, raise the half wave-plate and secure into position such that the laser beam passes through the centre of the element. The position along the optic axis need not be changed.

A.4 Alignment along the cell axis

i) Raise the beam-splitting cube and ensure that the transmitted and reflected laser beams pass through the cube close to the centre. Change only the height of the cube, and its orientation angle so that the edges of the cube are parallel to both optic and cell axes.

ii) Lower the optical elements along the cell axis, except lens 3 (i.e. drop elements I, J, K). This can be done in the same way as the other elements (removing them from the base if necessary). For easy access to the elements, the side screen marked M in Fig 1 may be removed. Turn on the laser to a low power, e.g. current of 25 A, for alignment.

iii) The purpose of lens 3 is to focus the laser beam reflected down the cell axis into a small spot (it is a convergent lens). The size of the spot should be smaller than the glass region of lens 4. If the spot is not aligned with the cell, its height may be altered by raising or lowering this lens, however it is best to align instead with lens 4 also raised.

iv) Raising lens 4, the heights of lenses 3 and 4 can be changed to minimise losses (reflections, or parts of the laser beam impinging outside the glass regions) at each element. Lens 4 is a divergent lens, changing the spot into a circular beam shape for passage through the quarter wave plate. The position of lens 4 along the cell axis should be altered until it is coincident with the focal point of lens 3 (i.e. the spot is focused to its smallest size when it hits this lens). The principle aim after alignment down the cell axis is that the laser beam incident on the cell should be uniformly distributed in a circular beam shape, such that the whole diameter of the cell is filled with the extent of the beam.

v) The position of lens 5 should not need to be altered from where it was initially, simply its height should be adjusted so that the losses at this element are minimal. Lens 5 alters the beam shape such that it fills the diameter of the cell. It produces light parallel to the cell axis (i.e. not divergent or convergent).

vi) Adjust height and position along the cell axis of lens 4 (loosen the base of the element, so it is free to move along the optical bench). Holding paper in front of the cell (as shown in Fig. A.8), check the alignment of the beam reflected from the beam-splitter, and adjust if necessary the orientation of the beam-splitter, and the position of lens 4.

The paper will display the extent of the beam falling outside of the cell, allowing easy correction by rotating the beam-splitter.

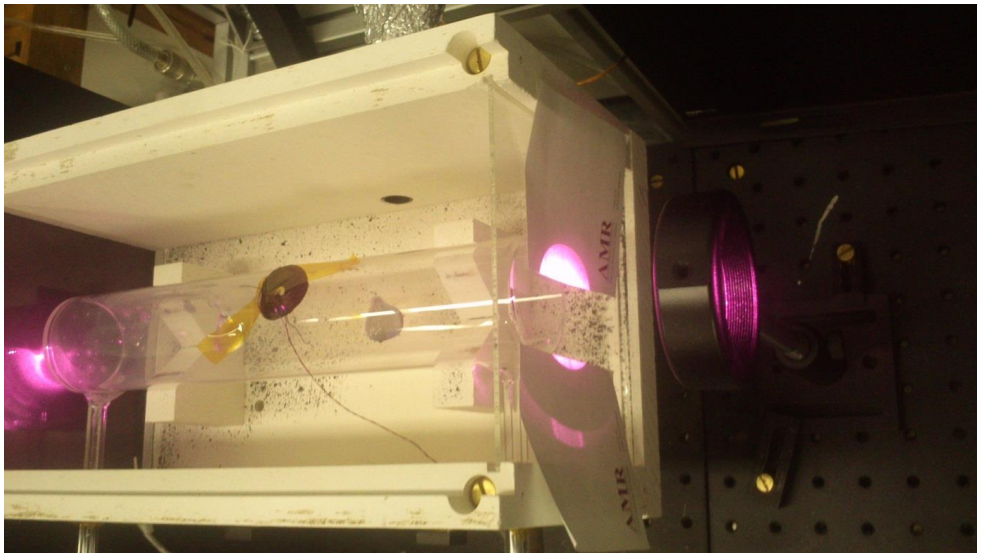

Figure A.9: Ensure that the circular laser beam encompasses the whole cell diameter. The position of the beam in the horizontal plane can be viewed by holding paper either side of the cell. This is the easiest method to determine any misalignment of the beam-splitting cube.

vii) Finally, mount the quarter waveplate and adjust its height until the laser beam passes through the centre of the element. Some losses at this element will be inevitable, but it may be useful to alter lenses 3 or 4 to fine-tune the alignment. The paper technique can be utilised to see exactly how much of the laser beam falls outside of the optically active region of the wave-plate.

A.5 Fine-tuning of the holographic grating

Now that all elements have been aligned, the emission profile of the laser must be correctly centred on the wavelength of choice, i.e. the Rb D1 line, at 794.77nm. This is done by carefully adjusting the position and orientation of the holographic grating at low laser powers. This process may be the most difficult and time-consuming, as the grating is the most sensitive element in the optical apparatus. Again this process requires two people.

i) Ensure that the centre frequency of the Ocean Optics spectrometer is at 794.77 nm. At a driving current of 90 A, it should be possible to have a narrow emission from the ECDL, centred on this wavelength.

ii) Working at a low laser power (25 A current), alter the position of the base of the holographic grating until the laser beam from the diode array lies on the grating surface. If any part of the laser beam is missing the grating surface, it can be seen on the back wall or back screen. After fixing the base in position (by tightening the screws to clamp it down), the element should be rotated about its base, such that the reflected and incident beams are concordant. This process is essentially a repeat of step (viii) in Section A.3, with the addition of using the Ocean Optics spectrometry software (the optical fibre picks up scattered light from the optical apparatus). Whilst rotating the grating as above, the software display should be monitored, since a narrow emission will be seen only when the two beams are aligned. (Otherwise a rather broad emission, spanning many nanometres, will be observed.)

iii) After both of these adjustments, if narrow emission is observed, the grating should be secured into position. This must be carefully done, as tightening the grating may itself shift the position such that a narrow emission is no longer observed. Note: The emission will still be far from resonance, since the laser power is very low.

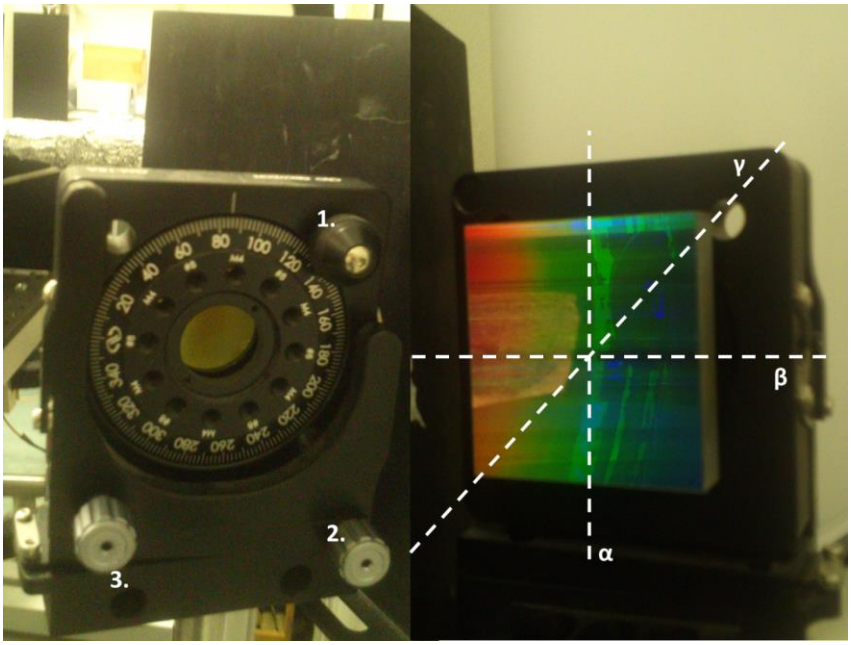

Figure A.10: The controls for adjusting the position and orientation of the holographic grating in three dimensions. Left: 3 principle dials for control over the grating; Right: axes about which the grating can be manoeuvred. Dial 1 requires an Allen key to use, and rotates the grating about the γ axis (this axis is perpendicular to the face of the grating as shown). Dial 2 acts as a fine tune to the feedback along the optic axis. It rotates the grating about the α axis (essentially performing the same action as rotating the whole element about its base). Dial 3 rotates the grating about the β axis and can be used to alter the lineshape of the laser emission, however is not used in practice on a regular basis.

vi) After the element is secured into position, the laser driving current should be increased to 90A. If the beam is close to resonance, dial 2 can be used for fine-tuning of the laser wavelength. At this stage it is unlikely that dials 1 or 3 are required. The grating, when optimised, should look as shown in Fig A.10. Note: If the grating is far off-resonance or does not produce a narrow emission, it is important to go back to step (ii) and adjust the position of the base and the orientation about the α axis, before returning to fine-tuning.

Appendix B

Publication list

B.1 Publications arising from this Thesis

Journal articles

1. **G. Norquay**, G. Leung, N. J. Stewart, G. M. Tozer, J. Wolber, and J. M. Wild, "Relaxation and exchange dynamics of hyperpolarized ^{129}Xe in human blood," *Magn. Reson. Med.* DOI: 10.1002/mrm.25417, 2014

2. **G. Norquay**, S. R. Parnell, X. Xu, J. Parra-Robles, and J. M. Wild, "Optimized production of hyperpolarized 129Xe at 2 bars for *in vivo* lung magnetic resonance imaging," *Journal of Applied Physics,* vol. 113, p. 044908, 2013.

Book chapters

1. **G. Norquay,** J. Wolber, and J. M. Wild, "129Xe chemical shift and spin-lattice relaxation dependences on blood oxygenation," in: *Hyperpolarized Xenon-129 Magnetic Resonance (Concepts, Production, Techniques and Applications)*, Chapter XX, 1st Edition, Royal Society of Chemistry, in press, 2015.

Refereed abstracts

1. **G. Norquay**, N. J. Stewart, J. M. Wild, "High 129Xe polarisation (80%) on a home-built SEOP system," *Proceedings of PiNG 14, École de Physique des Houches, France*, (Sept–Oct 2014). Poster presentation.

2. **G. Norquay**, N. J. Stewart, G. Leung, J. Wolber, J. M. Wild, "129Xe chemical shift and spin-lattice relaxation dependence on blood oxygenation," *Proceedings of PiNG 14, École de Physique des Houches, France*, (Sept–Oct 2014). Oral presentation.

3. **G. Norquay**, G. Leung, N. J. Stewart, G. M. Tozer, J. Wolber, and J. M. Wild, "Revisiting the ^{129}Xe relaxation rate in human blood and quantifying the relaxivity of deoxyhaemoglobin in the presence of ^{129}Xe," *Proceedings of the 22nd Annual Meeting of ISMRM, Milan, Italy*, 2292, (May 2014). Poster presentation and 1st prize winner of hyperpolarized noble gas study group poster competition.

4. **G. Norquay** and J. M. Wild, "Laser absorption and photon efficiency of a spin-exchange optical pumping ^{129}Xe polariser," *Proceedings of the 21st Annual Meeting of ISMRM, Salt Lake City, UT, USA*, 1477 (April 2013). Poster presentation and ISMRM Educational Stipend.

5. **G. Norquay**, G. Leung, G. M. Tozer, J. Wolber, J. M. Wild, "^{129}Xe-RBC T1 dependence on blood oxygen saturation," *Proceedings of the 21st Annual Meeting of ISMRM, Salt Lake City, UT, USA*, 1998 (April 2013). Poster presentation and ISMRM Educational Stipend.

6. G. Leung, **G. Norquay**, J. M. Wild, "^{129}Xe as a probe for MR oximetry," *Proceedings of the 21st Annual Meeting of ISMRM, Salt Lake City, UT, USA*, 0816 (April 2013). Oral presentation.

7. G. Leung, **G. Norquay**, J. Wolber, J. M. Wild, "Chemical shift of ^{129}Xe is dependent on red blood cell oxygenation," *Proceedings of the 21st Annual Meeting of ISMRM, Salt Lake City, UT, USA*, 1929 (April 2013). Poster presentation.

8. **G. Norquay**, S. R. Parnell and J. M. Wild, "A polariser for on demand production of hyperpolarised 129Xe for human lung MRI," *Proceedings of the European Respiratory Society, Barcelona, Spain,* (September 2013). Poster presentation.

9. **G. Norquay**, "^{129}Xe SEOP polarizer performance and applications in magnetic resonance," *Proceedings of the Annual BRSG Institute of Physics Conference*, *Rutherford Appleton Laboratory, Oxford*, *UK* (July 2013). Invited speaker.

10. G. Leung, **G. Norquay**, J. Parra-Robles, J. M. Wild, "Measuring red blood cell oxygenation *in vivo* using hyperpolarized 129Xe MRI," *Proceedings of the European Respiratory Society, Vienna, Austria,* (September 2012). Oral presentation.

11. **G. Norquay**, S. R. Parnell, X. Xu, J. Parra-Robles, J. M. Wild, "Optimised production of hyperpolarised ^{129}Xe for *in vivo* lung MRI at 2 bars," *Proceedings of the 4th International Symposium of XeMAT, Dublin, Ireland*, (June 2012). Oral presentation.

12. G. Leung, **G. Norquay**, J. Parra-Robles, J. M. Wild, "Chemical shift of dissolved ^{129}Xe in red blood cells *in vivo*," *Proceedings of the 4th International Symposium of XeMAT, Dublin, Ireland*, (June 2012). Oral presentation.

13. **G. Norquay**, S. R. Parnell, X. Xu, M. H. Deppe, G. M. Tozer, J. M. Wild, "Optimisation of xenon flow rate in spin exchange optical pumping for high polarisation high volume ^{129}Xe MRI," *17th Annual Meeting of the British Chapter of ISMRM, Manchester, UK*, (September 2011). Poster presentation and BC-ISMRM Student Stipend.

14. **G. Norquay**, S. R. Parnell, G. M. Tozer, J. M. Wild. "Dissolved-Phase Hyperpolarised ^{129}Xe relaxation times at different field strengths," *Cancer Imaging Conference*, *London, UK*, (April 2011). Poster presentation.

B.2 Other publications

Journal articles

1. F. C. Horn, B. A. Tahir, N. J. Stewart, G. J. Collier, **G. Norquay**, G. Leung, R. H. Ireland, J. Parra-Robles, H. Marshall, J. M. Wild, "Lung ventilation volumetry with same-breath acquisition of hyperpolarized gas and proton MRI," *NMR in Biomedicine,* vol. 27, pp. 1461-1467, Dec 2014

2. N. J. Stewart, G. Leung, **G. Norquay**, H. Marshall, J. Parra-Robles, P. S. Murphy, R. F. Schulte, C. Elliot, R. Condliffe, P. D. Griffiths, D. G. Kiely, M. K. Whyte, J. Wolber, J. M. Wild, "Experimental validation of the hyperpolarized 129Xe chemical shift saturation recovery technique in healthy volunteers and subjects with interstitial lung disease," *Magn. Reson. Med.* DOI: 10.1002/mrm.25400, 2014

3. G. Leung, **G. Norquay**, R. F. Schulte, J. M. Wild, "Radiofrequency pulse design for the selective excitation of dissolved ^{129}Xe," Magn. Reson. in Med. DOI:10.1002/mrm.25089, 2014.

4. J.M. Wild, H. Marshall, X Xu, **G. Norquay**, S. R. Parnell, M. Clemence, P. D. Griffiths, J. Parra-Robles. Simultaneous imaging of lung structure and function with triple-nuclear hybrid MR imaging. Radiology, vol. 267, pp. 251-255, Apr 2013.

5. X. Xu, **G. Norquay**, S. R. Parnell, M. H. Deppe, S. Ajraoui, R. Hashoian, J. M. Wild. Hyperpolarized ^{129}Xe gas lung MRI-SNR and T_2^* comparisons at 1.5 T and 3 T. Magnetic Resonance in Medicine, vol. 68 pp. 1900-1904, Dec 2012.

Refereed abstracts

1. N. J. Stewart, **G. Norquay**, J. Parra-Robles, H. Marshall, G. Leung P. S. Murphy, R. F. Schulte, C. A. Elliot, R. Condliffe, C. G. Billings, I. Smith, P. D. Griffiths, J. Wolber, M. K. B. Whyte, D. G. Kiely, J. M. Wild, "P273 Assessment Of Lung Microstructure In

Interstitial Lung Disease With Hyperpolarised Gas MRI," *Proceedings of British Thoracic Society, London, UK,* (December 2014). Poster presentation.

2. M. Rao, N. J. Stewart, **G. Norquay**, J. M. Wild, "Spectroscopy of dissolved 129Xe in the human brain at 1.5T," *Proceedings of PING 14*, *École de Physique des Houches, France*, (September to October 2014). Oral presentation.

3. N. J. Stewart, **G. Norquay**, J. M. Wild, "Feasibility of Human Lung Ventilation MR Imaging using Naturally-Abundant 129Xe with Optimised 3D SSFP," *Proceedings of PING 14*, *École de Physique des Houches, France*, (September to October 2014). Oral presentation.

4. N. J. Stewart, **G. Norquay**, H. Marshall, J. M. Wild, "Feasibility of high quality lung MRI with naturally-abundant hyperpolarized ^{129}Xe," *Proceedings of the European Respiratory Society, Munich, Germany,* 1729 (September 2014). Oral presentation.

5. N. J. Stewart, G. Leung, **G. Norquay**, H. Marshall, J. Parra-Robles, J. Wolber, R. F. Schulte, R. Condliffe, C. A. Elliot, I. Smith, C. G. Billings, P. S. Murphy, D. G. Kiely, M. K. Whyte, J. M. Wild, "Age-dependent changes in whole-lung septal thickness measured by 129Xe MRI: a comparison of healthy volunteers and subjects with ILD," *Proceedings of the European Respiratory Society, Munich, Germany,* 550 (September 2014).

6. N. J. Stewart, G. Leung, **G. Norquay**, H. Marshall, J. Parra-Robles, J. Wolber, R. F. Schulte, R. Condliffe, C. A. Elliot, P. S. Murphy, D. G. Kiely, M. K. Whyte, J. M. Wild, "Dissolved hyperpolarised ^{129}Xe MR as a probe of lung function in IPF and SSc," *Proceedings of the 21st Annual Meeting of ISMRM, Milan, Italy, USA*, 0775, (May 2014). Oral presentation.

7. N. J. Stewart, G. Leung, **G. Norquay**, H. Marshall, J. Parra-Robles, J. Wolber, R. F. Schulte, R. Condliffe, C. A. Elliot, P. S. Murphy, D. G. Kiely, M. K. Whyte, J. M. Wild, "Dissolved ^{129}Xe MRI – delayed gas

uptake indicates septal thickening in patients with idiopathic pulmonary fibrosis and systemic sclerosis," *Proceedings of the American Thoracic Society, San Diego, CA, USA* (May 2014). Poster presentation.

7. G. Leung, **G. Norquay**, R. F. Schulte, J. M. Wild, "Selective excitation of dissolved ^{129}Xe," *Proceedings of the 21st Annual Meeting of ISMRM, Salt Lake City, UT, USA*, 1449 (April 2013). Poster presentation.

8. X. Xu, G. Leung, **G. Norquay**, H. Marshall, J. Parra-Robles, J. M. Wild, "T_2^* measurements of dissolved-phase ^{129}Xe in the human lungs at 1.5T and 3T," *Proceedings of the 21st Annual Meeting of ISMRM, Salt Lake City, UT, USA*, 4119 (April 2013). Poster presentation.

9. J. M. Wild, H. Marshall, X. Xu, **G. Norquay**, S. R. Parnell, M. Clemence, P. D. Griffiths, J. Parra-Robles, "Imaging of lung structure and function in the same breath with triple nuclear (He-Xe-H) MRI," *Proceedings of the 21st Annual Meeting of ISMRM, Salt Lake City, UT, USA*, 0644 (April 2013). Poster presentation.

10. N. J. Stewart, G. Leung, **G. Norquay**, H. Marshall, J. Parra-Robles, J. Wolber, R. F. Schulte, R. Condliffe, C. A. Elliot, P. S. Murphy, D. G. Kiely, M. K. Whyte, J. M. Wild, "Dissolved ^{129}Xe lung MRI – delayed gas uptake indicates septal thickening in patients with interstitial lung disease," *19th Annual Meeting of the British Chapter of ISMRM, York, UK*, (September 2013). Oral presentation.

11. X. Xu, **G. Norquay**, H. Marshall, J. Parra-Robles, J. M. Wild, "T_2^* measurements of dissolved ^{129}Xe and simultaneous gas/dissolved ^{129}Xe imaging in the human lungs at 1.5T and 3T," *Proceedings of the 4th International Symposium of XeMAT, Dublin, Ireland*, (June 2012). Oral presentation.

12. J. Parra-Robles, **G. Norquay**, X. Xu, H. Marshall, J. M. Wild, "Non-Gaussian ^{129}Xe diffusion in human lungs," *Proceedings of the 4th International Symposium of XeMAT, Dublin, Ireland*, (June 2012). Oral presentation.

13. S. R. Parnell, **G. Norquay**, M. H. Deppe, J. Parra-Robles, J. M. Wild, "Enhancement of ^{129}Xe polarisation by off-resonant optical pumping," *Proceedings of the 21st Annual Meeting of ISMRM, Montreal, QC, Canada*, 0889 (May 2011). Poster presentation.

List of figures

List of tables

Bibliography

[1] G. Breit and I. I. Rabi, "Measurement of Nuclear Spin," *Physical Review,* vol. 38, pp. 2082-2083, 1931.

[2] I. I. Rabi and V. W. Cohen, "Measurement of Nuclear Spin by the Method of Molecular Beams The Nuclear Spin of Sodium," *Physical Review,* vol. 46, pp. 707-712, 1934.

[3] I. I. Rabi, "Space Quantization in a Gyrating Magnetic Field," *Physical Review,* vol. 51, pp. 652-654, 1937.

[4] F. Bloch, W. W. Hansen, and M. Packard, "Nuclear Induction," *Physical Review,* vol. 69, pp. 127-127, 1946.

[5] H. C. Torrey, E. M. Purcell, and R. V. Pound, "Theory of Magnetic Resonance Absorption by Nuclear Moments in Solids," *Physical Review,* vol. 69, pp. 680-680, 1946.

[6] J. T. Arnold, S. S. Dharmatti, and M. E. Packard, "Chemical Effects on Nuclear Induction Signals from Organic Compounds," *Journal of Chemical Physics,* vol. 19, pp. 507-507, 1951.

[7] P. C. Lauterbur, "Image Formation by Induced Local Interactions - Examples Employing Nuclear Magnetic-Resonance," *Nature,* vol. 242, pp. 190-191, 1973.

[8] M. S. Albert, G. D. Cates, B. Driehuys, W. Happer, B. Saam, C. S. Springer, Jr., and A. Wishnia, "Biological magnetic resonance imaging using laser-polarized 129Xe," *Nature,* vol. 370, pp. 199-201, 1994.

[9] M. Ebert, T. Grossmann, W. Heil, W. E. Otten, R. Surkau, M. Leduc, P. Bachert, M. V. Knopp, L. R. Schad, and M. Thelen, "Nuclear magnetic resonance imaging with hyperpolarised helium-3," *Lancet,* vol. 347, pp. 1297-1299, May 11 1996.

[10] J. P. Mugler, B. Driehuys, J. R. Brookeman, G. D. Cates, S. S. Berr, R. G. Bryant, T. M. Daniel, E. E. deLange, J. H. Downs, C. J. Erickson, W. Happer, D. P. Hinton, N. F. Kassel, T. Maier, C. D. Phillips, B. T. Saam, K. L. Sauer, and M. E. Wagshul, "MR imaging

and spectroscopy using hyperpolarized Xe-129 gas: Preliminary human results," *Magnetic Resonance in Medicine,* vol. 37, pp. 809-815, Jun 1997.

[11] H. Marshall, M. H. Deppe, J. Parra-Robles, S. Hillis, C. G. Billings, S. Rajaram, A. Swift, S. R. Miller, J. H. Watson, J. Wolber, D. A. Lipson, R. Lawson, and J. M. Wild, "Direct visualisation of collateral ventilation in COPD with hyperpolarised gas MRI," *Thorax,* January 27, 2012 2012.

[12] K. Ruppert, J. R. Brookeman, K. D. Hagspiel, and J. P. Mugler, 3rd, "Probing lung physiology with xenon polarization transfer contrast (XTC)," *Magn Reson Med,* vol. 44, pp. 349-57, Sep 2000.

[13] J. M. Wild, H. Marshall, X. Xu, G. Norquay, S. R. Parnell, M. Clemence, P. D. Griffiths, and J. Parra-Robles, "Simultaneous imaging of lung structure and function with triple-nuclear hybrid MR imaging," *Radiology,* vol. 267, pp. 251-5, Apr 2013.

[14] I. Dregely, J. P. Mugler, 3rd, I. C. Ruset, T. A. Altes, J. F. Mata, G. W. Miller, J. Ketel, S. Ketel, J. Distelbrink, F. W. Hersman, and K. Ruppert, "Hyperpolarized Xenon-129 gas-exchange imaging of lung microstructure: first case studies in subjects with obstructive lung disease," *J Magn Reson Imaging,* vol. 33, pp. 1052-62, May 2011.

[15] J. P. Mugler, 3rd and T. A. Altes, "Hyperpolarized 129Xe MRI of the human lung," *J Magn Reson Imaging,* vol. 37, pp. 313-31, Feb 2013.

[16] S. Mansson, J. Wolber, B. Driehuys, P. Wollmer, and K. Golman, "Characterization of diffusing capacity and perfusion of the rat lung in a lipopolysaccaride disease model using hyperpolarized 129Xe," *Magn Reson Med,* vol. 50, pp. 1170-9, Dec 2003.

[17] S. Patz, I. Muradyan, M. I. Hrovat, M. Dabaghyan, G. R. Washko, H. Hatabu, and J. P. Butler, "Diffusion of hyperpolarized 129Xe in the lung: a simplified model of 129Xe septal uptake and experimental results," *New Journal of Physics,* vol. 13, Jan 2011.

[18] Y. V. Chang, "MOXE: a model of gas exchange for hyperpolarized 129Xe magnetic resonance of the lung," *Magn Reson Med,* vol. 69, pp. 884-90, Mar 1 2013.

[19] N. J. Stewart, G. Leung, G. Norquay, H. Marshall, J. Parra-Robles, P. S. Murphy, R. F. Schulte, C. Elliot, R. Condliffe, P. D. Griffiths, D. G. Kiely, M. K. Whyte, J. Wolber, and J. M. Wild, "Experimental validation of the hyperpolarized 129Xe chemical shift saturation recovery technique in healthy volunteers and subjects with interstitial lung disease," *Magnetic Resonance in Medicine,* pp. n/a-n/a, 2014.

[20] W. Kilian, F. Seifert, and H. Rinneberg, "Dynamic NMR spectroscopy of hyperpolarized 129Xe in human brain analyzed by an uptake model," *Magn Reson Med,* vol. 51, pp. 843-7, Apr 2004.

[21] S. Peled, F. A. Jolesz, C. H. Tseng, L. Nascimben, M. S. Albert, and R. L. Walsworth, "Determinants of tissue delivery for 129Xe magnetic resonance in humans," *Magn Reson Med,* vol. 36, pp. 340-4, Sep 1996.

[22] K. S. Krane and D. Halliday, *Introductory nuclear physics*. New York: Wiley, 1987.

[23] M. H. Levitt, *Spin dynamics : basics of nuclear magnetic resonance*, 2nd ed. Chichester, England ; Hoboken, NJ: John Wiley & Sons, 2008.

[24] S. A. Smith, W. E. Palke, and J. T. Gerig, "The Hamiltonians of NMR. Part II," *Concepts in Magnetic Resonance,* vol. 4, pp. 181-204, 1992.

[25] C. P. Slichter, *Principles of magnetic resonance*, 3rd enl. and updated ed. Berlin ; New York: Springer, 1996.

[26] P. T. Callaghan, *Principles of nuclear magnetic resonance microscopy*. Oxford England: Oxford University Press, 1991.

[27] M. Mehring, *Principles of high-resolution NMR in solids*, 2nd, rev. and enl. ed. Berlin ; New York: Springer-Verlag, 1983.

[28] A. Abragam, *The principles of nuclear magnetism*. Oxford,: Clarendon Press, 1961.

[29] D. Canet, *Nuclear magnetic resonance : concepts and methods*. Chichester ; New York: Wiley, 1996.

[30] N. Bloembergen, E. M. Purcell, and R. V. Pound, "Relaxation Effects in Nuclear Magnetic Resonance Absorption," *Physical Review,* vol. 73, pp. 679-712, 1948.

[31] I. Solomon, "Relaxation Processes in a System of 2 Spins," *Physical Review,* vol. 99, pp. 559-565, 1955.

[32] J. E. Moore and G. Zouridakis, *Biomedical technology and devices handbook*. Boca Raton: CRC Press, 2004.

[33] A. Kastler, "Quelques suggestions concernant la production optique et la détection optique d'une inégalité de population des niveaux de quantifigation spatiale des atomes. Application à l'expérience de Stern et Gerlach et à la résonance magnétique," *J. Phys. Radium,* vol. 11, pp. 255-265, 1950.

[34] M. E. Weeks, "The discovery of the elements. XIII. Some spectroscopic discoveries," *Journal of Chemical Education,* vol. 9, p. 1413, 1932.

[35] T. J. Killian, "Thermionic Phenomena Caused by Vapors of Rubidium and Potassium," *Physical Review,* vol. 27, pp. 578-587, 1926.

[36] E. Rotenberg, D. W. Davis, Y. Amelin, S. Ghosh, and B. A. Bergquist, "Determination of the decay-constant of 87Rb by laboratory accumulation of 87Sr," *Geochimica et Cosmochimica Acta,* vol. 85, pp. 41-57, 2012.

[37] S. Appelt, A. B. Baranga, C. J. Erickson, M. V. Romalis, A. R. Young, and W. Happer, "Theory of spin-exchange optical pumping of He-3 and Xe-129," *Physical Review A,* vol. 58, pp. 1412-1439, Aug 1998.

[38] R. Benumof, "Optical Pumping Theory and Experiments," *American Journal of Physics,* vol. 33, pp. 151-160, 1965.

[39] G. P. Barwood, P. Gill, and W. R. C. Rowley, "Frequency Measurements on Optically Narrowed Rb-Stabilized Laser-Diodes at 780 Nm and 795 Nm," *Applied Physics B-Photophysics and Laser Chemistry,* vol. 53, pp. 142-147, Sep 1991.

[40] A. Banerjee, D. Das, and V. Natarajan, "Absolute frequency measurements of the D-1 lines in K-39, Rb-85, and Rb-87 with similar to 0.1 ppb uncertainty," *Europhysics Letters,* vol. 65, pp. 172-178, Jan 2004.

[41] E. Arimondo, M. Inguscio, and P. Violino, "Experimental Determinations of Hyperfine-Structure in Alkali Atoms," *Reviews of Modern Physics,* vol. 49, pp. 31-75, 1977.

[42] M. V. Romalis, E. Miron, and G. D. Cates, "Pressure broadening of Rb D-1 and D-2 lines by He-3, He-4, N-2, and Xe: Line cores and near wings," *Physical Review A,* vol. 56, pp. 4569-4578, Dec 1997.

[43] A. Sieradzan and F. A. Franz, "Quenching, Depolarization, and Transfer of Spin Polarization in Rb-N2 Collisions," *Physical Review A,* vol. 25, pp. 2985-2995, 1982.

[44] T. G. Walker and W. Happer, "Spin-exchange optical pumping of noble-gas nuclei," *Reviews of Modern Physics,* vol. 69, pp. 629-642, Apr 1997.

[45] W. Happer, E. Miron, S. Schaefer, D. Schreiber, W. A. Vanwijngaarden, and X. Zeng, "Polarization of the Nuclear Spins of Noble-Gas Atoms by Spin Exchange with Optically Pumped Alkali-Metal Atoms," *Physical Review A,* vol. 29, pp. 3092-3110, 1984.

[46] T. G. Walker, "Estimates of Spin-Exchange Parameters for Alkali-Metal Noble-Gas Pairs," *Physical Review A,* vol. 40, pp. 4959-4963, Nov 1 1989.

[47] R. M. Herman, "Theory of Spin Exchange between Optically Pumped Rubidium and Foreign Gas Nuclei," *Physical Review,* vol. 137, pp. 1062-1065, 1965.

[48] B. Driehuys, G. D. Cates, E. Miron, K. Sauer, D. K. Walter, and W. Happer, "High-volume production of laser-polarized Xe-129," *Applied Physics Letters,* vol. 69, pp. 1668-1670, Sep 16 1996.

[49] M. Haake, A. Pines, J. A. Reimer, and R. Seydoux, "Surface-enhanced NMR using continuous-flow laser-polarized xenon," *J Am Chem Soc,* vol. 119, pp. 11711-11712, Dec 3 1997.

[50] K. Knagge, J. Prange, and D. Raftery, "A continuously recirculating optical pumping apparatus for high xenon polarization and surface NMR studies," *Chemical Physics Letters,* vol. 397, pp. 11-16, Oct 11 2004.

[51] M. G. Mortuza, S. Anala, G. E. Pavlovskaya, T. J. Dieken, and T. Meersmann, "Spin-exchange optical pumping of high-density xenon-129," *Journal of Chemical Physics,* vol. 118, pp. 1581-1584, Jan 22 2003.

[52] I. C. Ruset, S. Ketel, and F. W. Hersman, "Optical pumping system design for large production of hyperpolarized Xe-129," *Physical Review Letters,* vol. 96, Feb 10 2006.

[53] G. Schrank, Z. Ma, A. Schoeck, and B. Saam, "Characterization of a low-pressure high-capacity 129Xe flow-through polarizer," *Physical Review A,* vol. 80, Dec 2009.

[54] A. L. Zook, B. B. Adhyaru, and C. R. Bowers, "High capacity production of $> 65\%$ spin polarized xenon-129 for NMR spectroscopy and imaging," *Journal of Magnetic Resonance,* vol. 159, pp. 175-182, Dec 2002.

[55] P. Nikolaou, A. M. Coffey, K. Ranta, L. L. Walkup, B. M. Gust, M. J. Barlow, M. S. Rosen, B. M. Goodson, and E. Y. Chekmenev, "Multidimensional Mapping of Spin-Exchange Optical Pumping in Clinical-Scale Batch-Mode Xe-129 Hyperpolarizers," *Journal of Physical Chemistry B,* vol. 118, pp. 4809-4816, May 8 2014.

[56] P. Nikolaou, A. M. Coffey, L. L. Walkup, B. M. Gust, N. Whiting, H. Newton, S. Barcus, I. Muradyan, M. Dabaghyan, G. D. Moroz, M. S. Rosen, S. Patz, M. J. Barlow, E. Y. Chekmenev, and B. M. Goodson, "Near-unity nuclear polarization with an open-source Xe-129 hyperpolarizer for NMR and MRI," *Proc Natl Acad Sci U S A,* vol. 110, pp. 14150-14155, Aug 27 2013.

[57] S. R. Parnell, M. H. Deppe, J. Parra-Robles, and J. M. Wild, "Enhancement of Xe-129 polarization by off-resonant spin exchange optical pumping," *Journal of Applied Physics,* vol. 108, Sep 15 2010.

[58] N. Whiting, P. Nikolaou, N. A. Eschmann, B. M. Goodson, and M. J. Barlow, "Interdependence of in-cell xenon density and temperature during Rb/Xe-129 spin-exchange optical pumping using VHG-narrowed laser diode arrays," *J Magn Reson,* vol. 208, pp. 298-304, Feb 2011.

[59] S. S. Kaushik, Z. I. Cleveland, G. P. Cofer, G. Metz, D. Beaver, J. Nouls, M. Kraft, W. Auffermann, J. Wolber, H. P. McAdams, and B. Driehuys, "Diffusion-weighted hyperpolarized 129Xe MRI in healthy volunteers and subjects with chronic obstructive pulmonary disease," *Magn Reson Med,* vol. 65, pp. 1154-65, Apr 2011.

[60] F. W. Hersman, I. C. Ruset, S. Ketel, I. Muradian, S. D. Covrig, J. Distelbrink, W. Porter, D. Watt, J. Ketel, J. Brackett, A. Hope, and S. Patz, "Large production system for hyperpolarized Xe-129 for human lung imaging studies," *Academic Radiology,* vol. 15, pp. 683-692, Jun 2008.

[61] I. A. Nelson and T. G. Walker, "Rb-Xe spin relaxation in dilute Xe mixtures," *Physical Review A,* vol. 65, Jan 2002.

[62] W. Happer, "Optical-Pumping," *Reviews of Modern Physics,* vol. 44, pp. 169-249, 1972.

[63] A. B. A. Baranga, S. Appelt, M. V. Romalis, C. J. Erickson, A. R. Young, G. D. Cates, and W. Happer, "Polarization of He-3 by spin exchange with optically pumped Rb and K vapors," *Physical Review Letters,* vol. 80, pp. 2801-2804, Mar 30 1998.

[64] W. C. Chen, T. R. Gentile, T. G. Walker, and E. Babcock, "Spin-exchange optical pumping of 3He with Rb-K mixtures and pure K," *Physical Review A,* vol. 75, p. 013416, 2007.

[65] I. C. Ruset, "Hyperpolarized 129Xe Production and Applications," University of New Hampshire, 2005.

[66] Y. Y. Jau, N. N. Kuzma, and W. Happer, "Magnetic decoupling of Xe-129-Rb and Xe-129-Cs binary spin exchange," *Physical Review A,* vol. 67, Feb 2003.

[67] Y. Y. Jau, N. N. Kuzma, and W. Happer, "High-field measurement of the Xe-129-Rb spin-exchange rate due to binary collisions," *Physical Review A,* vol. 66, Nov 2002.

[68] G. D. Cates, R. J. Fitzgerald, A. S. Barton, P. Bogorad, M. Gatzke, N. R. Newbury, and B. Saam, "Rb Xe-129 Spin-Exchange Rates Due to Binary and 3-Body Collisions at High Xe Pressures," *Physical Review A,* vol. 45, pp. 4631-4639, Apr 1 1992.

[69] C. V. Rice and D. Raftery, "Rubidium-xenon spin exchange and relaxation rates measured at high pressure and high magnetic field," *Journal of Chemical Physics,* vol. 117, pp. 5632-5641, Sep 22 2002.

[70] X. Zeng, Z. Wu, T. Call, E. Miron, D. Schreiber, and W. Happer, "Experimental-Determination of the Rate Constants for Spin Exchange between Optically Pumped K, Rb, and Cs Atoms and Xe-129 Nuclei

in Alkali-Metal Noble-Gas Vanderwaals Molecules," *Physical Review A,* vol. 31, pp. 260-278, 1985.

[71] B. Driehuys, G. D. Cates, and W. Happer, "Surface Relaxation Mechanisms of Laser-Polarized Xe-129," *Physical Review Letters,* vol. 74, pp. 4943-4946, Jun 12 1995.

[72] S. R. Parnell, E. B. Woolley, S. Boag, and C. D. Frost, "Digital pulsed NMR spectrometer for nuclear spin-polarized 3He and other hyperpolarized gases," *Measurement Science & Technology,* vol. 19, Apr 2008.

[73] B. Chann, I. Nelson, and T. G. Walker, "Frequency-narrowed external-cavity diode-laser-array bar," *Optics Letters,* vol. 25, pp. 1352-1354, Sep 15 2000.

[74] S. R. Parnell, M. H. Deppe, J. Parra-Robles, and J. M. Wild, "Enhancement of 129Xe polarization by off-resonant spin exchange optical pumping," *Journal of Applied Physics,* vol. 108, Sep 15 2010.

[75] S. R. Parnell, S. Boag, T. J. McKetterick, and J. M. Wild, "Low magnetic field manipulation of 3 He spins using digital methods," *Journal of Physics: Conference Series,* vol. 294, p. 012010, 2011.

[76] K. Teh, N. de Zanche, and J. M. Wild, "Radiation-damping effects in a birdcage resonator with hyperpolarised 3He gas NMR at 1.5T," *Journal of Magnetic Resonance,* vol. 185, pp. 164-172, 2007.

[77] M. E. Wagshul and T. E. Chupp, "Laser Optical-Pumping of High-Density Rb in Polarized He-3 Targets," *Physical Review A,* vol. 49, pp. 3854-3869, May 1994.

[78] D. K. Walter, W. M. Griffith, and W. Happer, "Energy Transport in High-Density Spin-Exchange Optical Pumping Cells," *Physical Review Letters,* vol. 86, pp. 3264-3267, 2001.

[79] B. Larson, O. Hausser, P. P. J. Delheij, D. M. Whittal, and D. Thiessen, "Optical-Pumping of Rb in the Presence of High-Pressure He-3 Buffer Gas," *Physical Review A,* vol. 44, pp. 3108-3118, Sep 1 1991.

[80] B. Chann, E. Babcock, L. W. Anderson, and T. G. Walker, "Skew light propagation in optically thick optical pumping cells," *Physical Review A,* vol. 66, Sep 2002.

[81] A. Fink, D. Baumer, and E. Brunner, "Production of hyperpolarized xenon in a static pump cell: Numerical simulations and experiments," *Physical Review A,* vol. 72, Nov 2005.

[82] S. R. Parnell, M. H. Deppe, S. Ajraoui, J. Parra-Robles, S. Boag, and J. M. Wild, "Measurement of laser heating in spin exchange optical pumping by NMR diffusion sensitization gradients," *Journal of Applied Physics,* vol. 107, May 1 2010.

[83] W. Zheng, Z. I. Cleveland, H. E. Möller, and B. Driehuys, "Gradient-induced longitudinal relaxation of hyperpolarized noble gases in the fringe fields of superconducting magnets used for magnetic resonance," *Journal of Magnetic Resonance,* vol. 208, pp. 284-290, 2011.

[84] N. D. Bhaskar, W. Happer, and T. McClelland, "Efficiency of Spin Exchange Between Rubidium Spins And Xe-129 Nuclei in a Gas," *Physical Review Letters,* vol. 49, pp. 25-28, 1982.

[85] E. Babcock, I. Nelson, S. Kadlecek, B. Driehuys, L. W. Anderson, F. W. Hersman, and T. G. Walker, "Hybrid Spin-Exchange Optical Pumping of 3He," *Physical Review Letters,* vol. 91, p. 123003, 2003.

[86] J. M. Wild, M. N. Paley, M. Viallon, W. G. Schreiber, E. J. van Beek, and P. D. Griffiths, "k-space filtering in 2D gradient-echo breath-hold hyperpolarized 3He MRI: spatial resolution and signal-to-noise ratio considerations," *Magn Reson Med,* vol. 47, pp. 687-95, Apr 2002.

[87] A. Fink and E. Brunner, "Optimization of continuous flow pump cells used for the production of hyperpolarized 129Xe: A theoretical study," *Applied Physics B: Lasers and Optics,* vol. 89, pp. 65-71, 2007.

[88] M. E. Wagshul and T. E. Chupp, "Optical pumping of high-density Rb with a broadband dye laser and GaAlAs diode laser arrays: Application to 3He polarization," *Physical Review A,* vol. 40, pp. 4447-4454, 1989.

[89] N. N. Kuzma, B. Patton, K. Raman, and W. Happer, "Fast nuclear spin relaxation in hyperpolarized solid Xe-129," *Physical Review Letters,* vol. 88, Apr 8 2002.

[90] G. D. Cates, D. R. Benton, M. Gatzke, W. Happer, K. C. Hasson, and N. R. Newbury, "Laser Production of Large Nuclear-Spin Polarization

in Frozen Xenon," *Physical Review Letters,* vol. 65, pp. 2591-2594, Nov 12 1990.

[91] M. Gatzke, G. D. Cates, B. Driehuys, D. Fox, W. Happer, and B. Saam, "Extraordinarily Slow Nuclear-Spin Relaxation in Frozen Laser-Polarized Xe-129," *Physical Review Letters,* vol. 70, pp. 690-693, Feb 1 1993.

[92] M. Limes, Z. Ma, E. Sorte, and B. Saam, "Crystallite Morphology and Longitudinal Relaxation in Soild 129Xe," in *Xemat*, Dublin, 2012, pp. P12, page 88.

[93] P. Mills and R. Plastow, "Single-Mode Operation of 1.55-Mu-M Semiconductor-Lasers Using a Volume Holographic Grating," *Electronics Letters,* vol. 21, pp. 648-649, 1985.

[94] G. J. Steckman, W. Liu, R. Platz, D. Schroeder, C. Moser, and F. Havermeyer, "Volume holographic grating wavelength stabilized laser diodes," *Ieee Journal of Selected Topics in Quantum Electronics,* vol. 13, pp. 672-678, May-Jun 2007.

[95] D. McMillen, T. Hudson, J. Wagner, and J. Singleton, "Holographic recording in specially doped lithium niobate crystals," *Optics Express,* vol. 2, pp. 491-502, 1998.

[96] K. Buse, S. Breer, H. Vogt, I. Nee, and E. Krätzig, "Thermally-fixed volume-phase holograms in lithium-niobate crystals for optical interconnects," in *Conference on Lasers and Electro-Optics*, Baltimore, Maryland, 1999, p. CWO2.

[97] B. L. Volodin, S. V. Dolgy, E. D. Melnik, E. Downs, J. Shaw, and V. S. Ban, "Wavelength stabilization and spectrum narrowing of high-power multimode laser diodes and arrays by use of volume Bragg gratings," *Optics Letters,* vol. 29, pp. 1891-1893, Aug 15 2004.

[98] L. Vaissie, "Brightlock® Pump Diodes Take The Heat Out Of High Power Lasers," *Photonics Online White Paper,* 2010.

[99] M. S. Albert, D. Balamore, D. F. Kacher, A. K. Venkatesh, and F. A. Jolesz, "Hyperpolarized 129Xe T1 in oxygenated and deoxygenated blood," *NMR in Biomedicine,* vol. 13, pp. 407-414, 2000.

[100] M. S. Albert, D. F. Kacher, D. Balamore, A. K. Venkatesh, and F. A. Jolesz, "T1 of 129Xe in blood and the role of oxygenation," *J Magn Reson,* vol. 140, pp. 264-73, Sep 1999.

[101] J. Wolber, A. Cherubini, A. S. Dzik-Jurasz, M. O. Leach, and A. Bifone, "Spin-lattice relaxation of laser-polarized xenon in human blood," *Proc Natl Acad Sci U S A,* vol. 96, pp. 3664-9, Mar 30 1999.

[102] J. Wolber, A. Cherubini, M. O. Leach, and A. Bifone, "On the oxygenation-dependent 129Xe T1 in blood," *NMR Biomed,* vol. 13, pp. 234-7, Jun 2000.

[103] C. H. Tseng, S. Peled, L. Nascimben, E. Oteiza, R. L. Walsworth, and F. A. Jolesz, "NMR of laser-polarized 129Xe in blood foam," *J Magn Reson,* vol. 126, pp. 79-86, May 1997.

[104] R. E. Benesch, R. Benesch, and M. E. Williamson, "The influence of reversible oxygen binding on the interaction between hemoglobin submits," *Proc Natl Acad Sci U S A,* vol. 48, pp. 2071-5, Dec 15 1962.

[105] D. Voet and J. G. Voet, *Biochemistry*, 4th ed. Hoboken, NJ: John Wiley & Sons, 2011.

[106] A. L. Lehninger, D. L. Nelson, and M. M. Cox, *Lehninger principles of biochemistry*, 6th ed. New York: W.H. Freeman, 2013.

[107] G. Fermi, M. F. Perutz, B. Shaanan, and R. Fourme, "The Crystal-Structure of Human Deoxyhemoglobin at 1.74a Resolution," *Journal of Molecular Biology,* vol. 175, pp. 159-174, 1984.

[108] B. Shaanan, "Structure of Human Oxyhemoglobin at 2.1 a Resolution," *Journal of Molecular Biology,* vol. 171, pp. 31-59, 1983.

[109] G. J. Ewing and S. Maestas, "Thermodynamics of Absorption of Xenon by Myoglobin," *Journal of Physical Chemistry,* vol. 74, pp. 2341-2344, 1970.

[110] M. Schiltz, R. Fourme, I. Broutin, and T. Prange, "The Catalytic Site of Serine Proteinases as a Specific Binding Cavity for Xenon," *Structure,* vol. 3, pp. 309-316, Mar 15 1995.

[111] T. Prange, M. Schiltz, L. Pernot, N. Colloc'h, S. Longhi, W. Bourguet, and R. Fourme, "Exploring hydrophobic sites in proteins with xenon or krypton," *Proteins-Structure Function and Genetics,* vol. 30, pp. 61-73, Jan 1 1998.

[112] J. Cohen, A. Arkhipov, R. Braun, and K. Schulten, "Imaging the Migration Pathways for O2, CO, NO, and Xe Inside Myoglobin," *Biophysical Journal,* vol. 91, pp. 1844-1857, 2006.

[113] V. M. Luna, J. A. Fee, A. A. Deniz, and C. D. Stout, "Mobility of Xe Atoms within the Oxygen Diffusion Channel of Cytochrome ba3 Oxidase," *Biochemistry,* vol. 51, pp. 4669-4676, 2012.

[114] M. D. Salter, G. C. Blouin, J. Soman, E. W. Singleton, S. Dewilde, L. Moens, A. Pesce, M. Nardini, M. Bolognesi, and J. S. Olson, "Determination of ligand pathways in globins: apolar tunnels versus polar gates," *J Biol Chem,* vol. 287, pp. 33163-78, Sep 28 2012.

[115] I. Birukou, D. H. Maillett, A. Birukova, and J. S. Olson, "Modulating Distal Cavities in the α and β Subunits of Human HbA Reveals the Primary Ligand Migration Pathway," *Biochemistry,* vol. 50, pp. 7361-7374, 2011.

[116] B. P. Schoenborn, H. C. Watson, and J. C. Kendrew, "Binding of Xenon to Sperm Whale Myoglobin," *Nature,* vol. 207, pp. 28-30, 1965.

[117] B. P. Schoenborn, "Binding of Xenon to Horse Haemoglobin," *Nature,* vol. 208, pp. 760-762, 1965.

[118] R. F. Tilton, Jr., I. D. Kuntz, Jr., and G. A. Petsko, "Cavities in proteins: structure of a metmyoglobin-xenon complex solved to 1.9 A," *Biochemistry,* vol. 23, pp. 2849-57, Jun 19 1984.

[119] D. de Sanctis, S. Dewilde, A. Pesce, L. Moens, P. Ascenzi, T. Hankeln, T. Burmester, and M. Bolognesi, "Mapping protein matrix cavities in human cytoglobin through Xe atom binding," *Biochemical and Biophysical Research Communications,* vol. 316, pp. 1217-1221, 2004.

[120] C. Savino, A. E. Miele, F. Draghi, K. A. Johnson, G. Sciara, M. Brunori, and B. Vallone, "Pattern of cavities in globins: The case of human hemoglobin," *Biopolymers,* vol. 91, pp. 1097-1107, 2009.

[121] D. G. Davis, M. E. Perlman, and R. E. London, "Direct measurements of the dissociation-rate constant for inhibitor-enzyme complexes via the T1 rho and T2 (CPMG) methods," *J Magn Reson B,* vol. 104, pp. 266-75, Jul 1994.

[122] O. Millet, J. P. Loria, C. D. Kroenke, M. Pons, and A. G. Palmer, "The static magnetic field dependence of chemical exchange

linebroadening defines the NMR chemical shift time scale," *J Am Chem Soc,* vol. 122, pp. 2867-2877, Mar 29 2000.

[123] A. Bifone, Y. Q. Song, R. Seydoux, R. E. Taylor, B. M. Goodson, T. Pietrass, T. F. Budinger, G. Navon, and A. Pines, "NMR of laser-polarized xenon in human blood," *Proc Natl Acad Sci U S A,* vol. 93, pp. 12932-6, Nov 12 1996.

[124] R. Y. Chen, F. C. Fan, S. Kim, K. M. Jan, S. Usami, and S. Chien, "Tissue-blood partition coefficient for xenon: temperature and hematocrit dependence," *J Appl Physiol Respir Environ Exerc Physiol,* vol. 49, pp. 178-83, Aug 1980.

[125] M. E. Fabry and M. Eisenstadt, "Water exchange between red cells and plasma. Measurement by nuclear magnetic relaxation," *Biophys J,* vol. 15, pp. 1101-10, Nov 1975.

[126] D. E. Woessner, "Nuclear Transfer Effects in Nuclear Magnetic Resonance Pulse Experiments," *Journal of Chemical Physics,* vol. 35, pp. 41-47, 1961.

[127] G. Norquay, S. R. Parnell, X. Xu, J. Parra-Robles, and J. M. Wild, "Optimized production of hyperpolarized 129Xe at 2 bars for in vivo lung magnetic resonance imaging," *Journal of Applied Physics,* vol. 113, p. 044908, 2013.

[128] Z. I. Cleveland, H. E. Moller, L. W. Hedlund, and B. Driehuys, "Continuously infusing hyperpolarized 129Xe into flowing aqueous solutions using hydrophobic gas exchange membranes," *J Phys Chem B,* vol. 113, pp. 12489-99, Sep 17 2009.

[129] Z. I. Cleveland, H. E. Moller, L. W. Hedlund, J. C. Nouls, M. S. Freeman, Y. Qi, and B. Driehuys, "In vivo MR imaging of pulmonary perfusion and gas exchange in rats via continuous extracorporeal infusion of hyperpolarized 129Xe," *PLoS One,* vol. 7, p. e31306, 2012.

[130] G. R. Kelman, "Digital computer subroutine for the conversion of oxygen tension into saturation," *J Appl Physiol,* vol. 21, pp. 1375-6, Jul 1966.

[131] L. Forlani, C. Ioppolo, E. Antonini, and M. A. Marini, "Calorimetric studies of oxyhemoglobin dissociation. II. Erythrocytic oxygen

depletion by sodium dithionite," *Journal of Inorganic Biochemistry,* vol. 23, pp. 109-117, 1985.

[132] C. Christoforides, L. H. Laasberg, and J. Hedley-Whyte, "Effect of temperature on solubility of O2 in human plasma," *J Appl Physiol,* vol. 26, pp. 56-60, Jan 1969.

[133] D. C. Look and D. R. Locker, "Time Saving in Measurement of NMR and EPR Relaxation Times," *Review of Scientific Instruments,* vol. 41, pp. 250-251, 1970.

[134] I. Kay and R. M. Henkelman, "Practical implementation and optimization of one-shot T1 imaging," *Magn Reson Med,* vol. 22, pp. 414-24, Dec 1991.

[135] C. Christoforides and J. Hedley-Whyte, "Effect of temperature and hemoglobin concentration on solubility of O2 in blood," *J Appl Physiol,* vol. 27, pp. 592-6, Nov 1969.

[136] L. Pauling and C. D. Coryell, "The Magnetic Properties and Structure of Hemoglobin, Oxyhemoglobin and Carbonmonoxyhemoglobin," *Proc Natl Acad Sci U S A,* vol. 22, pp. 210-6, Apr 1936.

[137] C. D. Coryell, L. Pauling, and R. W. Dodson, "The Magnetic Properties of Intermediates in the Reactions of Hemoglobin," *The Journal of Physical Chemistry,* vol. 43, pp. 825-839, 1939/07/01 1939.

[138] J. Astrup, B. K. Siesjo, and L. Symon, "Thresholds in cerebral ischemia - the ischemic penumbra," *Stroke,* vol. 12, pp. 723-5, Nov-Dec 1981.

[139] Y. Q. Song, "Spin polarization-induced nuclear Overhauser effect: An application of spin-polarized xenon and helium," *Concepts in Magnetic Resonance,* vol. 12, pp. 6-20, 2000.

[140] D. D. Ebbing and S. D. Gammon, *General chemistry*, 6th ed. Boston: Houghton Mifflin, 1999.

[141] S. H. Rahimtoola, "The hibernating myocardium," *Am Heart J,* vol. 117, pp. 211-21, Jan 1989.

[142] R. H. Thomlinson and L. H. Gray, "The histological structure of some human lung cancers and the possible implications for radiotherapy," *Br J Cancer,* vol. 9, pp. 539-49, Dec 1955.

[143] K. Hoenderdos and A. Condliffe, "The neutrophil in chronic obstructive pulmonary disease," *Am J Respir Cell Mol Biol,* vol. 48, pp. 531-9, May 2013.

[144] F. Kreuzer and C. G. Nessler, Jr., "Method of polarographic in vivo continuous recording of blood oxygen tension," *Science,* vol. 128, pp. 1005-6, Oct 24 1958.

[145] A. Chieregato, L. Targa, and R. Zatelli, "Limitations of jugular bulb oxyhemoglobin saturation without intracranial pressure monitoring in subarachnoid hemorrhage," *J Neurosurg Anesthesiol,* vol. 8, pp. 21-5, Jan 1996.

[146] C. S. Kidwell, J. R. Alger, and J. L. Saver, "Beyond mismatch: evolving paradigms in imaging the ischemic penumbra with multimodal magnetic resonance imaging," *Stroke,* vol. 34, pp. 2729-35, Nov 2003.

[147] S. Rockwell, I. T. Dobrucki, E. Y. Kim, S. T. Marrison, and V. T. Vu, "Hypoxia and radiation therapy: past history, ongoing research, and future promise," *Curr Mol Med,* vol. 9, pp. 442-58, May 2009.

[148] J. F. Dunn, J. A. O'Hara, Y. Zaim-Wadghiri, H. Lei, M. E. Meyerand, O. Y. Grinberg, H. Hou, P. J. Hoopes, E. Demidenko, and H. M. Swartz, "Changes in oxygenation of intracranial tumors with carbogen: a BOLD MRI and EPR oximetry study," *J Magn Reson Imaging,* vol. 16, pp. 511-21, Nov 2002.

[149] N. J. Taylor, H. Baddeley, K. A. Goodchild, M. E. Powell, M. Thoumine, L. A. Culver, J. J. Stirling, M. I. Saunders, P. J. Hoskin, H. Phillips, A. R. Padhani, and J. R. Griffiths, "BOLD MRI of human tumor oxygenation during carbogen breathing," *J Magn Reson Imaging,* vol. 14, pp. 156-63, Aug 2001.

[150] C. Baudelet and B. Gallez, "How does blood oxygen level-dependent (BOLD) contrast correlate with oxygen partial pressure (pO2) inside tumors?," *Magn Reson Med,* vol. 48, pp. 980-6, Dec 2002.

[151] S. Matsumoto, H. Yasui, S. Batra, Y. Kinoshita, M. Bernardo, J. P. Munasinghe, H. Utsumi, R. Choudhuri, N. Devasahayam, S. Subramanian, J. B. Mitchell, and M. C. Krishna, "Simultaneous imaging of tumor oxygenation and microvascular permeability using

Overhauser enhanced MRI," *Proc Natl Acad Sci U S A,* vol. 106, pp. 17898-903, Oct 20 2009.

[152] M. C. Krishna, S. English, K. Yamada, J. Yoo, R. Murugesan, N. Devasahayam, J. A. Cook, K. Golman, J. H. Ardenkjaer-Larsen, S. Subramanian, and J. B. Mitchell, "Overhauser enhanced magnetic resonance imaging for tumor oximetry: coregistration of tumor anatomy and tissue oxygen concentration," *Proc Natl Acad Sci U S A,* vol. 99, pp. 2216-21, Feb 19 2002.

[153] S. Hunjan, D. Zhao, A. Constantinescu, E. W. Hahn, P. P. Antich, and R. P. Mason, "Tumor oximetry: demonstration of an enhanced dynamic mapping procedure using fluorine-19 echo planar magnetic resonance imaging in the Dunning prostate R3327-AT1 rat tumor," *Int J Radiat Oncol Biol Phys,* vol. 49, pp. 1097-108, Mar 15 2001.

[154] A. J. Deninger, B. Eberle, M. Ebert, T. Grossmann, W. Heil, H. Kauczor, L. Lauer, K. Markstaller, E. Otten, J. Schmiedeskamp, W. Schreiber, R. Surkau, M. Thelen, and N. Weiler, "Quantification of regional intrapulmonary oxygen partial pressure evolution during apnea by 3He MRI," *J Magn Reson,* vol. 141, pp. 207-16, Dec 1999.

[155] S. B. Sherriff, R. C. Smart, and I. Taylor, "Clinical study of liver blood flow in man measured by 133Xe clearance after portal vein injection," *Gut,* vol. 18, pp. 1027-31, Dec 1977.

[156] R. E. Latchaw, H. Yonas, S. L. Pentheny, and D. Gur, "Adverse reactions to xenon-enhanced CT cerebral blood flow determination," *Radiology,* vol. 163, pp. 251-4, Apr 1987.

[157] B. Driehuys, S. Martinez-Jimenez, Z. I. Cleveland, G. M. Metz, D. M. Beaver, J. C. Nouls, S. S. Kaushik, R. Firszt, C. Willis, K. T. Kelly, J. Wolber, M. Kraft, and H. P. McAdams, "Chronic Obstructive Pulmonary Disease: Safety and Tolerability of Hyperpolarized 129Xe MR Imaging in Healthy Volunteers and Patients," *Radiology,* vol. 262, pp. 279-289, Jan 2012.

[158] J. Wolber, D. J. McIntyre, L. M. Rodrigues, P. Carnochan, J. R. Griffiths, M. O. Leach, and A. Bifone, "In vivo hyperpolarized 129Xe NMR spectroscopy in tumors," *Magn Reson Med,* vol. 46, pp. 586-91, Sep 2001.

[159] K. Nakamura, Y. Kondoh, A. Wakai, J. Kershaw, D. Wright, and I. Kanno, "129Xe spectra from the heads of rats with and without ligation of the external carotid and pterygopalatine arteries," *Magn Reson Med,* vol. 53, pp. 528-34, Mar 2005.

[160] K. W. Miller, N. V. Reo, A. J. Schoot Uiterkamp, D. P. Stengle, T. R. Stengle, and K. L. Williamson, "Xenon NMR: chemical shifts of a general anesthetic in common solvents, proteins, and membranes," *Proc Natl Acad Sci U S A,* vol. 78, pp. 4946-9, Aug 1981.

[161] S. D. Swanson, M. S. Rosen, K. P. Coulter, R. C. Welsh, and T. E. Chupp, "Distribution and dynamics of laser-polarized ^{129}Xe magnetization in vivo," *Magn Reson Med,* vol. 42, pp. 1137-45, Dec 1999.

[162] S. Patz, I. Muradian, M. I. Hrovat, I. C. Ruset, G. Topulos, S. D. Covrig, E. Frederick, H. Hatabu, F. W. Hersman, and J. P. Butler, "Human pulmonary imaging and spectroscopy with hyperpolarized 129Xe at 0.2T," *Acad Radiol,* vol. 15, pp. 713-27, Jun 2008.

[163] J. Wolber, A. Cherubini, M. O. Leach, and A. Bifone, "Hyperpolarized 129Xe NMR as a probe for blood oxygenation," *Magn Reson Med,* vol. 43, pp. 491-6, Apr 2000.

[164] M. F. Perutz, "Stereochemistry of cooperative effects in haemoglobin," *Nature,* vol. 228, pp. 726-39, Nov 21 1970.

[165] M. F. Perutz and H. Lehmann, "Molecular pathology of human haemoglobin," *Nature,* vol. 219, pp. 902-9, Aug 31 1968.

[166] A. D. Buckingham, T. Schaefer, and W. G. Schneider, "Solvent Effects in Nuclear Magnetic Resonance Spectra," *Journal of Chemical Physics,* vol. 32, pp. 1227-1233, 1960.

[167] J. Jokisaari, "Nmr of Noble-Gases Dissolved in Isotropic and Anisotropic Liquids," *Progress in Nuclear Magnetic Resonance Spectroscopy,* vol. 26, pp. 1-26, 1994.

[168] M. Luhmer and K. Bartik, "Group contribution analysis of xenon NMR solvent shifts," *Journal of Physical Chemistry A,* vol. 101, pp. 5278-5283, Jul 17 1997.

[169] M. J. Stephen, "The effect of molecular interaction on magnetic shielding constants," *Molecular Physics,* vol. 1, pp. 223-232, 1958/07/01 1958.

[170] C. J. Jameson and A. C. de Dios, "Abinitio calculations of the intermolecular chemical shift in nuclear magnetic resonance in the gas phase and for adsorbed species," *The Journal of Chemical Physics,* vol. 97, pp. 417-434, 1992.

[171] B. B. Howard, B. Linder, and M. T. Emerson, "Effect of Dispersion Interaction on Nuclear Magnetic Resonance Shifts," *Journal of Chemical Physics,* vol. 36, pp. 485-490, 1962.

[172] F. H. A. Rummens, "Use of Bayliss-Mcrae Dispersion Model in Nmr Solvent Effects," *Chemical Physics Letters,* vol. 31, pp. 596-598, 1975.

[173] Y. H. Lim, A. R. Calhoun, and A. D. King, "NMR chemical shifts of Xe-129 dissolved in liquid haloalkanes and their mixtures," *Applied Magnetic Resonance,* vol. 12, pp. 555-574, 1997.

[174] O. Zhernovaya, O. Sydoruk, V. Tuchin, and A. Douplik, "The refractive index of human hemoglobin in the visible range," *Phys Med Biol,* vol. 56, pp. 4013-21, Jul 7 2011.

[175] G. Lang and W. Marshall, "Mossbauer Effect in Some Haemoglobin Compounds," *Journal of Molecular Biology,* vol. 18, pp. 385-404, 1966.

[176] A. J. Deninger, B. Eberle, M. Ebert, T. Grossmann, G. Hanisch, W. Heil, H. U. Kauczor, K. Markstaller, E. Otten, W. Schreiber, R. Surkau, and N. Weiler, "3He-MRI-based measurements of intrapulmonary pO2 and its time course during apnea in healthy volunteers: first results, reproducibility, and technical limitations," *NMR Biomed,* vol. 13, pp. 194-201, Jun 2000.

[177] K. Cieslar, H. Alsaid, V. Stupar, S. Gaillard, E. Canet-Soulas, R. Fissoune, and Y. Cremillieux, "Measurement of nonlinear pO2 decay in mouse lungs using 3He-MRI," *NMR Biomed,* vol. 20, pp. 383-91, May 2007.

[178] K. Ruppert, "Detecting Pulmonary Capillary Blood Pulsations Using Hyperpolarized 129Xe CSSR," in *Proc. ISMRM*, 2013.

[179] M. L. Mazzanti, R. P. Walvick, X. Zhou, Y. P. Sun, N. Shah, J. Mansour, J. Gereige, and M. S. Albert, "Distribution of

Hyperpolarized Xenon in the Brain Following Sensory Stimulation: Preliminary MRI Findings," *PLoS One,* vol. 6, Jul 15 2011.